
Electronic Theses and Dissertations, 2004-2019

2018

Characterization, Classification, and Genesis of Seismocardiographic Signals

Amirtaha Taebi
University of Central Florida



Part of the [Mechanical Engineering Commons](#)

Find similar works at: <https://stars.library.ucf.edu/etd>

University of Central Florida Libraries <http://library.ucf.edu>

This Doctoral Dissertation (Open Access) is brought to you for free and open access by STARS. It has been accepted for inclusion in Electronic Theses and Dissertations, 2004-2019 by an authorized administrator of STARS. For more information, please contact STARS@ucf.edu.

STARS Citation

Taebi, Amirtaha, "Characterization, Classification, and Genesis of Seismocardiographic Signals" (2018). *Electronic Theses and Dissertations, 2004-2019*. 5832.

<https://stars.library.ucf.edu/etd/5832>

CHARACTERIZATION, CLASSIFICATION, AND GENESIS OF
SEISMOCARDIOGRAPHIC SIGNALS

by

AMIRTAHA TAEBI

M.Sc. in Bioengineering, Politecnico di Milano, Italy, 2013

B.Sc. in Mechanical Engineering, Sharif University of Technology, Iran, 2010

A dissertation submitted in partial fulfillment of the requirements
for the degree of Doctor of Philosophy
in the Department of Mechanical and Aerospace Engineering
in the College of Engineering & Computer Science
at the University of Central Florida
Orlando, Florida

Spring Term
2018

Major Professor: Hansen A. Mansy

© 2018 Amirtaha Taebi

ABSTRACT

Seismocardiographic (SCG) signals are the acoustic and vibration induced by cardiac activity measured non-invasively at the chest surface. These signals may offer a method for diagnosing and monitoring heart function. Successful classification of SCG signals in health and disease depends on accurate signal characterization and feature extraction.

In this study, SCG signal features were extracted in the time, frequency, and time-frequency domains. Different methods for estimating time-frequency features of SCG were investigated. Results suggested that the polynomial chirplet transform outperformed wavelet and short time Fourier transforms.

Many factors may contribute to increasing intrasubject SCG variability including subject posture and respiratory phase. In this study, the effect of respiration on SCG signal variability was investigated. Results suggested that SCG waveforms can vary with lung volume, respiratory flow direction, or a combination of these criteria. SCG events were classified into groups belonging to these different respiration phases using classifiers, including artificial neural networks, support vector machines, and random forest. Categorizing SCG events into different groups containing similar events allows more accurate estimation of SCG features.

SCG feature points were also identified from simultaneous measurements of SCG and other well-known physiologic signals including electrocardiography, phonocardiography, and echocardiography. Future work may use this information to get more insights into the genesis of SCG.

Keywords: Seismocardiography; heart vibrations; feature extraction; classification

*Dedicated to my beloved parents, Akbar and Fatima,
in appreciation of their never ending faith and
everlasting encouragement this dissertation is
affectionately dedicated!*

ACKNOWLEDGMENTS

Four years ago, when I came to Earth, I was a stranger in a strange land. Like all other Martians who landed on Earth since Valentine Michael Smith, I needed to “grok” the new condition. I was lucky enough that I was not confined at Bethesda Hospital. Instead, I was sent to the Biomedical Acoustics Research Laboratory where I worked on research under the supervision of Dr. Hansen Mansy which resulted in this Terran PhD dissertation. I would like to express my appreciation to him; without his supervision this study would not have become a reality. To Dr. Richard Sandler, whose professionalism and attention to details has made this experience enriching, are due my appreciation. I also extend my appreciation to Dr. Alain Kassab, Dr. Azadeh Vosoughi, and Dr. Helen Huang for their thoughtful comments which helped me to improve the quality of this work.

After moving to Earth, I could face a deep emotional and cultural shock. I was unaccustomed to the conditions on Earth. Living in a different planet with people who were different than me was scary and exciting. It was scary because it was different. Because it was different, it was also exciting. It does not matter how long after Mike you land on Earth. Even if your travel was in 2014, you still need to observe, learn, and face new challenges in this new strange land. Talking about blessings, in such a situation, having some fellow travelers, friends from your World who are more similar to you, is a blessing. Those friends do not let you feel alone, even if you are on another planet thousands of kilometers far away from Mars. They are the heavenly miracles that simply do not let you feel alone. Amirmahdi Honardoost, Alireza Safaei, and Zahra Tavakoli, for their true friendship and all the happy moments full of smiles and laughter, I give my warmest salutation to them. I want to simply say thanks to all my fantastic Martian friends, especially Mehdi

Alirezaei, Mahdi Kalayeh, Fardin Khalili, Farzad Vasheghani Farahani, and Mahdi Mirhosseini, who were always there for me in my happiness and sadness throughout this life experience.

Learning about the Terran culture was not easy, especially when it was coupled with my lack of human language knowledge. Finding Earthian friends, who not only taught me about their culture but also acquired some “psychokinetic” abilities to better understand me, was a blessing. My “water brothers”, Peshala Thibbotuwawa Gamage, Md Khurshidul Azad, Brian Solar, Andrea Miller, Andrew Spiewak, Brandon Henley, Taylor Alfonso, Andrew Bomar, Philippe Najaro, and Leslie Simms, are also due my salutation.

I was raised in a society where family has been defined as one of the most valuable blessings. In the encyclopedias of that land, the definition of love is very simple. If you love someone, you see all the beauty of the world in them. If you love someone, you do not see anything other than their face, do not hear anything other than their voice, and do not smell anything other than their fragrance. In the last four years, Wednesday nights at 11 pm and Saturday afternoons at 2:30 pm were my best moments of the week since I could see the energetic face and hear the kind voice of those who truly love me. Their generous presence in my life and heart, even from another planet thousands of kilometers far away from Earth, was a blessing that I will never be able to thoroughly appreciate. My beloved parents and my lovely baby brothers, Amirtaheer and Amirtayyeb, for all their unconditional love and encouragement, are due my most affectionate salutations. To my “Old Ones”, Mamanazi, Khanoom Joon, and Uncle Dayi Abdoreza, for sparkling my life with their charming presence, I also extend my warm salutation. My sister in law, Maryam, and my adorable and cute niece, Fatima Yas, are also due my deep salutation.

I love a universe with a blue Earth, red Mars, and yellow Saturn. If all the planets were blue as Earth, as Joseph Douglas wants, the universe would not be as eye-catching and beautiful as it is

now. I was planning to invite my parents to my graduation ceremony for a long time. However, it did not become a reality, maybe because Alice still could not get her husband in contact with Jubal. I will walk without being able to see the smiles on the, now old and wrinkled, faces of my beloved parents and feel the sparkles in their forever young hearts. However, I will walk while I am praying for their peace and a more peaceful universe where lovely people, like them, are not discriminated against on the grounds of their nationality, skin color, race, sex, or religion.

TABLE OF CONTENTS

LIST OF FIGURES	xvii
LIST OF TABLES	xxvii
LIST OF ABBREVIATIONS.....	xxxii
CHAPTER 1: INTRODUCTION	1
1.1 Seismocardiographic Signals	1
1.2 Parameters Affecting SCG Waveform.....	3
1.3 Applications	6
1.3.1 Wearable SCG.....	6
1.3.2 Non-contact SCG Measurement	8
1.3.3 Heartbeat Detection and Heart Rate Monitoring	9
1.4 Clinical Studies	9
1.4.1 Healthy Subjects.....	9
1.4.2 Subjects with Cardiovascular Disease	11
1.5 Dissertation Outline.....	12
CHAPTER 2: SIGNAL ACQUISITION AND PREPROCESSING.....	14
2.1 SCG Acquisition	14
2.1.1 Accelerometer Type and Location.....	17
2.2 SCG Segmentation	18
2.3 Noise Removal	19
2.3.1 Respiration and Building Vibration Noise.....	20
2.3.2 Noise Reduction Using Ensemble Empirical Mode Decomposition	22
2.3.2.1 Methodology.....	24

2.3.2.1.1	Synthetic SCG Signal and Noise Set.....	24
2.3.2.1.2	Ensemble Empirical Mode Decomposition.....	24
2.3.2.1.3	Misadjustment Analysis	26
2.3.2.2	Noise Reduction Results.....	26
2.3.2.3	Discussion.....	29
2.3.2.3.1	Filtering Performance of EEMD	29
2.3.2.4	Conclusions	31
2.4	Summary	31
CHAPTER 3:	FEATURE EXTRACTION	33
3.1	Time Domain Features	34
3.2	Frequency Domain Features.....	35
3.3	Time-frequency Features.....	35
3.3.1	Time-frequency Distribution Methods.....	38
3.3.1.1	Short-time Fourier Transform	39
3.3.1.2	Continuous Wavelet Transform.....	39
3.3.1.3	Chirplet Transform and Polynomial Chirplet Transform	40
3.3.2	Test Signals	42
3.3.2.1	Signal with Varying Frequency	42
3.3.2.2	Exponentially Decaying Sinusoid	42
3.3.2.3	Decaying Chirp.....	43
3.3.2.4	Double Chirp	43
3.3.2.5	Growing and Decaying Single Tone with Varying Frequency	43
3.3.2.6	Synthetic SCG Signal	44
3.3.3	IF Error Analysis.....	44

3.3.4	Data Acquisition of Human SCG.....	45
3.3.5	Results and Discussion.....	45
3.3.5.1	Signal with Varying Frequency	48
3.3.5.2	Exponentially Decaying Sinusoid	49
3.3.5.3	Decaying Chirp.....	50
3.3.5.4	Double Chirp	51
3.3.5.5	Growing and Decaying Single Tone with Varying Frequency	52
3.3.5.6	Synthetic SCG signal.....	52
3.3.5.7	Actual SCG Signal.....	54
3.3.5.8	Limitations.....	57
3.3.6	Conclusions.....	58
3.4	Noise Effect on Time-frequency Feature Extraction of SCG Signals	58
3.4.1	SCG Signals and Noise Preparation.....	59
3.4.1.1	Simulated SCG with Constant Frequencies.....	59
3.4.1.2	Simulated SCG with Varying Frequency	60
3.4.1.3	Data Acquisition of SCG.....	60
3.4.1.4	White Noise	61
3.4.2	TFD Techniques.....	61
3.4.3	Error Analysis	62
3.4.4	Results.....	62
3.4.5	Discussion	63
3.4.5.1	Simulated SCG with Constant Frequencies.....	63
3.4.5.2	Simulated SCG with Varying Frequency	67
3.4.5.3	Actual SCG in Noise	70

3.4.6	Conclusions	72
3.5	Summary	73
CHAPTER 4:	CLASSIFICATION	74
4.1	Supervised Approaches	74
4.1.1	Artificial Neural Network	75
4.1.2	Support Vector Machines	77
4.1.2.1	Kernel Methods	79
4.1.3	Random Forest	80
4.1.3.1	Decision Tree	80
4.1.3.2	Random Forest Algorithm	81
4.2	Unsupervised Approach	82
4.2.1	k-means Clustering	82
4.3	Adaptive Feature Extraction	83
4.3.1	Feature Extraction Algorithm	83
4.3.2	Human Studies	84
4.3.2.1	Participants	84
4.3.2.2	Experiment	84
4.3.2.3	Instrumentation	85
4.3.2.4	SCG Event Pre-processing	85
4.3.2.5	SCG Feature Extraction and Classification	86
4.3.3	Results	88
4.3.4	Discussions	90
4.3.4.1	Algorithm Performance	90
4.3.4.2	Limitations	90

4.3.5	Conclusions	90
4.4	SCG Signals Classification	91
4.5	Summary	94
CHAPTER 5:	HUMAN STUDIES	95
5.1	Respiration Effect.....	95
5.1.1	Methodology	96
5.1.1.1	Participants	96
5.1.1.2	Data Collection	97
5.1.1.3	Segmentation and Grouping based on Respiration.....	98
5.1.1.4	Grouping Criteria Effectiveness	99
5.1.2	Results	101
5.1.3	Discussions.....	103
5.1.3.1	Intrathoracic Pressure and Heart Displacement.....	103
5.1.4	Conclusions	104
5.2	Heart Rate Monitoring	104
5.2.1	Methodology	105
5.2.1.1	Participants	105
5.2.1.2	Human Studies.....	106
5.2.1.3	Instrumentation	106
5.2.1.4	Heart Rate Monitoring.....	107
5.2.2	Results	110
5.2.3	Discussions.....	110
5.2.3.1	Heart Rate Monitoring Algorithm Performance.....	110
5.2.3.2	Heart Rate Variability.....	111

5.2.3.3	Application in Cardiovascular Diagnosis	112
5.2.4	Conclusions	113
5.3	Efficient Grouping of SCG Events.....	113
5.3.1	Methodology	113
5.3.1.1	Participants	113
5.3.1.2	Instrumentation.....	114
5.3.1.3	Experiments	114
5.3.1.3.1	Normal Breathing.....	114
5.3.1.3.2	Pressure and Heart Displacement Effects.....	115
5.3.1.4	Signal Pre-processing	116
5.3.1.5	Grouping Criteria.....	118
5.3.1.6	Heart Rate Estimation.....	119
5.3.1.7	Cardiac Time Intervals	119
5.3.1.8	Feature Extraction.....	119
5.3.1.8.1	Time Domain.....	120
5.3.1.8.2	Frequency Domain	121
5.3.1.8.3	Feature Evaluation.....	122
5.3.1.9	Machine Learning.....	122
5.3.1.9.1	Supervised Approaches	122
5.3.1.9.2	Unsupervised Approach	124
5.3.2	Results	125
5.3.2.1	Dissimilarity Analysis	126
5.3.2.2	Heart Rate Analysis	133
5.3.2.3	Cardiac Time Intervals	138

5.3.2.4	Feature Evaluation.....	138
5.3.2.4.1	Time Domain Features.....	138
5.3.2.4.2	Frequency Domain Features.....	139
5.3.2.4.3	Combined Time and Frequency Domains Features.....	139
5.3.2.5	Classification.....	140
5.3.2.5.1	Subject-Specific Scenario.....	140
5.3.2.5.2	Leave-One-Subject-Out Scenario.....	141
5.3.2.5.3	Tri-axial vs uni-axial SCG.....	142
5.3.2.5.4	Breath-Hold Data.....	143
5.3.2.6	Clustering.....	144
5.3.3	Conclusions.....	145
5.4	Genesis of SCG Waves.....	146
5.4.1	Echocardiography.....	148
5.4.1.1	Data Acquisition.....	148
5.4.1.2	Data Pre-processing.....	149
5.4.1.2.1	Signals Synchronization.....	149
5.4.1.2.2	Doppler Velocity Profile Extraction.....	152
5.4.1.3	Results.....	153
5.4.1.3.1	Correlation between SCG Components and Heart Sounds.....	154
5.4.1.3.2	SCG Timing with Myocardial Strain.....	156
5.4.2	Finite Element Modeling.....	157
5.4.2.1	Methodology.....	158
5.4.2.2	Preliminary Findings.....	159
5.4.2.3	Future Work.....	160

5.5	Summary	161
CHAPTER 6:	CONCLUSIONS.....	162
6.1	Contributions.....	162
6.2	Future Work	162
APPENDIX A.	SCG ATTACK AND DECAY FEATURES	165
A.A.1	Introduction.....	166
A.A.2	Methodology.....	166
A.A.3	Results.....	168
A.A.3.1	Synthetic Damped Signal	168
A.A.3.2	Synthetic SCG	169
A.A.3.3	Attack and Decay Rate Results Summary	170
APPENDIX B.	CWT TFD SMOOTHING	178
A.B.1	Introduction.....	179
A.B.2	Methodology.....	179
A.B.3	Results.....	179
APPENDIX C.	FURTHER TFD RESULTS.....	183
A.C.1	Introduction.....	184
A.C.2	Results.....	184
APPENDIX D.	FURTHER EEMD RESULTS.....	186
A.D.1	Introduction.....	187
A.D.2	Methodology.....	187
A.D.3	Results.....	187
A.D.4	Conclusions.....	188
APPENDIX E.	PUBLICATIONS.....	191

REFERENCES 193

LIST OF FIGURES

Figure 1.1. Measured SCG signal showing 2 cardiac cycles. There are two SCG events (SCG1 and SCG2) for each cycle. These are labeled for the first cycle.....	2
Figure 1.2. Dissertation work flow.	13
Figure 2.1. CHAPTER 2 work flow.	14
Figure 2.2. Sensor location distribution in the recent SCG studies. These studies are listed in Table 2.1.	15
Figure 2.3. SCG signal segmentation algorithm. The top 3 panels show the x-, y-, and z-components of SCG signal. The last panel shows the subject respiratory flow signal.....	19
Figure 2.4. Time series (left) and periodogram (right) of building vibrations measured using PCB sensor on a desk with and without a subject sitting on the desk with two different amplification factors of 10 and 100.	21
Figure 2.5. Time series (left) and periodogram (right) of building vibrations measured using PCB sensor on a trampoline with and without a subject sitting on the trampoline with two different amplification factors of 10 and 100.	21
Figure 2.6. Time series (left) and periodogram (right) of SCG signals measured using PCB sensor on a desk and a trampoline with two different amplification factors of 10 and 100.	22
Figure 2.7. The effect of trial number (number of white noise series) on EEMD performance for reconstructed simulated SCG without added noise and with 10, 5 and 2 dB added noise.	27
Figure 2.8. Simulated SCG contaminated by Gaussian noise with SNR = 10 dB EEMD-derived IMF components (left). The signal was decomposed into 11 IMFs (subfigure a through k) and a residue (subfigure l). The power spectral density of the IMFs and residue (right).Most	

of the high-frequency Gaussian noise is concentrated and localized in the first IMF. However, some low amplitude noise can be seen above 45 Hz in the second IMF. Also, some parts of the SCG events (especially SCG2) are seen in the first IMF between 20 – 40 Hz which is not desirable.....28

Figure 2.9. Noise reduction from the simulated SCG contaminated with white Gaussian noise using EEMD-based partial reconstruction. (a) EEMDF₁, (b) EEMDF₂, (c) EEMDF₃, (d) EEMDF₄.....29

Figure 2.10. NRMSE analysis for simulated SCG contaminated with white noise with SNR values ranging from 1 to 20 dB.....30

Figure 3.1. Summary of the signal processing algorithm used in this study.46

Figure 3.2. Normalized root-mean-square error (NRMSE) between the actual and calculated IF for different TFD methods. Lower error values would indicate better TFD performance.....47

Figure 3.3. Synthetic test signal with varying frequency: (a) Time series. Left and right columns show the power spectral density and time-frequency distribution of the signal using: (b) STFT, (c) CWT-Morl, (d) CWT-Haar, (e) CWT-db4, (f) CWT-Coif5, and (g) PCT, respectively.48

Figure 3.4. Synthetic test signal with exponentially decaying sinusoid: (a) Time series. Left and right columns show the power spectral density and time-frequency distribution of the signal using: (b) STFT, (c) CWT-Morl, (d) CWT-Haar, (e) CWT-db4, (f) CWT-Coif5, and (g) PCT, respectively.....49

Figure 3.5. Synthetic test signal with decaying chirp: (a) Time series. Left and right columns show the power spectral density and time-frequency distribution of the signal using: (b) STFT,

(c) CWT-Morl, (d) CWT-Haar, (e) CWT-db4, (f) CWT-Coif5, and (g) PCT, respectively.....50

Figure 3.6. Synthetic test signal with double chirp: (a) Time series. Left and right columns show the power spectral density and time-frequency distribution of the signal using: (b) STFT, (c) CWT-Morl, (d) CWT-Haar, (e) CWT-db4, (f) CWT-Coif5, and (g) PCT, respectively.....51

Figure 3.7. Synthetic test signal with growing and decaying single tone with varying frequency: (a) Time series. Left and right columns show the power spectral density and time-frequency distribution of the signal using: (b) STFT, (c) CWT-Morl, (d) CWT-Haar, (e) CWT-db4, (f) CWT-Coif5, and (g) PCT, respectively.....53

Figure 3.8. Synthetic SCG signal containing two constant frequency components: (a) Time series. Left and right columns show the power spectral density and time-frequency distribution of the signal using: (b) STFT, (c) CWT-Morl, (d) CWT-Haar, (e) CWT-db4, (f) CWT-Coif5, and (g) PCT, respectively.....54

Figure 3.9. Actual SCG signal of two healthy subjects: (Left 2 columns) subject #7 (Right 2 columns) subject #3. For each subject (a) Time series. The time-frequency distribution using: (b) STFT, (c) CWT-Morl, (d) CWT-Haar, (e) CWT-db4, (f) CWT-Coif5, and (g) PCT is also shown. The power spectral density for each TFD is shown to the left of the distribution.....56

Figure 3.10. Bland-Altman plot for PCT and STFT IF. The solid line represents the mean (bias) value of differences between instantaneous frequencies. The dashed lines show the 95% confidence interval.....57

Figure 3.11. Block diagram describing the steps for generating the SCG signals contaminated with noise	61
Figure 3.12. Simulated SCG with constant frequencies, x_1 , contaminated by white noise sets for $-10 < \text{SNR} < 10$ dB: (a) Time series. Time-frequency representation using (b) PCT, and (c) SPWVD, respectively.	64
Figure 3.13. Simulated SCG with varying frequency, x_2 , contaminated by white noise sets for $-10 < \text{SNR} < 10$ dB: (a) Time series. Time-frequency representation using (b) PCT, and (c) SPWVD, respectively.	65
Figure 3.14. Actual SCG contaminated by white noise sets for $-10 < \text{SNR} < 10$ dB: (a) Time series. Time-frequency representation using (b) PCT, and (c) SPWVD, respectively.	66
Figure 3.15. NRMSE in estimating IF of the simulated SCG with constant frequencies (x_1) using PCT for different SNR. In this box-and-Whisker plot, the whisker ends represent the 1 st and 99 th percentiles.	68
Figure 3.16. NRMSE in estimating IF of the simulated SCG with constant frequencies (x_1) using SPWVD for different SNR. In this box-and-Whisker plot, the whisker ends represent the 1 st and 99 th percentiles.	68
Figure 3.17. NRMSE in estimating IF of the synthetic SCG with varying frequency (x_2) using PCT for different SNR. In this box-and-Whisker plot, the whisker ends represent the 1 st and 99 th percentiles.	69
Figure 3.18. NRMSE in estimating IF of the synthetic SCG with varying frequency (x_2) using SPWVD for different SNR. In this box-and-Whisker plot, the whisker ends represent the 1 st and 99 th percentiles.	70

Figure 3.19. NRMSE in estimating IF of the actual SCG using PCT for different SNR. In this box-and-Whisker plot, the whisker ends represent the 1st and 99th percentiles.71

Figure 3.20. NRMSE in estimating IF of the actual SCG using SPWVD for different SNR. In this box-and-Whisker plot, the whisker ends represent the 1st and 99th percentiles.....71

Figure 4.1. (top) A 10-sec portion of the SCG signal, (bottom) Lung volume signal that was used to group SCG events into two groups of high and low lung volume (HLV and LLV) events.86

Figure 4.2. Block diagram describing the signal processing and machine learning steps used in the current study.....88

Figure 4.3. (left) Equal-width bins configuration adopted from [30] vs (right) adaptive-width bins configuration proposed in this study for a feature vector length (i.e., number of bins) of 16.....88

Figure 4.4. Performance trend for SVM models using both AW and EW bins as the number of bins increase. The proposed adaptive feature extraction algorithm resulted in a higher accuracy and F_1 score consistently.....89

Figure 5.1. (a) The location of the accelerometer, ECG electrodes and spirometer on the subject body. The accelerometer and spirometer sensors were used to measure the SCG and respiratory flow rate signals, respectively. The dashed and dash-dot lines show the 4th intercostal space and sternal border, respectively. (b) A 5 s portion of simultaneously acquired SCG, ECG, and respiratory flow rate signals. (c) Summary of the signal processing algorithm used in this study.....97

Figure 5.2. Inspiratory and expiratory SCG events in time domain. The SCG events were categorized into two groups of inspiratory and expiratory using the respiration flow rate signal.99

Figure 5.3. Relative differences calculated from Equations (5-7.a) and (5-7.b) for inspiratory, expiratory, LLV, and HLV SCG events.103

Figure 5.4. (top) A 10-seconds portion of the SCG signal [Volts], (bottom) The lung volume signal [Volts] calculated from the integral of respiratory flow rate that was measured simultaneously with the SCG signal. The LLV and HLV portions of the lung volume signal are labeled.108

Figure 5.5. Flowchart of the heart rate monitoring study.109

Figure 5.6. The estimated LLV, HLV, and combined heart rate in (a) supine position, (b) 45-degree position first trial, (c) 45-degree position second trial, and (d) sitting position.111

Figure 5.7. Bland-Altman plot for HR_{ECG} and HR_{com} . The solid line represents the mean (bias) difference between the HR values. The dashed lines show the 95% confidence interval.111

Figure 5.8. Simultaneously acquired three-axis seismocardiogram, phonocardiogram, electrocardiogram, respiration flow rate (RFR) signals from one subject.115

Figure 5.9. Block diagram for (a) normal breathing, and (b) pressure and heart displacement effects experiments. Dashed line (– –): feedback to the subject to monitor or adjust specific parameters such as tidal volume and number of breath per minute. Solid line (—): acquired signals sent to the computer (or monitor). (c) Experimental setup.117

Figure 5.10. Cardiac time intervals definition. (top) ECG signal simultaneously recorded with (bottom) SCG signal. QRS and T waves are labeled on the ECG signal. The dominant peak

of the SCG signal as well as the minimums before and after it are shown on the SCG signal. The cardiac time intervals, CTI1 and CTI2, are shown. CTI3 through CTI6 can be similarly calculated.120

Figure 5.11. (a) Respiration cycle, Blue: inspiration, Yellow: expiration, (b) Lung volume cycle, Blue: HLV, Yellow: LLV.126

Figure 5.12. (a) LLV and HLV events were plotted as red and black circles on the LV signal, (b) dissimilarity analysis results. Green and blue solid lines mean that the SCG event was more similar to its own and alternate group ensemble average, respectively, (c) backward events were plotted on the LV signal. High-backward events were plotted with the alternate group color. For example, a high backward LLV event was plotted as a black circle.128

Figure 5.13. Dissimilarity analysis after (top) 1 cleaning iteration, (bottom) 2 cleaning iterations. The plot descriptions are similar to the plot descriptions for Figure 5.12.131

Figure 5.14. Number of early switching events compared to the total number of events in each group (top) before cleaning, (bottom) after one cleaning iteration. In these plots, each column height represents the total number of SCG events. Yellow columns show the number of early switching events. Green column show the number of high-backward events that are not early switching. Blue columns show the number of backward events that are not high-backward.....132

Figure 5.15. The ratio (%) of early switching and high-backward SCG events to the total number of events in (left) LLV and (right) HLV groups before and after one cleaning iteration. Black and red lines correspond to the number of events before and after the cleaning iteration, respectively. Dashed and solid lines represent the number of high-backward and early switching events, respectively.133

Figure 5.16. Heart rate estimations at different postural positions. HR estimation (blue) during HLV phase, (red) during LLV phase, (green) from the combination of HR_{LLV} and HR_{HLV} , (black) from SCG using equation (5-8), (cyan) from ECG using Pan-Tompkins algorithm.134

Figure 5.17. Heart rate estimation from SCG signal for different pressures at end-inspiration and end-expiration. The average of HR estimation during LLV and HLV in the two 45 degree trials were shown with red and blue dashed lines, respectively.135

Figure 5.18. Heart rate estimation using SCG signal during (a) inspiration and expiration, (b) HLV and LLV, (c) hybrid1 and hybrid2 groups after 1 cleaning iteration, and (d) hybrid1 and hybrid2 groups after 2 cleaning iterations. The HR estimation is shown for different postural positions (4 different trials for each subject). These positions include sitting, 45 degree-1, 45 degree-2, and supine positions, respectively.....136

Figure 5.19. Bland-Altman plot for heart rate estimations using (a) ECG and SCG, (b) SCG and SCGcom, and (c) ECG and SCGcom. The solid line represents the mean (bias) value of differences between instantaneous frequencies. The dashed lines show the 95% confidence interval.137

Figure 5.20. Clustering results for one of the subjects. SCG events are shown on (a) RFR and (b) LV signals with red and blue circles. Red and blue circles are the two output labels of the clustering algorithm.146

Figure 5.21. Experiment setup and ECG, PCG, and SCG sensor locations.149

Figure 5.22. (left) ECHO audio files and PCG signal. The phonocardiograph sensor was tapped 3 times to mark the signals. These marks were then used to find the time shift between ECHO

audio and PCG signal. The time shift values were shown in the figure, (right) Synchronized audio files (PCG and ECHO audio).....	150
Figure 5.23. (left) ECHO audio file at two sampling frequencies of (red line) 10 kHz and (blue line) 48 kHz, (right) Synchronized audio files, (dashed line) PCG and (blue and red lines) audio files recorded by the ECHO machine at 10 kHz.	150
Figure 5.24. Image processing steps to extract ECG waveform from the ECHO images. These ECG waveforms were then used for a better synchronization of ECHO images and SCG signals.	151
Figure 5.25. Image processing steps to extract Doppler velocity profiles from Doppler echocardiography images.....	153
Figure 5.26. Measuring ECG, SCG, PCG and respiration flow rate simultaneously using iWorx TA Control Module and LabScribe software (iWorx Systems, Inc., Dover, NH).	154
Figure 5.27. Synced ECHO image and SCG signal. The ECG, ECHO audio and PCG signals were also shown in the figure.	155
Figure 5.28. Synced ECHO image and SCG signal components. (from top to bottom) ECHO M-mode of aortic valve, heart sounds (PCG signal), band-pass filtered SCG signal between 30 and 100 Hz, SCG signal, band-pass filtered SCG signal between 1 and 30 Hz, High-pass filtered SCG signal with a cut-off of 100 Hz.	155
Figure 5.29. Simultaneous recording of ECHO, SCG and ECG, where several cardiac events can be identified in the SCG waveform such as: atrial systole (AS), mitral closing (MC), aortic valve opening (AO), isovolumic contraction (between MC and AO), rapid ejection (RE), aortic valve closure (AC), and rapid filling (RF).....	156

Figure 5.30. (top) CT scans of human thorax of a male subject, (bottom) computational geometry based on CT scan dimensions and simplified to add CAD features.....158

Figure 5.31. (a) Magnitude of the acceleration vector normal to the chest surface, (b) heart displacement due to the imposed boundary condition.....160

Figure 5.32. A more realistic geometry for future work. Here, the ribcage and spine are modelled with a more realistic geometry.....160

LIST OF TABLES

Table 2.1. Summary of acceleration sensors used for SCG data acquisition. Abbreviations used in the table: Acc: accelerometer, Gyr: gyroscope, 1-: uniaxial, 3-: triaxial, MEMS-: micro electromechanical systems, SP-: smart phone.	16
Table 2.2. NRMSE analysis for simulated SCG contaminated with white noise with SNR values ranging from 1 to 20 dB.....	30
Table 3.1. Center frequency of the wavelets used in the current study.	40
Table 3.2. Description of synthetic signals used in the current study.....	42
Table 3.3. Temporal and spectral resolution for different signals and TFD for frequencies between 10 and 70 Hz. The resolution of TFD was optimized to minimize the NRMSE for each synthetic signal. STFT tended to have coarser temporal and spectral resolution compared to PCT. Frequency resolution for CWT-based methods is given as a range with lower values corresponding to lower frequencies.	47
Table 3.4. Normalized root-mean-square error (NRMSE) between the actual and calculated IF for different TFD methods. Lower error values indicate more appropriate TFD.....	47
Table 3.5. Dominant frequencies of the actual SCG signals calculated using polynomial chirplet transform. The most dominant frequency for each subject is highlighted in bold.	56
Table 3.6. Statistical analysis results based on the Bland-Altman method (LOV: level of agreement).....	57
Table 3.7. General properties of the simulated signals used in the current study.....	59
Table 3.8. A summary of NRMSE analysis of simulated and actual SCG signals for different SNR. The NRMSE values are reported as: Median (IQR, Range). Here, the range is defined as the difference between 1 st and 99 th percentiles.	72

Table 4.1. Overview of the subjects' characteristics (mean \pm SD).....	84
Table 4.2. Average accuracies and F_1 scores of SVM models for different number of bins when using equal-width (EW) and adaptive-width (AW) bins.	89
Table 5.1. Overview of the subjects' characteristics (mean \pm SD).....	96
Table 5.2. RMS between SCG events in the inspiratory and expiratory groups and the ensemble averaged inspiratory/expiratory SCG event (Equation (5-6)). The values are shown as mean \pm SD. The number of SCG events in each group is shown in parenthesis. The last column shows the relative differences in percentage.	102
Table 5.3. RMS between SCG events in the HLV and LLV groups and the ensemble averaged HLV/LLV SCG event (Equation (5-6)). The values are shown as mean \pm SD. The number of SCG events in each group is shown in parenthesis. The last column shows the relative differences in percentage.	102
Table 5.4. Overview of the subjects' characteristics (mean \pm SD).....	106
Table 5.5. Estimated heart rate (beat per minute) using HLV and LLV SCG events during high and low lung volume in 3 different postural positions. The values are shown as mean \pm SD.	110
Table 5.6. The estimated combined heart rate (beat per minute) using Equation (5-9).	110
Table 5.7. The ratio between estimated heart rate during high and low lung volume HR_{HLV}/HR_{LLV}	112
Table 5.8. Overview of the subjects' characteristics (mean \pm SD).....	114
Table 5.9. Number of SCG events used for feature extraction and classification obtained from each subject. In this study, only the SCG signals recorded in 45 degree position were considered.	120

Table 5.10. Contingency table.	124
Table 5.11. A summary of number of SCG events for different subjects at different postural positions. The numbers are in the following format $x/y/z$ where x , y , and z represent the number of high-backward, backward, and total SCG events. In the second column, b4, 1, and 2 mean before cleaning, after 1 cleaning iteration, and after 2 cleaning iterations, respectively.	130
Table 5.12. Estimation of cardiac time interval [ms] using SCG and ECG signals during different phases of lung volume signal.	138
Table 5.13. Average accuracy obtained from the SVM model for different temporal features used for the classification of SCG events occurring during different phases of respiration and lung volume.	139
Table 5.14. Average accuracy obtained from the SVM model for different spectral features used for the classification of SCG events occurring during different phases of respiration and lung volume.	139
Table 5.15. Classification accuracy (%) and F_1 score (%) for the SS scenario.	141
Table 5.16. Classification accuracy (%) and F_1 score (%) for the LOSO scenario.	142
Table 5.17. Classification accuracy of the SVM model for different components of the SCG signal.	143
Table 5.18. Classification accuracy of the SVM model for the breath-hold data. Here, the hypothesis was that the end-inspiration and end-expiration SCG events should be similar to HLV and LLV SCG events, respectively. A high accuracy (and F_1 score) confirms the hypothesis. The classification results are reported for LV and hybrid grouping criteria.	144

Table 5.19. Clustering performance for respiratory flow rate (RFR) and lung volume (LV)
grouping criteria.....145

LIST OF ABBREVIATIONS

AC	Aortic valve closure
AF	Atrial fibrillation
AO	Aortic valve opening
ARI	Adjusted rand index
AW	Adaptive width
BMI	Body mass index
CT	Computerized tomography
CT	Chirplet transform
CTI	Cardiac time interval
CWT	Continuous wavelet transform
ECG	Electrocardiography
ECHO	Echocardiography
EEMD	Ensemble empirical mode decomposition
EFuNN	Evolving fuzzy neural networks
EMD	Empirical mode decomposition
EMw	Electro-mechanical window
EW	Equal width
FEM	Finite element modeling
FFT	Fast Fourier transform
FNN	Feed-forward neural networks
GSS	Graph similarity score
HF	Heart failure
HLV	High lung volume
HMM	Hidden Markov model
HR	Heart rate
HRV	Heart rate variability
ICT	Isovolumic contraction time
IF	Instantaneous frequency
IMF	Intrinsic mode function
IQR	Inter quartile range
IRT	Isovolumic relaxation time
LDV	Laser Doppler vibrometry
LLV	Low lung volume
LMS	Least mean square
LOSO	Leave-One-Subject-Out
LV	Lung volume
LVET	Left ventricular ejection time
MC	Mitral valve closure

MO	Mitral valve opening
MPM	Matrix pencil method
NN	Neural networks
NRMSE	Normalized root mean square error
PCG	Phonocardiography
PCT	Polynomial chirplet transform
PEP	Pre-ejection period
PPG	Photoplethysmography
PSD	Power spectral density
RBF	Radial basis function
RD	Relative difference
RE	Rapid ejection
ReLU	Rectified linear unit
RF	Random forest
RF	Rapid filling
RFR	Respiratory flow rate
RMSE	Root mean square error
RSA	Respiratory sinus arrhythmia
SCG	Seismocardiography
SCG1	First SCG component corresponding to the first heart sound
SCG2	Second SCG component corresponding to the second heart sound
SD	Standard deviation
SNR	Signal-to-noise ratio
SPWVD	Smoothed pseudo Wigner-Ville distribution
SS	Subject-Specific
STE	Speckle tracking echocardiography
STFT	Short time Fourier transform
SVM	Support vector machines
TFD	Time frequency distribution
TV	Tidal volume
wgn	White Gaussian noise
WT	Wavelet transform

CHAPTER 1: INTRODUCTION

Cardiovascular diseases are a leading causes of death in the world [1]. In the United States, based on 2010 data, 24% of total deaths was related to cardiovascular disease [2]. Current diagnostic methods include electrocardiography (ECG), echocardiography (ECHO), magnetic resonance imaging (MRI), and computerized tomography (CT) scan. ECG is the recording of heart electrical activity and does not directly reflect the mechanical cardiac activities. Direct recordings of signals that correlate with mechanical cardiac action can provide a potentially more complete information about cardiac health, which can help decrease morbidity mortality associated with heart disease.

Heart sounds are believed to be generated by the mechanical process of heart valve closure. Auscultation of heart sounds is a common test performed during physical examination and has been providing useful diagnostic information. Computer analysis of these sounds can provide additional quantitative diagnostic information that may be helpful for more automated screening patients suspected of heart disease. Seismocardiographic (SCG) signals are also believed to be generated by mechanical processes but are different from heart sounds as the former are the cardiac vibrations measured noninvasively at the chest surface [3–7]. These signals are believed to be caused by the mechanical processes associated with the heart activity, and therefore can be a tool to monitor both heart electrical and mechanical activities. This dissertation focuses on the study, analysis, and classification of SCG signals.

1.1 Seismocardiographic Signals

Measurement of cardiac vibrations was performed as early as the turn of the 20th century [8]. Many variations within this approach, such as vibrocardiography (VCG), kinetocardiography (KCG), ballistocardiography (BCG), cardiokymography (CKG), and apexcardiography have been

described [9–19]. These signals are believed to be caused by the mechanical processes associated with the heart activity (such as cardiac contraction, blood momentum changes, valve closure, etc.).

However, SCG signals are vulnerable to inter-subject variations such as body mass index, sex, age, and health conditions [4]. In addition, SCG vibrations have relatively low amplitudes that can be easily contaminated by building vibrations, motion artifacts (e.g. patient movements, muscle related disease, etc.) and respiration noise, which can lead to a misinterpretation of SCG signal features [20–22].

During each cardiac cycle, typical SCG contains two main events that can be called the first SCG (SCG1) and the second SCG (SCG2) as shown in Figure 1.1. The frequency content of SCG signals is dominated by low frequencies where the human auditory sensitivity is low and may not be sufficient to extract the characteristics of these signals [23,24]. Consequently, examination of SCG signals may not be optimally done by manual auscultation alone and a computer assisted analysis would likely help obtain enhanced qualitative and quantitative description of the signal characteristics.

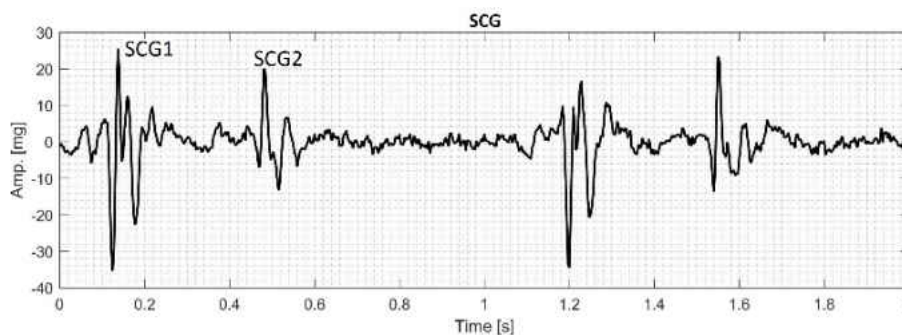


Figure 1.1. Measured SCG signal showing 2 cardiac cycles. There are two SCG events (SCG1 and SCG2) for each cycle. These are labeled for the first cycle.

This chapter reviews the recent findings in this field and the new applications of SCG signals. This includes the signal processing and instrumentation advances as well as some of the clinical applications of SCG signals which support their usefulness as a new cardiovascular diagnostic tool. There are literature that has previously reviewed the state of the art in this area [20,21].

Therefore, the main goal of this paper was to focus on the developments in the field during the last two years.

1.2 Parameters Affecting SCG Waveform

A main challenge in SCG studies is that SCG signals morphology changes with different parameters such as respiratory cycle, different gender, age, sensor location on the chest, health conditions, cardiac contractility, heart rhythm, and postural positions [4,25–27]. While these parameters can lead to significant inter and intra-subject variability, studying these confounding parameters can enhance our understanding of SCG, help group SCG cycles into groups with similar SCG events, reduce SCG signal variability and noise, and lead to more accurate definition of its features.

A number of studies pointed out SCG variability. For example, earlier studies [6,28] suggested that the SCG varied between inspiration and expiration. A recent study [29] reported that the SCG morphology appeared to mainly depend on the lung volume (and, hence, possibly the intrathoracic pressure) rather than respiratory phases (i.e. inspiration and expiration). This SCG morphology variation can also be used to automatically identify the lung volume (LV) states and respiratory phases by employing machine learning [30]. Another study used support vector machines to classify the SCG cycles occurring during the high and low lung volume [31].

Motion and postural position of the subject have also been shown to cause changes in SCG signals [20,32,33]. In an ongoing study, the effect of posture on the SCG signals was investigated for patients with heart failure (HF) [32]. The SCG signals were measured using a wearable unit in supine and seated positions. The SCG power spectral density (PSD) was estimated using the Welch's periodogram and the mean of PSD values were calculated in the 0-20 Hz band. The results showed that SCG signals contained high energy in bands greater than 8 Hz in the supine and seated

postures. Identification of body orientation (supine, 45 degree, or vertical), and therefore grouping of SCG signals according to chest orientation, is possible with the use of certain 3-axis accelerometers [33]. However, the position of the legs may also have a significant effect, as shown by the commonly reported differences between sitting upright and standing. Movement of the patient also produces a change in the SCG signal. The possibility of filtering noise from speaking, walking, and indistinct motions associated with workplace tasks has been demonstrated [34]. Understanding the effects of posture and movement on the SCG waveform is a step towards continuous collection of SCG signals from a patient from a wearable sensor. However, this need may be avoided through intermittent testing in a more controlled environment, such as the patient's home and through choosing a fixed subject position.

Exercise and the following period of recovery has also been demonstrated to produce changes in SCG signals. Exercise has been associated with an increase in the overall amplitude of the SCG signal, measured as the RMS power [35,36]. This increase in signal amplitude has been shown to correlate to increases in cardiac output observed during exercise [65]. The increase in cardiac output is a result of increased heart rate (controlled at the sinoatrial node) and increased contractility (controlled by beta-adrenergic tone in the myocytes). Exercise also produces changes in LVET and PEP, two important SCG signal measures with clinical relevance [33,36]. Exercise results in an increase in heart rate, which necessarily produces a decrease in the R-R interval measured on an ECG signal, and generally produces a decrease in other measured time intervals. Both LVET and PEP are decreased during exercise. The LVET decrease results from correlation of LVET to both heart rate and contractility. PEP has been found to stay constant with changes in heart rate, but will decrease during exercise due to the increase in contractility. These changes in LVET and PEP have been shown to be detectable through SCG, and the changes observed agree

with published literature [33,37]. Additionally, the exercise-induced decrease in PEP has been shown to shift the SCG signal power spectrum towards higher frequencies [38].

Digestive state and mood have effects on cardiac function through similar physiological mechanisms, and therefore could be expected to produce changes in SCG signal morphology. Ingestion of a carbohydrate-rich meal has been shown to increase cardiac output by 25% or more, due to increases in heart rate and stroke volume [39]. Mood or psychological stress can also cause changes in sympathetic tone, similar to the effect of exercise stress. Despite these conditions having the potential to effect SCG signals, systematic study of these topics is lacking. Since eating and mood are both variable throughout a patient's daily living, future study of these effects may be warranted in order to determine the nature of the effects on SCG signal morphology, and whether the effects on the SCG signal can be removed in post-processing.

The sensitivity of the sensor to the location where the sensor is placed is well-known and should be taken into consideration when analyzing SCG signals. Historically, investigators have placed accelerometers in different anatomical positions on their subjects, including the clavicle, the sternum, and various intercostal spaces [33,35,40]. A recent study [40] investigated the differences in SCG signals morphology at the common auscultation sites for the four heart valves (aortic, pulmonary, tricuspid, mitral), and found significant differences in morphology. That study also concluded, with the aid of sonographic measurements, that more feature points can be defined from this multi-point SCG measurement.

Due to the positional sensitivity of SCG signals, using the signal from an SCG monitor might be more challenging than using the conventional ECG signals. Unexperienced users, such as a typical patient, might not be able to repeatably place the SCG measurement hardware on the ideal location. Since the SCG signal is very sensitive to the sensor location on the chest, the SCG-based

cardiac time interval (CTI) estimations might change significantly with the accelerometer sensor location. This would then result in inaccurate device interpretation [41]. To overcome this issue, Ashouri and Inan [41] proposed a method to automatically detect when the sensor is not placed in a desired location by comparing the regression parameters from the acquired SCG and an SCG measured from the ideal position.

High spatial-resolution measurement of the SCG signal was carried out in a pilot study. Here, a laser vibrometer was used to perform non-contact SCG measurements. The laser beam was $< 2 \text{ mm}^2$ and the resulting SCG amplitude distribution is shown in Fig 4. This data suggests that when the sensor location changed by 1 cm, the SCG amplitude can vary by $> 30\%$. An accelerometer with larger contact area (3.5 cm^2) was also used and it was found that for sensor placement change of 1 cm, the SCG amplitude changed by only 5%. Due to this smaller change, the larger contact area may be beneficial in reducing SCG dependence on sensor placement. The effect of sensor contact area and more documentation of SCG spatial distributions need further investigation in future studies.

1.3 Applications

Various utilities of SCG signals have been discussed in literature. In this section, we review three main applications including wearable cardiac activity monitoring, non-contact cardiac activity monitoring, and heart rate monitoring.

1.3.1 Wearable SCG

Wearable technologies have been developed to continuously monitor the cardiac activity outside of the clinics and hospitals. This continuously monitoring might help detecting unusual cardiac activities before they end up in a serious issue, eventually improving the diagnosis and treatment stages, and reducing the healthcare costs. Current wearable cardiac activity monitoring

algorithms are mainly based on ECG signals. Recent studies have discussed the utility of SCG signals in wearable monitoring systems. For example, SCG-based technologies were proposed for monitoring the mechanical aspects of the cardiovascular function, including relative changes in cardiac output, contractility, and blood pressure [42]. SCG signals might be used to assess myocardial contractility via pre-ejection period (PEP) in wearable cardiac activity monitoring devices. Using SCGs in wearable devices, however, might be more challenging than using the conventional ECG signals. For example, the SCG signal is very sensitive to the sensor location on the chest. As a result, the SCG-based PEP estimation significantly changes with the accelerometer sensor location which might result in inaccurate device interpretation [41]. Unexperienced users, such as regular patients, might place the SCG measurement hardware on a location different than the ideal location. To overcome this issue, Ashouri and Inan [41] proposed a method to automatically detect when the sensor is not placed in a desired location by comparing the regression parameters from the acquired SCG and an SCG measured from the ideal position. SCG signals morphology is also very sensitive to postural artifacts. In an ongoing study, the effect of posture on the SCG signals was investigated for patients with HF [32]. The SCG signals were measured in supine, seated, and standing positions. The results showed that SCG signals contained high energy in bands greater than 8 Hz in the supine and seated postures. These results might also be used to evaluate the changes in posture from the SCG signals. Wearable devices might utilize tri-axial accelerometers and gyroscopes to record all the six axial and rotational components of the SCG signals. In an investigation [43], the y-component of the chest rotational vibration showed a lower sensitivity to walking noise than other components which might be useful for annotation of SCG signals in ambulant subjects.

Today, smartphones and smartwatches can be found everywhere. They can be potentially used for telemedicine to continuously monitor the patients in real time at a lower healthcare cost. SCG-based algorithms can be used in smartphones for continuous monitoring of heart rate variability (HRV) [44], and cardiac activity of patients suffering from heart disease [45]. For example, in a recent study, the feasibility and accuracy of measuring heart rate using a smartphone accelerometer has been assessed in different postural positions [46]. The heart rate was estimated using an algorithm based on amplitude thresholding. The heart rate derived from the smartphone accelerometer signal (SCG) was compared to the one extracted from ECG. Results showed that the conventional ECG-based heart rate monitoring method can be replaced by the proposed SCG-based technique with a high accuracy.

1.3.2 Non-contact SCG Measurement

In some applications, such as emergency medicine (burn patients), highly infectious patients, and premature baby care, attaching adhesive ECG electrodes or SCG kit would not be feasible. Therefore, it would be necessary to develop new efficient contactless techniques to monitor cardiac activity. A laser Doppler vibrometer (LDV) can acquire the vibrations of a patient skin without any physical contacts [10]. A non-contact SCG measurement might also remove some of the artifacts that are present in the SCG signals acquired by the accelerometers attached to the skin. The non-contact SCG might be recorded from different measurement points on the patient body. Metzler *et al.* [47] developed an algorithm that can automatically detect the suitable SCG measurement points using a LDV. Non-contact SCG might be used for estimating central arterial pressure and carotid arterial pressure waveforms [48,49]. CTIs such as LVET might also be estimated using an LDV. The LVET value from the non-contact SCG was comparable with the value derived from photoplethysmogram (PPG) [48].

1.3.3 Heartbeat Detection and Heart Rate Monitoring

Heart rate (HR) monitoring is a common way to monitor the cardiovascular function, and can identify some abnormalities such as arrhythmia. Different HR estimation methods have been proposed that were mostly based on ECG signal processing. SCG signals can also be used for HR estimation. For example, Cosoli *et al.* [50] suggested a general algorithm that can estimate HR from various signals, including SCG, ECG, phonocardiogram (PCG), and PPG. Considering the ECG signal as a gold standard, the SCG HR estimation was more accurate than PCG and PPG. Wahlstrom *et al.* [51] used a Hidden Markov Model (HMM) to determine different stages of a cardiac cycle which were then used for estimating beat-to-beat intervals. HR and HR variability can be estimated from beat-to-beat intervals of an SCG signal. Mafi [52] suggested an algorithm based on empirical mode decomposition and empirical wavelet transform that can extract HR from SCG signals. Tadi *et al.* [4] used a Hilbert adaptive beat identification technique to determine the heartbeat timings and inter-beat time intervals from SCG signals. An android application was implemented based on this algorithm that can monitor the subjects' heart rate in real time using the accelerometer sensor of the smartphone. Tadi *et al.* [53] proposed an algorithm based on S-transform, Shannon energy, and successive mean quantization transform to identify heartbeat and beat-to-beat interval from SCGs. The latter two algorithms had a high agreement with the ECG inter-beat interval values.

1.4 Clinical Studies

1.4.1 Healthy Subjects

Although SCG was initially aimed at providing clinical utility at hospitals, obstacles such as lack of proper instrumentations, understanding of the signal behavior and inter-subject variabilities hindered the application of this technique in cardiovascular diagnosis. However, today, advances

in sensor technologies as well as numerous research studies on the SCG signals have provided a better insight into this field. Considering the continuous massive mortality rate due to cardiovascular disease, a new line of research has emerged to re-evaluate the feasibility and utility of seismocardiography for real life clinical applications [54–56].

There are several studies conducted clinical investigations with a healthy population using modern sensors and analysis tools during the last two years. SCG has been used to estimate different cardiovascular parameters such as CTIs, pulse transit time, and blood pressure. For example, measurement of pulse transit time allows for non-invasive means of determining blood pressure changes associated with cardiovascular disease via analysis of aortic valve opening (AO) from SCG data [57]. For this purpose, the pulse transit time, which is defined as the time required for the blood pressure wave to travel from one location to another [58], was first measured from the SCG signals [59]. The measured pulse transit time was then used to estimate the patient blood pressure [60]. Based on similar techniques, a wrist-watch, consisting of an accelerometer and an optical sensor, was developed to monitor blood pressure [61]. In this “SeismoWatch”, the blood pressure is estimated from the travel time of the micro-vibrations propagating from the heart to the wrist when the watch is hold against the subject sternum.

Di Rienzo *et al.* [62] developed a system that measures SCG and PPG at multiple locations alongside with the ECG signal. The pulse transit time may then be derived from the PPG.

CTIs have been used for a long time by clinicians for prognosis and diagnosis of cardiovascular disease [63,64]. There are various SCG-based algorithms with different levels of accuracy that were proposed for estimating CTIs such as PEP, LVET, isovolumic contraction time (ICT), systolic time, and diastolic time in healthy subjects and patients with previous heart conditions [51,65]. Rivero *et al.* [66] proposed a new algorithm that uses continuous wavelet

transform as a base to determine the aortic valve opening and isovolumic moment points on the SCG signal without using the reference of SCG signal. The electro-mechanical window (EMw) is defined as the duration between the electrical and mechanical systole. EMw is a potential biomarker that can be utilized for diagnosing several cardiovascular diseases. ECG and PCG signals are conventionally used to determine EMw. However, Jain *et al.* [67] showed that SCG is a suitable alternative for PCG for estimating the EMw. SCG might also be used in extreme conditions to monitor cardiac mechanics. Analysis of SCG data recorded from the sleep patterns of a subject aboard the International Space Station (in microgravity) resulted in accurate identification of CTIs and SCG fiducial points (such as AO, AC, MO, MC, LVET, and PEP) with implications for future clinical application [68].

1.4.2 Subjects with Cardiovascular Disease

In addition to the clinical studies conducted on healthy populations, there are several studies that have focused on the application of SCG in patients with cardiovascular disease such as atrial fibrillation and valvular disease.

In 2015, about 17 million people died from cardiovascular diseases which was about 31% of total global mortality [69]. Heart sounds that are believed to be generated by opening and closure of heart valves can be used as a diagnostic marker of these diseases. Stethoscope and PCG are the common conventional methods for heart sound monitoring. SCG signals have been reported as a potential efficient alternative for PCG signals for monitoring of heart sound signals [70].

Today, electrocardiography is the main diagnostic method of atrial fibrillation (AF). A preclinical study [71] investigated the usefulness of SCG for AF detection. Results suggested that the amplitude of the SCG signal correlates to beat interval and significantly varies from beat to beat during AF. This study also suggested that the combination of SCG and ECG may reveal

certain behavior in the electromechanical delay characteristic of the AF which may lead to extra indicators for detecting AF.

Paukkunen *et al.* [72] showed that 3-D vector trajectory of SCG might be useful in diagnosing atrial flutter. The results of this study suggested that the intra-subject correlation of 3-D SCGs was strong. However, the signals had a very weak inter-subject correlation. Future studies might prove the utility of SCG 3-D vector trajectory for diagnosis of different cardiovascular disease and abnormalities.

1.5 Dissertation Outline

This dissertation is organized as follows. The methods used for SCG signal acquisition is discussed in CHAPTER 2. Three different accelerometers have been mainly used throughout the studies in this dissertation. The sensor locations as well as the sensor attachment methods to the subject body is described. The pre-processing of the SCG signals including noise reduction is discussed. A new noise reduction method based on ensemble empirical mode decomposition is proposed and used to clean the SCG signals from white Gaussian and respiratory noise.

CHAPTER 3 focusses on feature extraction. Time domain, frequency domain, and time-frequency domain features, that might be useful in SCG classification, are discussed. Different time-frequency distribution (TFD) methods are tested to find the most suitable tool for feature extraction from SCG signals. The effect of noise on the performance of different TFDs is also studied. This chapter helps choosing proper methods for SCG signal time-frequency feature extraction in absence and presence of noise.

CHAPTER 4 provides a brief theoretical overview of the three main classifiers that have been used in this dissertation. These classifiers include neural networks, support vector machines, and random forest. The chapter also reviews the recent studies that utilized machine learning technique

for SCG signal analysis. An adaptive feature extraction method for the classification of SCG signals is also proposed in this chapter.

Several human studies are presented in CHAPTER 5. Here, the physiological sources of the SCG signals are studied through investigation of ECG signals and ECHO images that were recorded simultaneously with the SCG signals. The effect of respiration and lung volume on the SCG signal morphology is also investigated. Possible ways of efficient clustering of similar SCG events are also studied in this chapter. SCG signals are used to estimate some of the common parameters that are used for cardiovascular function monitoring such as heart rate and cardiac time intervals.

CHAPTER 6 summarizes the main contributions of this dissertation to the field as well as potential improvements and future work. Figure 1.2 shows the dissertation work flow.

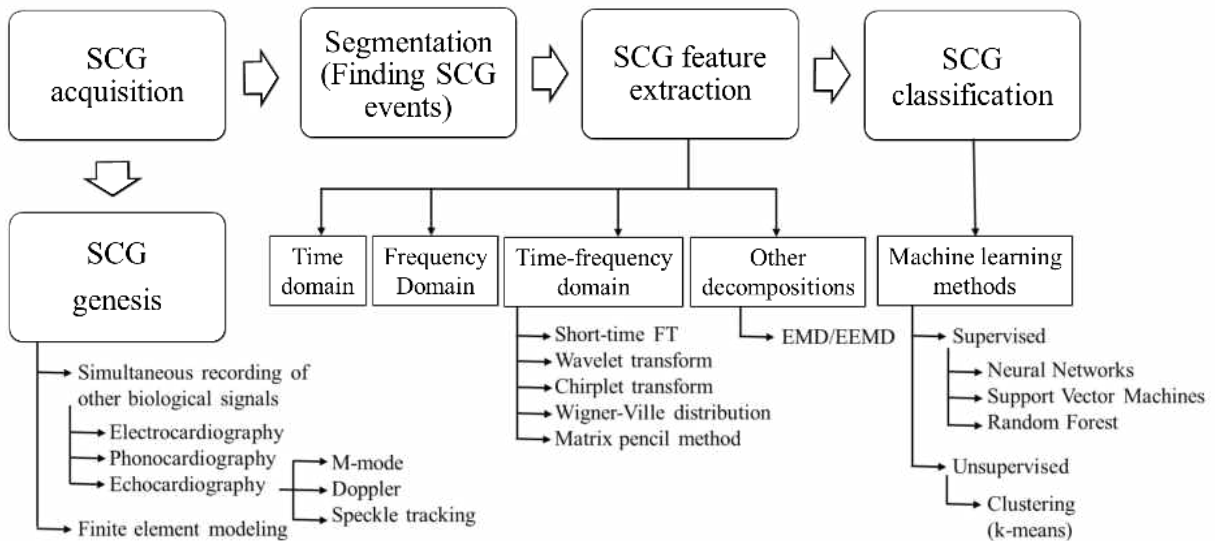


Figure 1.2. Dissertation work flow.

CHAPTER 2: SIGNAL ACQUISITION AND PREPROCESSING

The current chapter is organized as follows. Section 3.1 describes the SCG signal acquisition method. Sections 3.3 and 2.3 discuss the signal segmentation and noise reduction methods, respectively. Conclusions are provided in section 3.5. Figure 2.1 shows the work flow of this chapter.

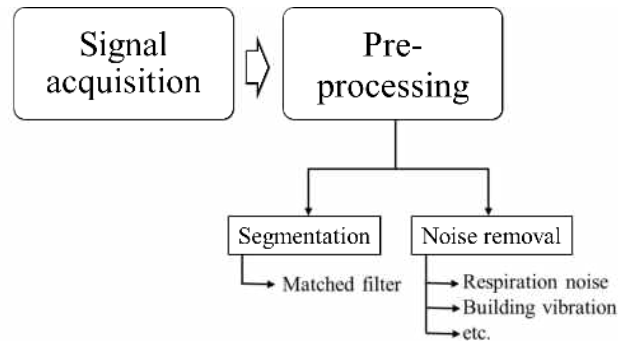


Figure 2.1. CHAPTER 2 work flow.

2.1 SCG Acquisition

SCG may be detected using displacement, velocity or acceleration sensor. In previous studies, different methods have been used for SCG measurement, including:

- Uniaxial/triaxial piezoelectric accelerometers [31,41,73,74]
- Uniaxial/triaxial MEMS accelerometers [34,43,70,75]
- Smartphone accelerometers and gyroscopes [46,76]
- Laser Doppler vibrometers [47,74]
- Microwave Doppler radars [77,78]
- Triaxial gyroscopes [43,75]

The sensors were typically placed on (or pointed at) the sternum or its left border. However, in some studies, other locations such as those close to the heart apex and heart valves were chosen

for data acquisition [34,40,70]. The information about sensor type, model and placement used for SCG measurement in the recent SCG studies are summarized in Table 2.1 and Figure 2.2.

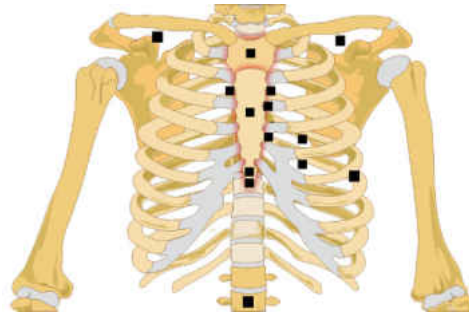


Figure 2.2. Sensor location distribution in the recent SCG studies. These studies are listed in Table 2.1.

In some applications, such as burn patients, highly infectious patients, and premature baby care, attaching adhesive ECG electrodes or SCG kit would not be feasible. Therefore, it would be necessary to develop new efficient contactless techniques to monitor cardiac activity. In that respect, LDV and microwave Doppler radar can acquire the vibrations of a patient skin without physical contacts [10]. A non-contact SCG measurement might also reduce some of the artifacts that are present in the SCG signals acquired by the accelerometers attached to the skin. LDV compares the frequency shift between the outgoing and reflected laser beam and the corresponding vibration velocity is evaluated [97]. Some of the considerations about the LDV SCG are as follow.

- The contactless nature of this measurement is its major advantage over other methods.
- LDV can take accurate measurements if the measured surface is reasonably reflective.
- The laser beam should be perpendicular to chest.
- Chest movement due to breathing results in movement of measurement point, therefore the SCG signal is not measured from a single point.

Table 2.1. Summary of acceleration sensors used for SCG data acquisition. Abbreviations used in the table: Acc: accelerometer, Gyr: gyroscope, 1-: uniaxial, 3-: triaxial, MEMS-: micro electromechanical systems, SP-: smart phone.

	Sensor Type	Sensor Model	Sensor Location
[30,72,79]	3-Acc	SCA610-C21H1A, Murata Electronic	1 cm above xiphoid
[34,70]	3-MEMS-Acc	MMA 7361, Freescale Semiconductor	heart apex
[67]	3-MEMS-Acc	MMA 7361, Freescale Semiconductor	above xiphoid
[80]	3-MEMS-Acc	Analog Devices	2 cm above xiphoid
[43,75,81]	3-MEMS-Acc	KXR5-2042, Kionix	left sternal border along the 3 rd rib
	3-MEMS-Gyr	MPU9150, Invensense	
[82]	3-Acc	ViSi Mobile, Sotera Wireless	chest wall
[65,83]	1-Acc	4381, Brüel & Kjær	above xiphoid
	1-Acc	393C, PCB Piezotronics	
[84,85]	1-Acc	DS1104, DSPACE	xiphoid process
[86]	3-Acc	ADXL 335, Analog Devices	chest wall
[46]	3-SP-Acc	iPhone6, Apple	midclavicular line and 4 th intercostal space, belly above navel
[29,87]	3-Acc	356A32, PCB Piezotronics	left sternal border along the 4 th intercostal space
[88]	3-Acc	X6-2mini, GCDC	left sternal border along the 4 th intercostal space
[71]	1-MEMS-Acc	SCA620, Murata Electronic	sternum – anterior chest
[4,53,89]	3-MEMS-Acc	MMA8451Q, Freescale Semiconductor	sternum
[40,90]	1-Acc	LIS331DLH, STMicroelectronics	mitral valve, tricuspid valve, aortic valve, pulmonary valve
[91]	3-MEMS-Acc	MMA 7361, Freescale Semiconductor	left sternal border along the 3 rd rib
[62]	3-MEMS-Acc	MMA8451Q, Freescale Semiconductor	sternum, aortic valve, heart apex
[92]	3-Acc	CXL01LF3, Crossbow Technology	manubrium
	1-Acc	7290-A, Endevco Microtron	xiphoid
[32,38,54,93]	3-Acc	BMA280, Bosch Sensortec GmbH	mid-sternum
[60]	3-MEMS-Acc	TSD109C, Biopac Systems	left sternal border along the 3 rd rib
[41]	3-Acc	356A32, PCB Piezotronics	sternum, upper and lower sternum
[94]	1-Acc	N/A	sternum
[68]	3-MEMS-Acc	MMA8451Q, Freescale Semiconductor	N/A
	3-Gyr	L3GD20, STMicroelectronics	
[95]	3-Acc	ADXL 335, Analog Devices	mid-sternum, upper sternum, lower sternum point of max impulse, below left clavicle, below right clavicle
[96]	3-MEMS-Acc 3-MEMS-Gyr	SparkFun, Intel Edison	sensor is clipped on subjects cloths
[77,78]	Microwave Doppler radar		-
[76]	3-SP-Acc	Xperia Z-series, Sony	chest
[47]	Laser Doppler vibrometer	PDV-100, Polytec	-

- LDV instrumentation is too bulky to fit into small cardiac monitoring devices.
- This method is also more expensive than other SCG recording methods.

The non-contact SCG might be recorded from different measurement points on the patient body, and used for estimating various cardiac parameters such as central arterial pressure and carotid arterial pressure waveforms [47–49]. CTIs such as LVET might also be estimated using LDV and microwave Doppler radar [48,78]. The LVET value from the non-contact SCG was similar to the value derived from PPG [48].

Microwave Doppler radar is another non-contact method that can be used for SCG measurements. When recording the SCG signal using microwave Doppler radars the SCG will exhibit in the phase variation of the microwave signal. SCG signals can then be extracted from this phase variation. The major advantage of this technique is its contactless nature. However, this method suffers from the reflection of background microwave signals (called radar clutter). The effective signals in the receiver might be decreased by the radar clutter resulting in a lower signal to noise ratio [78].

2.1.1 Accelerometer Type and Location

In this dissertation, the actual SCG signals were measured over the chest of healthy volunteers and subjects with heart disease. The sensor was placed at the left sternal border and the 4th intercostal space while subjects were in the sitting, supine, and 45 degree positions. The IRB of University of Central Florida (Orlando, FL) approved the study. All the healthy participants confirmed that they had no history of cardiovascular disease or disorders. The subjects heart rate was monitored during SCG data acquisition. In this research study, the SCG data were recorded using the following accelerometers:

- A GCDC triaxial accelerometer (Model: X6-2mini, GCDC, Waveland, MS): The accelerometer provides a digital signal at a native sampling frequency of 320 Hz. This sampling frequency would be helpful to investigate the higher frequency intra-cardiac events such as heart murmurs and valvular activity as well [28].
- A light weight PCB uniaxial accelerometer (Model: 352C65, PCB piezotronics, Depew, NY). The accelerometer output was amplified using an ICP sensor Signal Conditioner (Model: 480E09, PCB piezotronics, Depew, NY) with gain factor of 100. The signal was then acquired using an iWorx TA Control Module (iWorx Systems, Inc., Dover, NH) at a sampling frequency of 10 kHz.
- A light weight PCB triaxial accelerometer (Model: 356A32, PCB piezotronics, Depew, NY). The accelerometer output was amplified using a PCB Signal Conditioner (Model: 482C, PCB piezotronics, Depew, NY) with gain factor of 100. The signal was then acquired using an iWorx TA Control Module (iWorx Systems, Inc., Dover, NH) at a sampling frequency of 10 kHz.

2.2 SCG Segmentation

Segmentation is the process of detecting individual SCG events. Figure 2.3 shows the SCG event detection algorithm, in which the SCG events (SCG1 and SCG2) in each signal were found using a matched filter. In this algorithm, an SCG signal corresponding to one heart cycle was defined as a template. The filter then detects the SCG signal portions that match that template. The top 3 panels in Figure 2.3 show the x-, y-, and z-components of the SCG signal. The template is highlighted in black.

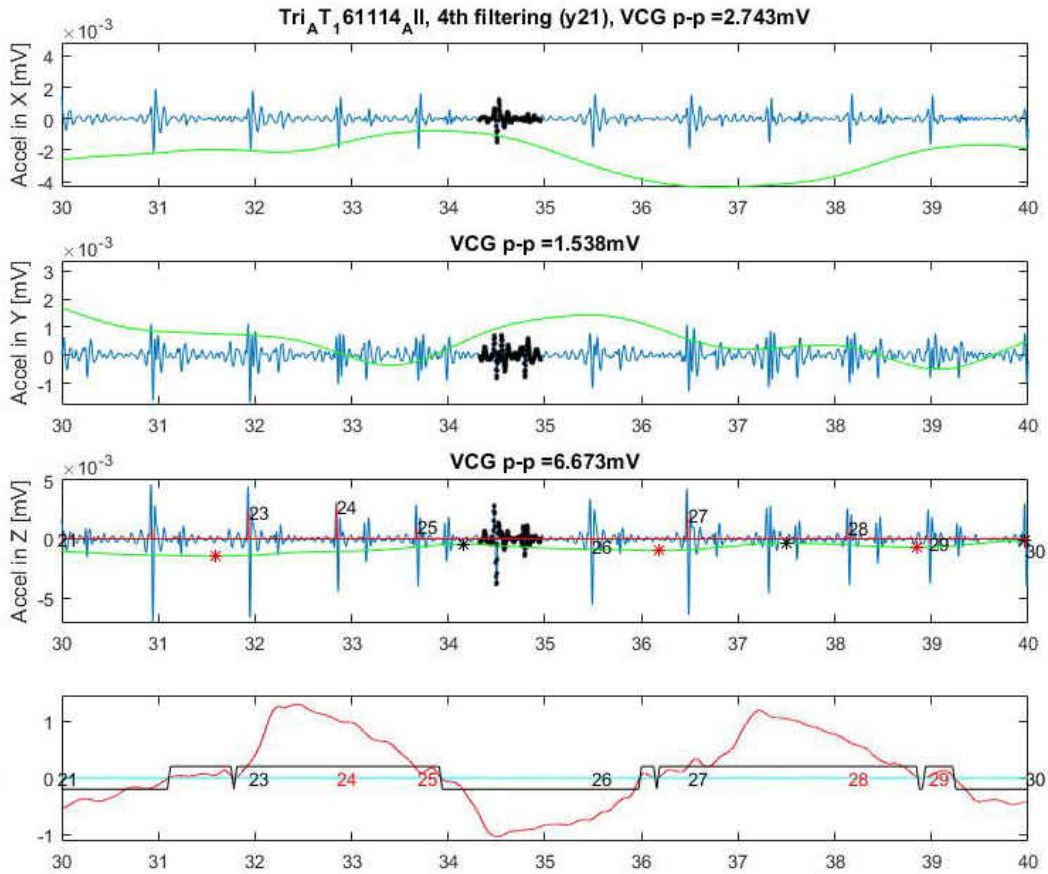


Figure 2.3. SCG signal segmentation algorithm. The top 3 panels show the x-, y-, and z-components of SCG signal. The last panel shows the subject respiratory flow signal.

2.3 Noise Removal

Recordings of biological signals such as SCG often contain contaminating noise. Noise sources may include sensor mechano-electronics, motion artifacts, and environmental vibrations. Depending on individual physiology and sensor location, the SCG signals may be obscured by these noises in the time-frequency plane, which may interfere with automated characterization of SCG.

Most research groups have applied conventional band-pass filters to remove baseline wandering, body movements and breathing artifacts from SCG signals [32,38,41,43,46,50,60,65,72,75,80–85,88,90,93–95,98]. However, a few studies have utilized/proposed more advanced noise removal techniques [22,33,86,93,99,100]. This dissertation

also investigated the utility of a filtering algorithm based on the ensemble empirical mode decomposition (EEMD) to remove respiratory and white Gaussian noise from SCG signals. Although the proposed algorithm provided a higher signal-to-noise ratio than other filters such as Wiener filter, digital band-pass filters were used in most studies in this dissertation due to their simplicity and lower computational cost.

2.3.1 Respiration and Building Vibration Noise

The digitized signal was band-pass filtered (0.5-100 Hz) to remove the respiratory noise resulting from breath sounds as well as slow chest wall movement due to breathing [101].

Figure 2.4 shows the time series and periodogram of the building vibrations measured at a desk with and without a subject sitting on it with amplification factors of 10 and 100. Figure 2.5 shows the time series and periodogram of the building vibrations measured at a trampoline with and without a subject sitting on it with amplification factors of 10 and 100. Figure 2.6 shows the time series and periodogram of a volunteer subject's SCG that laid down on a desk and trampoline and was amplified with gain factors of 10 and 100. Comparing the figures qualitatively, the SCG signals had very similar power spectrum distribution in all four cases. Also, investigating the SCG time series qualitatively, they looked like very similar. Therefore, this report suggests the following setup for the future SCG acquisitions: Subject lay down on the desk, and using a gain factor of 100 in PCB signal conditioner.

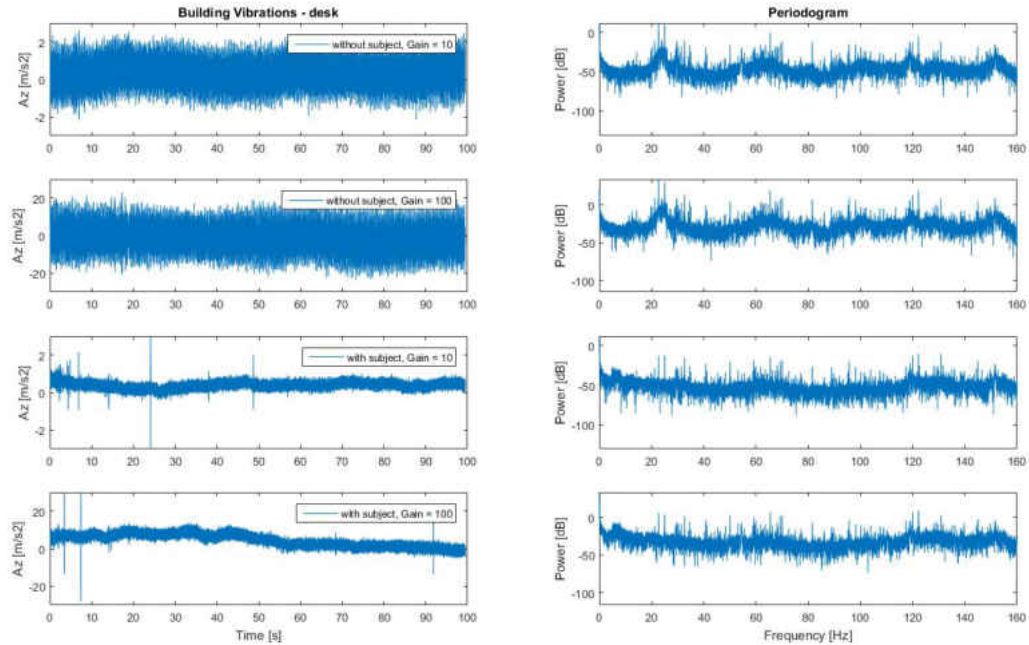


Figure 2.4. Time series (left) and periodogram (right) of building vibrations measured using PCB sensor on a desk with and without a subject sitting on the desk with two different amplification factors of 10 and 100.

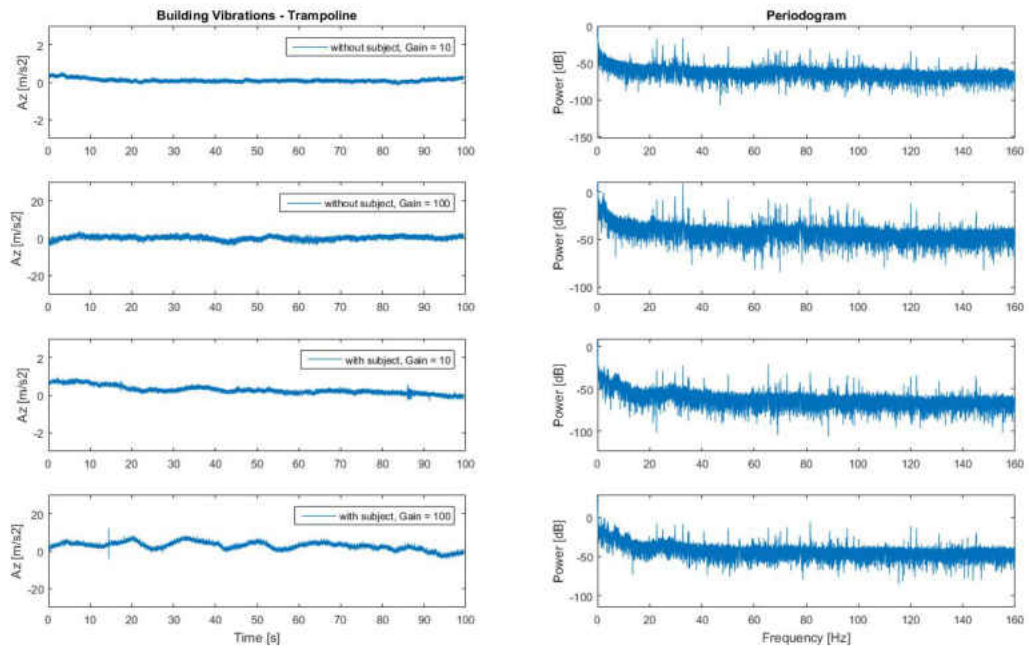


Figure 2.5. Time series (left) and periodogram (right) of building vibrations measured using PCB sensor on a trampoline with and without a subject sitting on the trampoline with two different amplification factors of 10 and 100.

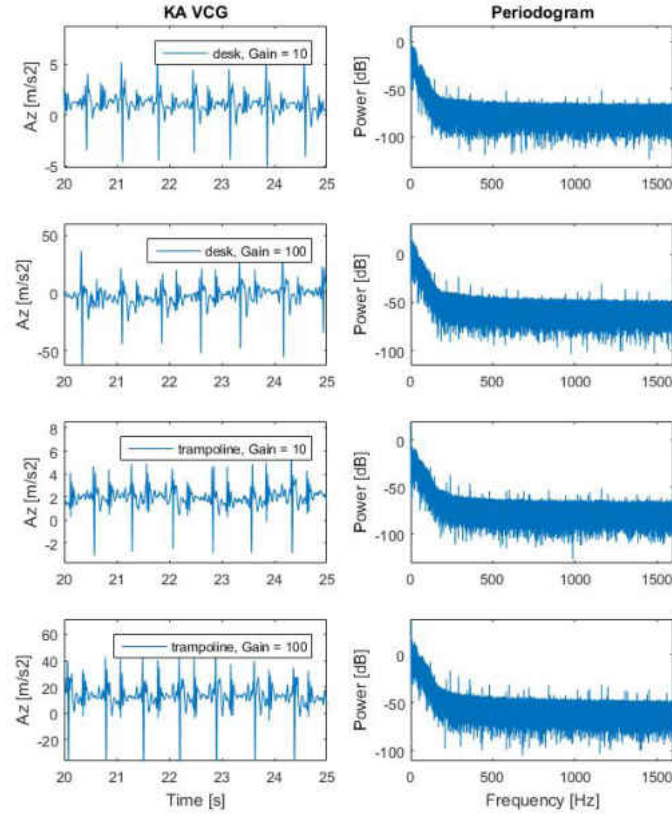


Figure 2.6. Time series (left) and periodogram (right) of SCG signals measured using PCB sensor on a desk and a trampoline with two different amplification factors of 10 and 100.

2.3.2 Noise Reduction Using Ensemble Empirical Mode Decomposition

Empirical mode decomposition (EMD) is a signal processing technique proposed for the analysis of non-stationary and nonlinear signals [102]. EMD has been successfully applied to solve numerous practical problems in various applications [103–110]. This technique decomposes a time series into a set of zero-mean underlying components called intrinsic mode functions (IMF). The main advantage of EMD is that it is an adaptive method. For example, the EMD algorithm depends only on the signal under analysis and does not require any *a priori* defined basis system. One of the main drawbacks of EMD is mode mixing that occurs when either signal of a similar scale resides in more than one IMF or an IMF consists of signals of broadly different scales [111]. This issue may cause some IMFs to become physically meaningless. Ensemble EMD (EEMD) was developed to overcome the EMD mode mixing issue [111]. The improved algorithm, EEMD, is

based on one of the most important properties of EMD, namely that EMD behaves as a dyadic filter bank when applied to white Gaussian noise [112,113]. The principle of EEMD is to add a finite number of white noise series to the signal of interest. These background white noise series provide a time-frequency reference frame for the original signal. The filter bank properties of EMD help the signal components to be projected on the proper scales of this reference frame. Since the white noise series are different in each trial, the noise cancels out for a sufficiently large number of ensembles, leaving only the persistent part of the signals. As a result, the components of similar scales are expected to reside in the same IMFs which reduces the mode mixing problem [111].

Seismocardiographic signals can contain useful information for diagnosing and monitoring of cardiac conditions [20]. However, SCG vibrations have relatively low amplitudes that can be easily contaminated by environmental vibration, patient movements, and respiration noise, which can lead to a misinterpretation of the SCG signal features. SCG as well as other biomedical signals such as heart sounds have nonlinear and non-stationary characteristics [114–126]. Hence linear methods may not be effective in analyzing these signals. EMD and EEMD were successfully used for noise cancellation and analysis of some biomedical signals [127–132]. For example, Blanco-Velasco *et al.* [133] utilized EMD to filter the high-frequency noise and baseline wander of ECG. Nimunkar & Tompkins [134] suggested an algorithm to remove power-line noise on ECG by adding a pseudo-high-frequency noise to IMFs. Krupa *et al.* [135] proposed an algorithm for denoising the cardiocography signals using partial sum of IMFs. Lemay & Vesin [136] compared the performance of an EMD-based algorithm with an IIR bandpass filter to improve the quality of atrial signals after QRST cancellation. Chang & Liu [137] investigated the effectiveness of EMD-based, EEMD-based, and FIR Wiener filters for removing the Gaussian noise from ECG, and concluded that EEMD outperformed the other two methods.

The current section investigates the utility of different filters for SCG noise cancellation. The performance of EEMD and Wiener filters was compared at different signal to noise ratios for a synthetic SCG signal. In order to assess the performance of different filtering methods, the root-mean-squared misadjustment between the clean and filter SCG amplitudes was calculated. The EEMD-based filter had a lower misadjustment than the Wiener filter. Therefore, this study suggests that the proposed EEMD-based filter may be more effective than Wiener filter in removing white Gaussian noise from actual SCG signals.

2.3.2.1 Methodology

2.3.2.1.1 Synthetic SCG Signal and Noise Set

A simulated SCG consisting of a pure tone at 40 Hz and a varying frequency component ranging from 7 to 20 Hz has been used in the present study. To evaluate the capability of EEMD-based filter in noise cancellation, the synthetic SCG signal was polluted by white Gaussian noise sets, n_{wgn} , with the signal-to-noise ratio (SNR) ranging from 1 to 20 dB.

2.3.2.1.2 Ensemble Empirical Mode Decomposition

The Hilbert Huang transform is developed for analysis of nonlinear and non-stationary signals. This technique consists of two core steps; empirical mode decomposition and Hilbert transform. The EMD decomposes the signal into IMFs with varying amplitude and frequency. These IMFs are assumed to be correlated to physical or physiological aspects of the signals under analysis [128,138]. More specifically, the EMD algorithm consists of the following steps [102]:

1. Identify all the local extrema of the signal, $x(t)$.
2. Determine the upper and lower envelopes of the signal with cubic spline using the local maxima and minima, respectively.
3. Calculate the local mean of the two envelopes, $m(t)$.

4. Calculate the difference between the signal and the local mean, $d(t) = x(t) - m(t)$.
5. Replace $x(t)$ with $d(t)$.
6. Repeat steps 1 through 5 until $d(t)$ becomes a zero-mean function. Then, $d(t)$ is called the first IMF, $c_1(t)$.
7. Subtract the IMF from the signal $r_1(t) = x(t) - c_1(t)$.
8. Repeat steps 1 through 7 to obtain the nth IMF after n iterations, $c_n(t)$.
9. The process stops when $r_n(t)$ becomes a monotonic function from which no more IMF can be extracted.

The EEMD that is proposed to solve the mode-mixing issue of the EMD, uses the following algorithm [111]:

1. Add a white noise series, $n_i(t)$, to the original signal, $x(t)$, to obtain $x_i(t) = x(t) + n_i(t)$.
2. Decompose $x_i(t)$ using EMD algorithm
3. Repeat steps 1 and 2 with NE (number of ensembles) different sets of white noise series to obtain NE sets of IMFs
4. Calculate the mean of the ensemble of IMFs to obtain the final signal intrinsic mode functions.

At the end of the process, the original signal can be reconstructed as:

$$x(t) = \sum_{i=1}^n c_i(t) + r(t) \quad (2-1)$$

where $c_i(t)$ and $r(t)$ are the i^{th} IMF and residue, respectively. The low and high scale IMFs contain the high-frequency and low-frequency components of the signal, respectively. Thus, EEMD-based low-pass and high-pass filters can be designed using the partial reconstruction of IMFs of interest. Since the white noise series usually has higher frequencies than SCG signals, they are expected to reside in the low scale IMFs. In the current study, an EEMD-based low-pass filter was used to remove the undesired noise sets as follows:

$$EEMDF_m = \sum_{i=m}^n c_i(t) + r(t) \quad (2-2)$$

where $1 \leq m < n$.

2.3.2.1.3 Misadjustment Analysis

The normalized root-mean-square error (NRMSE) between the filter and clean SCGs' amplitude was calculated as:

$$RMSE = \sqrt{\frac{\sum_{i=1}^L (VCG_{clean,i} - VCG_{filt,i})^2}{L}} \quad (2-3)$$

$$NRMSE = \frac{RMSE}{VCG_{max}} \quad (2-4)$$

where $VCG_{clean,i}$ and $VCG_{filt,i}$ are the clean and filtered SCG signal amplitude at time i , respectively. VCG_{max} and L are the maximum amplitude of the clean SCG and the SCG signal length. The performance of the EEMD-based filter was also compared with a Wiener filter [139] with a priori SNR estimation using Decision-Directed method [140].

2.3.2.2 Noise Reduction Results

The first step of EEMD algorithm consists of adding a finite number of white Gaussian noise series to the signal of interest. The number of added noise (number of ensembles) plays an important role in the EEMD performance. Figure 2.7 shows the NRMSE of the signal under analysis polluted with different levels of noise versus number of ensembles. The NRMSE decreased dramatically as number of ensembles increased from 1 to 100. For larger number of ensembles, the NRMSE decreased with a slower rate and finally reached a plateau. Large number of ensembles resulted in lower NRMSE, but also required more computational time. Therefore, a compromise between the NRMSE and computational efficiency is needed. In the current study,

number of ensembles of 150 was sufficient for the simulated SCG to achieve an acceptable NRMSE value.

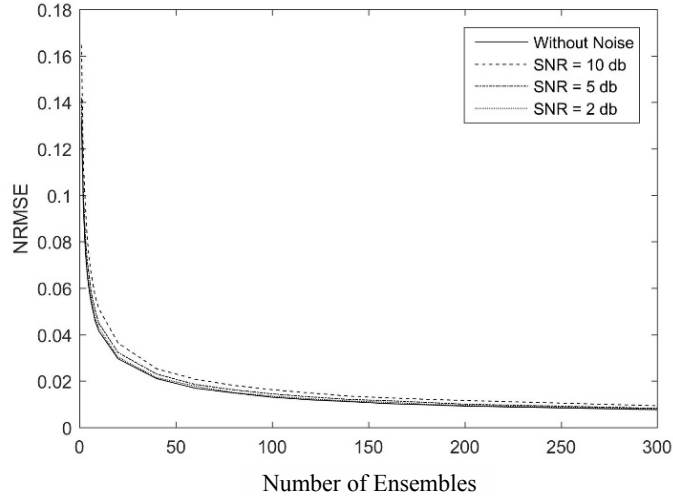


Figure 2.7. The effect of trial number (number of white noise series) on EEMD performance for reconstructed simulated SCG without added noise and with 10, 5 and 2 dB added noise.

The EEMD-derived IMFs of the simulated SCG with Gaussian noise and their PSD are shown in Figure 2.8. As expected, the EEMD behaved as a filter bank and decomposed the signal into IMF components each of which resided in a specific frequency range. Thus, the noise may be filtered by ignoring the lower IMF scales. Figure 2.8 shows that the signal is decomposed into 11 oscillatory components and a residue. The lower frequency component of the SCG events (i.e. the varying frequency component ranging from 20 to 7 Hz) was distributed in IMF #2 through #5, while the higher frequency component (i.e. the 40 Hz component) mainly allocated in IMF #2. The high frequency Gaussian noise was concentrated in the first IMF. Therefore, the signal contaminations can be reduced with partial reconstruction of IMF components by ignoring the low scale IMFs. This concept will be investigated further in the following section using the NRMSE parameter.

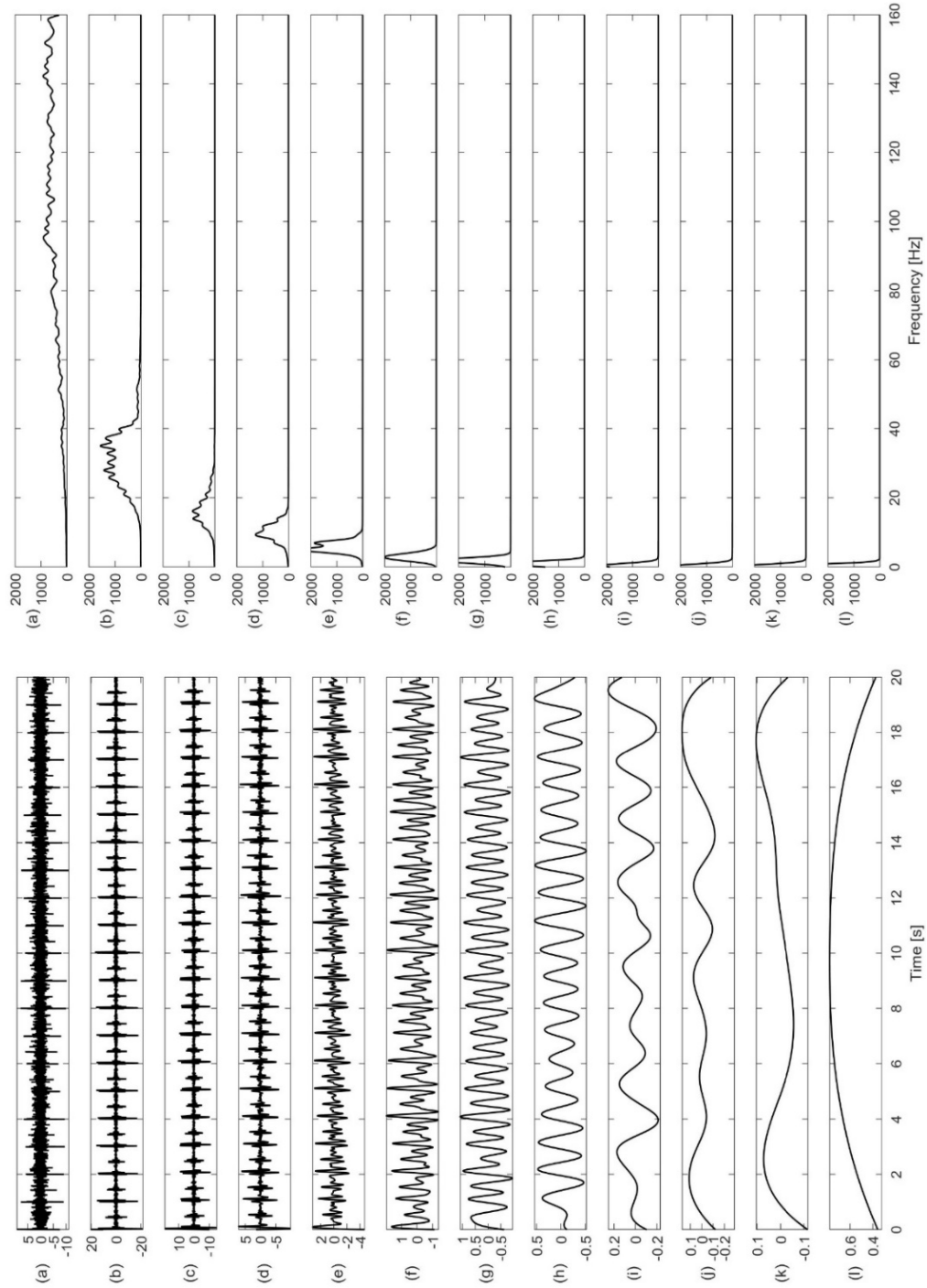


Figure 2.8. Simulated SCG contaminated by Gaussian noise with SNR = 10 dB EEMD-derived IMF components (left). The signal was decomposed into 11 IMFs (subfigure a through k) and a residue (subfigure l). The power spectral density of the IMFs and residue (right). Most of the high-frequency Gaussian noise is concentrated and localized in the first IMF. However, some low amplitude noise can be seen above 45 Hz in the second IMF. Also, some parts of the SCG events (especially SCG2) are seen in the first IMF between 20 – 40 Hz which is not desirable.

2.3.2.3 Discussion

EEMD is a signal-dependent technique that is convenient for nonlinear and non-stationary signals. In this section, the performance and efficiency of the EEMD-based noise filtration method was investigated and compared with traditional filters.

2.3.2.3.1 Filtering Performance of EEMD

Figure 2.9 shows the filtered SCG signals using partial summation of IMF components. The NRMSE between the filtered and clean SCG amplitude are shown in Figure 2.10. Both EEMD-based filter and the Wiener filter had improved noise cancellation performance as SNR increased. The Wiener filter and EEMDF₂ had the minimum NRMSE at $1 \leq \text{SNR} \leq 2$ dB and $4 \leq \text{SNR} \leq 16$ dB, respectively. The ratio EEMDF₂/Wiener fell by 48.85% from 1.095 to 0.560 as SNR increased from 1 to 20 dB, which indicates that EEMD-based filter was able to reduce the white Gaussian noise more efficiently than Wiener filter at higher signal-to-noise ratios. Overall, for the signal considered, the EEMD filter outperformed the Wiener filter for SNR values > 4 dB and had similar performance for $1 < \text{SNR} < 4$.

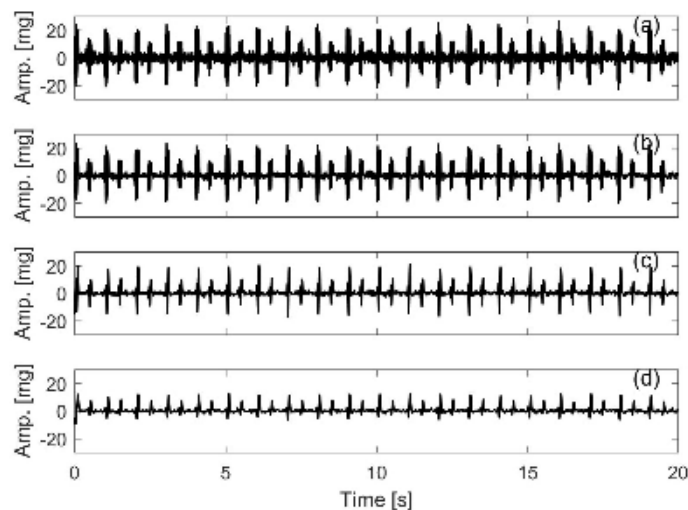


Figure 2.9. Noise reduction from the simulated SCG contaminated with white Gaussian noise using EEMD-based partial reconstruction. (a) EEMDF₁, (b) EEMDF₂, (c) EEMDF₃, (d) EEMDF₄.

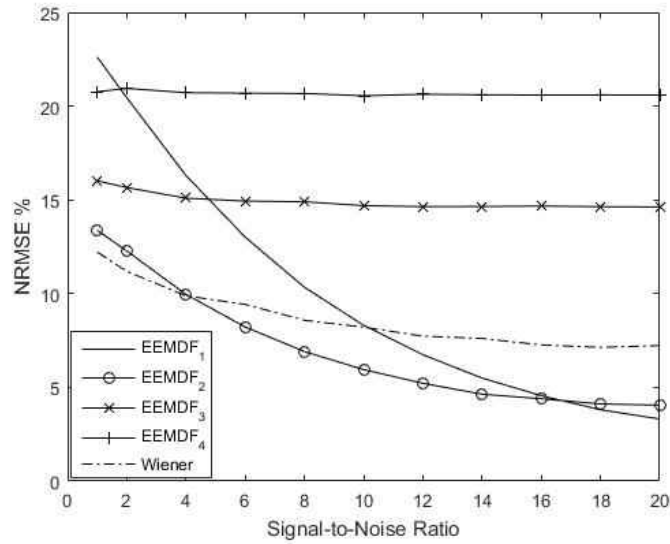


Figure 2.10. NRMSE analysis for simulated SCG contaminated with white noise with SNR values ranging from 1 to 20 dB.

Table 2.2. NRMSE analysis for simulated SCG contaminated with white noise with SNR values ranging from 1 to 20 dB.

		NRMSE for Simulated SCG with white noise (%)				
		EEMDF ₁	EEMDF ₂	EEMDF ₃	EEMDF ₄	Wiener
Signal-to-Noise Ratio [dB]	1	22.95	13.57	16.25	21.07	12.39
	2	20.50	12.46	16.01	21.15	11.06
	4	16.30	10.13	15.60	20.99	10.23
	6	12.99	8.23	15.11	20.87	9.02
	8	10.39	6.82	15.04	20.83	8.56
	10	8.39	5.98	15.02	20.85	8.18
	12	6.75	5.26	14.82	20.80	7.84
	14	5.55	4.85	14.93	20.79	7.52
	16	4.56	4.46	14.79	20.80	7.33
	18	3.86	4.20	14.76	20.78	7.36
20	3.32	4.07	14.80	20.87	7.26	

EMD and EEMD were designed to analyze nonlinear and non-stationary signals. The main advantage of EMD is that it is an adaptive method that depends only on the signal under analysis and does not require any a priori defined basis system. Instead, it decomposes the signal into IMFs that depend on the original signal alone. On the other hand, determining the physical phenomena associated with IMFs is not always possible and needs comprehensive understanding of the signal [141]. A main drawback of EMD is the “mode mixing”, which is either a similar scale residing in more than one IMF or an IMF consisting of signals of broadly different scales [111]. This issue may cause some IMFs to become physically meaningless. EEMD was developed to overcome the

EMD mode mixing issue. However, EEMD has relatively higher computational cost than both EMD and traditional band-pass filters. In the current study, EEMD was more effective than Wiener filter in white noise removal from SCG. The filter performance certainly depended on the number of IMFs left out. Performance was best in the current application when only the lowest IMF with the lowest scale is ignored.

2.3.2.4 Conclusions

Noise removal from biological signals like SCG can help provide higher quality information that would facilitate signal interpretation, which may help provide more accurate medical diagnosis. In the current study, the performance of EEMD-based filter for white noise removal from SCG signal was evaluated. To test the filter, a synthetic SCG signal was created and corrupted by white noise. The filter was then used to recover the original SCG signal. This was followed by calculating the normalized root-mean-squared misadjustment between the original and filtered signals. The performance of the EEMD and a Wiener filter was evaluated by comparing the associated misadjustments. Results of this analysis demonstrated that the EEMD filter had a lower normalized root-mean-squared misadjustment than the Wiener filter. The lower performance of the Wiener filter may be attributed to a relatively high non-linearity of the SCG signal under consideration. More studies may be warranted to document the effectiveness of EEMD filters for noise cancellation from actual SCG signals in health and disease. Future studies may also investigate the connection between the IMF and cardiac events, which in turn, may enhance our understanding of SCG signals and their relation to cardiac events.

2.4 Summary

In this chapter, SCG acquisition, segmentation, and noise removal methods were discussed. These steps are prerequisite to accurate feature extraction and signal classification described in

later chapters. Certain accelerometers were selected for signal acquisition due to their small size, lower cost, and relatively high signal-to-noise ratio. A template-based matched filter was effective in detecting SCG events. Several filtering methods were explored, and band-pass filtering was chosen due to its simplicity and lower computational cost.

CHAPTER 3: FEATURE EXTRACTION

Feature extraction is another step of processing of biomedical signals. Identifying the most significant features of the signal can result in an efficient signal classification since these features are eventually the inputs to classification algorithms such as neural networks (NN), random forest (RF), and support vector machines (SVM). Determining the most effective and accurate techniques to extract specific signal features is a necessary step that should be done before identification of useful features. For example, there are different methods to estimate the time-frequency distribution of a signal. Every method has its own advantages and disadvantages, and might be suitable for certain type of signals or at certain conditions. In this chapter, different time-frequency distribution techniques, including short-time Fourier transform, polynomial chirplet transform, wavelet transform with different mother functions, Wigner-Ville distribution and smoothed pseudo Wigner-Ville distribution, were used to estimate the temporal and spectral content of SCG signals. This is done to determine the most accurate methods for extracting time-frequency features of the SCG signals.

In the previous studies, feature extraction from SCG signals has mainly focused on the time-domain and the frequency domain through the fast Fourier transform (FFT). The time domain features included statistical features of the SCG signal, such as mean, median, and standard deviation, and features related to cardiac mechanics, such as CTIs. Frequency domain features included frequency coefficients obtained through the FFT and their statistical features.

The current chapter was organized as follows. Sections 3.1 and 3.2 list the features that might be useful for SCG signal classification in the time and frequency domains, respectively. Sections 3.3 and 3.4 discuss the SCG time-frequency features and suitable methods to extract them in the presence and absence noise. Conclusions are provided in section 3.5.

3.1 Time Domain Features

Statistical time-domain features included those containing information about the entire signal, and those from divided signal segments. Features from segments of the SCG signal were obtained by dividing the SCG signal into a specific number of equal-sized bins and calculating the arithmetic mean of each bin as a feature [30,142]. In contradistinction, a recent study divided the signal into bins of unequal size, where the signal parts with higher signal variation contained a higher concentration of bins [87]. The algorithm splits the bin with the highest standard deviation into two bins in a recursive fashion, until a certain criterion is met, such as reaching a desired number of bins. As opposed to obtaining features from divided segments of the SCG signal, features may be extracted from time-domain statistical characteristics of the entire SCG signal, such as mean, kurtosis, skewness, and standard deviation [41].

One study used heart rate variabilities, heart rates, and waveform fiducial point relations [76]. Time-domain features also included those related to certain cardiac activities. Also, through knowledge of the R and Q peaks and the SCG fiducial points (AO, AC, MO, and MC), CTIs can be calculated. These intervals include PEP, ICT, LVET, and Isovolumic Relaxation Time (IRT). Other metrics such as PEP/LVET ratio, (ICT+IRT)/LVET (also called Myocardial Performance Index), and the LVET/RR-interval ratio can also be determined [68,143]. Amplitudes and slopes associated with the fiducial points, such as MC to AO slope, were used in some studies [65,143]. In addition, the SCG signal features that are independent of fiducial points, such as maximas, minimas, and their associated widths of specific segments of the SCG signal were used [95]. Other time domain features that might be considered useful for SCG signal classification are:

- Duration of and intervals between SCG events
- Duration of different waves of the SCG event and intervals

- Timing relation between SCG waves and ECHO, ECG, and PCG
- Relative amplitude of different waves
- Attack and decay rate (see APPENDIX A)

3.2 Frequency Domain Features

Statistical frequency-domain features included those obtained from various frequency bands, and across the entire available frequency spectrum. Features from the frequency bands of the FFT from an averaged 3-dimensional SCG signal were obtained by calculating the median of each band [38]. One study calculated the approximate and spectral entropy of the 0-11 Hz frequency band [76]. The average power of various frequency bands (0-3 Hz, 3-6 Hz, ..., 15-18 Hz) were also obtained [41]. Various statistical metrics such as: arithmetic mean, median, standard deviation, skewness, kurtosis, mode, average power, sample entropy, spectral entropy, and the Kolmogorov complexity, were also calculated across the entire available frequency band [31,41].

Other frequency-domain features included frequency coefficients such as amplitudes and frequencies. Features were either obtained by taking the frequency amplitudes across a range of the frequency spectrum (0-512 Hz) [30], or by taking the frequencies and amplitudes at specific peaks of the spectrum, such as the 1st, 2nd, and 3rd peaks [41]. Other frequency domain features that might be considered useful for SCG signal classification are as follow:

- Dominant frequencies and relationship between them
- Frequencies of different waves
- Relative amount of energy in specific waves and frequency bands

3.3 Time-frequency Features

Many methods have been used for SCG analysis [10–12,144] including time-frequency analysis [22,117,118]. The current chapter focusses on extracting spectral features of SCG signals

using time-frequency distributions (TFDs). TFDs have been utilized in the analysis of a wide range of signals including biomedical signals such as electrocardiogram [145,146], electroencephalogram [147,148], phonocardiogram [149–152], and myoelectric signals [153]. The ability of TFD methods to provide an accurate time-frequency representation depends on the underlying assumptions associated with each method. One common approach for TFD estimation is the short-time Fourier transform (STFT). The STFT is relatively simple, but it may not effectively track steep changes in the time direction [149,154]. In addition, the STFT has static resolution in the time-frequency plane, which can result in resolution limitations. For example, improving the resolution of one of either time or frequency domains worsens the resolution in the other domain. The wavelet transform (WT) was proposed to overcome the resolution issues of the STFT, but the former also has its own resolution limitations [146]. For example, a wavelet shows coarser frequency resolution at higher frequencies and vice versa [155]. This property suggests that WT can be a proper candidate for TFD analysis of signals with discontinuity or steep changes. The wavelet theory can be divided into two important parts; continuous wavelet transform (CWT) and discrete wavelet transform (DWT). While DWT is usually used for signal filtering, denoising and compressing [152,156–159], CWT is more useful for the signal time-frequency analysis [149,153,160].

The chirplet transform (CT) is another transform that can be viewed as a generalization of both the STFT and WT [161]. It is a transform that involves a function of four parameters: time, frequency, scale and chirp rate; where chirp rate is defined as the instantaneous rate of change in the signal frequency [162]. Since the conventional CT is developed based on the linear chirp kernel, it may provide inaccurate TFD estimations for the signals that have nonlinear instantaneous frequency (IF) trajectory. Therefore, Peng *et al.* [154] proposed the polynomial chirplet transform

(PCT), which is based on a kernel with a polynomial nonlinear IF. This method is more suitable for the signals with IF trajectories that are continuous (either linear or nonlinear) functions of time.

All of the TFDs under discussion are bilinear (or quadratic) representations that combine the time and frequency domain signal information, i.e., they describe the temporal and spectral characteristics of the signal simultaneously. It is worthwhile noting that for a bilinear TFD, the PSD of a signal that contains two components differs from the summation of the PSD of the components. The cross terms (also called interference terms) in bilinear representations cause artifacts (e.g., extra peaks) in those regions of the time-frequency plane that energy spectral density of the signal components overlap [155].

There are no previous detailed studies that compared the performance of TFD for the analysis of SCG signals. There are, however, studies that addressed similar cardiac signals. For instance, Crowe *et al.* [146] proposed WT for the analysis of the ECG signals. WT has been also used to analyze ECG signals of patients with some cardiovascular pathology [145]. Obaidat [149] compared the resolution of STFT, WT, and Wigner-Ville distribution for the analysis of phonocardiogram signal. He concluded that WT provided more details of the first and second heart sounds that are acquired by a phonocardiograph. Debbal & Bereksi-Reguig [151] performed a time-frequency analysis of a phonocardiogram signal and compared the performance of STFT, WT and Wigner distribution. Their results suggested that WT revealed the time-frequency characteristics of the signal and was superior to STFT and Wigner distribution in distinguishing between different components of the first and second heart sound. Cherif *et al.* [152] used wavelet packet transform and discrete wavelet transform with different mother functions to filter murmurs from phonocardiogram signals. They concluded that discrete wavelet transform was more suitable for filtering the murmurs without affecting the heart sound and their components. Also, Ergen *et*

al. [160] investigated the characteristics of the phonocardiogram signals by using wavelets of 8 different mother functions and concluded that Morlet was the most appropriate wavelet to extract the features of heart sounds and murmurs.

Understanding different characteristics of SCG, including its TFD, may lead to a more comprehensive description of signals that are related to cardiac activity. Furthermore, successful automatic classification of SCG signals in health and disease can provide possible new methods for diagnosing and monitoring heart function. Time-frequency characteristics are potentially useful features that have been used for automatic classification of similar biomedical signals. However, there is no previous study that focused on determining the most suitable TFD for extracting features of SCG signals.

The objective of current section is to compare the performances of different TFDs for the analysis of SCG signals. The TFDs that can extract SCG features more accurately will be identified and used to analyze actual SCG signals. A brief description of the theory of STFT, WT, and PCT is provided in the following section. Results are then presented and discussed, followed by conclusions.

3.3.1 Time-frequency Distribution Methods

The TFD of the signals of interest was estimated using six different approaches: Short-Time Fourier Transform, Polynomial Chirplet Transform, and Continuous Wavelet Transform with Daubechies4 (CWT-db4), Coiflet5 (CWT-Coif5), Haar (CWT-Haar), and Morlet (CWT-Morl) as the mother functions. This section provides the definition and properties of the TFD methods under consideration.

3.3.1.1 Short-time Fourier Transform

The STFT is obtained by multiplying the signal to be transformed, $x(t)$, by a non-zero window function $w(t)$. Sliding the window function is then performed to add the time dimension and obtain a time-dependent frequency spectrum. This process can be represented by the equation:

$$\bar{X}_{STFT} = \int_{-\infty}^{+\infty} x(\tau)w(\tau - t)e^{-j\omega\tau}d\tau \quad (3-1)$$

where $w(t)$, t , and ω are the window function, time, and frequency, respectively. In this TFD method, the signal $x(t)$ is divided into a number of sub-records that are shorter than $x(t)$. To decrease spectral leakage, the sub-records are multiplied by another window function, and finally, FFT is applied to each sub-record. This approach assumes that the signal in each sub-record is stationary. When steep signal non-stationarity is absent in the sub-records, the STFT is expected to provide high quality estimates of the signal TFD for the whole signal duration. When signal non-stationarity is steeper, the sub-records can be shortened to reduce non-stationarity in individual sub-records and enhance temporal resolution. The shortened time records will, however, worsen the frequency resolution. Hence, refining temporal and spectral resolutions are two competing effects, and a compromise will be needed to reach accurate estimate of TFD.

3.3.1.2 Continuous Wavelet Transform

The CWT of the signal $x(t)$ is defined as follows,

$$\bar{X}_{WT} = \frac{1}{\sqrt{a}} \int_{-\infty}^{+\infty} x(\tau)\psi^*\left(\frac{\tau - t}{a}\right)d\tau = \sqrt{a} \int_{-\infty}^{+\infty} X(\omega)\Psi^*(a\omega)e^{j\omega t}d\omega \quad (3-2)$$

where a is a scale parameter that is inversely related to the frequency. Here, the frequency shifting operation in STFT is replaced by a time scaling operation in WT. The superscript * denotes the complex conjugate, and $\psi(t)$ is the chosen wavelet mother function. For small and large a values,

$\psi\left(\frac{\tau-t}{a}\right)$ becomes a contracted and stretched version of the mother function, respectively. Therefore, small and large a values may be appropriate for analysis of the high and low frequency components of the signal, respectively. $X(\omega)$ and $\Psi(\omega)$ are the Fourier transforms of $x(t)$ and $\psi(t)$, respectively. In contrast with STFT that uses the same sliding window at both of low and high frequencies, the CWT uses short and long windows at high and low frequencies, respectively. This feature can aid in obtaining better resolution from CWT compared to STFT at low frequencies. Since, the scale parameter in the CWT can be considered the inverse of the frequency, the local pseudo-frequency of the CWT may be approximated [163] by:

$$f = \frac{f_s f_c}{s} \quad (3-3)$$

where f is in hertz, and f_c , f_s , and s are the center frequency of the mother wavelet, sampling frequency, and translation parameter (which stands for time), respectively. The center frequencies of the mother wavelets used in the current study are listed in Table 3.1.

Table 3.1. Center frequency of the wavelets used in the current study.

Wavelet	Morlet	Haar	Daubechies4	Coiflet5
Center frequency (Hz)	0.8125	0.9961	0.7143	0.6897

The pure WT results in a TFD that consists of discrete regions. In this study, different smoothing techniques were tested to obtain a smoothed CWT TFD (see APPENDIX B).

3.3.1.3 Chirplet Transform and Polynomial Chirplet Transform

In the time-frequency analysis, the chirplet transform of a signal $x(\tau)$ can be expressed as [154],

$$\bar{X}_{CT}(t_0, \omega, \alpha; \sigma) = \int_{-\infty}^{+\infty} \bar{z}(t) w_{(\sigma)}(t - t_0) e^{-j\omega t} dt \quad (3-4)$$

where $w_{(\sigma)}$ is a nonnegative, symmetric, and normalized real function. t_0 , ω and α are time, frequency and chirp rate respectively. $z(t)$ is the analytic associate of the signal $x(t)$, and $\bar{z}(t)$ is defined as,

$$\bar{z}(t) = z(t)\Phi_{\alpha}^R(t)\Phi_{\alpha}^M(t, t_0) \quad (3-5)$$

where $\Phi_{\alpha}^R(t)$ and $\Phi_{\alpha}^M(t, t_0)$ are the frequency rotating operator and the frequency shift operator respectively and defined as,

$$\Phi_{\alpha}^R(t) = e^{-j\alpha t^2/2} \quad (3-6)$$

$$\Phi_{\alpha}^M(t, t_0) = e^{j\alpha t_0 t} \quad (3-7)$$

$\Phi_{\alpha}^R(t)$ rotates the analytical associate of the signal by an angle $\theta = \tan^{-1}(-\alpha)$ and $\Phi_{\alpha}^M(t, t_0)$ shifts a frequency component from ω to $\omega + \alpha t_0$.

For the signals with nonlinear IF trajectory, CT may not accurately track the signal IF [154]. Therefore, the PCT with nonlinear frequency rotating and shift operators and a polynomial kernel is defined to improve the performance of the conventional CT when applied to the signals with nonlinear IF trajectory.

$$\begin{aligned} \bar{X}_{PCT}(t_0, \omega, \alpha_1, \alpha_2, \dots, \alpha_n; \sigma) \\ = \int_{-\infty}^{+\infty} z(t)\Phi_{\alpha_1, \alpha_2, \dots, \alpha_n}^R(t)\Phi_{\alpha_1, \alpha_2, \dots, \alpha_n}^M(t, t_0)w_{(\sigma)}(t - t_0)e^{-j\omega t} dt \end{aligned} \quad (3-8)$$

where $\Phi_{\alpha_1, \alpha_2, \dots, \alpha_n}^R(t)$ and $\Phi_{\alpha_1, \alpha_2, \dots, \alpha_n}^M(t, t_0)$ are the nonlinear frequency rotating operator and the frequency shift operator and defined as,

$$\Phi_{\alpha_1, \alpha_2, \dots, \alpha_n}^R(t) = e^{-j\sum_{k=2}^{n+1} \frac{1}{k}\alpha_{k-1}t^k} \quad (3-9)$$

$$\Phi_{\alpha_1, \alpha_2, \dots, \alpha_n}^M(t, t_0) = e^{j\sum_{k=2}^{n+1} \alpha_{k-1}t_0^{(k-1)}t} \quad (3-10)$$

The PCT can produce a TFD with higher resolution compared to conventional CT for both linear and nonlinear chirp signals [154].

3.3.2 Test Signals

To compare the performance of the different methods in estimating the TFD of SCG, several synthetic signals were generated and analyzed using the above TFD methods. This analysis will provide an estimation of the resolution and accuracy of each method. In this regard, the following synthetic signals were generated. The properties of the generated signals are summarized in Table 3.2.

Table 3.2. Description of synthetic signals used in the current study.

Signal description	Frequency range (Hz)	Peak-to-peak amplitude (V)	Signal length above 5% of peak to peak amplitude (ms)
Varying frequency, x_1	23 to 45	2.0	250
Exp. decaying sinusoid, x_2	30	2.3	230
decaying chirp, x_3	0 to 33	2.4	75
double chirp, x_4^*	7 to 33	3.2	4000
growing and decaying single tone, x_5	7 to 66	3.0	4000
synthetic SCG, $x_6^{* \#}$	20 and 40	2.8	112

*Signals with more than one dominant frequency component, # signals with quite regions

3.3.2.1 Signal with Varying Frequency

The signal consists of one sinusoid (Figure 3.3.a), with an IF law that follows the relation:

$$IF_1 = -3125 t^3 + 130.5 t^2 + 189 t + 18.25 \text{ (Hz)} \quad (3-11)$$

where the time vector varies in the range $0 \leq t \leq 0.25$,

$$x_1(t) = \sin(2\pi(-781.25 t^3 + 43.5 t^2 + 94.5 t + 18.25)(t + 0.1)) \quad (3-12)$$

3.3.2.2 Exponentially Decaying Sinusoid

This signal consists a sinusoid (Figure 3.4.a), with a constant IF of

$$IF_2 = 30 \text{ (Hz)} \quad (3-13)$$

$$x_2(t) = 1.5e^{-15(t-0.1)} \sin(2\pi(30)(t - 0.1)) ; \text{ where } 0.1 \leq t \leq 0.45 \quad (3-14)$$

3.3.2.3 Decaying Chirp

The signal (Figure 3.5.a) consists of a sinusoid with the IF of

$$IF_3 = 50(62.5t^2 - 339.4t + 345.5) \text{ (Hz)} \quad (3-15)$$

and amplitude of $1.5e^{-15(t-0.1)}$; where $0.1 \leq t \leq 0.45$,

$$x_3(t) = 1.5e^{-15(t-0.1)} \sin\left(100\pi\left(\frac{62.5}{3}t^2 - \frac{339.4}{2}t + 345.5\right)(t - 0.1)\right) \quad (3-16)$$

3.3.2.4 Double Chirp

The signal (Figure 3.6.a) consists of two chirp components with different amplitudes and IF,

$$IF_4 = \left(5 + \frac{100t}{7}\right) \quad \text{and} \quad \left(13 + \frac{160t}{7}\right) \quad (3-17)$$

$$x_4(t) = 0.7 \cos\left(2\pi\left(5 + \frac{50t}{7}\right)t\right) + A_4 \cos\left(2\pi\left(13 + \frac{80t}{7}\right)t\right) \quad (3-18)$$

where $0 \leq t \leq 4$ and A_4 is defined as follows,

$$A_4 = 0.5 + 0.1t \quad (3-19)$$

3.3.2.5 Growing and Decaying Single Tone with Varying Frequency

The signal (Figure 3.7.a) consists of a quick grow and a slow decay part with the IF of

$$IF_5 = 1.95t^2 - 18t + 30.5; \text{ where } 0 \leq t \leq 4 \quad (3-20)$$

$$x_5(t) = A_5 \sin(2\pi(0.65t^2 - 9t + 30.5)t) \quad (3-21)$$

where the signal amplitude is,

$$A_5(t) = \begin{cases} -1.82t^2 + 3.55t & 0 < t \leq 0.65 \\ -0.077t^2 - 0.077t + 1.58 & 0.65 < t \leq 4 \end{cases} \quad (3-22)$$

3.3.2.6 Synthetic SCG Signal

In this study, a synthetic SCG signal (Figure 3.8.a) is simulated and described by

$$x_6(t) = -A_6 \sin(2\pi(20)t + 94) + 0.9A_6 \sin(2\pi(40)t + 188) \quad (3-23)$$

It consists of two sinusoids with IF of

$$IF_6 = 20 \text{ and } 40 \text{ (Hz)} \quad (3-24)$$

and the signal amplitude varies according to,

$$A_6(t) = \begin{cases} 0 & 0 < t \leq 0.25 \\ 0.5 - 0.5 \cos(14\pi(t - 0.75)) & 0.25 < t \leq 0.40 \\ 0 & 0.40 < t \leq 0.70 \\ 0.45 - 0.45 \cos(14\pi(t - 0.75)) & 0.70 < t \leq 0.83 \\ 0 & 0.83 < t \leq 1.00 \end{cases} \quad (3-25)$$

3.3.3 IF Error Analysis

The different TFD methods were used to estimate IF of the synthetic signals, which have known IFs. To assess the performance of the different methods, the root mean square error (RMSE) between actual and estimated IF values was calculated as:

$$RMSE = \sqrt{\frac{\sum_{i=1}^n (IF_{actual,i} - IF_{estimated,i})^2}{n}} \quad (3-26)$$

where $IF_{actual,i}$ and $IF_{estimated,i}$ are the signal actual and estimated IF at time i , respectively.

RMSE values can also be normalized by dividing RMSE by the mean actual instantaneous frequency, \overline{IF}_{actual} , of each signal such that:

$$NRMSE = \frac{RMSE}{\overline{IF}_{actual}} \quad (3-27)$$

NRMSE was used in the current study as a measure of the accuracy of the different TFD techniques in estimating IF, where lower NRMSE values would indicate higher accuracy.

3.3.4 Data Acquisition of Human SCG

The above TFD methods were also used to analyze actual SCG signals. The actual SCG signals were measured over the chest of 8 healthy volunteers (age: 30 ± 11 years, height: 1.71 ± 0.07 m, weight: 73.66 ± 11.69 kg (mean \pm SD)) using a light-weight triaxial accelerometer (X6-2mini, GCDC, Waveland, MS) after IRB approval (at University of Central Florida). All participants confirmed that they had no history of cardiovascular disease or disorders. The subjects heart rate was 66.37 ± 2.45 bpm (mean \pm SEM) during SCG data acquisition. The sensor was placed at the left sternal border and the 4th intercostal space while subjects were in the supine position. The accelerometer provides a digital signal at a native sampling frequency of 320 Hz. This sampling frequency would be helpful to investigate the higher frequency intra-cardiac events such as heart murmurs and valvular activity as well [28]. The digitized signal was band-pass filtered (0.5-100 Hz) to remove the respiratory noise resulting from breath sounds as well as slow chest wall movement due to breathing [101]. In this study, the dorso-ventral acceleration tended to be stronger than other acceleration components, which agrees with previous studies [20]. Hence, attention in the current study was focused on extracting the TFD of the dorso-ventral acceleration. Matlab (R2015b, The MathWorks, Inc, Natick, MA) was used to process all signals. The overall algorithm is summarized in Figure 3.1.

3.3.5 Results and Discussion

Figure 3.3 through Figure 3.8 show the time series and TFD of the synthetic signals under consideration. The TFD were calculated using STFT (with a Hamming window), CWT-Morl, CWT-Haar, CWT-db4, CWT-Coif5, and PCT in subfigures b, c, d, e, f, and g, respectively. The PSD was calculated from the TFDs, was normalized with respect to the signal energy, and

presented in the left side of the Figure 3.3 through Figure 3.8. Here, spectral information is shown for frequencies up to 70 Hz as there is no significant energy seen above that frequency.

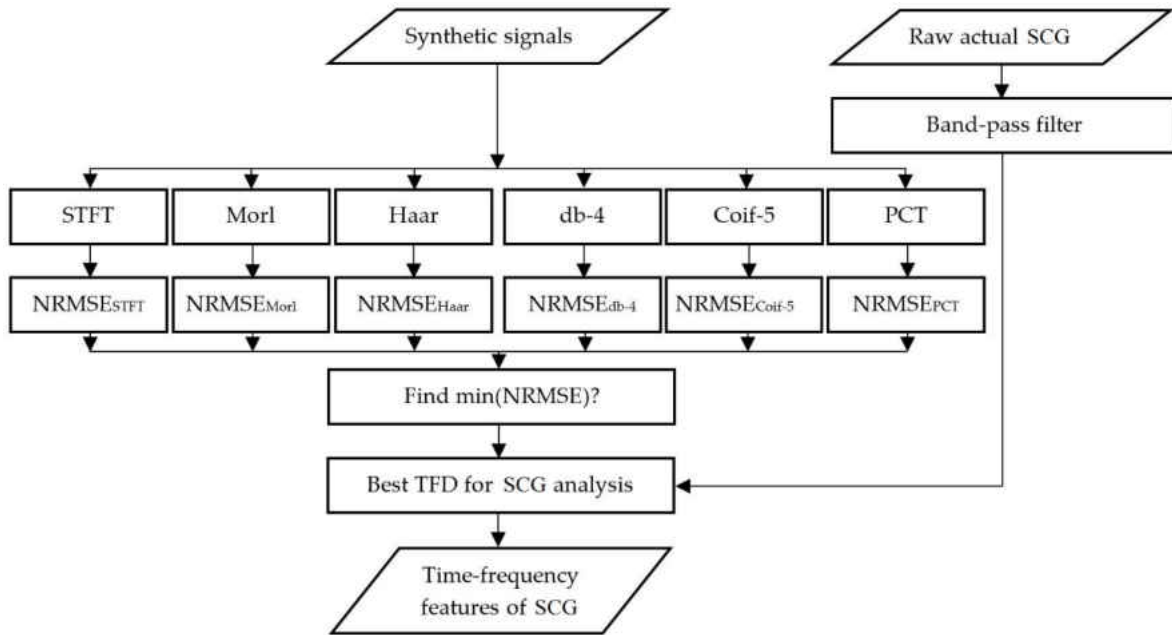


Figure 3.1. Summary of the signal processing algorithm used in this study.

Temporal and spectral resolutions of different TFD are listed in Table 3.3. The NRMSE between the actual and calculated IF are reported in Table 3.4 for different TFD. The time and frequency resolutions of each TFD were optimized for each test signal such that the NRMSE was minimized. As seen in Table 3.3, STFT had coarser temporal resolution compared to other methods. For example, the temporal resolution was 12.5 ms for STFT and 3.1 ms for all other methods. The frequency resolution for STFT and PCT (at minimum NRMSE) was frequency independent but different for different signals. The resolution mostly ranged from 0.6 to 2.5 Hz and from 0.2 to 0.25 Hz for STFT and PCT, respectively. The spectral resolution (at minimum NRMSE) for CWT-based transforms was frequency dependent (ranging from about 0.4 to 19 Hz for frequencies of 10 to 70 Hz) with finer resolution at lower frequencies. Coarser resolution is undesirable as it may result in higher errors in IF estimation.

Table 3.3. Temporal and spectral resolution for different signals and TFD for frequencies between 10 and 70 Hz. The resolution of TFD was optimized to minimize the NRMSE for each synthetic signal. STFT tended to have coarser temporal and spectral resolution compared to PCT. Frequency resolution for CWT-based methods is given as a range with lower values corresponding to lower frequencies.

		STFT	Morl	Haar	db4	Coif5	PCT
Temporal resolution (ms)	All signals, x_{1-6}	12.5	3.1	3.1	3.1	3.1	3.1
	varying frequency, x_1	2.5000	0.4000-13.0000	0.3213-15.9377	0.4517-19.0476	0.4361-18.3908	0.2133
Spectral resolution (Hz)	exponentially decaying sinusoid, x_2	2.5000	0.4000-13.0000	0.3213-15.9377	0.4517-19.0476	0.4361-18.3908	0.2036
	decaying chirp, x_3	2.5000	0.4000-13.0000	0.3213-15.9377	0.4517-19.0476	0.4361-18.3908	0.2036
	double chirp, x_4	0.6250	0.4000-13.0000	0.3213-15.9377	0.4517-19.0476	0.4361-18.3908	0.2462
	growing and decaying single tone with varying frequency, x_5	1.2500	0.4000-13.0000	0.3213-15.9377	0.4517-19.0476	0.4361-18.3908	0.2462
	synthetic SCG, x_6	0.6250	0.4000-13.0000	0.3213-15.9377	0.4517-19.0476	0.4361-18.3908	0.2462

Table 3.4. Normalized root-mean-square error (NRMSE) between the actual and calculated IF for different TFD methods. Lower error values indicate more appropriate TFD.

	STFT	Morl	Haar	db4	Coif5	PCT
varying frequency, x_1	0.0248	0.0477	0.2958	0.1954	0.1411	0.0069
exp. decaying sinusoid, x_2	0.1857	0.5393	0.6463	0.4848	0.3599	0.0056
decaying chirp, x_3	0.5737	0.4717	0.3733	0.4081	0.3736	0.0850
double chirp, x_4	0.1232	0.7467	0.5651	0.6612	0.7507	0.0671
growing and decaying single tone, x_5	0.0109	0.1666	0.1756	0.1393	0.1706	0.0179
synthetic SCG, x_6	0.0199	0.1084	0.4876	0.3419	0.2370	0.0214

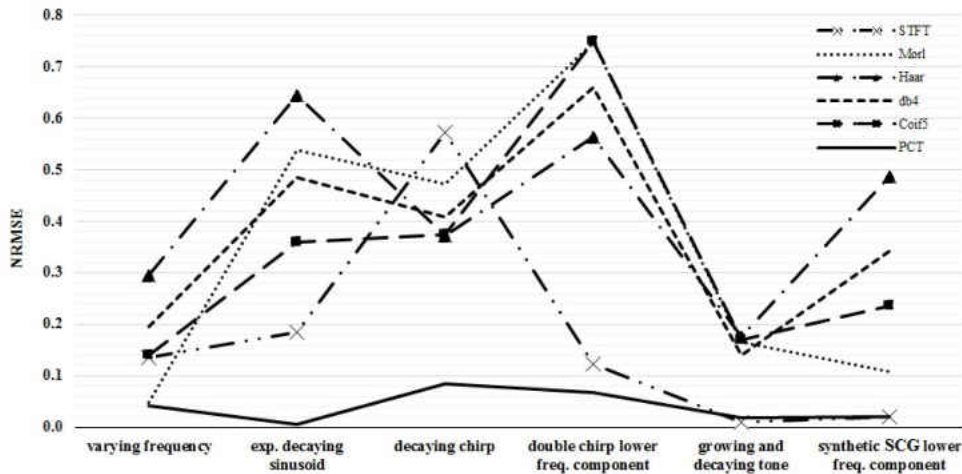


Figure 3.2. Normalized root-mean-square error (NRMSE) between the actual and calculated IF for different TFD methods. Lower error values would indicate better TFD performance.

3.3.5.1 Signal with Varying Frequency

TFD of the signal with nonlinearly varying frequency, x_I , is shown in Figure 3.3. Although CWT methods had comparable temporal and spectral resolution, CWT-Morl appeared to have a better TFD estimate than other CWT methods (Figure 3.3.c-f). The different CWT techniques tracked the signal IF with different levels of accuracy. As can be seen in Table 3.4, the error in estimating IF (among the CWT-based techniques) is lowest and highest for CWT-Morl and CWT-Haar, respectively. CWT-Morl estimated the signal IF more accurately than STFT, although the former had a slightly coarser spectral resolution in the frequency range of this signal. PCT had the lowest error in IF estimation among all methods.

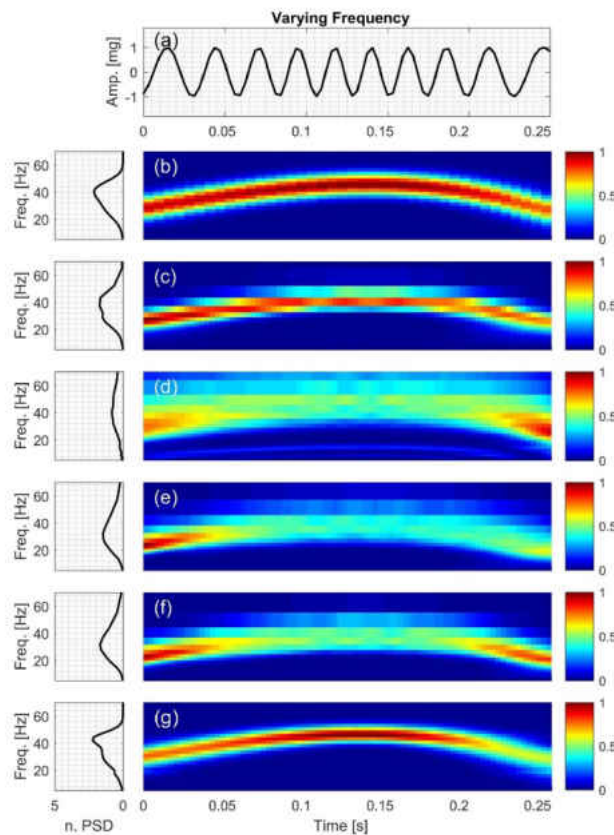


Figure 3.3. Synthetic test signal with varying frequency: (a) Time series. Left and right columns show the power spectral density and time-frequency distribution of the signal using: (b) STFT, (c) CWT-Morl, (d) CWT-Haar, (e) CWT-db4, (f) CWT-Coif5, and (g) PCT, respectively.

Figure 3.3 also shows evidence of leakage and edge effects where the CWT-based techniques appeared to have more leakage and edge effects compared to STFT and PCT.

3.3.5.2 Exponentially Decaying Sinusoid

For the exponentially decaying sinusoid, x_2 (Figure 3.4.g), PCT gave the most accurate IF estimation as seen in Table 3.4. STFT had a lower NRMSE compared to CWT-based methods. CWT-Coif5 estimated the signal IF with less NRMSE compared to other wavelet-based techniques. CWT-Haar appeared to have the highest spectral leakage, which may have affected the PSD distribution and resulted in a more broad-band PSD than other methods, Figure 3.4.d. On the other hand, PCT and STFT had the lowest leakage as evidenced by the sharper peak in the PSD plots.

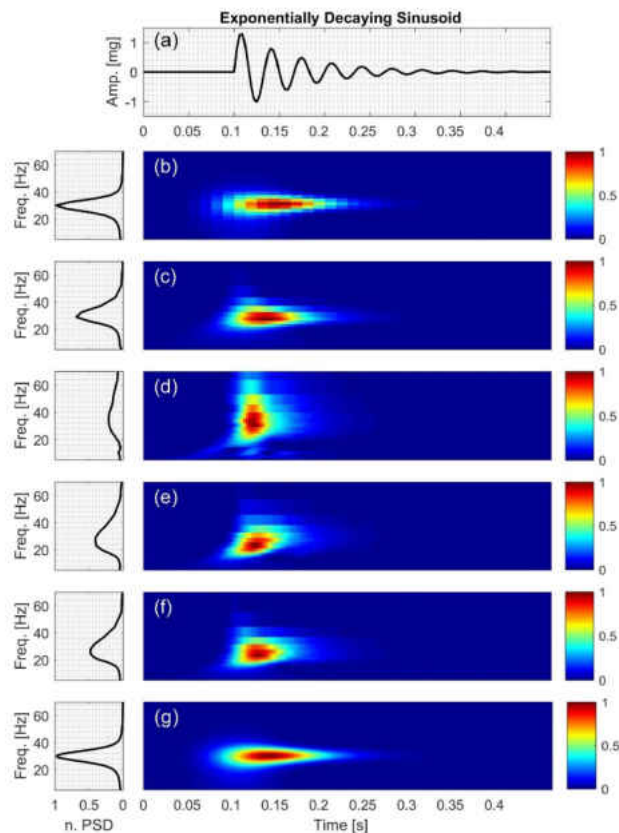


Figure 3.4. Synthetic test signal with exponentially decaying sinusoid: (a) Time series. Left and right columns show the power spectral density and time-frequency distribution of the signal using: (b) STFT, (c) CWT-Morl, (d) CWT-Haar, (e) CWT-db4, (f) CWT-Coif5, and (g) PCT, respectively.

3.3.5.3 Decaying Chirp

For the decaying chirp signal, x_3 , PCT estimated the signal IF more accurately than all other methods with an NRMSE value of 0.0850. In addition, CWT-Haar was more accurate than STFT and other CWT-based methods. Figure 3.5 also indicates that all of the TFD techniques had different levels of leakage as can be seen in their PSD plots. The PSD estimate for CWT-Haar shows more leakage than all methods although its IF estimate was superior to other CWT-based methods and STFT. The simpler structure of this mother function may have contributed to its increased ability to track time varying IF (and hence the smaller NRMES value).

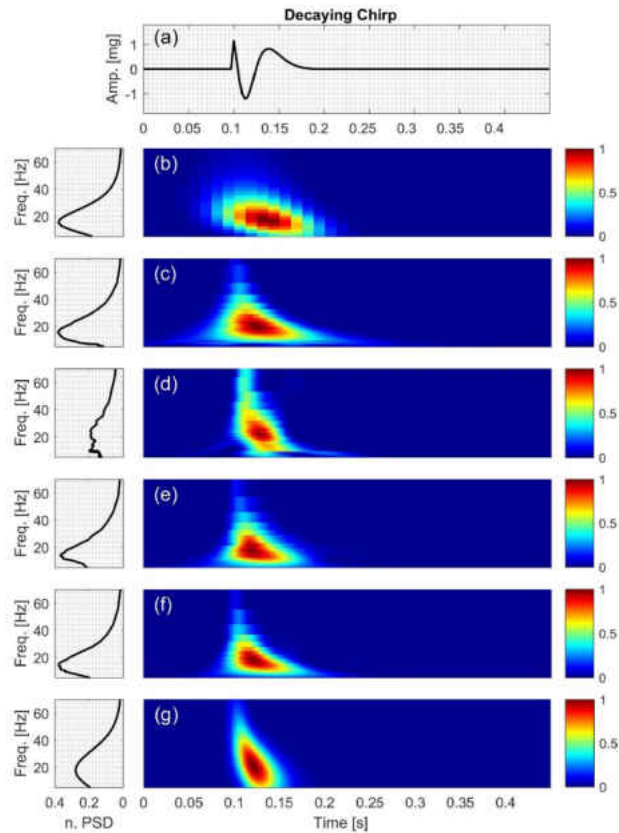


Figure 3.5. Synthetic test signal with decaying chirp: (a) Time series. Left and right columns show the power spectral density and time-frequency distribution of the signal using: (b) STFT, (c) CWT-Morl, (d) CWT-Haar, (e) CWT-db4, (f) CWT-Coif5, and (g) PCT, respectively.

3.3.5.4 Double Chirp

In double chirp signal (Figure 3.6), the difference between the two frequency components was chosen to increase with time. All TFD techniques were capable of estimating IF of the lower frequency component but CWT-based methods did not properly capture the higher frequency component, which led to a relatively high NRMSE (0.5651-0.7507) in IF estimation. STFT and PCT had lower error in estimating the signal IF with an NRMSE of 0.1232 and 0.0671, respectively (Table 3.4).

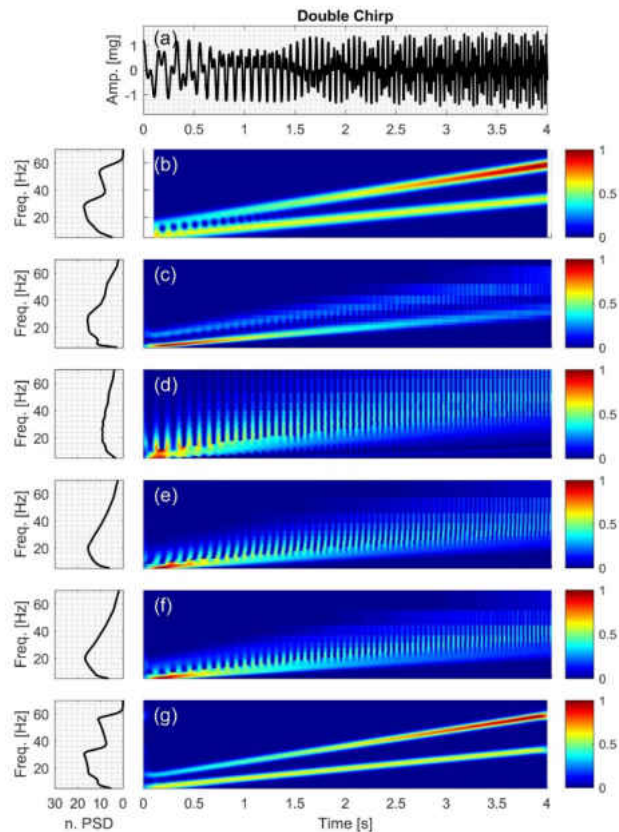


Figure 3.6. Synthetic test signal with double chirp: (a) Time series. Left and right columns show the power spectral density and time-frequency distribution of the signal using: (b) STFT, (c) CWT-Morl, (d) CWT-Haar, (e) CWT-db4, (f) CWT-Coif5, and (g) PCT, respectively.

The ability of the different methods in distinguishing between the two frequency components of the signal varied. For example, by examining Figure 3.6.b it can be seen that STFT was less

successful in distinguishing between the two frequency components at lower frequencies than at higher frequencies.

Interference terms that are common to bilinear methods were also seen. For example, in Figure 3.6.b, the effects of interference terms were clear at lower frequencies where the two spectral components were closer (and consequently have overlapping energies) in the time-frequency plane. At higher frequencies, the two signal components appeared to be sufficiently separated so that cross term artifacts were not noticeable.

Stronger interference term effects were encountered in CWT methods (Figure 3.6.c-f), which may have hindered, at least in part, their ability to detect the high frequency component. PCT estimation, on the other hand, resulted in unnoticeable interference term effects at all frequency values, which may have contributed to lowering the NRMSE.

3.3.5.5 Growing and Decaying Single Tone with Varying Frequency

Figure 3.7 shows the time-frequency distribution for the growing and decaying single tone with varying frequency, x_5 . CWT-based methods had coarser frequency resolution and larger NRMSE compared to PCT and STFT. In addition, CWT TFD appeared to have broader spectral peaks compared to other methods, which is consistent with increased leakage. Figure 3.7.b and Figure 3.7.g show that PCT had finer resolution in both the time and frequency domain compared to STFT, however, both methods had similar NRMSE (Table 3.4) and similar PSD.

3.3.5.6 Synthetic SCG signal

The synthetic SCG consists of two frequency components at 20 and 40 Hz. Figure 3.8.d-f show that CWT-Haar, CWT-db4 and CWT-Coif5 did not distinguish between the two components with noticeable leakage between them. While CWT-Morl demonstrated less leakage, it showed more leakage compared to STFT and PCT. Consequently, CWT-Morl, STFT and PCT more

clearly discriminated between the two signal components compared to the other CWT methods. The PSD graphs of CWT-Haar, CWT-db4 and CWT-Coif5 showed only one peak, while other methods correctly showed two peaks that correspond to the actual signal components.

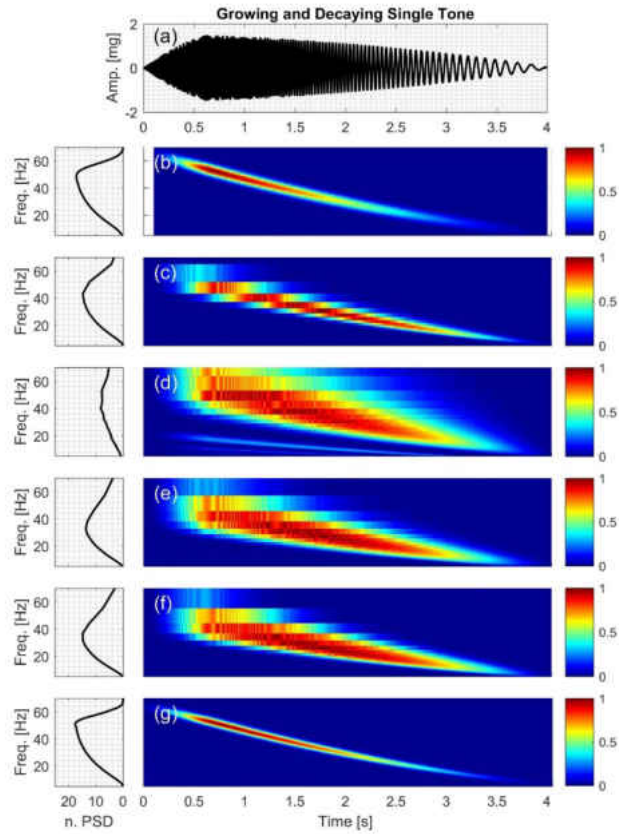


Figure 3.7. Synthetic test signal with growing and decaying single tone with varying frequency: (a) Time series. Left and right columns show the power spectral density and time-frequency distribution of the signal using: (b) STFT, (c) CWT-Morl, (d) CWT-Haar, (e) CWT-db4, (f) CWT-Coif5, and (g) PCT, respectively.

TFD of the synthetic signals in the current study suggest that PCT consistently had lower NRMSE, less artifacts, and lower leakage. PCT also provided better discrimination between signal frequency components. PCT performance was better than STFT for most synthetic signals, which may be due to the finer resolution of the former. PCT and STFT had more accurate estimations of IF than CWT methods in most cases, especially for signals with multiple frequencies. The performance of CWT methods varied depending on the wavelet mother function and signal under consideration, but did not seem to provide noticeable advantages over STFT or PCT. Among the

wavelet mother functions, Morlet had more accurate estimation of synthetic SCG IF, which is consistent with earlier studies of similar signals [160,164]. These trends will be helpful for interpreting the TFD results of actual SCG signals. Since PCT provided more accurate IF values than STFT and CWT, the current study will primarily rely on PCT for estimating the spectral content of actual SCG signals.

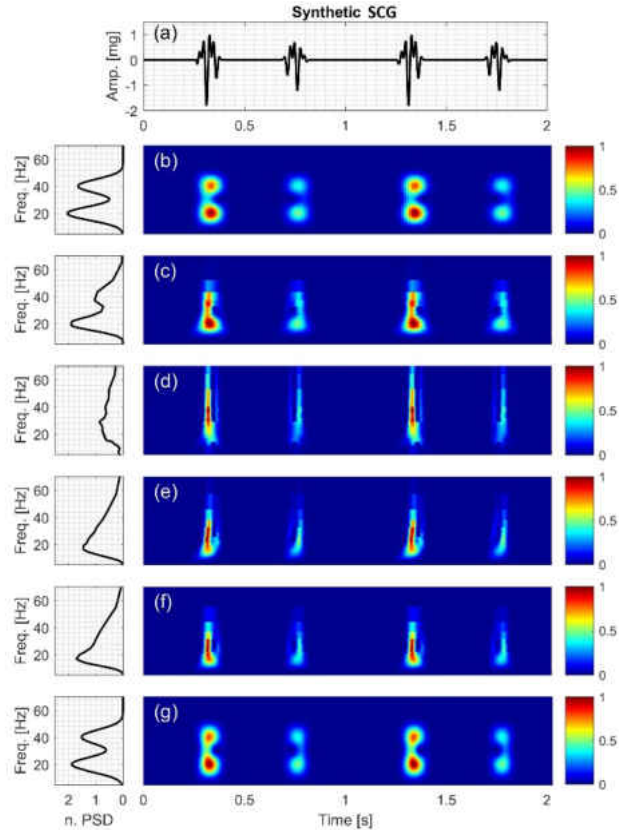


Figure 3.8. Synthetic SCG signal containing two constant frequency components: (a) Time series. Left and right columns show the power spectral density and time-frequency distribution of the signal using: (b) STFT, (c) CWT-Morl, (d) CWT-Haar, (e) CWT-db4, (f) CWT-Coif5, and (g) PCT, respectively.

3.3.5.7 Actual SCG Signal

TFDs of the dorso-ventral component of actual SCGs are shown in Figure 3.9 for two cardiac cycles in 2 different healthy subjects. Data from the rest of the study subjects were similar and are shown in APPENDIX C. In these figures, the spectral information is shown for frequencies up to 80 Hz as there was no significant energy seen above that frequency. Figure 3.9 suggests that there

were two SCG events (which may be called SCG1 and SCG2) for each cardiac cycle. Here, SCG1 and SCG2 appeared to be localized in the time-frequency domain. SCG1 tended to have higher amplitude than SCG2 and different frequency content. While Figure 3.9 (and APPENDIX C) showed noticeable inter-subject variability, beat-to-beat variability appeared lower, which is consistent with previous studies [165].

The different TFDs were able to identify SCG spectral peaks with different level of success. For example, PCT and STFT suggested that there were about three dominant frequencies in the actual SCG signal (f_1, f_2, f_3). The peaks related to these frequencies were more clearly seen in the PSD of the STFT and PCT (Figure 3.9.b and Figure 3.9.g, respectively). However, these peaks were less distinguishable in the spectral estimates of the CWT-Haar, CWT-db4 and CWT-Coif5 (Figure 3.9.d to Figure 3.9.f), where the PSD showed a broad band spectrum rather than separate peaks. It is to be noted that although the peak at f_3 existed in PCT and STFT spectrum for all subjects, it was not always clear in the figures because of its low amplitude. The frequencies at the spectral peaks were calculated using PCT. Calculated frequencies are listed in Table 3.5 and correspond to $f_1 = 9.20 \pm 0.48$, $f_2 = 25.84 \pm 0.77$ and $f_3 = 50.71 \pm 1.83$ Hz (mean \pm SEM). The value of f_3 suggests that it may be a harmonic of f_2 . However, f_2 and f_3 did not appear to be harmonics of f_1 , which suggests that f_2 and f_3 may have potentially originated from a source that is different from f_1 . These dominant frequencies take place around the time of strongest SCG wave, which is believed to correspond to ventricular systole [20,166]. Previous studies [35] suggested that the energy associated with frequencies > 18 Hz (such as f_2 and f_3 in the current study) may be related to valve closure, while lower frequencies (e.g., f_1 in the current study) are related to heart muscle contraction. Changes in these frequencies may, then, be reflective of ventricular

contractility and valve closing. Accurate detection of these changes in the same subject may, therefore, prove useful for monitoring cardiac function.

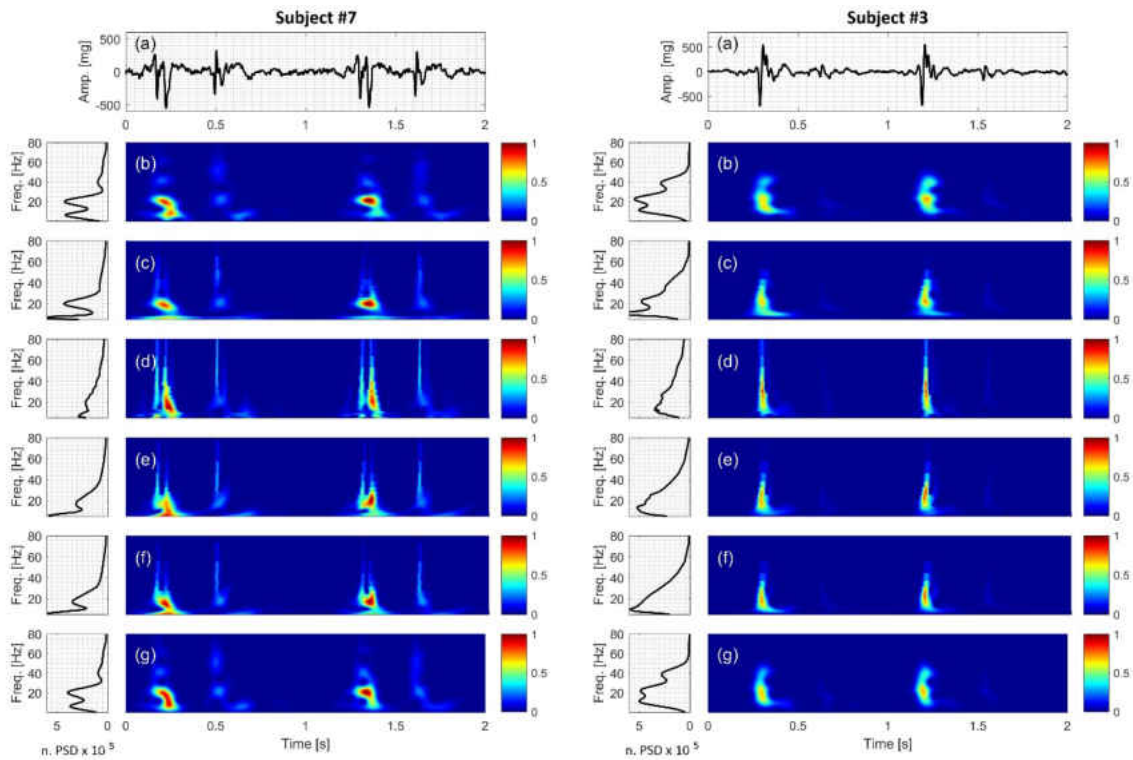


Figure 3.9. Actual SCG signal of two healthy subjects: (Left 2 columns) subject #7 (Right 2 columns) subject #3. For each subject (a) Time series. The time-frequency distribution using: (b) STFT, (c) CWT-Morl, (d) CWT-Haar, (e) CWT-db4, (f) CWT-Coif5, and (g) PCT is also shown. The power spectral density for each TFD is shown to the left of the distribution.

Table 3.5. Dominant frequencies of the actual SCG signals calculated using polynomial chirplet transform. The most dominant frequency for each subject is highlighted in bold.

Subject No.	Heart rate (bpm)	f_1 (Hz)	f_2 (Hz)	f_3 (Hz)
1	78	6.15	22.89	56.12
2	72	11.08	30.52	71.38
3	70	11.32	21.91	38.65
4	60	8.86	17.23	26.09
5	58	5.41	28.31	53.17
6	62	7.63	32.98	61.05
7	62	6.15	19.94	40.12
8	69	16.98	32.98	59.08

Comparing Figure 3.9.g with Figure 3.5.g and Figure 3.8.g, one can also conclude that the mid-frequency component, f_2 , of the SCG1 had a slightly decreasing frequency with time (in some subjects). This behavior was not seen for the low and frequency component in most subjects.

Figure 3.9 also shows some SCG beat-to-beat spectral variability that was not clearly demonstrated

before. However, further investigation is required to see if these trends are consistent for larger numbers of heart beats and more diverse subject populations.

Agreement between the two TFD with the best performance in the current study was assessed using Bland-Altman analysis (Figure 3.10). In this plot, the solid line represents the mean value of differences between instantaneous frequencies, while the dashed lines show the 95% confidence interval (mean \pm 1.96 SD). These values are also listed in Table 3.6. These results suggest general agreement between PCT and STFT. However, there were some disagreements, which might be due to the inability of STFT to track steep changes in the instantaneous frequency [149,154].

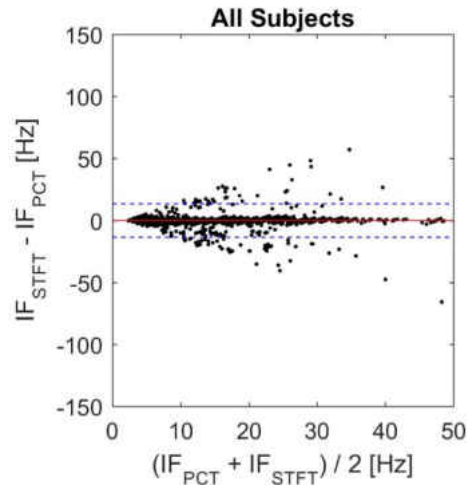


Figure 3.10. Bland-Altman plot for PCT and STFT IF. The solid line represents the mean (bias) value of differences between instantaneous frequencies. The dashed lines show the 95% confidence interval.

Table 3.6. Statistical analysis results based on the Bland-Altman method (LOV: level of agreement).

Bias (Hz)	Upper LOV (Hz)	Lower LOV (Hz)
0.7593	17.32	-15.80

3.3.5.8 Limitations

The primary limitation of the study is the small number of subjects participated. Future studies need to be carried out with larger number of subjects from a diverse population covering a wide range characteristics including age, weight, race, and clinical status.

3.3.6 Conclusions

The objective of this study was to compare the ability of six different approaches in providing accurate TFD estimates for SCG signals. Methods included STFT, PCT, and CWT with 4 different mother functions. In the current study, the temporal resolution of the STFT was coarser than other methods while the spectral resolution of PCT was the finest among all methods especially above 10 Hz.

The accuracy of different methods in determining the IF was tested using synthetic signals with known TFD and the estimated IF was compared to actual IF values. CWT performance varied depending on which mother function was used. However, for the simulated SCG signal, the Morlet mother function resulted in more accurate IF values among CWT methods. The errors in estimating IF were lowest for PCT followed by STFT for most test signals. This was particularly true for signals with multiple frequencies including the simulated SCG signal. These results may be attributed to the finer temporal and spectral resolution of PCT and suggest that the method would be a better choice for estimating the TFD characteristics of SCG signals. TFD of actual SCGs was also estimated and PCT results showed that this signal typically had three spectral peaks that tend to be slightly time-dependent in some subjects. More studies may be warranted to document the TFD characteristics of SCG signals in health and disease in larger populations.

3.4 Noise Effect on Time-frequency Feature Extraction of SCG Signals

Time-frequency distribution has been used to document temporal and spectral features of SCG [144,167] as well as other biomedical signals [115–117,151,153,160,168]. However, SCG signals are often contaminated with noise, which can be from physiological sources (e.g., respiration and muscle contraction), or external sources (e.g., building vibrations and instrument noise). Various methods have been utilized to remove noise from electrocardiographic and phonocardiographic

signals [169–173]. But, to the best of authors’ knowledge, there are no studies that focused on the analysis of SCG in the presence of noise. While a common objective of many signal analysis methods is to remove noise, addition of Gaussian noise assists data analysis in certain cases [174–179]. Noise removal is important as it may interfere with the operation of signal analysis methods. The current study aims at studying the effects of noise on the performance of two TFD methods that may be used for SCG analysis: polynomial chirplet transform (PCT) and smoothed pseudo Wigner-Ville distribution (SPWVD). A brief description of the calculation methods is given in section 3.4.2. Results are presented and discussed in sections 3.4.4 and 3.4.5, respectively, followed by conclusions in section 3.4.6.

This section describes the simulated signals used and the methods of SCG data acquisition. The TFD performance evaluation method is also described.

3.4.1 SCG Signals and Noise Preparation

Two simulated SCGs were generated and added to background white noise with different SNR values. The general properties of the simulated signals are listed in Table 3.7.

Table 3.7. General properties of the simulated signals used in the current study.

Signal description	Peak to peak amplitude	Signal length above 5% of peak to peak amplitude (ms)	Frequency or Frequency range (Hz)
Simulated SCG with constant freq., x_1	2.8	112	20 and 40
Simulated SCG with varying freq., x_2	2.4	112	7 to 20, and 40

3.4.1.1 Simulated SCG with Constant Frequencies

This signal consisted of two sinusoids with IF of 20 and 40 Hz, which can be described by

$$x_1(t) = -A_1 \sin(2\pi(20)t + 94) + 0.9A_1 \sin(2\pi(40)t + 188) \quad (3-28)$$

where the signal amplitude varied according to,

$$A_1 = \begin{cases} 0 & 0 < t \leq 0.25 \\ 0.5 - 0.5 \cos(2\pi(7t - 5.25)) & 0.25 < t \leq 0.40 \\ 0 & 0.40 < t \leq 0.70 \\ 0.45 - 0.45 \cos(2\pi(7t - 5.25)) & 0.70 < t \leq 0.85 \\ 0 & 0.85 < t \leq 1.00 \end{cases} \quad (3-29)$$

3.4.1.2 Simulated SCG with Varying Frequency

This signal consisted of two sinusoids with constant and varying IFs, which can be described by

$$x_2 = A_2(y_1 + y_2) \quad (3-30)$$

where y_1 and y_2 were defined as,

$$y_1 = -0.5 \sin(2\pi(40)t) \quad (3-31)$$

$$y_2 = \begin{cases} 0 & 0 < t \leq 0.25 \\ z & 0.25 < t \leq 0.40 \\ 0 & 0.40 < t \leq 0.70 \\ z & 0.70 < t \leq 0.85 \\ 0 & 0.85 < t \leq 1.00 \end{cases} \quad (3-32)$$

where,

$$z = \sin(2\pi(870 t^2 - 215 t + 20)t) \quad 0 \leq t \leq 0.15 \quad (3-33)$$

The signal amplitude also varied according to,

$$A_2 = \begin{cases} 0 & 0 < t \leq 0.25 \\ 0.5 - 0.5 \cos(2\pi(7t - 5.25)) & 0.25 < t \leq 0.40 \\ 0 & 0.40 < t \leq 0.70 \\ 0.25 - 0.25 \cos(2\pi(7t - 5.25)) & 0.70 < t \leq 0.85 \\ 0 & 0.85 < t \leq 1.00 \end{cases} \quad (3-34)$$

3.4.1.3 Data Acquisition of SCG

After IRB approval, a light-weight (2 gm) accelerometer (PCB piezotronics, Depew, NY) was placed at the left sternal border and the 4th intercostal space over the chest of healthy volunteers to measure the SCG signal. The signal was digitized at a rate of 3200 Hz and down-sampled to 320 Hz. Since respiratory noise have significant energy above 100 Hz [119], signals were filtered using

a low-pass filter with a cut-off of 100 Hz to remove that noise. Matlab (R2015b, The MathWorks, Inc, Natick, MA) was used to both acquire and process all signals.

3.4.1.4 White Noise

White noise with different levels of SNR ranging from -10 to 10 dB was generated and added to the simulated and actual SCG signals. The steps for generating the noise-added signals are shown in Figure 3.11.

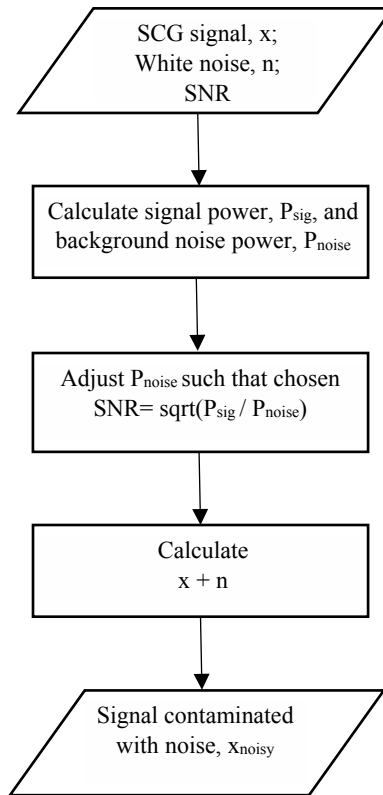


Figure 3.11. Block diagram describing the steps for generating the SCG signals contaminated with noise

3.4.2 TFD Techniques

Time-frequency distribution of the signals was estimated using two different TFD techniques; PCT and SPWVD. The theoretical details of these methods can be found elsewhere [154], [155].

3.4.3 Error Analysis

The performance of each technique was assessed using the root-mean-square error (RMSE) between the signal actual and estimated IF values. The RMSE was calculated as:

$$RMSE = \sqrt{\frac{\sum_{i=1}^n (IF_{act,i} - IF_{est,i})^2}{n}} \quad (3-35)$$

where $IF_{act,i}$ and $IF_{est,i}$ are the actual and estimated IF at time i , respectively. RMSE values were normalized as:

$$NRMSE = \frac{RMSE}{\overline{IF}_{act}} \quad (3-36)$$

where \overline{IF}_{act} is the mean actual instantaneous frequency of each signal. NRMSE was used in this study to measure the accuracy of TFD techniques in estimating IF, where lower NRMSE values would indicate higher accuracy.

For each SNR level, each signal was contaminated with 100 different white noise sets and analysis was performed for each case. Since the generated noise was different in each trial, analysis resulted in a range of errors (instead of one error value) at each SNR level. The results of the error analysis are presented in box-and-whisker plots in the Discussion section where the whisker ends represent the 1st and 99th percentiles. The error range was defined as the difference between these two percentiles. In addition, the Inter quartile range (IQR) was also calculated as the difference between the 75th and 25th percentiles.

3.4.4 Results

Figure 3.12 and Figure 3.13 show the time series, time-frequency representation and PSD of the noise-added simulated signals. The PSD was calculated from the time-frequency representations, and normalized with respect to the signal energy. Since there is no significant energy seen above 70 Hz, the spectral information is only shown for frequencies up to this limit.

The time-frequency representation and PSD of the actual SCG, which was polluted by white noise with different SNR values, were also estimated using the PCT and SPWVD, and shown in Figure 3.14. The figures show the data for only one noise set since the results for other noise sets were similar.

3.4.5 Discussion

3.4.5.1 Simulated SCG with Constant Frequencies

The first simulated SCG consisted of two constant frequency components. At each SNR, 100 different white noise sets were added to the signal, and the performance of TFD techniques in estimating the signal IF was assessed. Figure 3.12 shows that for the noise-added simulated SCGs at $\text{SNR} > 3$ dB, the time-frequency representation and the PSD did not appear significantly different from the ones for the signal without noise. For $-3 < \text{SNR} < 3$ dB, some extra energy peaks were seen in the time-frequency plane in addition to the signal actual frequency components. However, the PSD plots still showed two dominant peaks (representing two dominant frequency components at 20 and 40 Hz). At these SNRs, the signal frequency components appeared distorted. For example, at $\text{SNR} = -3$ dB, the TFD demonstrated some varying frequency behavior rather than a pure tone, which may lead to a misleading interpretation of the results. At $\text{SNR} = -6$ dB, PCT correctly depicted the two dominant frequencies of the signal, while the SPWVD showed an extra third peak at 55 Hz. The time-frequency representations of the signal were completely contaminated with noise at $\text{SNR} = -10$ dB, which resulted in power spectrums with more than 2 frequency peaks.

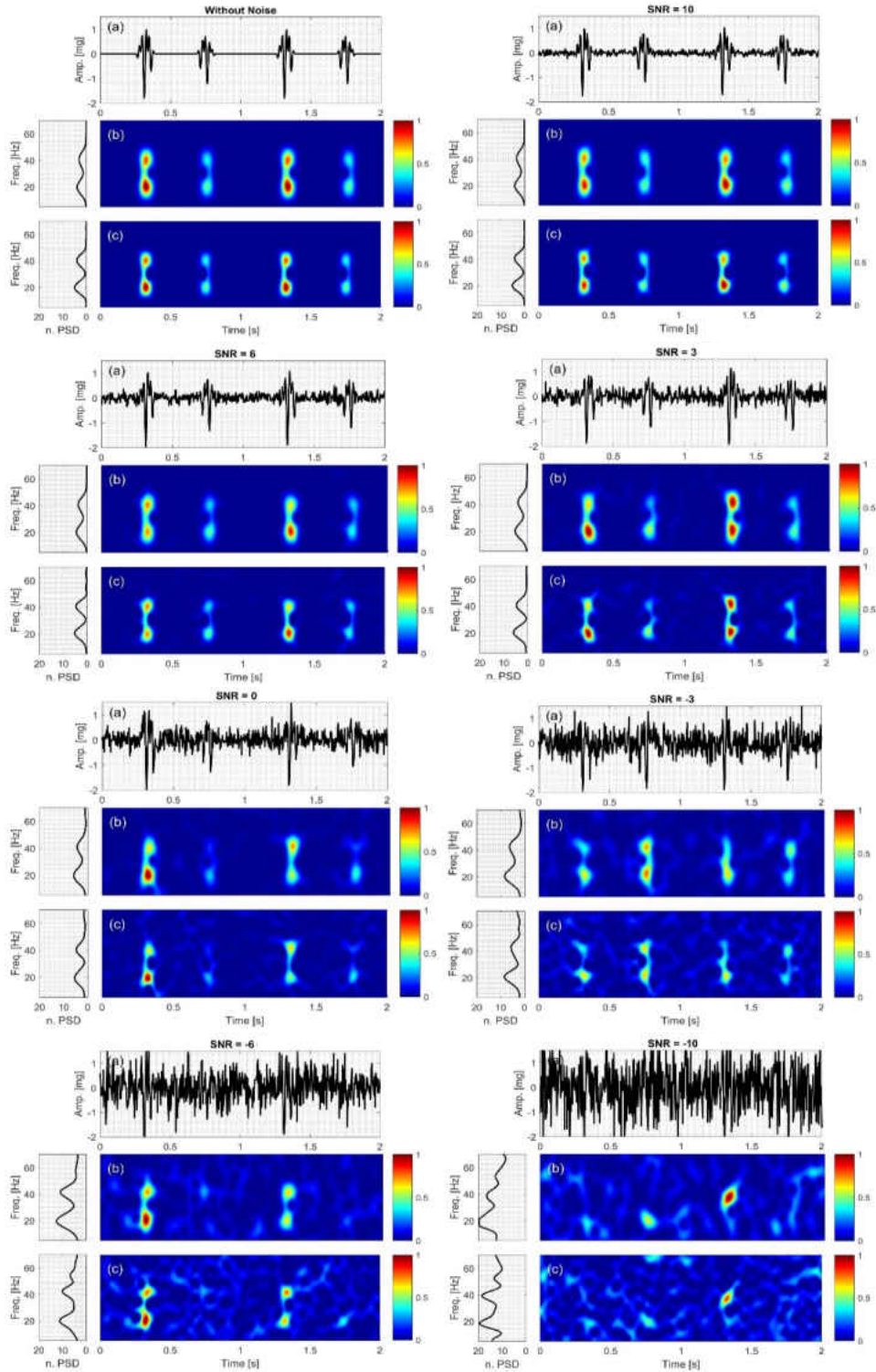


Figure 3.12. Simulated SCG with constant frequencies, x_1 , contaminated by white noise sets for $-10 < \text{SNR} < 10$ dB: (a) Time series. Time-frequency representation using (b) PCT, and (c) SPWVD, respectively.

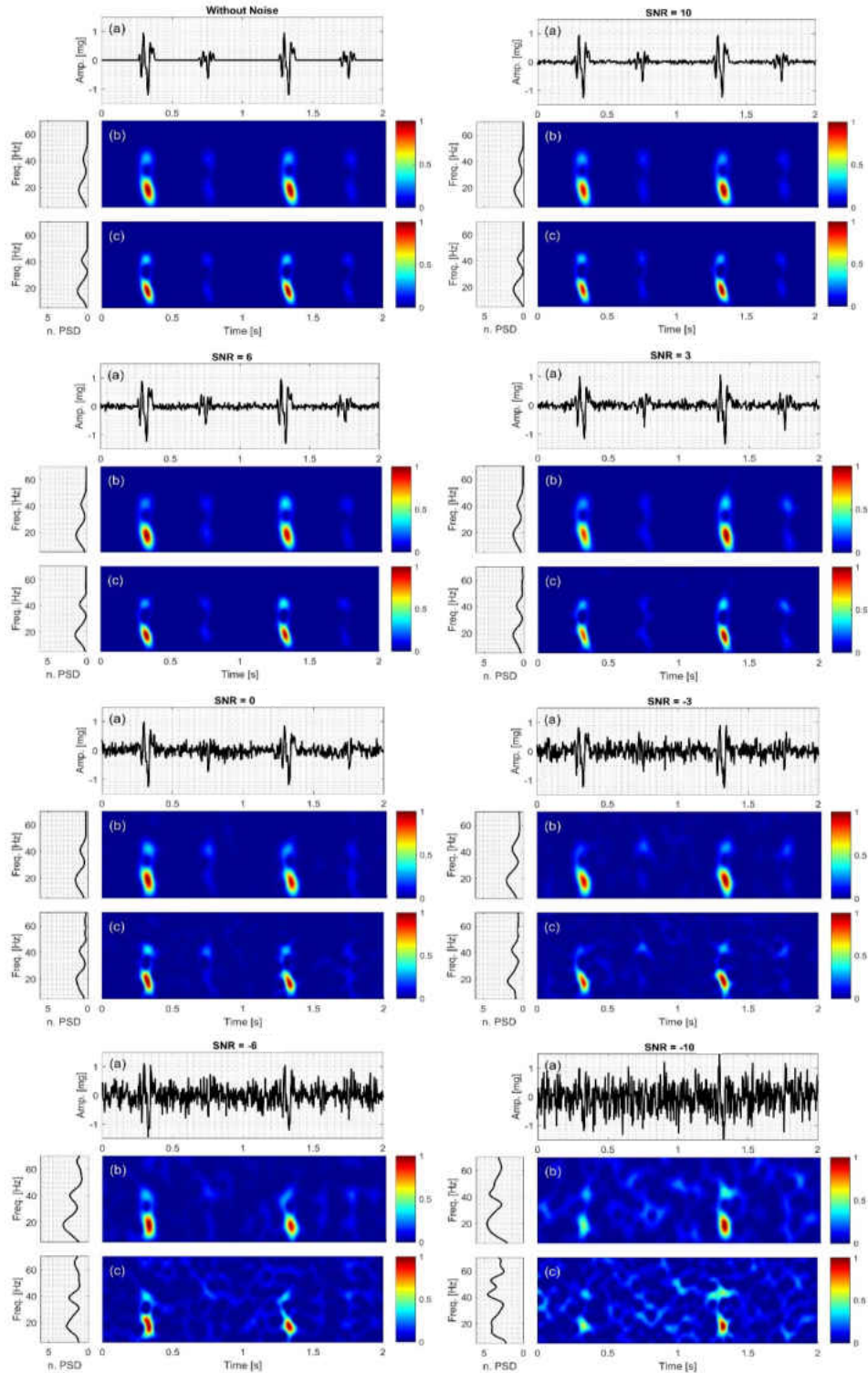


Figure 3.13. Simulated SCG with varying frequency, x_2 , contaminated by white noise sets for $-10 < \text{SNR} < 10$ dB: (a) Time series. Time-frequency representation using (b) PCT, and (c) SPWVD, respectively.

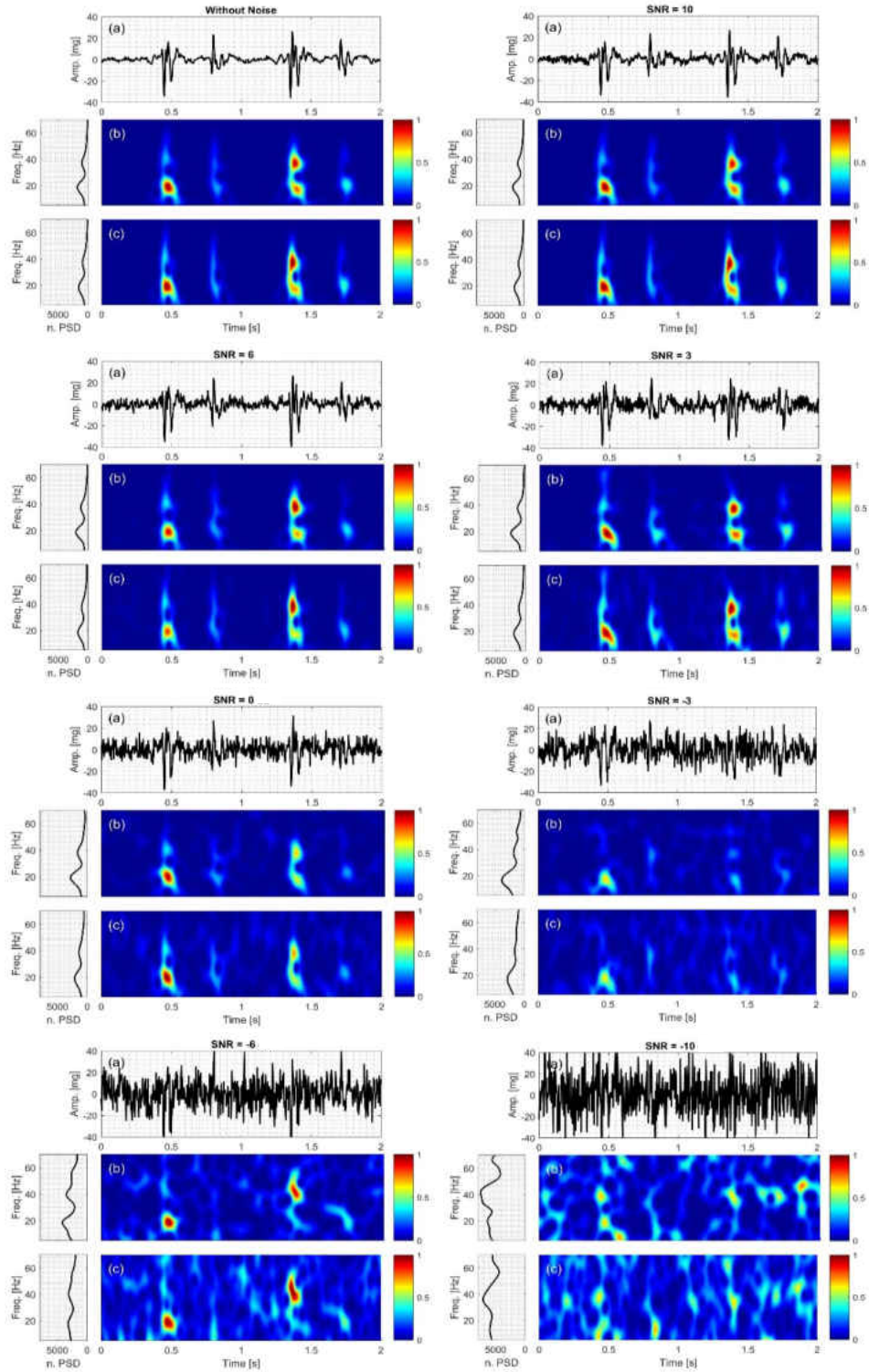


Figure 3.14. Actual SCG contaminated by white noise sets for $-10 < \text{SNR} < 10$ dB: (a) Time series. Time-frequency representation using (b) PCT, and (c) SPWVD, respectively.

Figure 3.15 and Figure 3.16 show the NRMSE box-and-whisker plots for PCT and SPWVD, respectively. These plots suggested that PCT and SPWVD estimated the signal IF with higher NRMSE when the signal was polluted with noise. In general, the NRMSE medians and IQR increased as the SNR decreased for both PCT and SPWVD. The NRMSE median varied from 0.022 to 1.931 and from 0.032 to 0.979 for PCT and SPWVD, respectively, when SNR decreased from ∞ to -10 dB. At SNRs > 0 dB, PCT had lower NRMSE median and 75th percentile compared to SPWVD. At lower SNR values (e.g. SNR = -3 and -6 dB), SPWVD estimated the signal IF with lower NRMSE median value and IQR. Therefore, for the simulated SCG with constant frequencies, one can conclude that PCT is more appropriate for IF estimation at higher SNRs, while SPWVD outperforms the PCT at lower SNR values.

3.4.5.2 *Simulated SCG with Varying Frequency*

The second simulated SCG consisted of a constant and a varying frequency component. The TFD techniques were used to estimate the IF of the varying frequency component. At each SNR, the simulated signal was contaminated with 100 different white noise sets. Figure 3.13 shows that the time-frequency representations of the contaminated simulated SCGs with SNR > 3 dB were very similar to that without noise. For SNR ≤ 0 dB, the signal frequency components started to become distorted and extra energy peaks emerged in the time-frequency planes. These extra energy peaks were more clearly noticeable in the SPWVD than PCT. In addition, for SNR < -3 dB, a third power peak was shown up in the SPWVD PSD plot. Altogether, at lower SNR values, PCT provided time-frequency representations and PSD plots that are lesser affected by the presence of white noise than SPWVD.

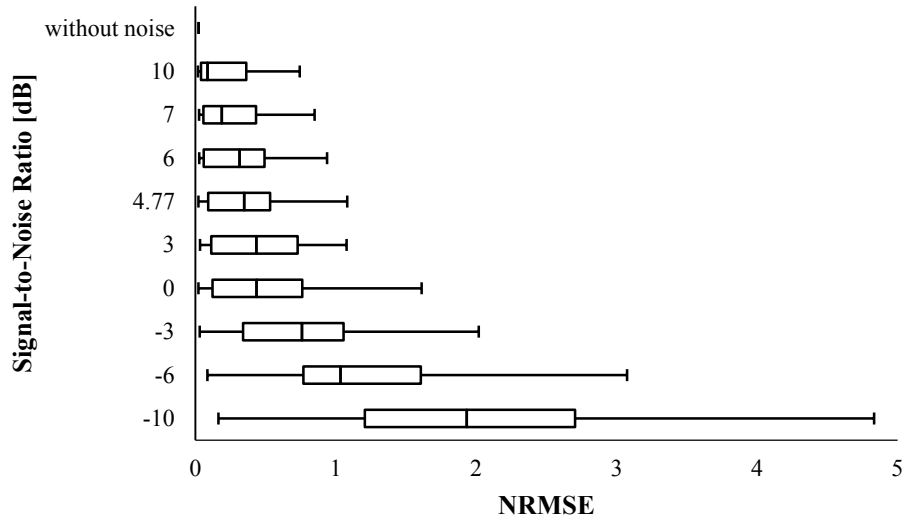


Figure 3.15. NRMSE in estimating IF of the simulated SCG with constant frequencies (x_l) using PCT for different SNR. In this box-and-Whisker plot, the whisker ends represent the 1st and 99th percentiles.

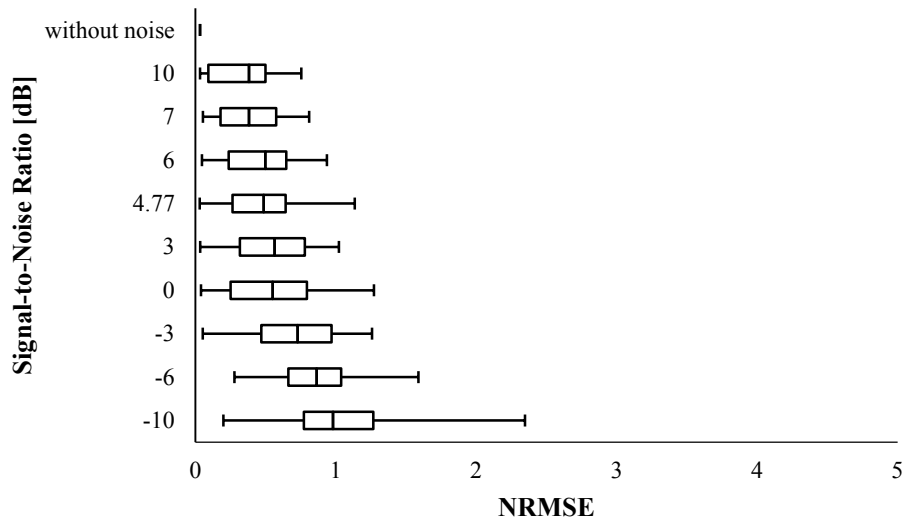


Figure 3.16. NRMSE in estimating IF of the simulated SCG with constant frequencies (x_l) using SPWVD for different SNR. In this box-and-Whisker plot, the whisker ends represent the 1st and 99th percentiles.

The results of the IF error analysis of the simulated SCG with varying frequency were described as box-and-whisker plots in Figure 3.17 and Figure 3.18. For $\text{SNR} \geq -6$ dB, PCT had almost the same NRMSE median (~ 0.285) as that without noise, however, both NRMSE IQR and range increased as SNR decreased. At $\text{SNR} = -10$ dB, the NRMSE median drastically increased to

~ 0.668. SPWVD also estimated the IF with an almost unvaried median NRMSE value of 0.235 at $\text{SNR} \geq 0$ dB, which was very close to NRMSE for the case without noise. But, for SNRs smaller than 0 dB, the IF estimation error of SPWVD rose to about 0.587. For both PCT and SPWVD, smaller SNR value leads to a higher NRMSE IQR. Altogether, SPWVD consistently had lower NRMSE median (~ 0.235 vs ~ 0.285) and higher NRMSE IQR and range for $\text{SNR} \geq -6$ dB. Considering that a lower uncertainty in IF estimation may be desirable, one can conclude that PCT may be preferred over SPWVD for estimating IF of a noisy signal. In summary, the error analysis for the simulated signals suggests that:

- For SCG signals with time-varying frequency components, PCT may provide more accurate estimation of IF in the presence of white noise.
- For SCG signals with time-independent frequency components, PCT may give more accurate IF estimations when $\text{SNR} > 3$ dB.

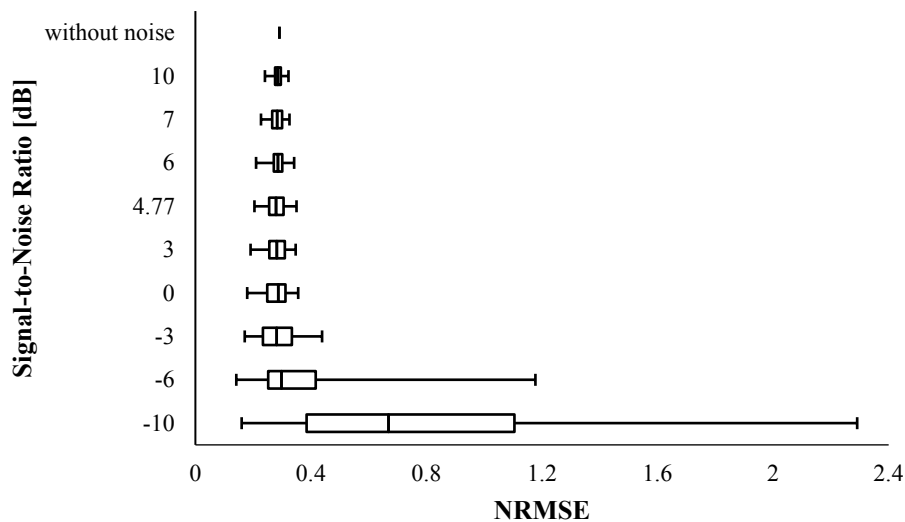


Figure 3.17. NRMSE in estimating IF of the synthetic SCG with varying frequency (x_2) using PCT for different SNR. In this box-and-Whisker plot, the whisker ends represent the 1st and 99th percentiles.

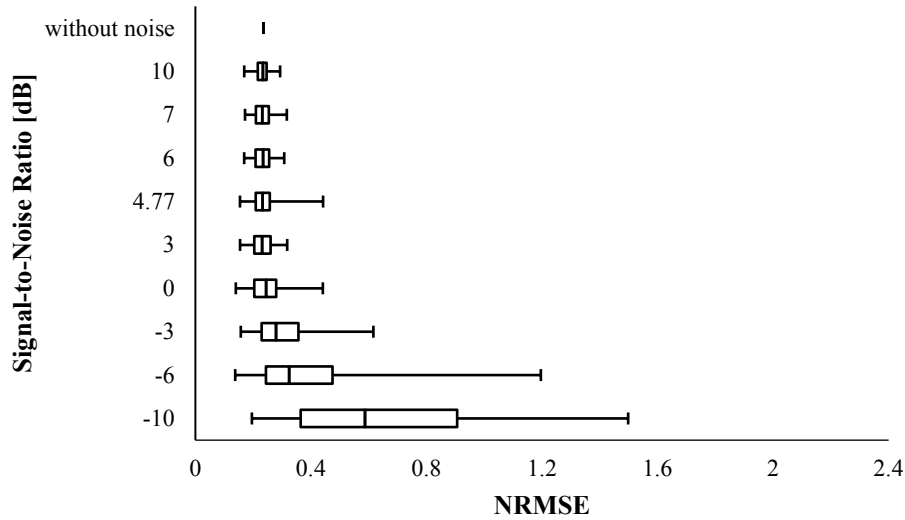


Figure 3.18. NRMSE in estimating IF of the synthetic SCG with varying frequency (x_2) using SPWVD for different SNR. In this box-and-Whisker plot, the whisker ends represent the 1st and 99th percentiles.

3.4.5.3 Actual SCG in Noise

The actual SCG was also contaminated by white noise with different SNRs. Figure 3.14 shows the time series, time-frequency representations and PSD plots of the actual SCG at different SNR values. For higher SNR values (e.g. $\text{SNR} \geq 6$ dB), the time-frequency representation and PSD of the signal were not significantly affected by the white noise presence. For $\text{SNR} < 6$ dB, the time-frequency representation started to become distorted. For instance, at $\text{SNR} = -3$ dB, the SCG1 higher frequency component started to disappear from the time-frequency representation. At lower SNRs, more extra energy peaks were shown up in the time-frequency plane. For example, the PSD of the actual SCG without noise had 2 peaks, however, the PSD graph had more than 2 peaks for small SNRs (e.g. $\text{SNR} = -6$ dB).

Since the actual IF of the SCG signal was not known, it was not possible to perform a same exact error analysis that had been done for the simulated SCGs. Instead, the performance of TFD techniques in estimating the SCG IF was evaluated using the following measure:

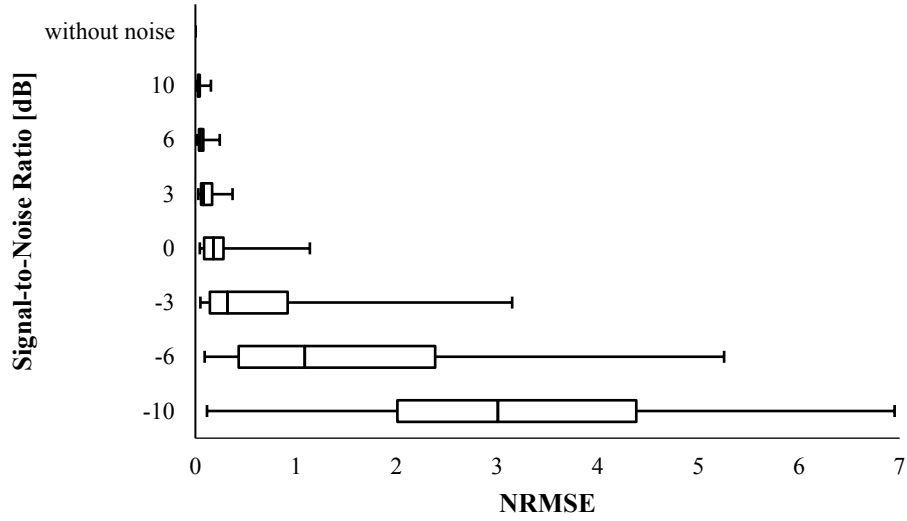


Figure 3.19. NRMSE in estimating IF of the actual SCG using PCT for different SNR. In this box-and-Whisker plot, the whisker ends represent the 1st and 99th percentiles.

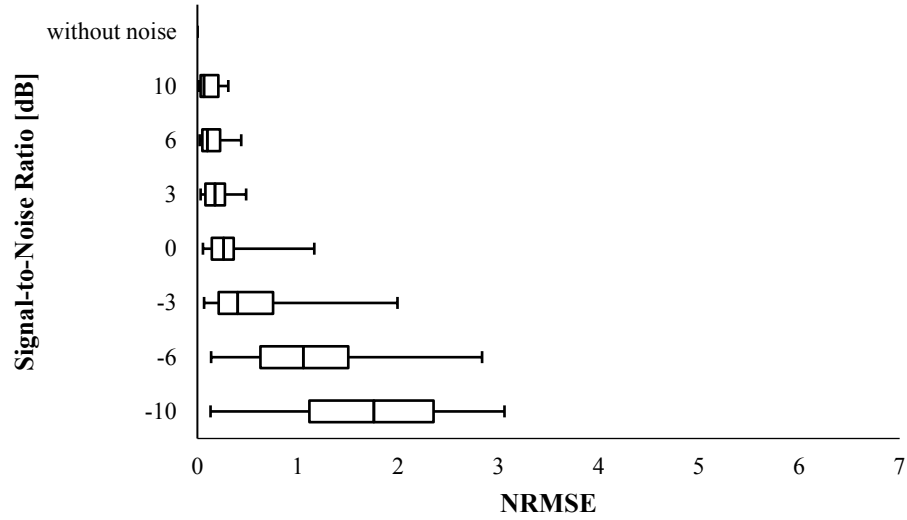


Figure 3.20. NRMSE in estimating IF of the actual SCG using SPWVD for different SNR. In this box-and-Whisker plot, the whisker ends represent the 1st and 99th percentiles.

$$NRMSE_{VCG} = \sqrt{\frac{\sum_{i=1}^n (IF_{\infty,i} - IF_{noisy,i})^2}{n}} / \overline{IF}_{\infty} \quad (3-37)$$

where $IF_{\infty,i}$ and $IF_{noisy,i}$ were the estimated IF of the SCG without noise and the noise-added SCG at time i , respectively; and \overline{IF}_{∞} was mean of the estimated IF of the signal without noise. The actual

SCG was polluted by 100 different white Gaussian noise sets at each SNR value. Then, Equation 58 was used to find the error in estimating IF. The error analysis results are presented in Figure 3.19 and Figure 3.20. It can be seen that PCT estimated the signal IF with lower NRMSE median and IQR at $\text{SNR} \geq 0$ dB. The median, IQR and range of NRMSE values are listed in Table 3.8 for the simulated and actual SCGs at signal-to-noise ratios from -10 to 10 dB.

Table 3.8. A summary of NRMSE analysis of simulated and actual SCG signals for different SNR. The NRMSE values are reported as: Median (IQR, Range). Here, the range is defined as the difference between 1st and 99th percentiles.

		Signal-to-Noise Ratio (dB)							
		-10	-6	-3	0	3	6	10	without noise
Simulated SCG with constant frequencies	PCT	1.93 (1.50, 4.67)	1.03 (0.84, 2.99)	0.76 (0.72, 1.99)	0.43 (0.64, 1.59)	0.43 (0.61, 1.04)	0.31 (0.43, 0.91)	0.09 (0.32, 0.72)	0.02 (0.00, 0.00)
	SPWVD	0.98 (0.49, 2.15)	0.86 (0.38, 1.31)	0.73 (0.50, 1.21)	0.55 (0.54, 1.23)	0.56 (0.46, 0.99)	0.50 (0.41, 0.89)	0.38 (0.41, 0.72)	0.03 (0.00, 0.00)
Simulated SCG with varying frequency	PCT	0.67 (0.72, 2.13)	0.30 (0.16, 1.03)	0.28 (0.10, 0.27)	0.29 (0.06, 0.18)	0.28 (0.05, 0.16)	0.28 (0.03, 0.13)	0.28 (0.02, 0.08)	0.29 (0.00, 0.00)
	SPWVD	0.59 (0.54, 1.30)	0.32 (0.23, 1.06)	0.28 (0.13, 0.46)	0.24 (0.08, 0.30)	0.23 (0.06, 0.16)	0.23 (0.05, 0.14)	0.23 (0.03, 0.12)	0.23 (0.00, 0.00)
Actual SCG	PCT	3.00 (2.37, 6.83)	1.09 (1.95, 5.16)	0.32 (0.77, 3.10)	0.18 (0.19, 1.09)	0.08 (0.11, 0.34)	0.05 (0.04, 0.22)	0.03 (0.01, 0.14)	N/A
	SPWVD	1.76 (1.24, 2.93)	1.05 (0.88, 2.70)	0.40 (0.54, 1.93)	0.26 (0.22, 1.11)	0.17 (0.19, 0.45)	0.10 (0.18, 0.41)	0.06 (0.18, 0.29)	N/A

3.4.6 Conclusions

The goal of this study was to compare the ability of the polynomial chirplet transform and smoothed pseudo Wigner-Ville distribution in providing accurate time-frequency estimates for SCG signals contaminated by white noise. The accuracy of the different methods in determining the IF was tested using two simulated SCG signals. The estimated and actual signal IF were compared. Results suggest that at high SNRs, PCT was more accurate than SPWVD in estimating the frequency components of a signal with time-independent IF. For a signal with varying frequency components, SPWVD resulted in a smaller median error but larger error range than

PCT. Since lower error range (i.e. lower uncertainty) may be desirable, PCT may be chosen over SPWVD in estimating the IF of a SCG with time-varying frequency components. More studies may be warranted to document the time-frequency characteristics of SCG signals in health and disease.

3.5 Summary

In this chapter, features that might be useful in SCG classification were investigated. This step is necessary to obtain a high accuracy in signal classification. Potential SCG features in time, frequency, and time-frequency domain were discussed. Different time-frequency distributions were considered to find the most suitable one for SCG feature extraction in the presence and absence of noise.

CHAPTER 4: CLASSIFICATION

In biomedical signal processing, the goal of classification is to automatically distinguish signals from normal and different pathological states. For example, clinicians judge if patients suffer from cardiac pathologies by looking at their electrocardiography or listening to their heart sound. Incorrect disease identification may not only result in waste of diagnosis resources but also delays treatment or causes death. Automated classification of physiological signals may help healthcare providers in more accurate, efficient, and timely diagnosis.

The current chapter explores the utility of different methods for SCG classification. Methods included unsupervised (e.g., k -means) and supervised (e.g., NN, SVM, RF) approaches. This chapter is organized as follows. Sections 4.1 and 4.2 give an overview on different supervised and unsupervised machine learning approaches used in this study. Section 4.3 proposes an algorithm for SCG temporal feature extraction. Section 4.4 gives a review of the state of the art.

4.1 Supervised Approaches

For this dissertation, three machine learning classification algorithms were used for binary classification: SVM, RF, and Feed-Forward Neural Network (FNN). These were used to classify the SCG events as occurring during either high or low lung volume phases. The classification procedure can be generalized as the mapping of a feature vector with n features, $x \in \mathbb{R}^n$, to a single output, $y \in \{0, 1\}$. The output is a prediction of what output the input maps to. Given an input of sample size m and number of features n , $X \in \mathbb{R}^{m \times n}$, and the labels for each sample, $Y \in \mathbb{R}^m$, our classification model can be represented as $F(X, \Theta, \Gamma)$, where Θ are the weighed parameters, and Γ are the hyperparameters.

If we take a subset of samples $p \in m$ as training data, $X_{train} \in \mathbb{R}^{p \times n}$, and a subset as testing data $q = m - p$, $X_{test} \in \mathbb{R}^{q \times n}$, we can train and test the classification model respectively. The model is trained by constraining:

$$Y_{train} = F(X_{train}, \Theta, \Gamma) \quad (4-1)$$

And minimizing a cost function, $J(X, Y, \Theta)$, to obtain the optimized Θ^* :

$$\Theta^* = \arg \min_{\Theta} J(X_{train}, Y_{train}, \Theta) \quad (4-2)$$

The cost function varies depending on the classification model, but it is generally a metric of how well the model fits the data it is constrained to. Note that an intermediate cross-validation subset can be used for choosing a Γ that results in optimizing the classification accuracy on the cross-validation subset. However, in this study we used the k -fold cross-validation (discussed later) method to make use of all the training samples for training both Θ and Γ . We can test the accuracy of the classification model by predicting the classification, Y_{pred} , of the test input subset:

$$Y_{pred} = F(X_{test}, \Theta^*, \Gamma) \quad (4-3)$$

The classification accuracy can be measured by summing the total amount of correct predictions over the total amount of samples:

$$Accuracy = \frac{1}{q} \sum_{i=1}^q (1 - (Y_{test,i} - Y_{pred,i})^2) \quad (4-4)$$

4.1.1 Artificial Neural Network

Neural Networks are a class of machine learning models that are loosely modeled after the physiological neuron process. For this study we used an FNN for classification, which are the most commonly implemented. A FNN maps an input x to a class, y , through a series of intermediate computations based on the architecture of the FNN. The architecture of a FNN can be defined by the first layer, number of hidden layers, number of units per hidden layer, and the

last layer. The first layer of m units is the input, $X \in \mathbb{R}^{m \times n}$, and the last layer is the output, $Y \in \mathbb{R}^m$.

Every unit before the last layer has a linear model:

$$z_{i+1} = \mathbf{w}_i^\top \mathbf{a}_i + b_i \quad (4-5)$$

that maps the outputs from each unit, \mathbf{a}_i , to the units in the next layer. The first layers units can be represented as \mathbf{a}_0 . Every unit then transforms the result of this linear model through an activation function, $f(z)$:

$$\mathbf{a}_{i+1} = f(z_{i+1}) \quad (4-6)$$

Two activation functions of interest are the rectified linear unit (ReLU) and the sigmoid logistic function. ReLU is defined by:

$$f(z) = \max\{0, z\} \quad (4-7)$$

ReLU is recommended as the activation function for the units preceding the last layer. It replaces negative inputs with a value of 0 and keeps values that are non-negative. The sigmoid function is defined by:

$$\sigma(z) = \frac{1}{1 + e^{-z}} \quad (4-8)$$

Sigmoid functions are recommended as the activation function of the output units for binary classification, as it bounds the output in the interval of $[0, 1]$. The goal of binary classification is to limit our model to two outputs, 0 and 1. Typically, if the output of the sigmoid is greater than or equal to 0.5, it is assigned 1, and 0 otherwise:

$$f(z) = \begin{cases} 1 & \text{if } \sigma(z) \geq 0.5 \\ 0 & \text{otherwise.} \end{cases} \quad (4-9)$$

Through this we can limit the output to 0 and 1 for binary classification. The parameters for the linear models \mathbf{w} and \mathbf{b} are trained through the minimization of a cost function, $J(\mathbf{w}, \mathbf{b})$, which in this study is the binary cross-entropy:

$$J(\mathbf{w}, \mathbf{b}) = -\frac{1}{m} \sum_{i=1}^m [y_i \ln(a_{output,i}) + (1 - y_i) \ln(1 - a_{output,i})] \quad (4-10)$$

where y represents the true labels, and a_{output} represents the output of the FNN. The parameters are optimized through a process called gradient descent, where gradient of the cost function with respect to the parameters is used to adjust the parameters through an iterative process, with the goal of minimizing the cost function.

4.1.2 Support Vector Machines

For the case of binary classification, the goal is to create a decision boundary separating two classes. Formally, the goal is to create a canonical hyperplane dividing the space in order to provide maximum separation between the different classes. Samples that lie on one side of the decision boundary are identified as belonging to one class, and those that lie on the other side as another class. Depending on where unknown samples lie in relation to the decision boundary, they are classified as one of the two classes. Taking two classes, for this example being positive and negative classes, we can define the following function:

$$f(\mathbf{x}) = \mathbf{w} \cdot \mathbf{x} + b \quad (4-11)$$

with a weight vector \mathbf{w} orthogonal to the decision boundary, input vector \mathbf{x}_i for $i = (1, 2, \dots, m)$, and a constant b . When the function is negative, then the sample belongs to the negative class. If the function is positive, the sample belongs to the positive class. The goal is to find \mathbf{w} and \mathbf{b} such that the decision boundary has the widest distance between the two classes. To do this we start by setting constraints:

$$\mathbf{w} \cdot \mathbf{x}^+ + b \geq 1 \quad (4-12)$$

$$\mathbf{w} \cdot \mathbf{x}^- + b \leq -1 \quad (4-13)$$

For \mathbf{x}^+ being positive samples and \mathbf{x}^- being negative samples. We then define y to be $+1$ for positive samples and -1 for negative samples. Therefore:

$$\mathbf{y}_i(\mathbf{w} \cdot \mathbf{x}_i + b) - 1 \geq 0 \quad (4-14)$$

For all samples along the decision boundaries, for both positive and negative samples, the following constraint is made:

$$\mathbf{y}_i(\mathbf{w} \cdot \mathbf{x}_i + b) - 1 = 0 \quad (4-15)$$

Looking at the decision boundary, having a vector pointing to a positive sample on the decision boundary, \mathbf{x}^+ and a vector pointing to a negative sample on the decision boundary, \mathbf{x}^- , the vector orthogonal to the decision boundary, \mathbf{w} , it can be seen that the width of the decision boundary is:

$$width = (\mathbf{x}^+ + \mathbf{x}^-) \cdot \frac{\mathbf{w}}{\|\mathbf{w}\|} \quad (4-16)$$

Substituting the results from equation (4-11) into (4-12):

$$width = \frac{2}{\|\mathbf{w}\|} \quad (4-17)$$

The objective is to maximize the width, and this is done by minimizing $\frac{1}{2} \|\mathbf{w}\|^2$. This can be done with the method of Lagrange multipliers using the constraint given by equation (4-11):

$$L = \frac{1}{2} \|\mathbf{w}\|^2 - \sum_i^m \alpha_i [\mathbf{y}_i(\mathbf{w} \cdot \mathbf{x}_i + b) - 1] \quad (4-18)$$

$$\frac{\partial L}{\partial \mathbf{w}} = \mathbf{w} - \sum_i^m \alpha_i \mathbf{y}_i \cdot \mathbf{x}_i = 0 \quad (4-19)$$

$$\frac{\partial L}{\partial b} = - \sum_i^m \alpha_i \mathbf{y}_i = 0 \quad (4-20)$$

where α_i are Lagrangian multipliers. Substituting equations (4-16) and (4-15) into (4-14) and simplifying:

$$L = \sum_i^m \alpha_i - \frac{1}{2} \sum_i^m \sum_j^m \alpha_i \alpha_j \mathbf{y}_i \mathbf{y}_j (\mathbf{x}_i \cdot \mathbf{x}_j) \quad (4-21)$$

This can then be maximized with respect to α_i through numerical optimization techniques. However, it will only provide a solution if a hyperplane can be made separating the two classes.

If a separation cannot be made, then there will be no adequate solution. To solve this problem, the feature space can be transformed into a higher dimension which allows separation of the classes. This is done by replacing the inner product, $\mathbf{x}_i \cdot \mathbf{x}_j$, with the inner product of transformation functions, $\Phi(\mathbf{x}_i) \cdot \Phi(\mathbf{x}_j)$. Finding the transformation functions could prove to be difficult, but the inner product of the transformation functions is what is needed, not the transformation functions themselves. The inner product of the transformation functions can be found using kernel methods.

4.1.2.1 Kernel Methods

Kernel methods are introduced and a kernel function here can be defined as the inner product of the transformation functions:

$$K(\mathbf{x}_i, \mathbf{x}_j) = \Phi(\mathbf{x}_i) \cdot \Phi(\mathbf{x}_j) \quad (4-22)$$

Specifically, in this study, the Radial-Basis-Function (RBF) kernel is used and is defined as:

$$K(\mathbf{x}_i, \mathbf{x}_j) = e^{-\gamma \|\mathbf{x}_i - \mathbf{x}_j\|} \quad (4-23)$$

where γ is a free hyperparameter. Substituting (4-18) and (4-19) into (4-17) to get the new Langrangian to optimize:

$$L = \sum_i^m \alpha_i - \frac{1}{2} \sum_i^m \sum_j^m \alpha_i \alpha_j \mathbf{y}_i \mathbf{y}_j e^{-\gamma \|\mathbf{x}_i - \mathbf{x}_j\|} \quad (4-24)$$

and (4-15) into (4-1) to get the new decision function:

$$f(\mathbf{z}) = \sum_{i=1}^m \mathbf{y}_i \alpha_i K(\mathbf{x}_i, \mathbf{z}) + b \quad (4-25)$$

$$Y_{test,i} = \sum_{i=1}^m \mathbf{y}_i \alpha_i K(\mathbf{x}_{train,i}, \mathbf{x}_{test,i}) + b \quad (4-26)$$

which assigns the sample according to the sign of its value (negative or positive.) The optimized bias term, b^* , can be readily found by solving equation (4-15) for points along the decision boundary:

$$b^* = -\frac{1}{2} (\max_i \mathbf{w}^* \cdot \mathbf{x}_i + \min_i \mathbf{w}^* \cdot \mathbf{x}_i) \quad (4-27)$$

4.1.3 Random Forest

Random forests can be used for most types of learning tasks, including classification. The classification at the output of a random forest is obtained from the average output of an ensemble of decision trees, $\{T_b\}_1^B$, each which are of themselves classification models.

4.1.3.1 Decision Tree

A decision tree is a graphical structure composed of nodes. The nodes are arranged in a hierarchical fashion where one node successively splits into different nodes until the terminal nodes are reached. For this study, binary trees are used, where nodes split into exactly two daughter nodes: left and right. A node j begins with a set of samples, S_j , which represents a sample of training pairs (x, y) , and splits into two daughter nodes, S_j^L and S_j^R , such that:

$$S_j = S_j^L \cup S_j^R, \quad S_j^L \cap S_j^R = \emptyset \quad (4-28)$$

Every node represents a Boolean question about a specific feature from the input data point. If the value of this feature is above or below a certain threshold, the input traverses down to the left or right daughter node. This continues until the terminal nodes, also called the leaf nodes. The label that is most present at a terminal node represents the classification output at that node, and is represented as which class, y^* it has the highest probability of being:

$$y^* = \arg \max_{y \in \{0,1\}} (p(y|x)) \quad (4-29)$$

The splitting decision made at each node is automatically learned through a weak learner function:

$$h(x, \Theta) \mapsto \{0,1\} \quad (4-30)$$

where Θ are the parameters for the weak learner. The objective function the weak learner attempts to maximize is the information gained through splitting the node in a particular way. The more

distinct the separation is, the higher the information gain. The information gain, I , is represented as:

$$I = H(S) - \sum_{i \in \{L,R\}} \frac{|S^i|}{|S|} H(S^i) \quad (4-31)$$

where H is entropy, and is represented as:

$$H(S) = - \sum_{y \in \{0,1\}} p(y) \log(p(y)) \quad (4-32)$$

The node can split the data by aligning axes (axis-aligned weak learner) through a subset of $p \in n$ features, and determining which axis splits the samples resulting in the highest information gain. Successive nodes are split in this fashion until certain stopping criteria are met, such as tree depth. The stopping criteria in this study was when the splitting resulted in only one type of class remaining in a daughter node.

4.1.3.2 Random Forest Algorithm

A random forest is an ensemble of many decision trees that are generated through a random process. This results in higher generalization. The decision tree can be randomized by selecting a bootstrap sample N from m samples, and randomly selecting a subset of p features at every node to be analyzed. The number of trees in a random forest is itself a hyperparameter, with a higher number of trees generally resulting in a higher generalization at the expense of computational run-time.

The training algorithm can be summarized as:

1. From $b = 1$ to B :
 - a. Select a bootstrap sample of size N from the training data.
 - b. Build a decision tree, T_b , for the bootstrapped data, by repeating these steps until the stopping criteria is met:

- i. Select p variables from the available n .
 - ii. Find the best feature/axis-aligned split among the p .
 - iii. Split the node into two daughter nodes.
2. Output the ensemble of trees $\{T_b\}_1^B$

When classifying the test data, the results from all the individual trees are averaged, and the input data is classified as the prediction which has the highest value:

$$Y_{pred,i} = \arg \max_{y \in \{0,1\}} \frac{1}{B} \sum_{i=1}^B p_i(y, X_{test,i}) \quad (4-33)$$

4.2 Unsupervised Approach

Clustering is an unsupervised machine learning approach in which the data is separated into a set of groups, or clusters, where the data in each group share similar features. For example, clustering creates groups of data such that the data in each cluster are more similar to each other, and different than data in other clusters. In this dissertation, k -means algorithm was used for SCG events clustering.

4.2.1 k -means Clustering

This method divides the input data into k clusters where each cluster has a centroid. Each data point then goes to the cluster whose centroid it is closest to. The k -means algorithm is an iterative process which can be summarized as follows:

1. Select k random centroids in the n dimensional space
2. Assign each data point to its closest centroid
3. Calculate mean of data points assigned to each cluster
4. Reassign location of each centroid to the mean of its cluster
5. Repeat steps 1 through 4 until the centroid locations do not change anymore

4.3 Adaptive Feature Extraction

This section proposes and tests a new feature extraction method that adaptively creates a feature vector. The proposed feature extraction algorithm was then used to classify SCG events into low and high lung volume (LLV and HLV) classes. The performance of the proposed method was compared to the available non-adaptive feature extraction methods [30].

4.3.1 Feature Extraction Algorithm

The time-domain feature extraction method for SCG signals proposed by Zakeri [30] divides each SCG event into a fixed number of equal-width bins. It then uses the signal average within each bin as a feature. The grouped averages from the bins constitutes the feature vector, which will have a reduced dimensionality compared with the original signal. However, in this method, there may be bins that lack additional useful information (i.e., may have redundant values) and, hence, do not significantly improve the classification accuracy.

The feature extraction algorithm proposed in this paper aims at solving this potential issue by removing possible redundancies. In addition to dimensionality reduction, the proposed algorithm prioritizes the parts of the SCG signal that has more variations by assigning more bins to those parts.

The algorithm begins by specifying a threshold, which is a certain fraction of the signal's peak-to-peak amplitude. The threshold is chosen such that it, later, would result in a certain number of bins. In the next step the entire SCG event is considered as one bin and the signal standard deviation within the bin is calculated. When the standard deviation is above the specified threshold, the bin is divided into 2. For the new bins to approximately have equal lengths, it is preferable (but not necessary) that the SCG event contains power of 2 data points. The standard deviation calculations are then repeated for the newly created bins, and more new bins will be created until

every bin meets the threshold criteria. The outputs of this process are two vectors, where one vector contains the adaptively-spaced bins and the other contains the signal averages within each bin. The pseudo-code for the proposed algorithm is provided in Algorithm 4.1.

Algorithm 4.1 Adaptive-width binning of SCG signals

```

1: Input: SCG events
2: Output: Indices for adaptive feature vector
3:  $Y =$  SCG event,  $\exists x \in Z^+$  such that  $\text{length}(Y) = 2^x$ 
4:  $T =$  Threshold
5:  $\text{Indices} = [0, \text{length}(Y) - 1]$ 
6:  $a \leftarrow 0, b \leftarrow 1$ 
7:  $T \leftarrow \alpha \times (\max(Y) - \min(Y))$ , where  $\alpha \in [0, 1]$ 
8: while  $\text{Indices}[a] \neq \text{length}(Y) - 1$  then
9:     if  $\text{SD}(Y[\text{Indices}[a] : \text{Indices}[b]]) > T$  then
10:          $C \leftarrow \text{floor}((\text{Indices}[b] - \text{Indices}[a]) / 2)$ 
11:          $\text{Indices} \leftarrow \text{sort}([\text{Indices}, C])$ 
12:     else
13:          $a \leftarrow a + 1$ 
14:          $b \leftarrow b + 1$ 
15:     end if
16: end while

```

4.3.2 Human Studies

4.3.2.1 Participants

The experimental protocol used in this study was approved by the institutional review board of the University of Central Florida, Orlando, FL. A total of 7 adults participated in our study. The subjects provided their informed consent and reported no history of cardiovascular disease verbally. The age, height, and weight of the subjects were obtained and are reported in Table 4.1.

Table 4.1. Overview of the subjects' characteristics (mean \pm SD).

Age (years)	29.4 \pm 4.5
Height (cm)	173.1 \pm 9.8
Weight (kg)	82.2 \pm 18.3
Number of subjects	7

4.3.2.2 Experiment

For breathing pattern and tidal volume (TV) consistency, the subjects were instructed on how to breathe. For this purpose, a ventilator (Model: 613, Harvard Apparatus, South Natick, MA) was used to train subjects to breath with the same respiratory rate and inspiratory:expiratory (I:E) ratio. The respiratory rate and I:E ratio were set to 12 breath per minute and 1:3, respectively. The TV

for each subject was calculated in real time as time integral of the respiratory flow rate (RFR) signal. During the experiment, TV was displayed on a computer screen and was about 10 to 15 mL/kg for all subjects. The subjects rested on a folding bed with their chest tilted at 45 degrees and the signals of interest were recorded for 2 trials of 5 minutes each.

4.3.2.3 Instrumentation

A triaxial accelerometer (Model: 356A32, PCB Piezotronics, Depew, NY) measured all SCG signals. A signal conditioner (Model: 482C, PCB Piezotronics, Depew, NY) with a gain factor of 100 was used to amplify the accelerometer output. The accelerometer was attached with a double-sided medical-grade tape at the 4th intercostal space and the left sternal border. The sensor location was chosen to attain a high signal-to-noise ratio [22,167]. The accelerometer z-axis was perpendicular to the chest surface of the subject, while the y- and x-axes were aligned parallel to the mediolateral and axial directions, respectively. The RFR was measured using a spirometer (Model: A-FH-300, iWorx Systems, Inc., Dover, NH), that was calibrated by the manufacturer. The expiration and inspiration produced negative and positive flow rate signal amplitudes, respectively. A Control Module (Model: IX-TA-220, iWorx Systems, Inc., Dover, NH) was used to simultaneously acquire the voltage signal for RFR, ECG, and SCG signals.

All above signals were simultaneously acquired with sampling rate of 10 kHz. To remove the remaining respiratory sound noise, the SCG signals were filtered using a low-pass filter with a cut-off of 100 Hz since lung sounds have significant energy above this cut-off frequency [101]. All signals were processed using Matlab (R2015b, The MathWorks, Inc., Natick, MA).

4.3.2.4 SCG Event Pre-processing

The SCG events in each signal were found using matched filtering with a template consisting of a previously identified SCG. The LV signal was then used to group SCG events into two groups

of high and low lung volume. The SCG events that occurred during high and low lung volumes were called HLV and LLV SCG events, respectively (Figure 4.1). The SCG events duration were chosen to contain 4096 (corresponding to ~ 700 milliseconds), which was sufficiently long to contain the SCG event. This was to ensure that all signals had equal length, and that the number of points for each event equals a power of 2 to best satisfy the algorithm's requirement.

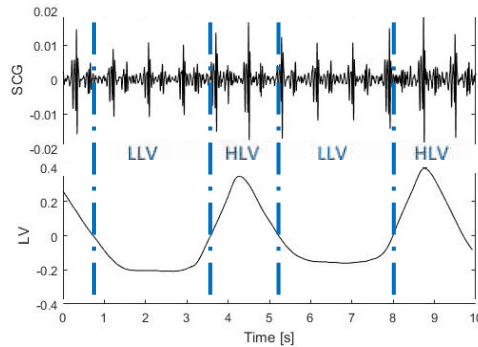


Figure 4.1. (top) A 10-sec portion of the SCG signal, (bottom) Lung volume signal that was used to group SCG events into two groups of high and low lung volume (HLV and LLV) events.

4.3.2.5 SCG Feature Extraction and Classification

Feature extraction included dividing the SCG signal into bins (16, 32, 64, 128, 256, 512, and 1024), calculating the mean of each bin, and treating this as the feature vector. This corresponds to feature vectors of length 16, 32, 64, 128, 256, 512, and 1024. This method was adopted from Zakeri [30]. The original method divided the signal into evenly spaced bins, and the new proposed method divides the signal into bins adaptively spaced using the introduced algorithm. However, when the proposed method is used, the location of the bins may be different for each SCG event, resulting in the possible transformation of each event to a different feature space. Hence, the adaptive method was instead applied to the ensemble average of all SCG events, and single set of bins was determined. The resulting bins were then used to create the feature vectors for the individual SCG events. After bins were finalized, the signal variability in each bin for the

individual SCG events were checked to ensure that the variability does not exceed the threshold by more than 5%.

An SVM algorithm was used to classify the SCG events into two classes of LLV and HLV. The classifier used was the RBF SVM. The subject-specific training scenario was employed such that a different classification model was built for each individual subject. There was a total of 3986 samples (i.e. SCG events), 1813 HLV and 2173 LLV. Per subject, there was an average of 259 ± 48 HLV, 310 ± 42 LLV, and 569 ± 76 total samples.

The k -fold cross-validation method ($k = 10$) was used to evaluate the identification accuracy [180]. The accuracy was defined as the ratio of the number of correctly identified samples to the total number of samples in the test set. For each subject, the final accuracy of the model was obtained by averaging the 10 accuracies resulted from the k -fold cross-validation. The F_1 score was used as another evaluation metric [181]. The F_1 score was calculated as the harmonic mean of *sensitivity* and *precision*,

$$F_1 = 2 \times (\textit{sensitivity} \times \textit{precision}) / (\textit{sensitivity} + \textit{precision}) \quad (4-34)$$

where *sensitivity* and *precision* were defined as,

$$\textit{sensitivity} = TP / (TP + FN) \quad (4-35)$$

$$\textit{precision} = TP / (TP + FP) \quad (4-36)$$

where TP , FN , and FP were true positive, false negative, and false positive, respectively. The hyper parameters of the SVM models were chosen through an exhaustive grid search, with the goal of maximizing the 10-fold cross-validation accuracy. The signal processing and machine learning steps for classification of LLV and HLV SCG events are shown in Figure 4.2. The feature extraction and machine learning analysis was implemented with Python libraries Scikit-Learn [182] and SciPy/NumPy [183].

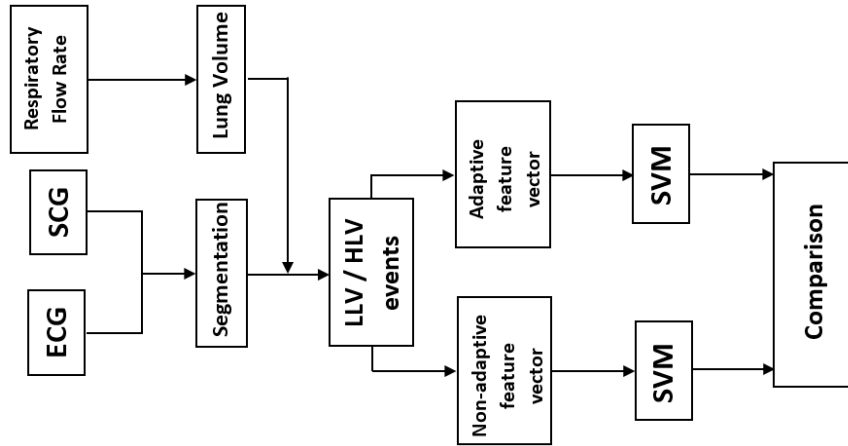


Figure 4.2. Block diagram describing the signal processing and machine learning steps used in the current study.

4.3.3 Results

Figure 4.3 shows the proposed adaptive algorithm (adaptively-spaced bins) compared to the non-adaptive method (evenly-spaced bins) used in [30] for 16 bins.

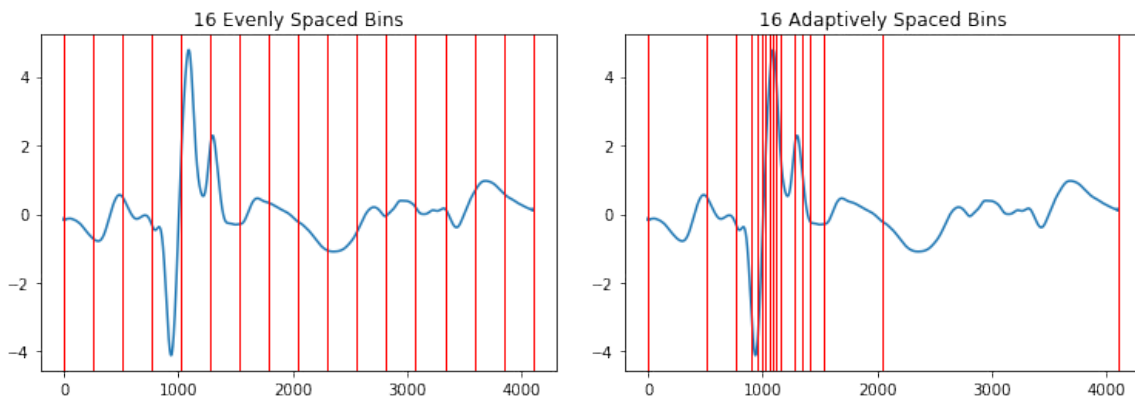


Figure 4.3. (left) Equal-width bins configuration adopted from [30] vs (right) adaptive-width bins configuration proposed in this study for a feature vector length (i.e., number of bins) of 16.

The classification of SCG events using the equal-width (EW) and adaptive-width (AW) bins began with a relatively small number of bins (16 bins). The performance analysis of the models was first done with these wider bins since it was less computationally expensive. The number of bins were then increased to find the number of bins at which the accuracy of the EW model reaches a plateau. This process is similar to mesh independency assessment in finite element analysis

[124,125,184–190]. The identification accuracy for the SVM model for EW and AW bins feature vectors are listed in Table 4.2 for 7 different number of bins of 16, 32, 64, 128, 256, 512, and 1024. As the number of bins increased from 16 to 1024, the accuracy of the EW increased from 65% to 91% while the accuracy of the AW seemed to be stay around 91% for all number of bins used. Similarly, the F_1 score of the model using EW raised from 63% to 89% by increasing the number of bins from 16 to 1024. However, the F_1 scores of the model using adaptive feature vector were similar for different bin numbers. The accuracies and F_1 scores for the models using both the AW and EW bins converged as the number of bins increased, as displayed in Figure 4.4. The accuracy and F_1 scores reached their maximum at a much smaller number of bins for the AW method, which can save calculation cost.

Table 4.2. Average accuracies and F_1 scores of SVM models for different number of bins when using equal-width (EW) and adaptive-width (AW) bins.

Bins	Acc. EW	Acc. AW	F_1 EW	F_1 AW
16	0.65 ± 0.07	0.90 ± 0.05	0.63 ± 0.08	0.91 ± 0.05
32	0.66 ± 0.07	0.91 ± 0.04	0.60 ± 0.14	0.92 ± 0.04
64	0.67 ± 0.07	0.91 ± 0.04	0.65 ± 0.06	0.93 ± 0.04
128	0.70 ± 0.06	0.92 ± 0.04	0.70 ± 0.08	0.92 ± 0.04
256	0.83 ± 0.07	0.92 ± 0.04	0.82 ± 0.08	0.92 ± 0.04
512	0.87 ± 0.07	0.92 ± 0.04	0.87 ± 0.07	0.91 ± 0.05
1024	0.91 ± 0.05	0.92 ± 0.04	0.89 ± 0.07	0.91 ± 0.05

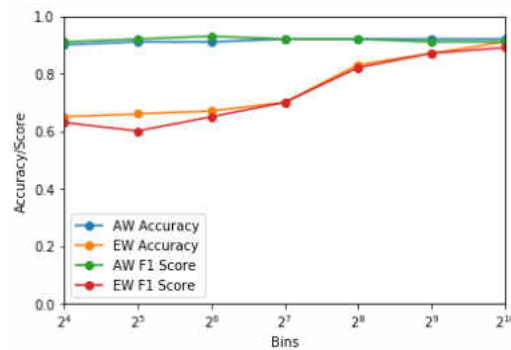


Figure 4.4. Performance trend for SVM models using both AW and EW bins as the number of bins increase. The proposed adaptive feature extraction algorithm resulted in a higher accuracy and F_1 score consistently.

4.3.4 Discussions

4.3.4.1 Algorithm Performance

The performance of the SVM using AW or EW bins was comparable for high number of bins (1024 in the current study). The performance remained relatively constant from 16 to 1024 bins for AW bins, whereas reducing the number of bins significantly worsened the classification performance when EW bins were used. These results demonstrated that the AW bins resulted in higher accuracies at smaller number of bins, and therefore it was more computationally efficient. The improved performance of the adaptive feature extraction method might be due to higher density of bins around SCG1 (the relatively strong signal region around index 1000 of the SCG event shown in Figure 4.3). SCG1 contains important physiological events such as aortic valve opening, mitral valve closure, isovolumic contraction, and rapid ejection [191,192]. Therefore, focusing on this segment of the SCG event might increase the SVM classification accuracy.

4.3.4.2 Limitations

The primary limitation of the study is the small number of subjects and SCG event samples. More SCG events might result in a higher classification accuracy of the SVM models using both the AW and EW bins. Therefore, future studies need to enroll a larger number of subjects.

4.3.5 Conclusions

In this study, a SVM machine learning method was developed to identify the SCG events occurring during different phases of LV. To select features, an adaptive feature extraction algorithm was proposed. The proposed algorithm was found to be an efficient, reliable, and accurate approach to extract SCG features compared to the available feature extraction methods in literature. The feature extraction algorithm proposed in this study can be used in the study of other biomedical signals. In this study, the signal variability in temporal bins was measured by

calculating the signal standard deviation. The proposed algorithm performance might be improved by employing other indicators of the signal complexity.

4.4 SCG Signals Classification

The signals obtained from the body are generally disturbed with noise and interference, and due to these factors and others, characteristics of the signal that provide clinically important information may not be observable by a human. However, improvements in biomedical signal analysis have been made through the use of machine learning techniques [193]. Applications of predictive methods are increasingly used in the field of medicine and biomedical signal processing, including for SCG analysis. Applications of machine learning techniques include classification, regression, graph similarity, and Hidden Markov Models.

Classification methods include the use of SVM, Logistic Regression (LR), NN, and decision trees. An early study using NN [143] classified patients as either having Coronary Artery Disease (CAD) or as low risk normal. They predicted CAD with a sensitivity of 80% and a specificity of 80%. One study [30,142] developed a method using a support vector machine that classified SCG signals as occurring during inspiration or expiration. They implemented two different training scenarios, leave-one-subject-out (LOSO): which trained the SVM on all but one subject, and tested on the subject left out, and subject-specific: which trained and tested on each subject individually. The average accuracies for LOSO and SS were 88.1% and 95.4% respectively. Similarly, another study [31] sought to classify with a SVM SCG signals according to their LV phase as opposed to respiration cycle. Their motivation was that the similarity of SCG signals grouped according to their LV phase was higher than when grouped according to their respiration cycle [29]. Three training scenarios were used to train a model for: SCG1 (first heart sound), SCG2 (second heart sound), and SCG (complete cardiac cycle). The classification accuracies for the three training

scenarios: SCG1, SCG2, and SCG, were 75%, 77%, and 75% respectively. Another study completed by Taebi *et al.* [87] compared the classification accuracies for two time-domain feature extraction methods: dividing the signal into evenly-spaced bins [30,142], to one using adaptively-spaced bins. The classification accuracies using the evenly-spaced bins was 65% for 16 bins and reached an accuracy of 91% at 1024 bins. The adaptively-spaced bins had a classification accuracy of 91% at 16 bins, and 91% again at 1024 bins. The binning was heavily concentrated around SCG1, suggesting this region in the time-domain may contain relatively useful information. A recent study [76] sought to detect atrial fibrillation using the measuring systems within a smartphone. The phone's inertial-measurement-unit (IMU), which contains both an accelerometer and gyroscope, were used to measure SCG and GCG. Three classifiers (SVM with and without a kernel function, and a random forest) were trained and testing with the LOSO training scenario. The SVM with a kernel function obtained the highest performance with a sensitivity of 93.8%, specificity of 100.0%, and a classification accuracy of 97.4%.

Classification methods were also used to help identify fiducial points, where one study [65] used LR and a SVM to identify specific slopes of the SCG signal to estimate the locations of the IM, AO, and AC points. One study [194] trained an Evolving Fuzzy Neural Network (EFuNN) to detect the presence of artifacts in an SCG signal, such as movements due to daily physical activity. The input to the EFuNN were both raw SCG signals and their envelopes, and they were labeled by experts as either "good" or "artefactual." The EFuNN was trained to correctly identify artifacts in both the raw SCG signals and their envelopes. A J-48 decision tree with adaptive boosting was trained for binary classification to classify the SCG signal as being measured from an accelerometer placed on the sternum, or placed in another position [41]. Their motivation was that

PEP estimation can differ depending on the placement of the accelerometer. Precision and recall was used to evaluate the performance of the classifier, which were 0.83 and 0.82 respectively.

An Extreme Gradient Boosting (XGBoost) regression model was trained to predict the PEP of SCG signals collected at different sensor locations (sternum, left and right clavicles, and point of maximum impulse) [95]. The true PEP values were obtained through knowledge of the ECG R peak and the impedance cardiogram (ICG) B-point. Their model was evaluated by the root mean squared error (RMSE), and through a repeated cross-validation assessment. The results of the different sensor placements and combinations were compared, as well as comparing the XGBoost model against other regression models, such as the random forest. The XGBoost model with the sensors combination of sternum and left clavicle resulted in the lowest RMSE.

Graph similarity analysis [38] through the use of k-Nearest Neighbor graphs was done on SCG signals of HF patients identified as compensated (outpatient) and decompensated (hospitalized). The patients were subjected to a 6-minute walk test (6MWT) followed by 5 minutes of recovery. Two k-nearest neighbor graphs were constructed for each patient and the graph similarity scores (GSS) between the rest and recovery phases were computed. The average GSS was 35 ± 3.9 for the compensated patients and 44 ± 4.1 for the decompensated, $P < 0.01$. This suggests that the decompensated patients had less cardiovascular reserve and were not able to modulate their hemodynamics or cardiac contractility as effectively as the compensated patients during exercise. The GSS metric was also suggested to possibly be more sensitive than other factors to assess cardiac improvements in the patient.

A HMM-based method was used in one study [51] to estimate the heart rate, HRV, and CTI from an SCG signal. The states of the HMM represented the stages in the cardiac cycle. The expectation-maximization algorithm was used for learning the SCG signal, and the Viterbi

sequence was used to estimate the cardiac state. This model was superior in performance to two other methods: enveloped-based and spectral-based. Machine learning methods are used in CHAPTER 5 of this dissertation to classify SCG signals.

4.5 Summary

In this chapter, the potential classifiers for the classification of SCG signals were investigated. These classifiers were then used in the human studies described in CHAPTER 6. A novel adaptive algorithm for SCG temporal feature extraction was also proposed. The algorithm resulted improved classification accuracy.

CHAPTER 5: HUMAN STUDIES

In this chapter, different human studies were conducted using the methods that have been described in the previous chapters. The effect of respiration on the SCG morphology and heart rate were investigated in sections 5.1 and 5.2, respectively. In section 5.3, several criteria were used to group similar SCG events into two different clusters where SCG events in each cluster are more similar to each other. Efficient grouping of SCG events into clusters containing minimal variability leads to a more precise estimation of SCG characteristics. In section 5.4, the physiological sources of the SCG waveforms were studied using other common modalities such as echocardiography and electrocardiography. In this section, a finite element model of simplified thoracic structures was also developed to estimate surface response to subsurface vibratory sources.

5.1 Respiration Effect

SCG was previously used to estimate the respiration rate, which was found comparable to that derived from a reference respiration belt [6]. SCG signal morphology was reported to vary with different factors, including respiration cycle (inspiration vs expiration), sensor location on the chest, etc. [28,40]. The effect of respiratory cycle has been studied [6] on some of the SCG features such as timing interval changes. However, the effect of respiration on the SCG signal morphology needs more attention [20]. During inspiration, the diaphragm moves downward, the chest wall expands, the intrathoracic pressure decreases, the lungs inflate [195], and the heart position is displaced almost linearly with the diaphragm [196]. The decreased intrathoracic pressure increases the pulmonary blood volume, leading to an increase and decrease in the right and left atrial filling, and reduction in the left ventricular stroke volume [197]. These hemodynamic changes can affect the SCG signal morphology.

As described, the SCG variation during a respiration cycle has been mentioned before. This study, however, aims at investigating the possible physiological correlates of this morphological variation. For this purpose, the SCG events in a recording were first grouped based on the criteria that are physiologically measurable (e.g. inhalation and exhalation), and then the best criterion that could group similar SCG events together was identified. That criterion was then studied to explain why SCG morphology varies during the respiration cycle. Achievements of this study include quantification of the differences in SCG signals due to respiration, and determination of optimal respiration criterion for grouping the different SCG waveforms. Materials and methods are given in section 5.1.1. Results are presented and discussed in sections 5.1.2 and 5.1.3, respectively, followed by conclusions in section 5.1.4.

5.1.1 Methodology

5.1.1.1 Participants

The study protocol was approved by the institutional review board of the University of Central Florida, Orlando, FL. A total of 7 young individuals with no history of cardiovascular disease participated in the study after informed consent. Mean age, height, weight, body mass index (BMI), and heartbeat of the subjects were obtained and reported in Table 5.1.

Table 5.1. Overview of the subjects' characteristics (mean \pm SD).

Age (years)	24.3 \pm 5.0
Height (cm)	170.8 \pm 8.2
Weight (kg)	78.7 \pm 13.0
Heart rate (bpm)	66.6 \pm 9.0
BMI (kg/m ²)	26.9 \pm 3.4
Number of subjects	7

5.1.1.2 Data Collection

All participants were instructed to lay supine on a table and breathe normally. The SCG signal was measured using a triaxial accelerometer (Model: 356A32, PCB Piezotronics, Depew, NY). The accelerometer output was amplified using a signal conditioner (Model: 482C, PCB Piezotronics, Depew, NY) with a gain factor of 100. The sensor was placed at the left sternal border and the 4th intercostal space using a double-sided tape since this location tended to have high signal-to-noise ratio. The accelerometer's x- and y-axes were aligned parallel to the anteroposterior and mediolateral directions, respectively, while the z-axis was aligned in dorso-ventral direction. In this study, the z-component of acceleration tended to be strongest, similar to previous studies [20]. Therefore, attention in the current study was focused on the analysis of this acceleration

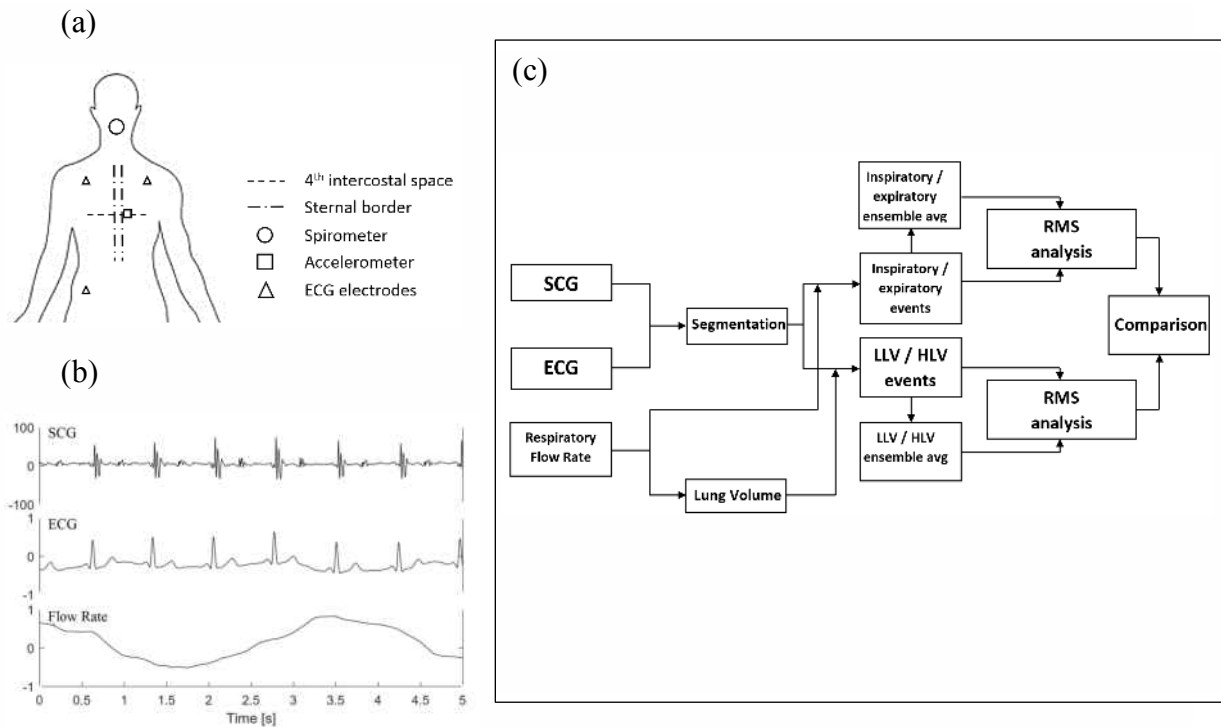


Figure 5.1. (a) The location of the accelerometer, ECG electrodes and spirometer on the subject body. The accelerometer and spirometer sensors were used to measure the SCG and respiratory flow rate signals, respectively. The dashed and dash-dot lines show the 4th intercostal space and sternal border, respectively. (b) A 5 s portion of simultaneously acquired SCG, ECG, and respiratory flow rate signals. (c) Summary of the signal processing algorithm used in this study.

component. The RFR of the subjects was measured using a pre-calibrated spirometer (Model: A-FH-300, iWorx Systems, Inc., Dover, NH). The flow rate signal had positive and negative amplitude during the inspiration and expiration, respectively. The voltage signal for both RFR and SCG signals were acquired using a Control Module (Model: IX-TA-220, iWorx Systems, Inc., Dover, NH). The LV was calculated as the integral of the RFR. The sensors locations are shown in Figure 5.1.a.

5.1.1.3 Segmentation and Grouping based on Respiration

The SCG events in each signal were found using a matched filtering with a template consisting of a previously identified SCG. The filtering algorithm was obtained from [198]. The matched filter coefficients, $w(t)$, were calculated as

$$w(t) = l(L - t + 1) \tag{5-1}$$

where $l(t)$, L , and $t = 1, 2, \dots, L$ were the library template (an SCG event manually chosen by the user), number of sample points in the template, and the coefficient index, respectively. The filter output, $y(t)$, was then calculated as

$$y(t) = w(t) * x(t) \tag{5-2}$$

where $x(t)$ was the raw SCG signal. The filter output had maximums at locations that the raw SCG signal best matched the template. The envelope of the filter output was found using Hilbert transform. The peaks of this envelope signal with an amplitude above a certain threshold were then identified. The indices of the peaks were then used to determine the location of the SCG events. Identified SCG events were checked manually to confirm the absence of distorted SCG (for example due to motion artifacts). SCG events were then divided into two groups using two different respiratory criteria. First, the RFR was used to group the SCG events into inspiratory and

expiratory groups corresponding to positive and negative respiratory flows, respectively.

Figure 5.2 shows the inspiratory and expiratory SCG events for a healthy subject.

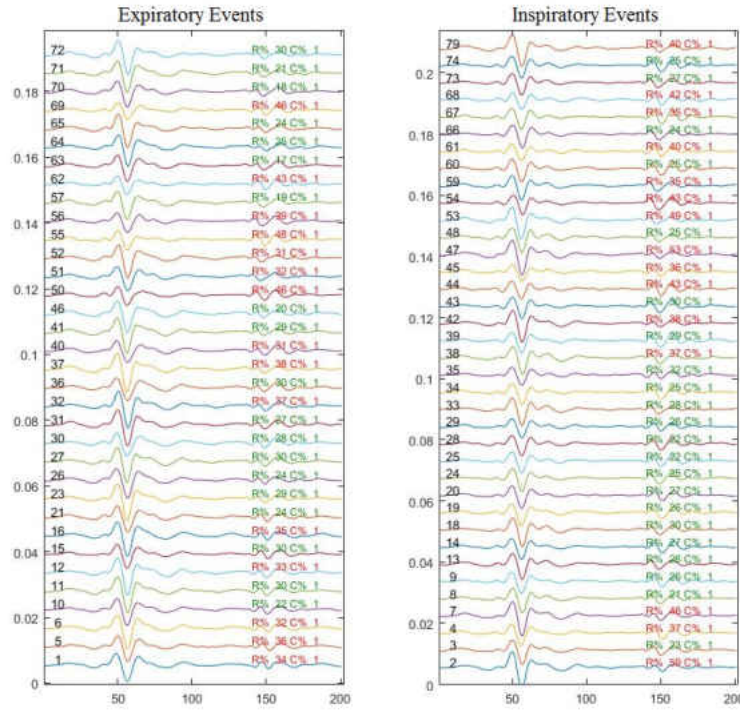


Figure 5.2. Inspiratory and expiratory SCG events in time domain. The SCG events were categorized into two groups of inspiratory and expiratory using the respiration flow rate signal.

Similarly, the LV was used to group SCG events. Here the average LV was first calculated, and low and high lung volumes (i.e., LLV and HLV) were defined as those below and above the mean LV. The SCG events were then labeled as LLV and HLV events, depending on if they occurred during LLV or HLV, respectively. The two grouping methods were then compared to determine which criterion is more effective in grouping similar SCG events. The details of quantifying the SCG event similarity and effectiveness of the grouping criteria are described in the next section.

5.1.1.4 Grouping Criteria Effectiveness

After separating the SCG events into two groups (e.g., inspiratory and expiratory), they were aligned in time (by minimizing the cross-correlation function), and an ensemble average SCG was

calculated for each group separately. To quantify the dissimilarity of each SCG with respect to the two groups, the difference between each SCG waveform and the average waveform of both groups was calculated. Then the RMS (root-mean-square) of these differences were determined using equation (5-3). This quantity was then divided by the RMS amplitude of the average waveform for each group (equation (5-4)).

$$DRMS_{SCG_{i,j}} = RMS(SCG_{i,j} - SCG_{avg,j}) \quad (5-3)$$

$$RMS_{SCG_{i,j}} = \left| \frac{DRMS_{SCG_{i,j}}}{RMS_{SCG_{avg,j}}} \right| \times 100 \quad (5-4)$$

where $i \in [1, \dots, \text{number of events in each group}]$, j is the group (i.e., inspiration or expiration), and

$$RMS_{SCG_{avg,j}} = RMS(SCG_{avg,j}) \quad (5-5)$$

where $SCG_{avg,j}$ is the ensemble averaged SCG event of group j . The average dissimilarity of grouped SCG events was calculated as,

$$\overline{RMS}_{SCG_j} = \sum_i RMS_{SCG_{i,j}} \quad (5-6)$$

This is calculated within the same group as well as with respect to the alternate group. For example, for events that were grouped as inspiratory, their average dissimilarity was calculated with respect to inspiratory (i.e., same group) and expiratory (i.e., alternative group), separately. The difference between these two average dissimilarities is indicative of how well was the grouping and can be calculated from,

$$RD_{FRi} = \left(\overline{RMS}_{SCG_{i \in j, insp}} - \overline{RMS}_{SCG_{i \in j, exp}} \right) / \overline{RMS}_{SCG_{i \in j, insp}} \quad (5-7.a)$$

where RD_{FR} is the normalized difference of mean dissimilarity of inspiratory events with respect to inspiratory and expiratory groups, respectively. The same dissimilarity difference was calculated for expiratory events.

Another grouping choice for SCG events that was tested in the current study was based on low and high lung volume, LLV and HLV, respectively. Here, dissimilarities were also calculated to determine the dissimilarity of each SCG event group with respect to its own group and the alternative group. For example, for LLV SCG events, the difference between average dissimilarities relative to LLV and HLV groups was calculated from,

$$RD_{LV_i} = \left(\overline{RMS}_{SCG_{i \in j, LLV}} - \overline{RMS}_{SCG_{i \in j, HLV}} \right) / \overline{RMS}_{SCG_{i \in j, LLV}} \quad (5-7.b)$$

To determine which grouping criterion (i.e., inspiration vs expiration or LLV vs HLV) provide better grouping of SCG events, the difference in the average dissimilarity was compared. For example, the RD_{FR} and RD_{LV} were compared for each subject. This will help determine whether the respiratory flow rate or lung volume more effectively separate SCG events.

5.1.2 Results

The mean dissimilarity of inspiratory events with respect to same or alternative group (i.e., inspiratory and expiratory groups, respectively) are listed in Table 5.2 (Column 2 and 3, respectively). Column 4 shows the number of events in the group. The same information is listed for the expiratory group in columns 5, 6, and 7, respectively. The difference in dissimilarity between alternate and same group is listed in columns 8 and 9, respectively, where positive values indicate more dissimilarity with the alternate group compared to the same group. The difference was positive in 6 out of 7 subjects. Hence it can be concluded that in most subjects, the mean dissimilarity within the same group was smaller than that for the alternative group, indicating proper grouping. The fact that two different morphologies of SCG can be separated based on respiration is consistent with reports that the SCG morphology changes with different phases of

respiration [28]. For one subject (subject #6), the expiratory events were more dissimilar to their group than the inspiratory group. For this subject, the two mean dissimilarities were close (~ 48.5).

Results of grouping SCG based on LV (i.e. LLV vs HLV) are presented in Table 5.3, where the format is parallel to Table 5.2. The SCG events in each group (LLV and HLV) were more similar to their own group.

The RD_{FR} and RD_{LV} values (listed in the last column of Table 5.2 and Table 5.3, respectively) are a measure of how well SCG grouping was. These results show that the LV signal was more successful than the flow rate signal in grouping the SCG events into two different groups (Figure 5.3) where the events in each group are morphologically similar to each other.

Table 5.2. RMS between SCG events in the inspiratory and expiratory groups and the ensemble averaged inspiratory/expiratory SCG event (Equation (5-6)). The values are shown as mean \pm SD. The number of SCG events in each group is shown in parenthesis. The last column shows the relative differences in percentage.

Subject #	RMS between inspiratory events and ...			RMS between expiratory events and ...			Relative Difference (%)	
	Averaged inspiratory SCG	Averaged expiratory SCG	<i>n</i>	Averaged inspiratory SCG	Averaged expiratory SCG	<i>n</i>	$RD_{FR_{insp}}$	$RD_{FR_{exp}}$
	$\overline{RMS}_{SCG_{insp,insp}} \pm SD$	$\overline{RMS}_{SCG_{exp,exp}} \pm SD$		$\overline{RMS}_{SCG_{exp,insp}} \pm SD$	$\overline{RMS}_{SCG_{exp,exp}} \pm SD$			
1	25.0252 \pm 6.0923	33.2976 \pm 7.3152	(53)	28.4763 \pm 7.5722	24.0721 \pm 7.2852	(55)	33.06	18.29
2	42.1056 \pm 12.3828	46.6644 \pm 12.0475	(38)	50.7218 \pm 11.9698	47.8863 \pm 13.2326	(54)	10.83	5.92
3	47.7511 \pm 13.4712	61.4332 \pm 15.1620	(37)	56.7565 \pm 20.0213	49.7977 \pm 21.2623	(35)	28.65	13.97
4	45.8798 \pm 13.6270	64.3130 \pm 18.7429	(28)	65.5481 \pm 14.5013	43.6113 \pm 15.7970	(55)	40.18	50.30
5	33.5099 \pm 9.16038	36.2629 \pm 7.9248	(46)	36.3790 \pm 10.1633	31.8645 \pm 8.5258	(28)	8.21	14.17
6	32.6761 \pm 2.1323	45.2334 \pm 8.3686	(26)	48.2500 \pm 17.0370	48.9503 \pm 11.3665	(53)	38.43	-1.43
7	33.2406 \pm 8.8591	44.2626 \pm 7.9633	(36)	40.0089 \pm 8.6755	33.1932 \pm 8.1408	(43)	33.16	20.53

Table 5.3. RMS between SCG events in the HLV and LLV groups and the ensemble averaged HLV/LLV SCG event (Equation (5-6)). The values are shown as mean \pm SD. The number of SCG events in each group is shown in parenthesis. The last column shows the relative differences in percentage.

Subject #	RMS between LLV events and ...			RMS between HLV events and ...			Relative Difference (%)		
	Averaged LLV SCG	Averaged HLV SCG	<i>n</i>	Averaged LLV SCG	Averaged HLV SCG	<i>n</i>	$RD_{LV_{LLV}}$	$RD_{LV_{HLV}}$	
	$\overline{RMS}_{SCG_{LLV,LLV}} \pm SD$	$\overline{RMS}_{SCG_{LLV,HLV}} \pm SD$		$\overline{RMS}_{SCG_{HLV,LLV}} \pm SD$	$\overline{RMS}_{SCG_{HLV,HLV}} \pm SD$				
1	22.4070 \pm 5.6409	34.1765 \pm 9.4193	(53)	31.4550 \pm 5.4819	24.9368 \pm 6.8360	(58)	52.52	26.14	+
2	46.1731 \pm 11.3189	49.5236 \pm 14.7105	(46)	63.2857 \pm 11.2033	43.2033 \pm 13.2348	(42)	7.26	46.48	+
3	47.5796 \pm 12.7507	87.6964 \pm 13.8409	(32)	86.4990 \pm 18.5154	51.9888 \pm 20.0642	(39)	84.31	66.38	+
4	44.0150 \pm 11.3531	77.7045 \pm 21.2454	(44)	69.7121 \pm 9.4823	34.0905 \pm 12.6197	(37)	76.54	104.49	+
5	30.4948 \pm 8.1303	44.8703 \pm 7.6175	(44)	59.2533 \pm 10.8211	25.3256 \pm 7.1247	(31)	47.14	133.97	+
6	33.1170 \pm 10.1451	63.0525 \pm 13.6690	(51)	69.8478 \pm 18.9298	37.1869 \pm 10.4012	(31)	90.39	87.83	+
7	26.0518 \pm 6.7255	60.4353 \pm 13.9944	(40)	43.9254 \pm 8.3870	34.5265 \pm 7.9952	(36)	131.98	27.22	+

The “+” sign in the right column indicates that the dissimilarity results improved when lung volume was used instead of respiratory flow rate.

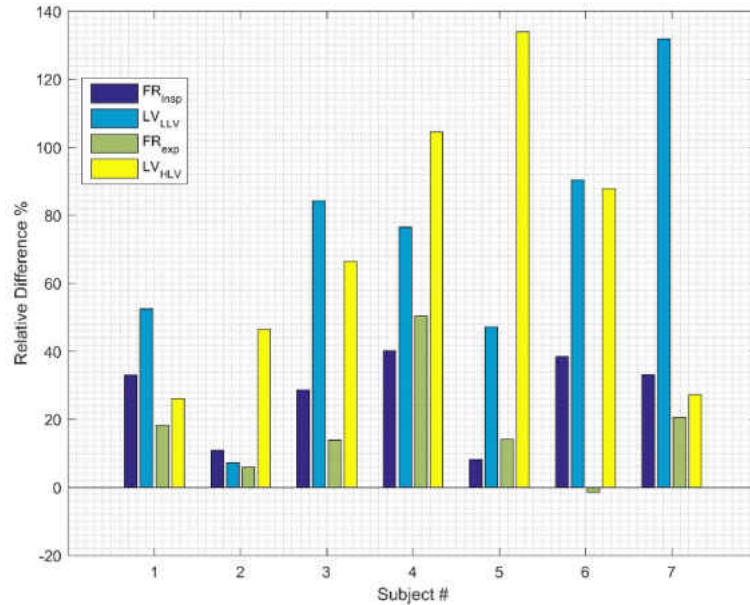


Figure 5.3. Relative differences calculated from Equations (5-7.a) and (5-7.b) for inspiratory, expiratory, LLV, and HLV SCG events.

5.1.3 Discussions

5.1.3.1 Intrathoracic Pressure and Heart Displacement

The chest wall expansion and downward movement of the diaphragm during inspiration causes a more negative intrathoracic pressure and a downward movement of the heart. The negative pressure increases the expansion of the right atrium, right ventricle and thoracic superior and inferior vena cava, which causes the intravascular and intra-cardiac pressures to fall. As a result, the transmural pressure (the difference between pressure inside the heart chamber and the intrathoracic pressure) increases. This causes a rise in cardiac chamber expansion, preload and stroke volume through the Frank-Starling mechanism. The opposite phenomena happens during expiration [197]. It can then be concluded that intrathoracic pressure variations due to respiration changes the heart chamber pressures, preload, stroke volume and stroke work [199]. These mechanical changes are expected to affect the heart muscle contractile movements and blood flow momentum which can manifest themselves as variations in SCG signal morphologies.

5.1.4 Conclusions

The results of this study showed that the SCG demonstrated morphological differences during respiration. SCG events were grouped according to their waveform morphology. Two grouping criteria were implemented. One grouping relied on inspiratory vs. expiratory flow while the other relied on LLV vs HLV (which corresponds to high and low intrathoracic pressure). The second criterion resulted in more similarity within the SCG groups, suggesting that intrathoracic pressure variations can lead to detectable SCG morphology changes. Studying the effect of respiration allows separating SCG into groups with similar events. This reduces SCG waveform variability and enables more precise estimation of SCG characteristics. In addition, because respiration triggers known changes in physiological parameters (such as intrathoracic pressure, stroke volume, etc.), it allows studying the effects of these parameters on SCG. Such investigations can help enhance our understanding of SCG genesis, and explain SCG changes with cardiac pathology. Future studies may perform comparisons between the spectral characteristics of two groups of SCG (e.g., LLV vs HLV) as this might reveal further useful SCG characteristics and may contribute to further elucidate SCG genesis. In addition, artificial intelligence methods such as neural networks or support vector machines might be used to classify the SCG events into two groups. An ongoing study [31] aims at developing classification algorithms for this purpose.

5.2 Heart Rate Monitoring

Heart rate is a common parameter for monitoring cardiovascular function and can identify some abnormalities such as arrhythmia. There are various HR estimation methods that are mostly based on ECG signal processing.

SCG is a technique that measures heart induced vibrations at the chest surface [88]. SCG signal is similar to the familiar phonocardiography, but is largely in the subsonic (below 20 Hz)

range. As such, SCG-based methods might provide information that are complementary to other cardiac monitoring methods such as electrocardiography and echocardiography [117,118,200,201]. SCG signals can also be used for HR estimation. For example, Cosoli *et al.* [50] suggested a general algorithm that can estimate HR from various signals, including SCG, ECG, PCG, and PPG. Considering the ECG signal as a gold standard in their study, the SCG HR estimation was more accurate than PCG and PPG. Wahlstrom *et al.* [51] used a HMM to determine different stages of a cardiac cycle which were then used for estimating beat-to-beat intervals. HR and HR variability can be estimated from beat-to-beat intervals of an SCG signal. Mafi [52] suggested an algorithm based on empirical mode decomposition and empirical wavelet transform that can extract HR from SCG signals. Tadi *et al.* [4] used a Hilbert adaptive beat identification technique to determine the heartbeat timings and inter-beat time intervals from SCG signals. An android application was implemented based on this algorithm that can monitor the subjects' heart rate in real time using accelerometers [4]. Tadi *et al.* [53] proposed an algorithm based on S-transform, Shannon energy, and successive mean quantization transform to identify heartbeat and beat-to-beat interval from SCGs. The latter two algorithms had a high agreement with the ECG inter-beat interval values.

Previous studies reported that the SCG signals can have different morphology during high and low lung volume phases [29,31,87]. This section presents an algorithm for heart rate monitoring using seismocardiography during low and high lung volumes.

5.2.1 Methodology

5.2.1.1 Participants

The study protocol was approved by the Institutional Review Board of the University of Central Florida, Orlando, FL. A total of 7 young male subjects were included in our study. The

subjects gave their informed consent, and reported no history of cardiovascular disease. The age, height, and weight of the subjects are reported in Table 5.4.

Table 5.4. Overview of the subjects' characteristics (mean \pm SD).

Age (years)	29.4 \pm 4.5
Height (cm)	173.1 \pm 9.8
Weight (kg)	82.2 \pm 18.3
Number of subjects	7

5.2.1.2 Human Studies

For consistency in breathing pattern and TV, the subjects were first trained to control their inspiratory:expiratory (I:E) ratio and respiratory rate utilizing a volume controlled ventilator (Model: 613, Harvard Apparatus, South Natick, MA). The I:E and respiratory rate were set to 1:3 and 12 breath per minute, respectively. For each subject, the TV was calculated in real time from the RFR signal. The TV was displayed to the subjects on a computer screen during the experiment and was kept at 10 to 15 mL/kg.

The subjects were asked to rest on a folding bed and the signals of interest were recorded in three different postural positions; 90 degree (sitting), 45 degree, and 0 degree (supine). The signals were recorded for 1.5 minute at 0 and 90 degrees, while they were acquired for a longer time period (2 trials of 5 minutes each) at 45 degree. The longer time was to check for signal drift over time.

5.2.1.3 Instrumentation

A triaxial accelerometer (Model: 356A32, PCB Piezotronics, Depew, NY) was used to record all SCG signals. A signal conditioner (Model: 482C, PCB Piezotronics, Depew, NY) was then used to amplify the accelerometer output with a gain factor of 100. The sensor was affixed to the left sternal border at the level of the 4th intercostal space using a double-sided medical-grade tape. This location was chosen due to its high signal-to-noise ratio [22,167]. The accelerometer's z-axis was aligned perpendicular to the subject chest surface, while the x- and y-axes were aligned

parallel to the axial and mediolateral directions, respectively. The RFR of the subjects was measured using a pre-calibrated spirometer (Model: A-FH-300, iWorx Systems, Inc., Dover, NH). The inspiration and expiration produced positive and negative flow rate signal amplitudes, respectively. The voltage for RFR, ECG, and SCG signals were acquired simultaneously using a Control Module (Model: IX-TA-220, iWorx Systems, Inc., Dover, NH). The LV was calculated as the integral of the RFR.

All the signals were acquired simultaneously at a sampling frequency of 10 kHz and down-sampled to 320 Hz. The SCG signals were then filtered using a low-pass filter with a cut-off of 100 Hz to remove the remaining respiratory sound noise, which have significant energy above this cut-off frequency [101]. Matlab (R2015b, The MathWorks, Inc., Natick, MA) was used to process all signals.

5.2.1.4 Heart Rate Monitoring

Previous studies [29,31] suggested that the LV can affect the SCG signal morphology. In this study, after SCG signal segmentation, the LV signal was used to group the SCG cycles into two groups of high and low lung volume (HLV and LLV, respectively). Figure 5.4 shows a 10-seconds portion of a SCG signal lined up with the LV. The LLV and HLV parts of the lung volume were labeled in the figure. The SCG events that occurred during low and high lung volumes were subsequently called LLV and HLV SCG events, respectively. These events were then used to measure the heart rate during LLV and HLV (HR_{LLV} and HR_{HLV} , respectively). The HR was estimated using any two consecutive HLV or LLV SCG events as follows

$$HR_j = 1 / (t_{SCG_{j+1}} - t_{SCG_j}) \quad (5-8)$$

where j is the index of SCG events in the LLV or HLV group. t_{SCG_j} and HR_j are the time of the j^{th} SCG event peak and the estimated heart rate from the j^{th} and $j+1^{\text{th}}$ SCG events. Equation 6-8

resulted in an inaccurate HR estimation when the two consecutive events were in two different LLV (or HLV) cycles such as the two LLV events encircled in Figure 5.4. Although these LLV events are consecutive, they occur at the beginning and end of two different low lung volume cycles. Therefore, the time distance between them was not representative of a cardiac cycle duration. This longer time distance would result in a HR estimation that was lower than the actual HR. Hence to avoid this, a HR minimum threshold of 50 bpm was chosen. All the estimated HR values that were lower than this threshold were eliminated. Algorithm 5.1 shows a pseudo-code for the proposed heart rate monitoring algorithm.

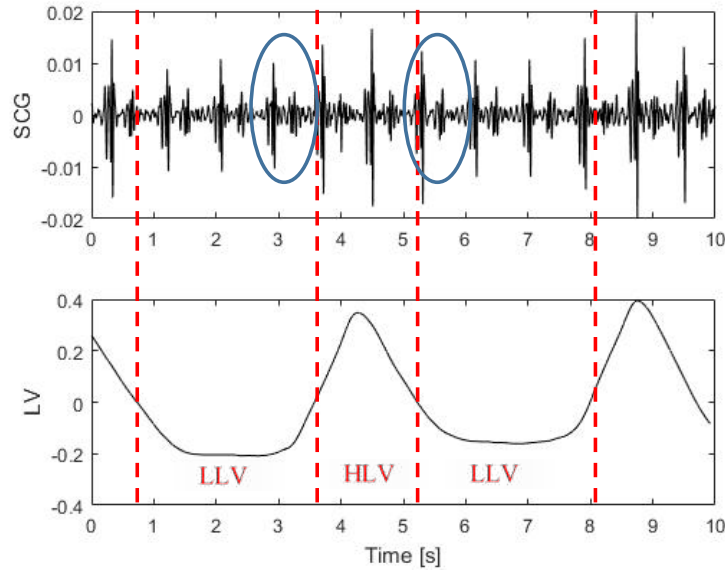


Figure 5.4. (top) A 10-seconds portion of the SCG signal [Volts], (bottom) The lung volume signal [Volts] calculated from the integral of respiratory flow rate that was measured simultaneously with the SCG signal. The LLV and HLV portions of the lung volume signal are labeled.

The subject combined HR was also estimated from the HR_{LLV} and HR_{HLV} as follows

$$HR = \left(\sum_{i=1}^m HR_{LLV_i} + \sum_{j=1}^n HR_{HLV_j} \right) / (m + n) \quad (5-9)$$

where m and n are the total number of LLV and HLV events, respectively. The ECG signal was used as a gold standard in this study. The performance of the proposed SCG HR monitoring

algorithm was tested against the standard ECG measurements. Figure 5.5 shows the study flowchart.

Algorithm 5.1 Calculate heart rate during HLV and LLV

```

1: Input: SCG events, i (number of SCG events), respiratory flow rate signal, t (time vector)
2: Output: HRLLV, HRHLV
3: LV = integral of respiratory flow rate
4: for all i values do
5:     if LV > 0 then
6:         SCGHLV[j] ← SCG[i]
7:         for all SCGHLV events do
8:             HR[j] ← 1 / ( t(SCGHLV[j + 1]) - t(SCGHLV[j]) )
9:             if HR[j] < 50 then
10:                ignore HR[j]
11:            else
12:                HRHLV[j] ← HR[j]
13:            end if
14:        end for
15:    else if LV < 0 then
16:        SCGLLV[k] ← SCG[i]
17:        for all SCGLLV events do
18:            HR[k] ← 1 / ( t(SCGLLV[k + 1]) - t(SCGLLV[k]) )
19:            if HR[k] < 50 then
20:                ignore HR[k]
21:            else
22:                HRLLV[k] ← HR[k]
23:            end if
24:        end for
25:    end if
26: end for

```

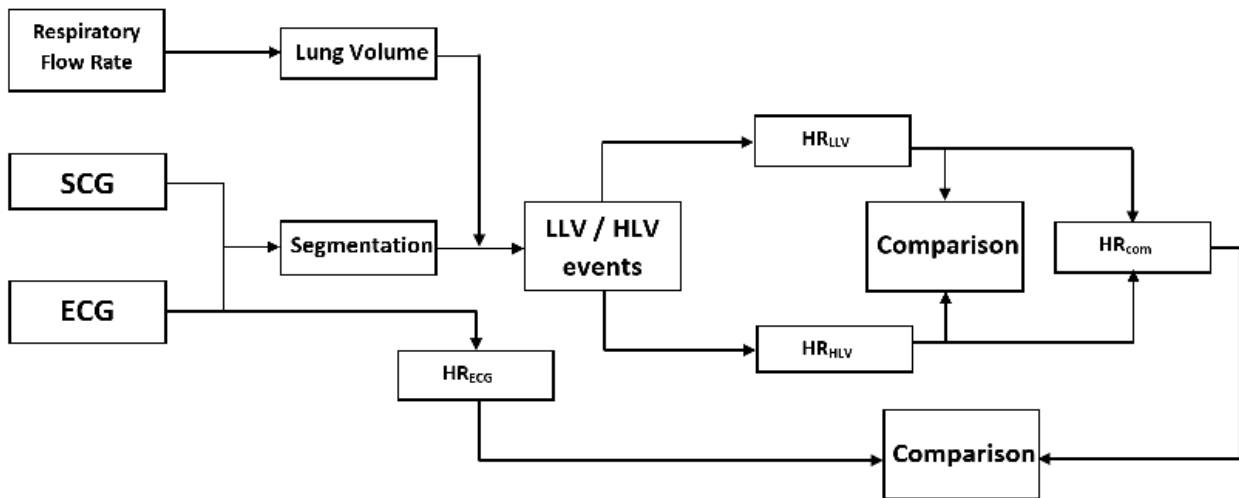


Figure 5.5. Flowchart of the heart rate monitoring study.

5.2.2 Results

Table 5.5 shows the estimated heart rate using HLV and LLV SCG events during high and low lung volumes in the 3 different postural positions considered in this study. Results showed that all subjects had a higher HR during HLV compared to LLV in all postural positions. The combined HR estimations were listed in Table 5.6. Figure 5.6 compared the estimated LLV, HLV and combined HR at different postural positions for all the subjects.

5.2.3 Discussions

5.2.3.1 Heart Rate Monitoring Algorithm Performance

Agreement between the ECG and SCG HR estimations was assessed using Bland-Altman analysis (Figure 5.7). In this plot, the solid line represents the mean value of differences between ECG and SCG HR estimations, while the dashed lines show the 95% confidence interval (mean \pm 1.96 SD). These results suggest general agreement between the proposed algorithm and the standard ECG method.

Table 5.5. Estimated heart rate (beat per minute) using HLV and LLV SCG events during high and low lung volume in 3 different postural positions. The values are shown as mean \pm SD.

Subject #	Supine		45 degree - 1		45 degree - 2		Sitting	
	LLV	HLV	LLV	HLV	LLV	HLV	LLV	HLV
1	55.9 \pm 2.9	69.0 \pm 1.8	63.3 \pm 3.4	72.2 \pm 6.2	63.0 \pm 4.0	70.7 \pm 4.2	70.7 \pm 3.7	74.4 \pm 1.2
2	65.9 \pm 0.9	66.6 \pm 1.0	65.3 \pm 3.1	66.1 \pm 3.8	61.2 \pm 2.7	63.9 \pm 1.9	63.6 \pm 1.5	66.0 \pm 2.2
3	75.2 \pm 1.8	80.3 \pm 1.6	74.5 \pm 4.0	78.7 \pm 4.2	71.8 \pm 4.5	75.9 \pm 4.2	71.5 \pm 2.2	81.3 \pm 3.1
4	65.2 \pm 3.3	76.4 \pm 3.3	60.4 \pm 4.4	70.0 \pm 5.0	59.4 \pm 4.4	68.5 \pm 5.0	66.9 \pm 4.1	75.5 \pm 3.3
5	76.9 \pm 5.9	82.4 \pm 6.6	73.0 \pm 3.9	77.4 \pm 3.7	67.7 \pm 3.6	73.5 \pm 3.8	66.6 \pm 2.2	72.6 \pm 2.0
6	74.8 \pm 4.8	83.2 \pm 4.2	73.6 \pm 4.3	78.2 \pm 4.2	70.7 \pm 6.1	75.2 \pm 5.5	68.1 \pm 3.7	73.4 \pm 3.5
7	71.9 \pm 2.4	78.3 \pm 2.0	70.7 \pm 4.1	78.3 \pm 4.5	72.0 \pm 4.2	79.2 \pm 4.2	72.7 \pm 4.7	80.8 \pm 5.8

Table 5.6. The estimated combined heart rate (beat per minute) using Equation (5-9).

Subject #	Supine	45 degree Trial 1	45 degree Trial 2	Sitting
1	62.2	67.9	66.3	72.1
2	66.2	65.6	62.1	64.3
3	77.2	76.1	73.1	75.3
4	69.4	64.0	63.8	70.6
5	79.1	75.2	70.7	69.6
6	78.6	75.9	73.1	70.9
7	74.7	73.3	75.0	75.3

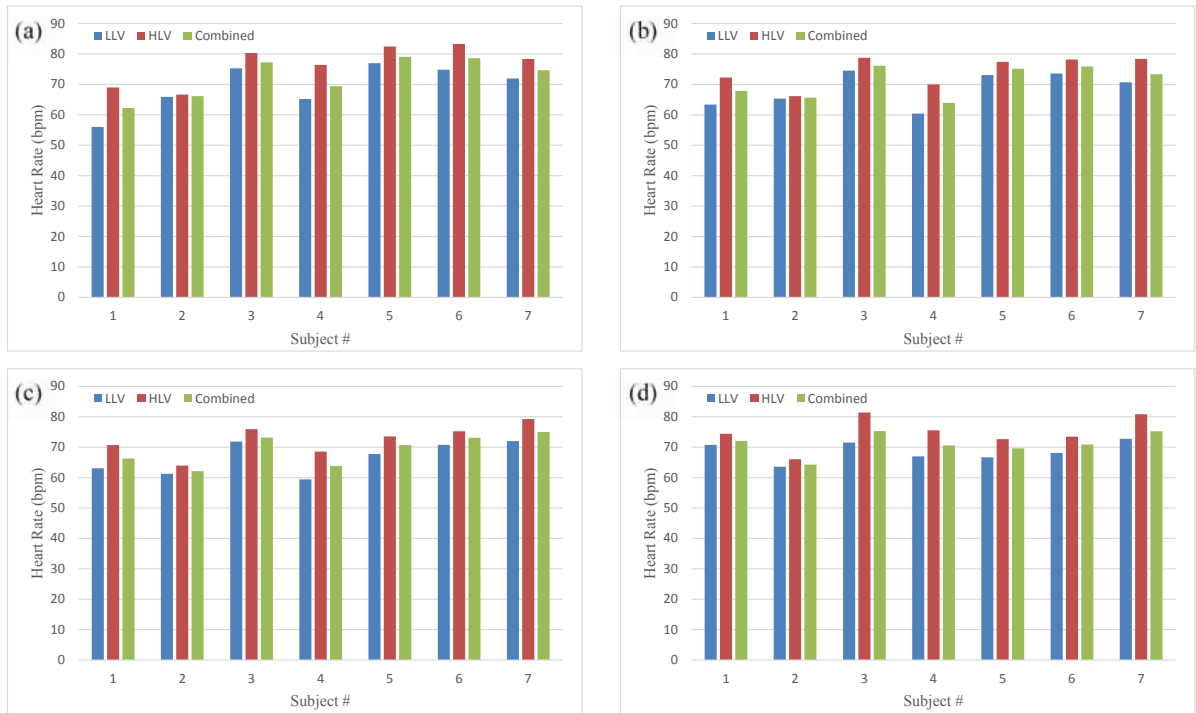


Figure 5.6. The estimated LLV, HLV, and combined heart rate in (a) supine position, (b) 45-degree position first trial, (c) 45-degree position second trial, and (d) sitting position.

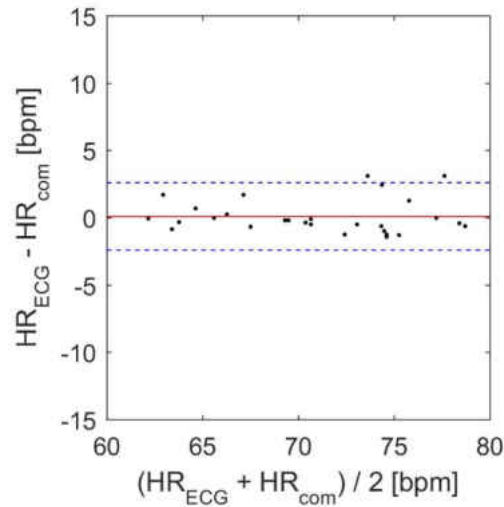


Figure 5.7. Bland-Altman plot for HR_{ECG} and HR_{com} . The solid line represents the mean (bias) difference between the HR values. The dashed lines show the 95% confidence interval.

5.2.3.2 Heart Rate Variability

Table 5.7 shows the ratio between estimated HR during HLV and LLV (HR_{HLV}/HR_{LLV}) for all the subjects. For all the subjects and all the postural position, the ratio was larger than 1

indicating that subjects had a higher HR during HLV compared to LLV. The HR_{HLV}/HR_{LLV} ratio was 1.11 ± 0.07 , 1.08 ± 0.05 , 1.09 ± 0.04 , and 1.09 ± 0.04 for supine, 45 degree-first trial, 45 degree-second trial, and sitting positions, respectively. This can be due to the known physiological phenomenon of Respiratory Sinus Arrhythmia (RSA) [202]. RSA is an independent reflex, the exact explanation of which is not completely known. Although RSA was once explained as a secondary response of other known reflexes, the current understanding is that RSA is a separate physiological reflex [203]. A plausible justification for the evolution of RSA is related to ventilation-perfusion matching in the lungs. At high volume, the lungs are full of air (high ventilation) and an increase in heart rate will increase the amount of blood flow to the lungs (high perfusion). The opposite response is observed at low lung volume. A more well-known example of ventilation-perfusion matching is hypoxic pulmonary vasoconstriction, a reflex where blood vessels in the lungs constrict in response to low oxygen levels. This reflex reduces perfusion to areas of the lungs that have low ventilation, such as an area filled with fluid from pneumonia. The benefit of ventilation-perfusion matching is to ensure that all blood leaving the lungs has high O_2 saturation.

Table 5.7. The ratio between estimated heart rate during high and low lung volume HR_{HLV}/HR_{LLV} .

Subject #	Supine	45 degree - 1	45 degree - 2	Sitting
1	1.232449	1.140859	1.121364	1.051743
2	1.011316	1.011928	1.044089	1.038266
3	1.066846	1.05692	1.056712	1.13778
4	1.171733	1.158869	1.15357	1.128024
5	1.071803	1.059745	1.085252	1.089598
6	1.112487	1.062655	1.063825	1.078311
7	1.088873	1.108319	1.101045	1.111293

5.2.3.3 Application in Cardiovascular Diagnosis

CTIs have been widely used as clinical metrics for cardiovascular diagnosis. Results of the current study showed that the HR varies between different phases of the LV. This indicates that the cardiac cycles duration changes with the LV, which can lead to varying CTIs for different

phases of the LV. Therefore, categorizing SCG cycles into two groups of LLV and HLV that contain SCG cycles with similar morphology can allow more accurate estimation of CTIs, and better signal characterization, and classification.

5.2.4 Conclusions

In this section, an ECG-independent algorithm for heart rate monitoring was proposed. This algorithm was used to estimate the heart rate of a control group during different phases of the LV. The proposed algorithm performance was tested against the standard ECG measurements. Results showed good agreement between the proposed and standard method. In addition, the new method was able to detect HR changes with respiration.

5.3 Efficient Grouping of SCG Events

In section 5.1, SCG events were grouped using RFR and LV signals. Results showed that LV might group SCG events into two groups where the events in each group are more similar to each other. In this section we try to find an efficient method to group similar SCG events. Categorizing SCG events into different groups containing similar events allows more accurate estimation of SCG features, and better signal characterization, and classification.

5.3.1 Methodology

5.3.1.1 Participants

The study protocol was approved by the institutional review board of the University of Central Florida, Orlando, FL. The subjects gave their informed consent to the study. A total of 10 young individuals with no history of cardiovascular disease were included in our study. Age, height, weight, and body mass index (BMI) of the subjects were obtained and reported in Table 5.8.

Table 5.8. Overview of the subjects' characteristics (mean \pm SD).

Age (years)	27.5 \pm 5.4
Height (cm)	173.6 \pm 8.9
Weight (kg)	81.3 \pm 15.4
BMI (kg/m ²)	26.9 \pm 4.0
Number of subjects	10

5.3.1.2 Instrumentation

All participants were instructed how to perform the experiments as it will be discussed in the next section. The SCG signal was measured using a triaxial accelerometer (Model: 356A32, PCB Piezotronics, Depew, NY). The accelerometer output was amplified using a signal conditioner (Model: 482C, PCB Piezotronics, Depew, NY) with a gain factor of 100. The sensor was placed at the left sternal border along the 4th intercostal space using a double-sided paper tape since this location tended to have a high signal-to-noise ratio [88]. The accelerometer's x- and y-axes were aligned parallel to the anteroposterior and mediolateral directions, respectively, while the z-axis was aligned perpendicular to the subject chest. The RFR of the subjects was measured using a pre-calibrated spirometer (Model: A-FH-300, iWorx Systems, Inc., Dover, NH). The flow rate signal had positive and negative amplitude during the inspiration and expiration, respectively. The voltage signal for both RFR and SCG signals were acquired using a Control Module (Model: IX-TA-220, iWorx Systems, Inc., Dover, NH). The LV was calculated as the integral of the RFR.

5.3.1.3 Experiments

5.3.1.3.1 Normal Breathing

The primary goal of this study was to investigate the effects of breathing and its physiological consequences on SCG signals. For consistency in breathing pattern, the subjects were first trained how to breath. For this purpose, a volume controlled ventilator (Model: 613, Harvard Apparatus, South Natick, MA) was used to instruct subjects to breath with the same inspiratory:expiratory (I:E) ratio and respiratory rate. The I:E and respiratory rate were set to 35% and 12 breath per

minute, respectively. For each subject, the TV was calculated in real time from the LV signal. The TV was displayed to the subjects during the experiment and they were asked to keep it within 10 to 15 mL/kg.

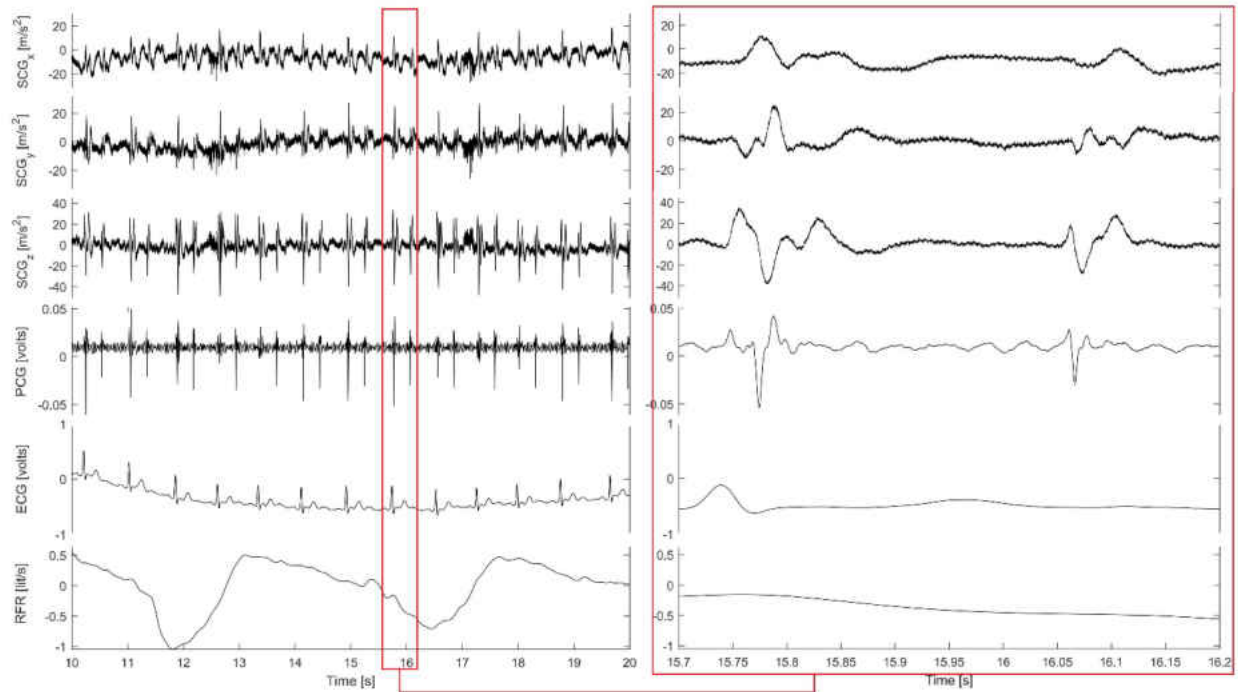


Figure 5.8. Simultaneously acquired three-axis seismocardiogram, phonocardiogram, electrocardiogram, respiration flow rate (RFR) signals from one subject.

The subjects were asked to lay down on a folding bed and the signals of interest were recorded in three different postural positions; 90 degree (sitting), 45 degree, and 0 degree (supine). The signals were recorded for 1.5 minute at 0 and 90 degrees, while they were acquired for a longer time period (2 trials of 5 minutes) at 45 degree since this position has been chosen to be used for the rest of the experiment. Figure 5.9.a shows the block diagram for this experiment.

5.3.1.3.2 Pressure and Heart Displacement Effects

In the 45 degree position, the SCG, PCG, and ECG signals were recorded at end-inspiration and end-expiration phases while the subjects have been asked to apply three different pressure including -20, 0, and 20 cm H₂O to their chest. The pressures were measured using a manometer

(Dwyer Instruments, Inc., Michigan City, IN). The signals were recorded for 3×20 seconds at each condition. Figure 5.9.b shows the block diagram for this experiment.

The hypothesis for this experiment was that SCG events occurring during different respiration phases are morphologically different because:

1. Heart moves upward and downward during a respiration cycle. When the subject inhales, diaphragm moves downward, resulting in a downward displacement of heart, and vice versa.
2. The pressure inside lung changes during a respiration cycle which affects the intrathoracic pressure and pressure around heart.

The main goal of this experiment was to control the effect of heart displacement and pressure around heart on the SCG signals morphology.

5.3.1.4 Signal Pre-processing

All the signals were measured simultaneously at a sampling frequency of 10 kHz and down-sampled to 320 Hz. However, for the machine learning part of the study, the SCG events were mean padded to a length of 8096. This was to ensure that the lengths of all signals were equal and of a power of 2, for convenience. The SCG signals were then filtered using a low-pass filter with a cut-off of 100 Hz to remove the respiratory noise, which have significant energy above this cut-off frequency [101]. The SCG events in each signal were found using a matched filtering with a template consisting of a previously identified SCG. The SCG events were then grouped into two groups where SCG events in each group were more similar to each other. This is explained in detail in section 5.3.1.5. Matlab (R2015b, The MathWorks, Inc., Natick, MA) was used to process all signals.

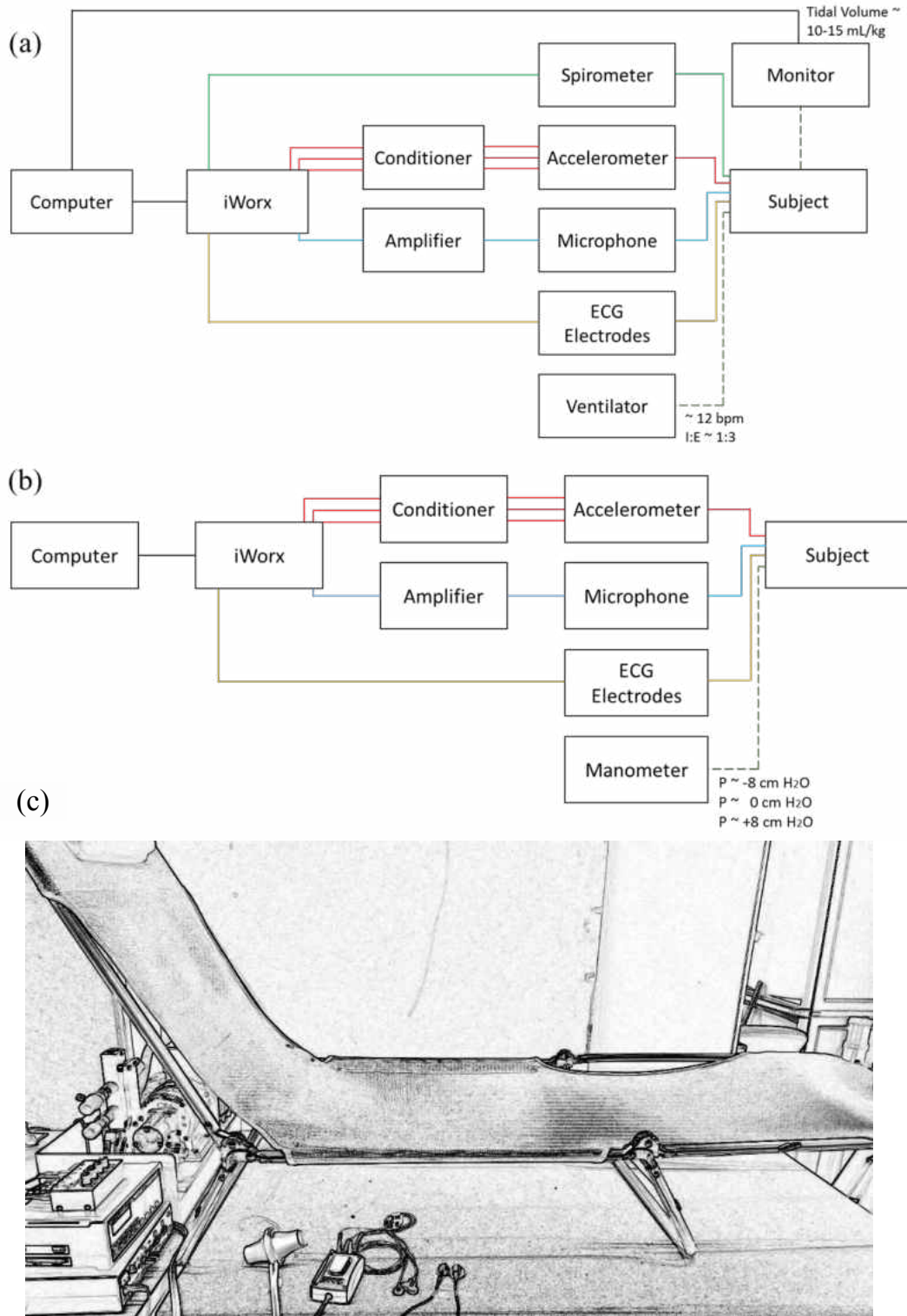


Figure 5.9. Block diagram for (a) normal breathing, and (b) pressure and heart displacement effects experiments. Dashed line (– –): feedback to the subject to monitor or adjust specific parameters such as tidal volume and number of breath per minute. Solid line (—): acquired signals sent to the computer (or monitor). (c) Experimental setup.

5.3.1.5 Grouping Criteria

The SCG events were categorized into two groups using 3 different criteria. The RFR was first used to categorize the SCG events as inspiratory and expiratory events (first criterion). The SCG events were then grouped into two groups of HLV and LLV using the LV signal (second criterion). At this stage a dissimilarity analysis similar to the one described in 5.1.1.4 was performed. The HLV and LLV SCG events that were more similar to the alternate ensemble average were moved automatically between the groups (third grouping, hybrid criterion). The process of automatic moving SCG events between HLV and LLV clusters was called the “cleaning process”. Algorithm 5.2 describes the cleaning process.

Algorithm 5.2 Cleaning process

```

1: Input: HLV SCG events ( $SCG_{HLV}$ ), LLV SCG events ( $SCG_{LLV}$ )
2: Output: HLV and LLV SCG events that should move to the alternate group
3:  $SCG_{HLV,avg} = \text{mean}(SCG_{HLV})$ 
4:  $SCG_{LLV,avg} = \text{mean}(SCG_{LLV})$ 
5: for all  $SCG_{HLV}$  events do
6:      $D_{HLV,HLV}[j] = \text{Dissimilarity}(SCG_{HLV}[j], SCG_{HLV,avg})$ 
7:      $D_{HLV,LLV}[j] = \text{Dissimilarity}(SCG_{HLV}[j], SCG_{LLV,avg})$ 
8: end for
9:  $D_{HLV,rms} = \text{rms}(D_{HLV,HLV})$ 
10: for all  $SCG_{HLV}$  events do
11:     if  $D_{HLV,HLV}[j] > D_{HLV,LLV}[j]$  then
12:          $SCG_{HLV,backward}[jj] \leftarrow SCG_{HLV}[j]$ 
13:         if  $D_{HLV,HLV}[j] - D_{HLV,LLV}[j] > 0.5 D_{HLV,rms}$  then
14:              $SCG_{HLV,backward,high}[jjj] \leftarrow SCG_{HLV}[j]$ 
15:         end if
16:     end if
17: end for
18: for all  $SCG_{LLV}$  events do
19:      $D_{LLV,LLV}[k] = \text{Dissimilarity}(SCG_{LLV}[k], SCG_{LLV,avg})$ 
20:      $D_{LLV,HLV}[k] = \text{Dissimilarity}(SCG_{LLV}[k], SCG_{HLV,avg})$ 
21: end for
22:  $D_{LLV,rms} = \text{rms}(D_{LLV,LLV})$ 
23: for all  $SCG_{LLV}$  events do
24:     if  $D_{LLV,LLV}[k] > D_{LLV,HLV}[k]$  then
25:          $SCG_{LLV,backward}[kk] \leftarrow SCG_{LLV}[k]$ 
26:         if  $D_{LLV,LLV}[k] - D_{LLV,HLV}[k] > 0.5 D_{LLV,rms}$  then
27:              $SCG_{LLV,backward,high}[kkk] \leftarrow SCG_{LLV}[k]$ 
28:         end if
29:     end if
30: end for
31: for all  $jjj$  values do
32:     move  $SCG_{HLV,backward,high}[jjj]$  from  $SCG_{HLV}$  to  $SCG_{LLV}$  and update  $SCG_{LLV}$  group
33: end for
34: for all  $kkk$  values do
35:     move  $SCG_{LLV,backward,high}[kkk]$  from  $SCG_{LLV}$  to  $SCG_{HLV}$  and update  $SCG_{HLV}$  group
36: end for

```

5.3.1.6 Heart Rate Estimation

Subjects heart rate was estimated using SCG and ECG signals. The Pan-Tompkins algorithm was used for the HR estimation using ECG as a gold standard. The SCG HR estimation was calculated based on the algorithm explained in 5.2.1.4 SCG signal was also used to calculate HR during HLV and LLV phases.

5.3.1.7 Cardiac Time Intervals

6 CTIs were defined as follows and were calculated for the HLV and LLV SCG events. First, the QRS and T waves were identified on the ECG events. Then, the dominant peak as well as the minimums before and after it were identified for the corresponding SCG event. These minimums were called Min1 and Min2, respectively. The CTIs were then calculated as:

- CTI1 and CTI2: The time period between {SCG dominant peak and ECG-R} and {SCG dominant peak and ECG-T}, respectively.
- CTI3 and CTI4: The time period between {SCG Min1 and ECG-R} and {SCG Min1 and ECG-T}, respectively.
- CTI5 and CTI6: The time period between {SCG Min2 and ECG-R} and {SCG Min2 and ECG-T}, respectively.

Figure 5.10 shows an ECG event simultaneously recorded with an SCG event. ECG QRS and T waves as well as SCG peak, Min1, and Min2 are labeled in this figure.

5.3.1.8 Feature Extraction

For the feature extraction and classification, only the SCG signals recorded in 45 degree position were used. After signal segmentation, SCG events were categorized into inspiratory/expiratory or HLV/LLV groups as explained earlier. Temporal and spectral features of

these events were extracted using the methods described in this section. These features were then used as the inputs of the machine learning algorithms. Table lists the number of SCG events that was used for feature extraction and classification.

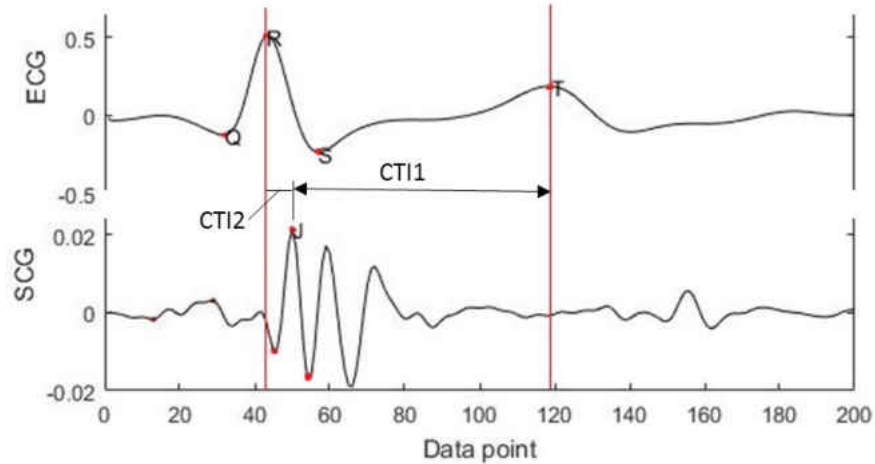


Figure 5.10. Cardiac time intervals definition. (top) ECG signal simultaneously recorded with (bottom) SCG signal. QRS and T waves are labeled on the ECG signal. The dominant peak of the SCG signal as well as the minimums before and after it are shown on the SCG signal. The cardiac time intervals, CTI1 and CTI2, are shown. CTI3 through CTI6 can be similarly calculated.

Table 5.9. Number of SCG events used for feature extraction and classification obtained from each subject. In this study, only the SCG signals recorded in 45 degree position were considered.

Subject #	No. of HLV events	No. of LLV events	Total
1	174	371	545
2	253	344	597
3	211	281	492
4	244	399	643
5	300	391	691
6	328	311	639
7	297	293	590
8	302	265	567
9	265	401	666
10	200	330	530
Total	2574	3386	5960

5.3.1.8.1 Time Domain

To extract the time domain features, an algorithm similar to the one described in 4.3 was used. This method divided the signal into bins such that binning of the signal was performed discriminately, where areas of the signal corresponding to higher variation received a higher number of bins. The algorithm used in this section has a minor difference compared to the one

described in Algorithm 4.1. The current adaptive feature extraction algorithm divides the bin corresponding the highest standard deviation in a recursive fashion, until some criteria is met, such as reaching the desired number of bins. The adaptive-width bins led to a higher classification accuracy than the equal-width bins. In CHAPTER 4, it was shown that the use of adaptive feature extraction resulted in similar accuracy when using 16 bins up to 1024. When using regular sized bins, the accuracy converged to the same accuracy only after 1024 bins. Using the adaptive width bins allows us to extract most of the performance gained from increasing the number of bins with only 16 bins. Because of this and considering that the number of features should not exceed the sample size, the feature extraction method employing the adaptive-width bins will be used to obtain the statistical time-domain features.

The statistical time-domain features used in this thesis were obtained by dividing the signal into 32 bins adaptively, then calculating statistical features from each bin. This study will calculate the mean, median, and standard deviation. The efficacy of each statistical feature will be assessed.

5.3.1.8.2 Frequency Domain

The frequency features were extracted in the following fashion in the current study. The FFT of each SCG event was calculated. The FFT was then divided into frequency bands. Since SCG mainly contains frequencies lower than 70 Hz (See section 3.3.5.7), the frequency range of 0 to 63 Hz was divided into 16 frequency bands, each with a frequency resolution of 4 Hz (0-3, ..., 60-63 Hz). The median and average power of each frequency band was calculated as the frequency features of the SCG events. The average power is obtained by squaring the magnitudes of the amplitudes to obtain the power spectrum, and then calculating the average. The first 32 frequency coefficients (amplitudes of the FFT spectrum), corresponding to 0-32 Hz, were used as other frequency features.

All the time and frequency features were scaled, as follows, to make sure that they fall in a similar range.

$$x_{scaled} = \frac{x - \bar{x}}{\sigma} \quad (5-10)$$

5.3.1.8.3 Feature Evaluation

An evaluation was performed to determine which features result in the highest classification accuracy. For this purpose, an SVM classifier was used to classify the z component of SCG signals into two clusters for each grouping criterion since it was more consistent than both the RF and NN. To generalize the results, data from all subjects was considered, i.e. the SVM was trained and tested on a dataset containing all the subjects' SCG events. A random split of 50% of the data was used for training, where the other half of the data was used for testing. This process was repeated 10 times. The evaluation metric was the average classification accuracy across 10 iterations. The default SVM hyperparameter settings for the Sci-Kit learn library ($C = 1.0$, $\text{gamma} = 1/n$, where n is the number of features) were used for feature evaluation.

5.3.1.9 Machine Learning

5.3.1.9.1 Supervised Approaches

Three different supervised classifiers, including support vector machines, neural networks, and random forest, were employed to classify the SCG events into different binary groups described in section 5.3.1.5. One of the goals of machine learning might be to maximize the performance for a predictive task. However, assessing the performance of the classifier model is not always as simple as evaluating the classification accuracy on the training set. For example, the model may be subject to overfitting which might result in a poor classification performance on a new set of data. To mitigate this issue, the data can be split into three sets, i.e., a training set, a

validation set, and a test set [204]. The model is trained on the training set, the hyperparameters are chosen to obtain the highest accuracy on the validation set, and the model is assessed on the test set. The test set evaluates the ability of the model to predict new data, while the validation set helps us not choose the hyperparameters in such a way that the model is optimized for the training data only. However, dividing the data into three sets might lessen the amount of data available for training. k -fold cross-validation is a technique that might be used to answer to this concern. k -fold cross-validation [205] first divides the training set into k equal-sized folds. It then trains the model on $k - 1$ folds, and tests it on the remaining 1 fold. This process repeats k times. The performance measure is the average classification accuracy of the k iterations of the k -fold cross-validation technique. Therefore, k -fold cross-validation allows us to divide the data into only a training set and test set. Here, the hyperparameters are chosen to maximize the average accuracy of the k -fold cross-validation. The suggested value for k in literature is generally 5 or 10.

For this study, a 10-fold cross-validation was used for model selection. Two different evaluation scenarios were employed, subject-specific (SS) and leave-one-subject-out (LOSO). In the SS scenario the model's performance was assessed when the model was trained and tested on a specific subject while LOSO assessed the model's performance when it was tested with a new subject's data. In this study, SS was performed by using 80% of the subject's data for training/validation, and 20% for testing. LOSO used 9/10 subjects' data to perform training/validation, and the remaining subject for testing.

Two metrics were used to evaluate the classification performance. These metrics include the F_1 score and final accuracy of the model. The final accuracy was obtained by averaging the 10 accuracies resulted from the k -fold cross-validation. These are described in more detail in section 4.3.2.5.

5.3.1.9.2 Unsupervised Approach

k -means clustering was also used to divide the SCG events into two clusters (i.e., $k = 2$). This method divided SCG events into two groups with similar SCG events in each group. After the SCG events were clustered into two clusters, the relations between those clusters and physiological phenomena such as respiratory flow direction and LV were investigated. For example, the output clusters of the k -means algorithm were compared with the HLV/LLV or inspiratory/expiratory SCG groups to determine how consistent the output cluster labels were with each grouping criterion (those criteria that were explained in section 5.3.1.5). This comparison was performed using two evaluation metrics, purity and adjusted rand index (ARI). Purity defines how accurate the clustering algorithm labeled the data, i.e.

$$Purity = accuracy(Cluster\ labels, Actual\ labels) \quad (5-11)$$

where $0 < Purity < 1$. Purity values close to 0 and 1 represent bad and perfect clustering, respectively.

The ARI is a metric that determines how well the clustering labels are in agreement with an external labeling criteria. For example, for the case of two known classes (U_1 and U_2) and two clusters (c_1 and c_2), ARI can be explained using the contingency table (Table 5.10). $n_{i,j}$ is the number of times that the given class appears in the corresponding cluster. a_i , b_j , and N are the sums across the columns, rows, and total size of the input data, respectively.

Table 5.10. Contingency table.

		Cluster		
		c_1	c_2	sum
Class	U_1	$n_{1,1}$	$n_{1,2}$	a_1
	U_2	$n_{2,1}$	$n_{2,2}$	a_2
	sum	b_1	b_2	N

The ARI can then be calculated as follows

$$ARI = \frac{Index - Expected Index}{Maximum Index - Expected Index} \quad (5-12)$$

where

$$Index = \sum_{i,j} \binom{n_{i,j}}{2} \quad (5-13)$$

$$Expected Index = \frac{\sum_i \binom{a_i}{2} \sum_j \binom{b_j}{2}}{\binom{N}{2}} \quad (5-14)$$

$$Maximum Index = \frac{\sum_i \binom{a_i}{2} + \sum_j \binom{b_j}{2}}{2} \quad (5-15)$$

ARI values close to 0 and 1 represent random and perfect clustering, respectively. The feature extraction and machine learning analysis were implemented with Python libraries Scikit-Learn [182] and SciPy/NumPy [183].

5.3.2 Results

As mentioned in section 5.3.1.3 subjects were instructed to breath with an I:E ratio of 35%. Figure 5.11 shows the inspiration/expiration phases of the respiration cycle as well as LLV/HLV of the LV for all the 10 subjects. The duration of the respiration and LV phases were calculated from the sign functions of the RFR and LV signals, respectively. For each subject, the 1st, 2nd, 3rd, and 4th columns corresponded to the sitting, 45 degree – 1, 45 degree – 2, and supine positions, respectively. Figure 5.11 shows that all the subjects, except subject #6, breathed with an I:E ratio similar to the one that they were asked for. However, subject #6 breathed with an I:E ratio larger than 50%. LV phases show that subjects spent more time in the LLV rather than HLV.

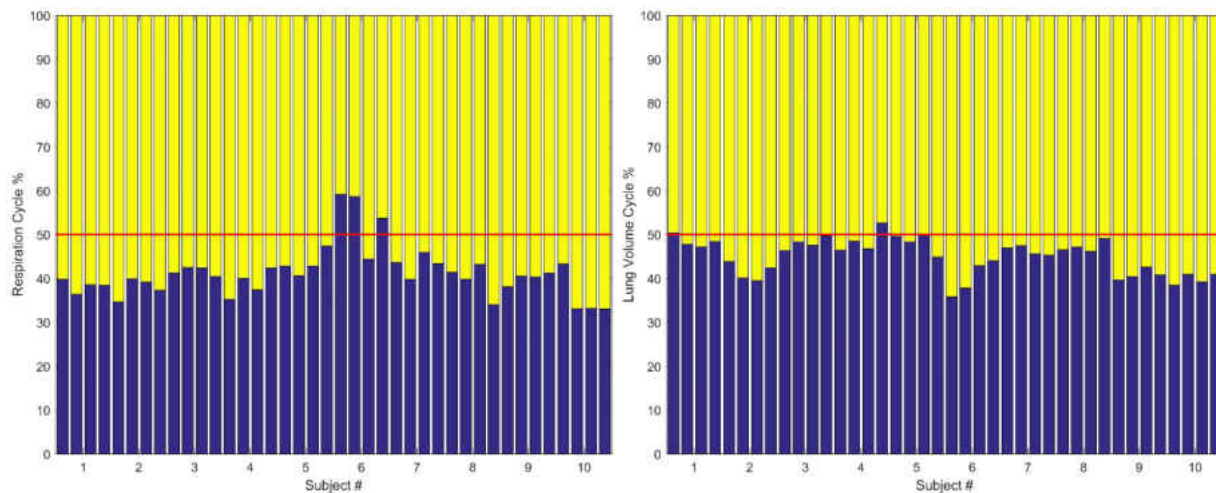


Figure 5.11. (a) Respiration cycle, Blue: inspiration, Yellow: expiration, (b) Lung volume cycle, Blue: HLV, Yellow: LLV.

5.3.2.1 Dissimilarity Analysis

Dissimilarity analysis was performed to quantify if the SCG events in each group are more similar to the ensemble average of their own group or the ensemble average of the alternate group. Based on the results of the dissimilarity analysis, the SCG events in each group might be updated resulting in two groups that contain more similar SCG events (hybrid criterion).

In Figure 5.12(a), HLV and LLV events were labeled (with black and red circles, respectively) on the LV signal for one of the subjects in supine position. Figure 5.12(b) presented dissimilarity analysis results. In this plot, a green solid line means that the SCG event was more similar to its own group ensemble average, while a blue solid line indicates that the SCG event was more similar to the average of the alternate group. The events that were more similar to the alternate average were called “backward events”. The length of each solid line is related to the difference between dissimilarity of the SCG event to its own group and the alternate group ensemble average. Therefore, as longer the green line is the SCG event is more similar to its own ensemble average. However, a longer blue line recommends that the SCG event might need to move to the alternate

group. Figure 5.12(c) shows the LLV and HLV backward events. Those backward events that satisfy the criteria described in line 13 and 26 of algorithm 5.2 (i.e. high-backward events) were plotted as circles with the alternate group color (i.e. high-backward LLV and HLV events were plotted in black and red, respectively). It is worth noting that:

$$SCG_{backward} \in \{total\ SCG\ events\} \quad (5-16)$$

$$SCG_{backward,high} \in \{SCG_{backward}\} \quad (5-17)$$

After the manual inspection of SCG events for different subjects, it seemed that some of the HLV/LLV SCG events tended to belong to the alternate group before the LV signal sign switches between positive and negative (i.e., at $LV = 0$ which is the current threshold for grouping SCG events into HLV and LLV groups). These groups of SCG events were labeled as “early switching” events. More careful inspection revealed that lots of “high-backward” events are “early switching” as well. To verify this assumption, the LLV and HLV groups were updated using 2 iterations of cleaning process. The number of early switching events in each group was then found and compared to the number of backward and total events in the corresponding group after each cleaning iteration. Early switching events were identified using Algorithm 5.3.

Algorithm 5.3 Early switching event finder

```

1: Input:  $LV, SCG_{HLV,backward,high}, SCG_{LLV,backward,high}$ 
2: Output: Early switching events
3:  $iSCG_{HLV,backward,high}$  = index of the  $SCG_{HLV,backward,high}$ 
4:  $iSCG_{LLV,backward,high}$  = index of the  $SCG_{LLV,backward,high}$ 
5: for all  $SCG_{HLV,backward,high}$  events do
6:     if slope ( $LV [iSCG_{HLV,backward,high}[jjj] - a : iSCG_{HLV,backward,high}[jjj] + a]$ )  $< 0$  then
7:          $SCG_{LLV,early-switching}[kkkk] \leftarrow SCG_{HLV,backward,high}[jjj]$ 
8:     end if
9: end for
10: for all  $SCG_{LLV,backward,high}$  events do
11:     if slope ( $LV [iSCG_{LLV,backward,high}[kkk] - a : iSCG_{LLV,backward,high}[kkk] + a]$ )  $> 0$  then
12:          $SCG_{HLV,early-switching}[jjjj] \leftarrow SCG_{LLV,backward,high}[kkk]$ 
13:     end if
14: end for

```

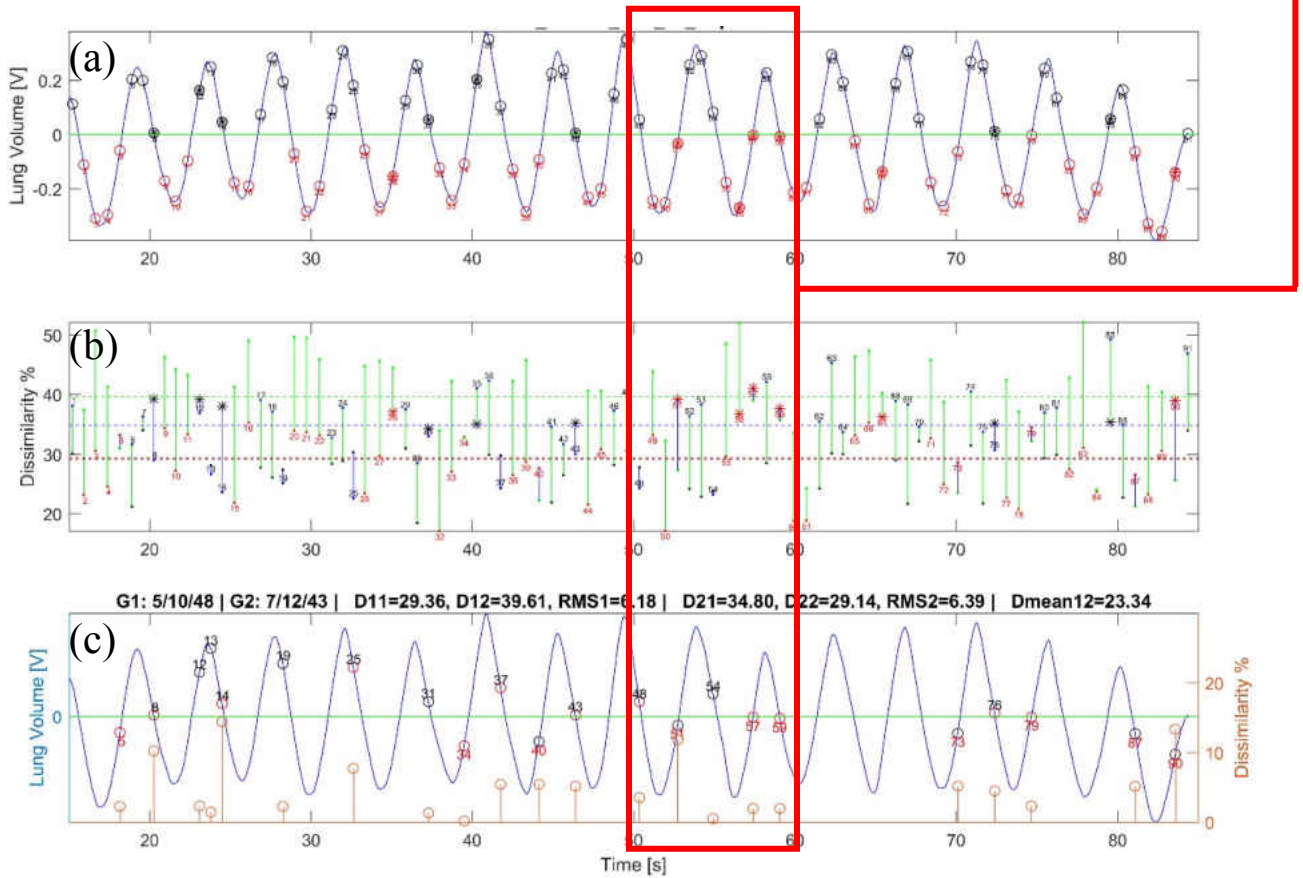
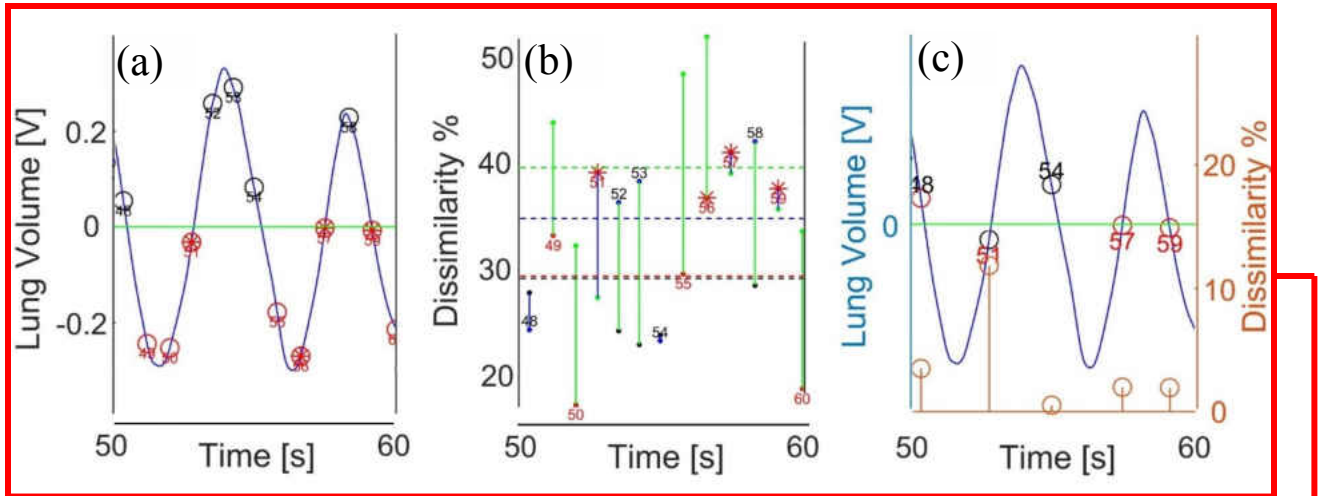


Figure 5.12. (a) LLV and HLV events were plotted as red and black circles on the LV signal, (b) dissimilarity analysis results. Green and blue solid lines mean that the SCG event was more similar to its own and alternate group ensemble average, respectively, (c) backward events were plotted on the LV signal. High-backward events were plotted with the alternate group color. For example, a high backward LLV event was plotted as a black circle.

It is also worth mentioning that:

$$SCG_{early-switching} \in \{SCG_{backward}\} \quad (5-18)$$

Figure 5.13 shows the dissimilarity analysis results after 1 and 2 cleaning process iterations. The number of LLV and HLV SCG events might be reported in $x/y/z$ format, where x , y , and z represent the number of high-backward, backward, and total SCG events. For example, for the trial shown in Figure 5.12 and Figure 5.13, the number of LLV and HLV events before cleaning were 5/10/48 and 7/12/43, respectively. After 1 cleaning iteration, 5 high-backward LLV events moved to the HLV group, while 7 high-backward HLV events moved to the LLV group to form the updated hybrid groups. Therefore, the number of events changed to 3/5/50 and 2/7/41, respectively. After the 2nd cleaning iteration these numbers were updated to 0/1/49 and 2/4/42, respectively.

The average dissimilarity of SCG events in each group to their own and alternate ensemble average was also calculated from Equation (5-6) before and after the cleaning iterations. The \overline{RMS} between LLV events and LLV group ensemble average decreased from 29.36 to 28.34 and 27.58 after 1 and 2 cleaning iterations, respectively. The dissimilarity (\overline{RMS}) of LLV events to the alternate ensemble average increased from 39.61 to 42.86 and 43.43 after 1 and 2 cleaning iterations, respectively. Similar trends were obtained for the HLV events. These results showed that the cleaning process helped clean dissimilar SCG events from LLV and HLV groups for this subject. Thus, the events in the hybrid groups were more similar to their own ensemble average rather than the alternate ensemble average. Data from rest of the study subjects were similar and summarized in Figure 5.14 and Figure 5.15.

Figure 5.14 shows the number of early switching events compared to the total number of events in each group. In this figure, the 1st, 2nd, 3rd, and 4th columns for each subject corresponded to the sitting, 45 degree – 1, 45 degree – 2, and supine positions, respectively.

Table 5.11. A summary of number of SCG events for different subjects at different postural positions. The numbers are in the following format $x/y/z$ where x , y , and z represent the number of high-backward, backward, and total SCG events. In the second column, b4, 1, and 2 represent before cleaning, after 1 cleaning iteration, and after 2 cleaning iterations, respectively.

subject #		Sitting		45 degree 1		45 degree 2		Supine	
		G1	G2	G1	G2	G1	G2	G1	G2
1	b4	0/ 1/ 39	3/ 6/ 35	3/ 4/145	55/64/146	6/ 7/134	46/55/120	2/ 2/ 32	7/ 8/ 37
	1	0/ 1/ 42	3/ 6/ 32	1/ 2/197	7/13/ 94	2/ 2/174	9/14/ 80	0/ 0/ 37	1/ 2/ 32
	2	1/ 2/ 45	2/ 6/ 29	0/ 1/203	1/ 5/ 88	0/ 0/181	0/ 7/ 73	0/ 0/ 38	0/ 1/ 31
2	b4	0/ 0/ 41	14/18/ 33	14/27/175	5/ 9/118	9/21/184	3/ 6/120	2/ 4/ 48	3/ 4/ 36
	1	0/ 0/ 55	5/ 5/ 19	6/21/166	2/ 5/127	4/14/178	0/ 5/126	1/ 2/ 49	2/ 2/ 35
	2	0/ 0/ 60	0/ 0/ 14	5/16/162	2/ 4/131	4/10/174	0/ 7/130	1/ 1/ 50	0/ 2/ 34
3	b4	1/ 7/ 45	3/ 6/ 36	1/ 1/125	29/52/110	10/26/131	7/42/126	0/ 1/ 38	1/ 1/ 33
	1	0/ 7/ 47	0/ 2/ 34	4/15/153	18/24/ 82	31/44/128	22/42/129	0/ 0/ 39	0/ 3/ 32
	2	0/ 7/ 47	0/ 2/ 34	12/20/167	4/ 7/ 68	14/20/119	17/23/138	0/ 0/ 39	0/ 3/ 32
4	b4	1/ 2/ 42	4/ 6/ 42	12/18/171	53/70/161	3/10/153	37/55/158	0/ 4/ 43	6/22/ 44
	1	0/ 1/ 45	2/ 3/ 39	4/ 6/212	23/31/120	2/12/187	21/33/124	1/ 6/ 49	4/21/ 38
	2	0/ 1/ 47	0/ 1/ 37	0/ 2/231	8/16/101	6/12/206	11/19/105	2/ 7/ 52	7/15/ 35
5	b4	5/ 5/ 43	5/ 6/ 44	8/23/175	21/42/177	22/36/166	59/77/173	5/10/ 48	7/12/ 43
	1	0/ 0/ 43	0/ 1/ 44	16/35/188	15/28/164	25/37/203	32/33/136	3/ 3/ 50	2/ 7/ 41
	2	0/ 0/ 43	0/ 1/ 44	28/39/187	22/44/165	15/19/210	2/ 2/129	0/ 1/ 49	2/ 4/ 42
6	b4	3/ 6/ 53	0/ 0/ 33	22/50/187	0/ 0/127	34/71/180	0/ 0/145	0/ 6/ 48	0/ 4/ 41
	1	0/ 3/ 50	0/ 0/ 36	19/38/165	0/ 0/149	21/42/146	0/ 0/179	0/ 6/ 48	0/ 4/ 41
	2	0/ 3/ 50	0/ 0/ 36	11/28/146	0/ 1/168	9/26/125	0/ 0/200	0/ 6/ 48	0/ 4/ 41
7	b4	1/ 1/ 44	1/ 1/ 35	12/18/150	0/ 0/126	10/14/164	1/ 1/150	0/ 0/ 48	0/ 0/ 41
	1	0/ 0/ 44	0/ 0/ 35	3/13/138	0/ 0/138	4/ 8/155	0/ 0/159	0/ 0/ 48	0/ 0/ 41
	2	0/ 0/ 44	0/ 0/ 35	3/ 9/135	0/ 0/141	0/ 6/151	0/ 0/163	0/ 0/ 48	0/ 0/ 41
8	b4	2/ 3/ 41	0/ 1/ 36	34/54/151	0/ 1/133	3/12/151	0/ 0/132	3/ 5/ 36	4/ 5/ 37
	1	1/ 1/ 39	0/ 1/ 38	31/36/117	3/ 6/167	0/13/148	0/ 0/135	0/ 2/ 37	1/ 5/ 36
	2	0/ 0/ 38	0/ 1/ 39	0/ 1/ 89	13/20/195	0/13/148	0/ 0/135	0/ 1/ 38	0/ 5/ 35
9	b4	4/ 7/ 60	0/ 0/ 38	4/27/194	20/37/133	8/30/194	5/24/145	1/ 7/ 55	0/ 1/ 46
	1	3/ 4/ 56	0/ 0/ 42	7/32/210	11/24/117	3/24/191	6/27/148	0/ 6/ 54	0/ 1/ 47
	2	0/ 2/ 53	0/ 0/ 45	9/33/214	10/18/113	4/24/194	8/24/145	0/ 6/ 54	0/ 1/ 47
10	b4	2/ 4/ 43	0/ 0/ 30	7/15/160	4/10/112	4/11/165	12/17/ 93	0/ 1/ 47	8/ 9/ 30
	1	0/ 3/ 41	0/ 0/ 32	1/ 9/157	3/ 9/115	0/ 6/173	4/ 7/ 85	0/ 0/ 55	2/ 3/ 22
	2	0/ 3/ 41	0/ 0/ 32	2/ 8/159	1/ 7/113	0/ 6/177	1/ 3/ 81	0/ 0/ 57	1/ 3/ 20

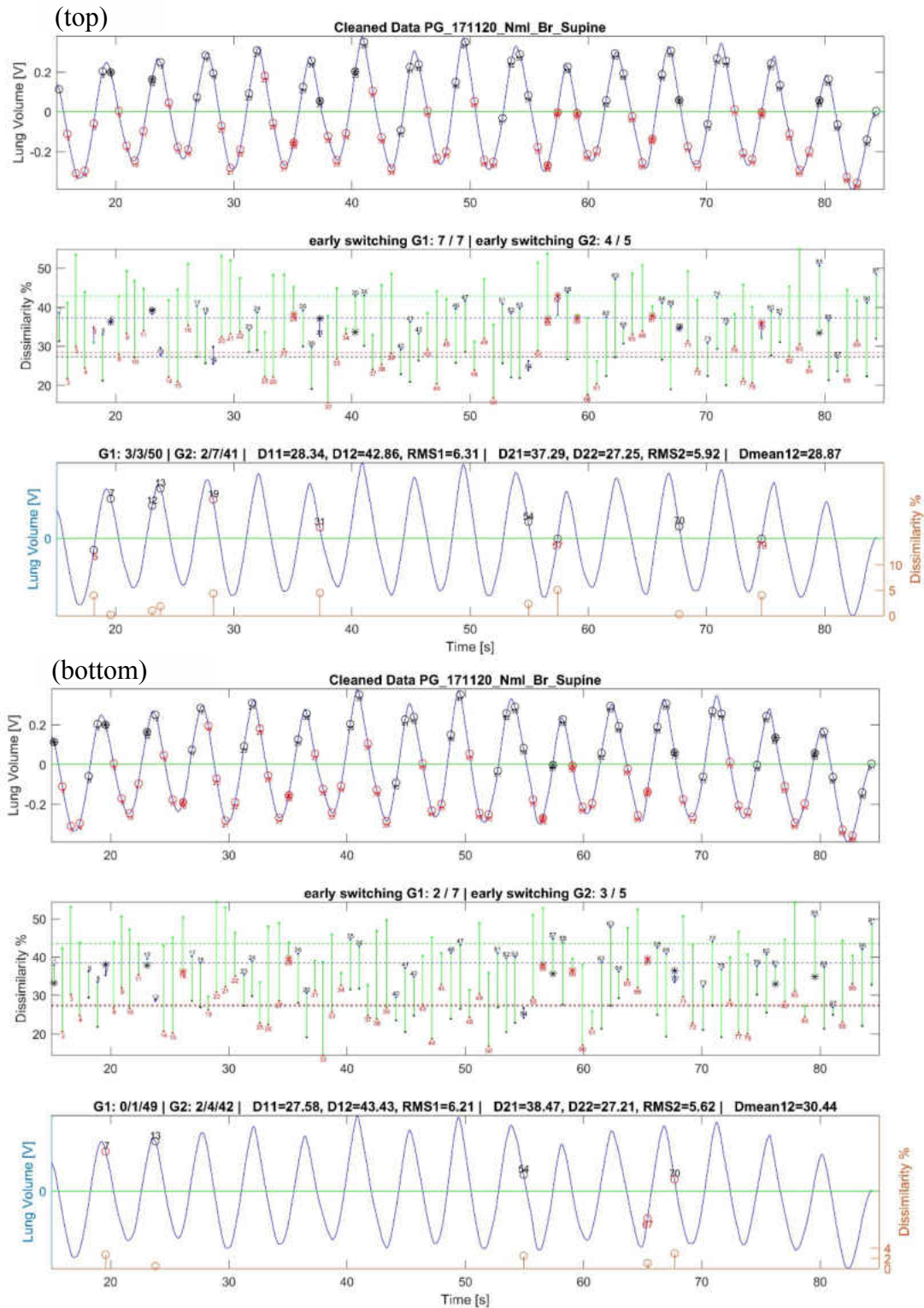


Figure 5.13. Dissimilarity analysis after (top) 1 cleaning iteration, (bottom) 2 cleaning iterations. The plot descriptions are similar to the plot descriptions for Figure 5.12.

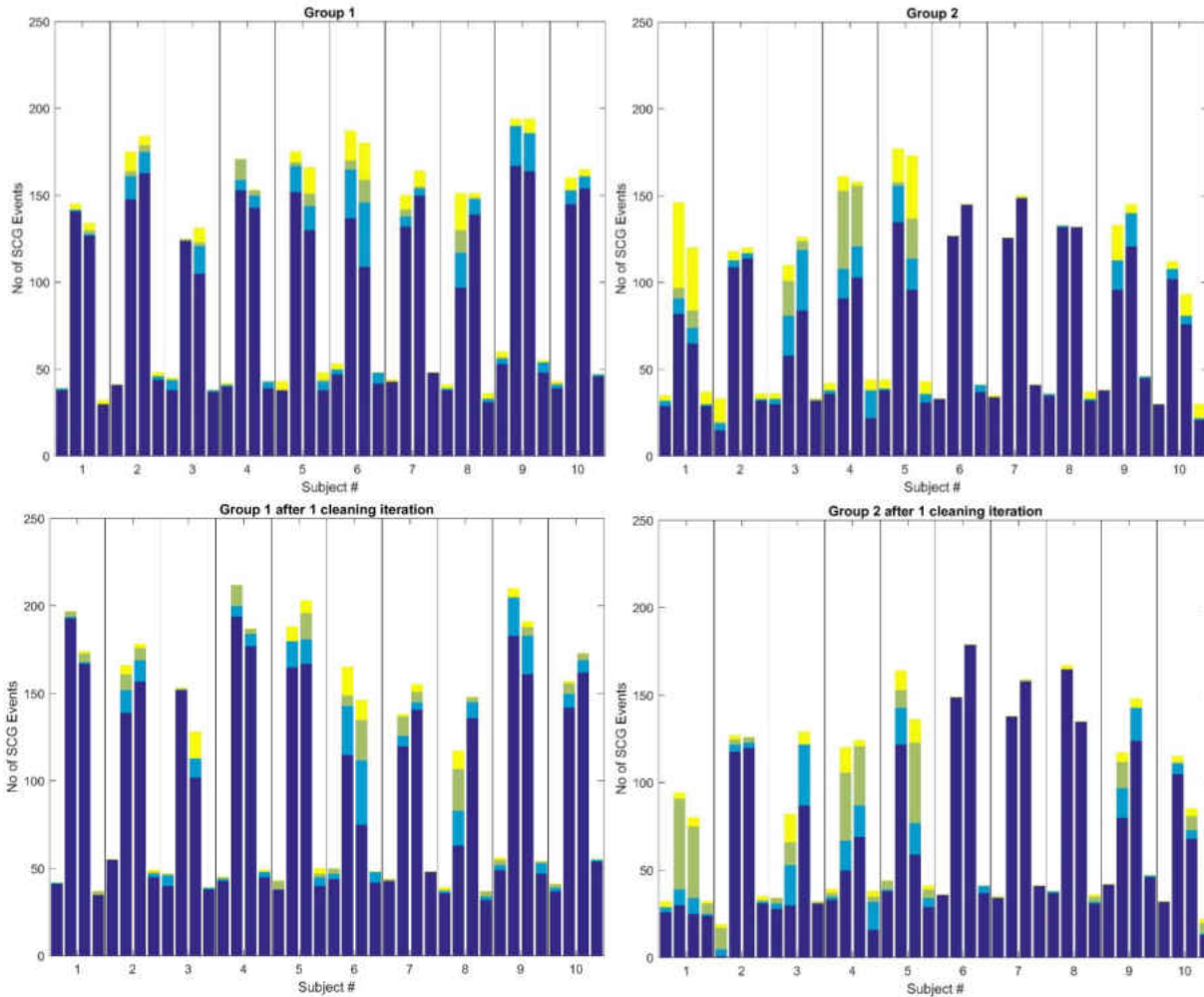


Figure 5.14. Number of early switching events compared to the total number of events in each group (top) before cleaning, (bottom) after one cleaning iteration. In these plots, each column height represents the total number of SCG events. Yellow columns show the number of early switching events. Green column show the number of high-backward events that are not early switching. Blue columns show the number of backward events that are not high-backward.

Each column height shows the total number of SCG events. The yellow column shows the number of early switching events, while the blue and green columns are the backward events that \notin high-backward events and high-backward events that \notin early switching events. In other words

- Yellow column: early switching events
- Yellow column + green column: high-backward events
- Yellow column + green column + blue column: backward events

- Yellow column + green column + blue column + violet column: total number of events

Figure 5.14 shows that, before the cleaning, most high-backward events were early switching in all subjects, except in subject #4 at 45 degree position. This is not, however, true when SCG groups were updated after 1 cleaning iteration. Figure 5.15 confirms this statement. In this figure, the ratio of high-backward and early switching events to the total number of events are shown in each SCG group for all the subjects. The dashed and solid lines corresponded to the ratio of high-backward and early switching events to the total number of events, respectively.

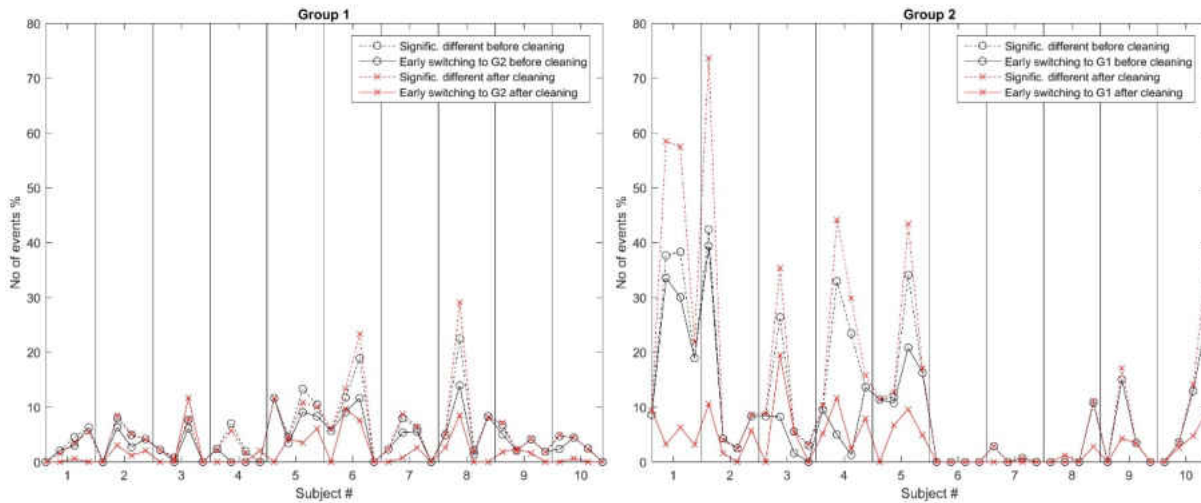


Figure 5.15. The ratio (%) of early switching and high-backward SCG events to the total number of events in (left) LLV and (right) HLV groups before and after one cleaning iteration. Black and red lines correspond to the number of events before and after the cleaning iteration, respectively. Dashed and solid lines represent the number of high-backward and early switching events, respectively.

5.3.2.2 Heart Rate Analysis

Subjects HR was estimated using both ECG and SCG signals at different postural positions. Results are shown in Figure 5.16. Figure 5.17 shows the HR estimation from SCG signal for different pressures at end-inspiration and end-expiration. For all subjects, except subjects #1 and #9, the HR was higher in $P = -20$ cm H₂O at the end-expiration phase.

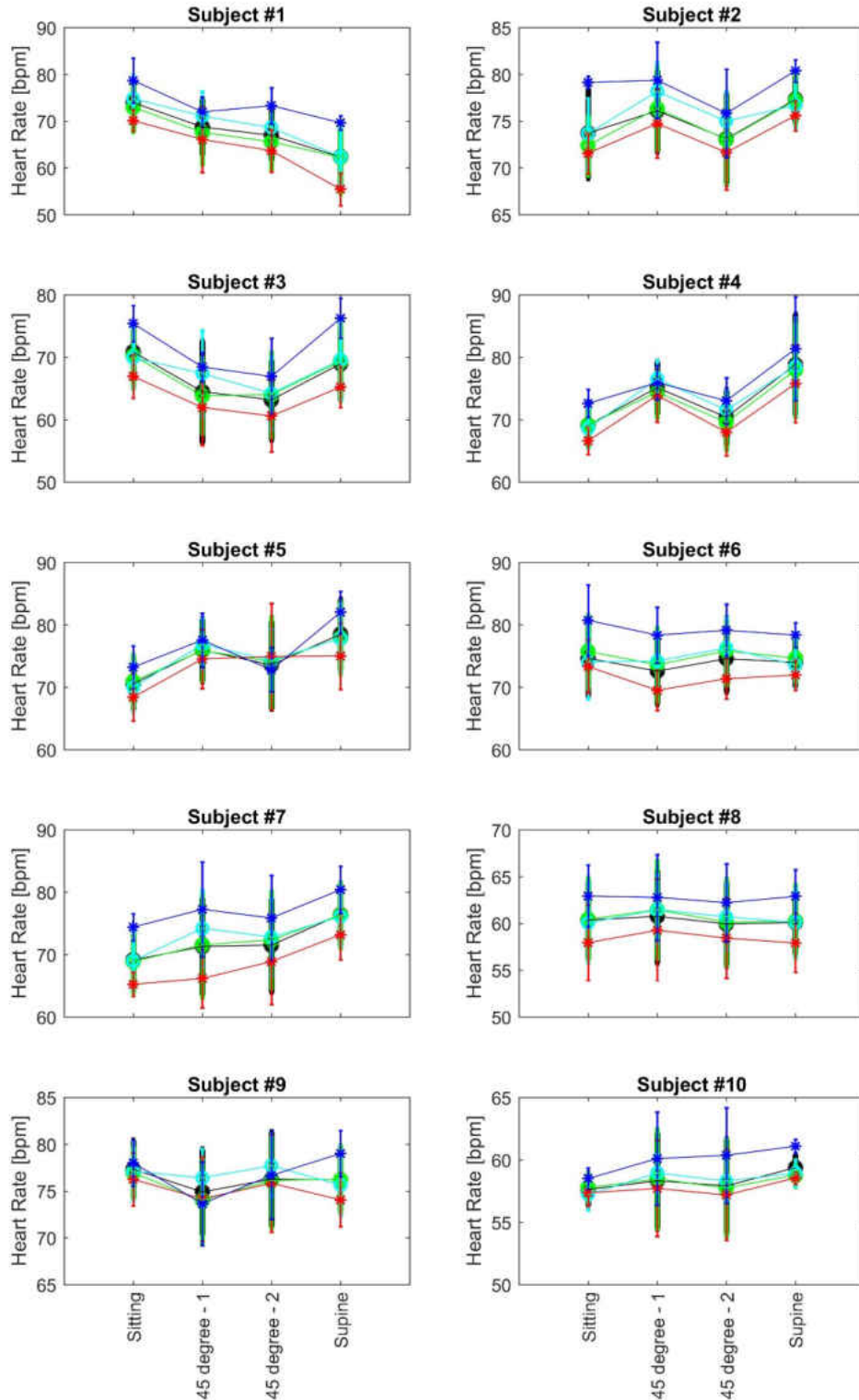


Figure 5.16. Heart rate estimations at different postural positions. HR estimation (blue) during HLV phase, (red) during LLV phase, (green) from the combination of HR_{LLV} and HR_{HLV}, (black) from SCG using equation (5-8), (cyan) from ECG using Pan-Tompkins algorithm.

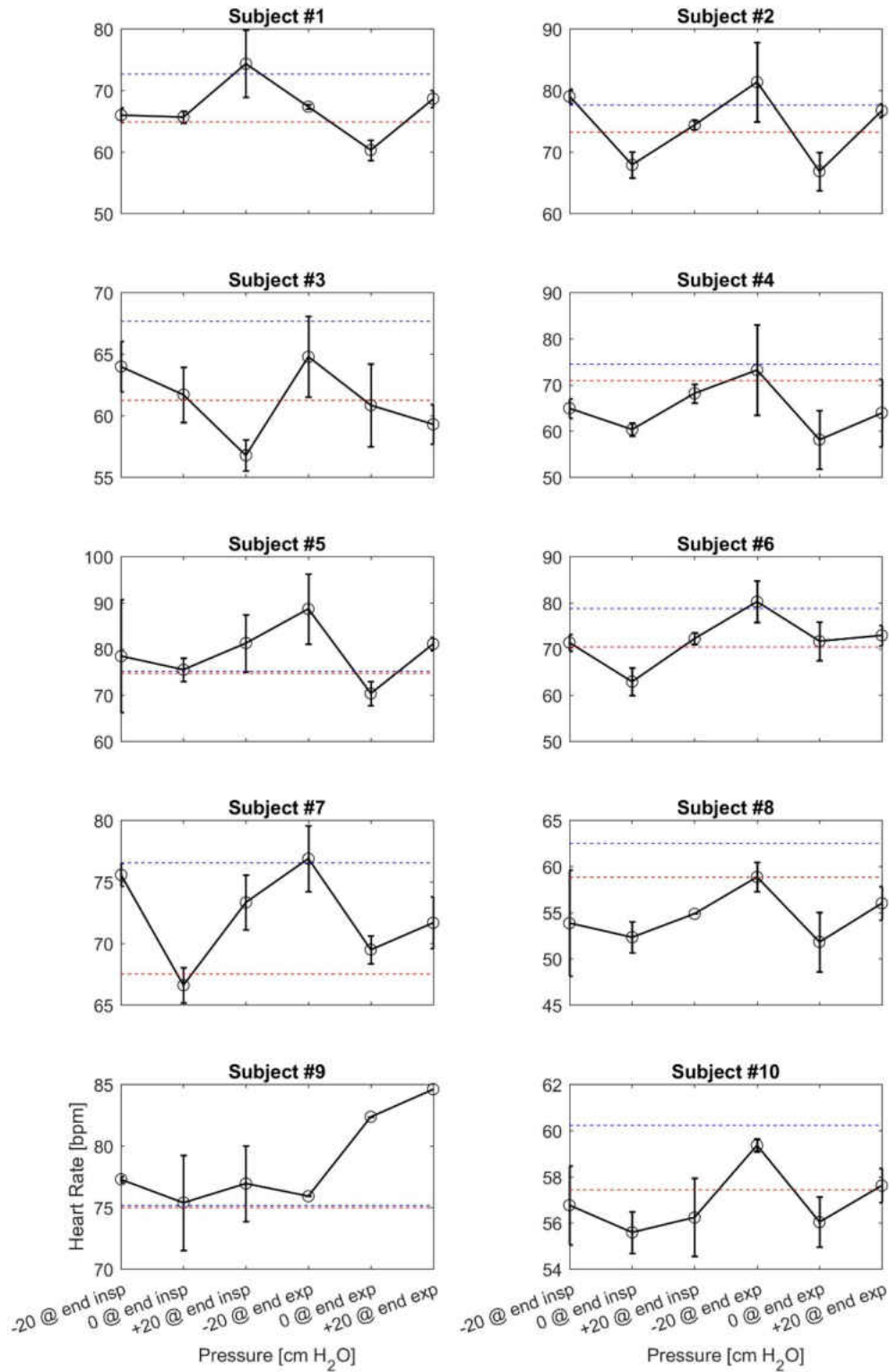


Figure 5.17. Heart rate estimation from SCG signal for different pressures at end-inspiration and end-expiration. The average of HR estimation during LLV and HLV in the two 45 degree trials were shown with red and blue dashed lines, respectively.

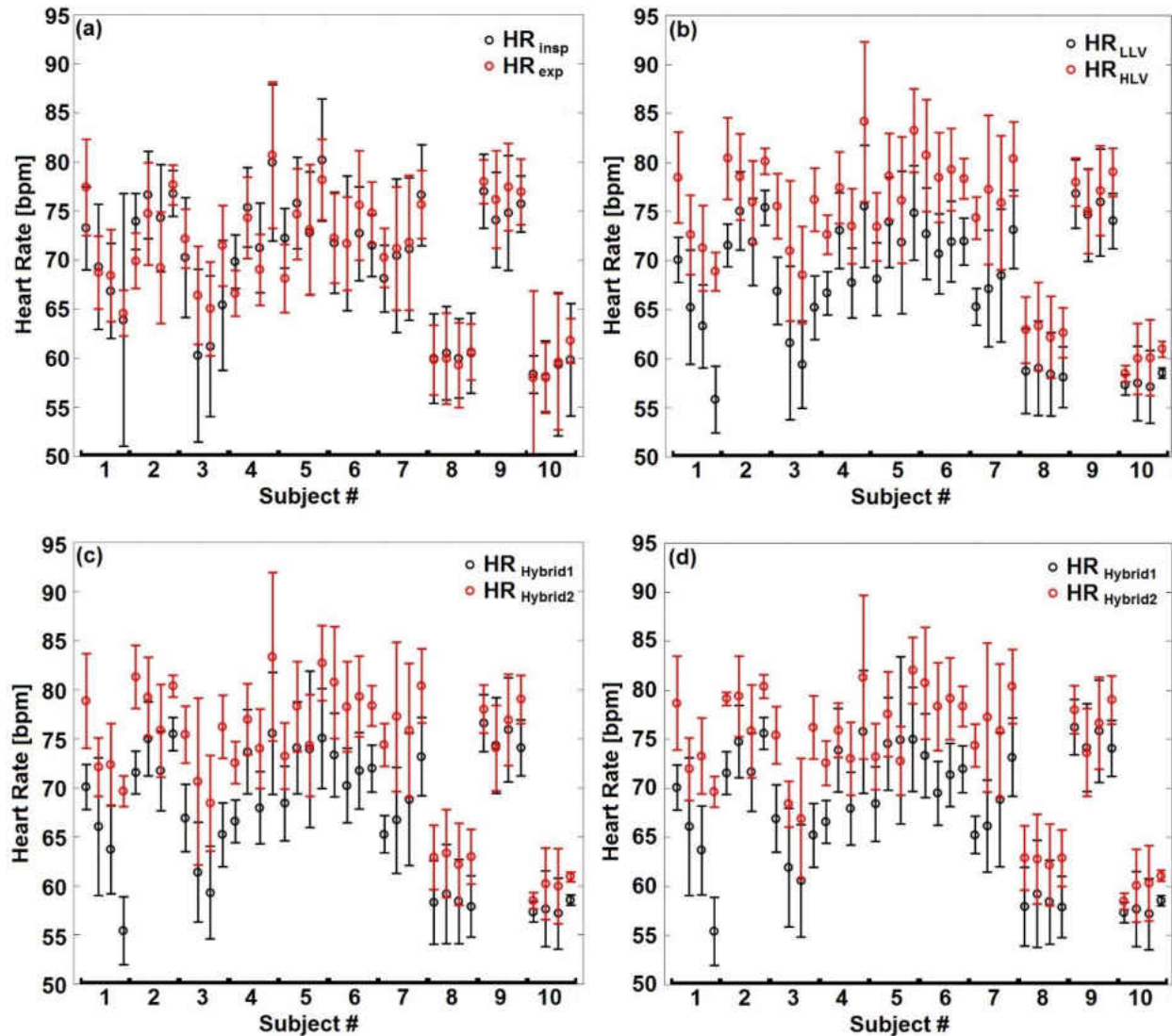


Figure 5.18. Heart rate estimation using SCG signal during (a) inspiration and expiration, (b) HLv and LLv, (c) hybrid1 and hybrid2 groups after 1 cleaning iteration, and (d) hybrid1 and hybrid2 groups after 2 cleaning iterations. The HR estimation is shown for different postural positions (4 different trials for each subject). These positions include sitting, 45 degree-1, 45 degree-2, and supine positions, respectively.

The heart rate was also estimated during different phases of the respiration cycle. Figure 5.18(a) shows the HR during inspiration and expiration. HR estimations during LLv and HLv are shown in Figure 5.18(b). Figure 5.18(c-d) show the HR estimation for the hybrid groups after 1 and 2 cleaning iterations, respectively. In these plots, the circles and whiskers show the mean HR estimation and $\pm 1SD$, respectively. HR during LLv was more different than HR during

HLV compared to HR difference during inspiration and expiration. This might also indicate that LV was a better criterion than RFR to divide SCG events into two clusters, since HR directly depends on the duration of cardiac cycles. For example, when HR during LLV is different than during HLV, it means that the time duration of one cardiac cycle (and therefore SCG event) during LLV is different than during HLV. Results show that HR was higher during HLV compared to LLV for all subjects. These results were consistent with the findings of section 5.2.

Agreement between different HR estimation methods was assessed using Bland-Altman analysis (Figure 5.19). In this plot, the solid line represents the mean value of differences between ECG and SCG HR estimations, while the dashed lines show the 95% confidence interval (mean \pm 1.96 SD). These results suggest general agreement between different methods, specifically the SCG and the standard Pan-Tompkins method (the top panel in Figure 5.19).

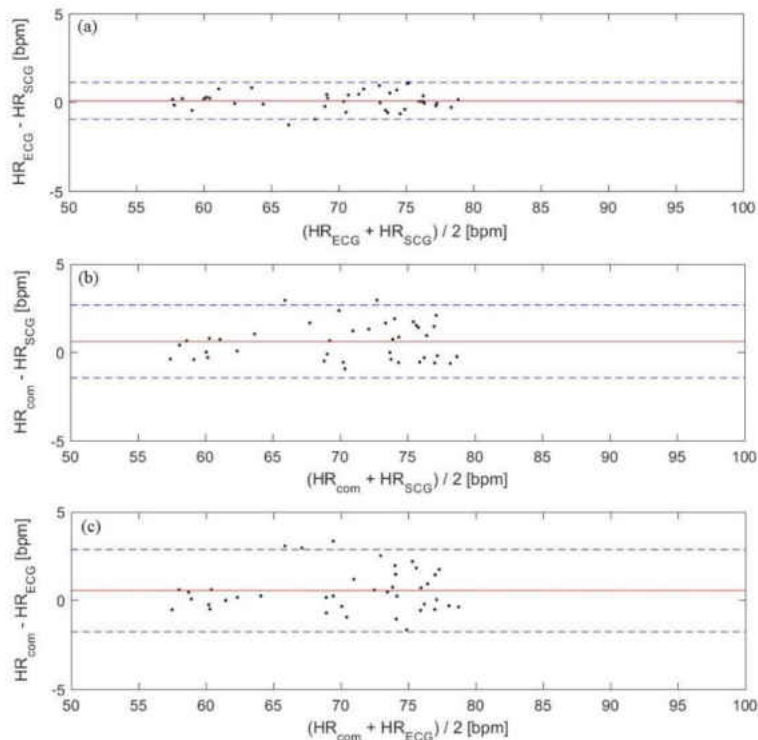


Figure 5.19. Bland-Altman plot for heart rate estimations using (a) ECG and SCG, (b) SCG and SCGcom, and (c) ECG and SCGcom. The solid line represents the mean (bias) value of differences between instantaneous frequencies. The dashed lines show the 95% confidence interval.

5.3.2.3 Cardiac Time Intervals

LVET, PEP, and QS2 were estimated for each subject using ECG and SCG signals. The results are listed in Table 5.12.

Table 5.12. Estimation of cardiac time interval [ms] using SCG and ECG signals during different phases of lung volume signal.

Subject #	LVET		PEP		QS2	
	LLV	HLV	LLV	HLV	LLV	HLV
1	218.75	228.12	125.00	121.87	343.75	350.00
2	225.00	203.12	118.75	121.87	343.75	325.00
3	228.12	250.00	112.50	100.00	340.62	350.00
4	196.87	237.50	128.12	121.87	325.00	359.37
5	275.00	265.62	100.00	93.75	375.00	359.37
6	281.25	259.37	109.37	115.62	390.62	375.00
7	271.87	256.25	115.62	109.37	387.50	365.62
8	243.75	256.25	109.37	106.25	353.12	362.50
9	218.75	240.62	125.00	121.87	343.75	362.50
10	321.87	306.25	115.62	112.50	437.50	418.75

5.3.2.4 Feature Evaluation

The z- component of the SCG signal was used for feature evaluation. A random 50/50 split of data was taken for training/testing from all subjects. These features were fed to the SVM model 10 times to classify the inspiratory/expiratory or LLV/HLV SCG events. The classification accuracy was evaluated each time. The average accuracies were then used to compare the effectiveness of different features.

5.3.2.4.1 Time Domain Features

3 different time domain features were used in this study for the classification of SCG events occurring during different phases of respiration and LV. Table 5.13 lists the average accuracy obtained from the SVM model using these features. Results show that temporal features led to a higher classification accuracy for the LV criterion compared to RFR. Among the three temporal features, standard deviation (SD) resulted in a higher accuracy for the classification of LLV and HLV SCG events. Inspiratory and expiratory events were classified more accurately using the mean value of each adaptive bin. However, for both criteria (i.e. LV and RFR), the SVM model

had the highest accuracy when all three temporal features were used together (accuracy of 89.9% and 85%).

Table 5.13. Average accuracy obtained from the SVM model for different temporal features used for the classification of SCG events occurring during different phases of respiration and lung volume.

	Mean	Median	SD	All
LV	85.4	85.5	87.8	89.9
RFR	82.6	81.2	79.1	85.0

5.3.2.4.2 Frequency Domain Features

Out of the three frequency features used in this study, the frequency coefficients resulted in a higher classification accuracy for both criteria. When the three different features were used together, the SVM model demonstrated a better performance for the classification of LLV and HLV events. However, using all the frequency features together (compared to the frequency coefficients alone) did not provide a higher classification accuracy for the RFR criterion. In general, the classifier accuracy, when the spectral features were used, was higher for the LV criterion compared to RFR.

The combination of frequency features resulted in a better classification accuracy compared to the combination of frequency features (92.9% vs 89.9%).

Table 5.14. Average accuracy obtained from the SVM model for different spectral features used for the classification of SCG events occurring during different phases of respiration and lung volume.

	Median	Avg Power	Freq. Coeff.	All
LV	78.9	82.3	92.4	92.9
RFR	72.5	73.7	88.3	87.3

5.3.2.4.3 Combined Time and Frequency Domains Features

When all the temporal and spectral features were used together, the SVM model resulted in a 92.9% and 88.6% accuracy for the LV and RFR criteria, respectively.

5.3.2.5 Classification

The classifiers under consideration, i.e. SVM, RF, and NN, were used to classify SCG events in different scenarios, including

- Classifying the SCG events into three sets of clusters including HLV/LLV, inspiratory/expiratory, hybrid1/hybrid2 (cleaned HLV/LLV) SCG groups using the z component of SCG signal in a subject specific scenario.
- Classifying the SCG events into three sets of clusters including HLV/LLV, inspiratory/expiratory, hybrid1/hybrid2 (cleaned HLV/LLV) SCG groups using the z component of SCG signal in a leave one subject out scenario.
- Classifying the SCG events into two sets of clusters including HLV/LLV and inspiratory/expiratory SCG groups using a 3-D SCG as well as its 1-D components.

5.3.2.5.1 Subject-Specific Scenario

The classification accuracy of different classifiers under consideration is reported in Table 5.15 for the SS scenario. The results are listed for 3 different grouping criteria, i.e. LV, RFR, and the hybrid groups after 1 cleaning iteration. All the classifiers had the highest accuracy and F_1 score for the hybrid groups followed by LV and RFR. For the hybrid criterion, the SVM and RF resulted in the highest and lowest accuracies (98.56% and 95.91%), respectively. Table 5.15 shows the highest and lowest accuracy was obtained by NN and SVM for the LV criterion. The {accuracy, F_1 score} for these classifiers was {95.05%, 94.81%} and {94.72%, 94.48%}, respectively. For the RFR criterion, the maximum total accuracy was obtained with NN (93.95%) followed by SVM and RF (93.67% and 89.82%, respectively).

Table 5.15. Classification accuracy (%) and F_1 score (%) for the SS scenario.

	Subject #	LV		RFR		Hybrid	
		Accuracy	F_1 score	Accuracy	F_1 score	Accuracy	F_1 score
SVM	1	96.67	96.23	86.67	84.62	100.00	100.00
	2	98.11	97.56	94.34	92.31	99.06	98.73
	3	95.76	95.65	99.15	98.99	97.46	97.56
	4	95.61	95.24	94.74	93.88	95.61	95.80
	5	94.78	94.66	89.55	89.23	97.76	97.60
	6	94.50	94.23	98.17	97.30	97.25	96.00
	7	89.90	89.36	93.94	93.48	100.00	100.00
	8	92.97	92.80	91.41	91.85	100.00	100.00
	9	92.81	92.86	95.68	94.23	100.00	100.00
	10	96.12	96.18	93.02	89.89	98.45	98.15
	Avg.	94.72	94.48	93.67	92.58	98.56	98.38
RF	1	96.67	96.23	86.67	84.31	100.00	100.00
	2	98.11	97.56	96.23	94.74	97.17	96.10
	3	94.92	94.55	94.07	92.78	97.46	97.52
	4	98.25	98.08	85.96	81.82	96.49	96.61
	5	95.52	95.38	85.82	85.50	93.28	92.44
	6	96.33	96.08	92.66	89.19	92.66	88.57
	7	89.90	89.13	87.88	87.50	91.92	90.00
	8	96.09	95.87	87.50	87.88	96.09	96.64
	9	89.21	89.36	89.21	84.54	97.12	96.72
	10	94.57	94.81	92.25	88.37	96.90	96.30
	Avg.	94.96	94.70	89.82	87.66	95.91	95.09
NN	1	97.50	97.09	90.00	88.89	100.00	100.00
	2	97.17	96.30	96.23	94.74	99.06	98.73
	3	95.76	95.65	98.31	98.00	98.31	98.36
	4	97.37	97.14	92.98	92.00	97.37	97.44
	5	95.52	95.45	90.30	90.08	96.27	96.06
	6	95.41	95.15	98.17	97.30	96.33	94.59
	7	89.90	89.36	94.95	94.62	95.96	95.24
	8	94.53	94.40	89.06	89.06	99.22	99.34
	9	92.81	92.86	94.96	93.20	97.84	97.56
	10	94.57	94.66	94.57	92.31	99.22	99.07
	Avg.	95.05	94.81	93.95	93.02	97.96	97.64

5.3.2.5.2 Leave-One-Subject-Out Scenario

Similar type of results were obtained for the LOSO scenario and is reported in Table 5.16. In this scenario, the cleaning process did not seem to improve the classifiers performance. Instead, the classifiers had a lower accuracy when the hybrid grouping was used. For the LV scenario, SVM and RF had the highest and lowest accuracies, respectively. SVM and RF resulted in the highest and lowest accuracies for the RFR criterion as well. However, the accuracies obtained for this criterion was in general higher than those obtained for LV. The classification accuracies were significantly lower for LOSO scenario compared to the SS scenario. This might be due to high intersubject variability of SCG waveforms since in the LOSO scenario the classifier used 9/10

subject's data for training and was tested on the remaining subject. The SCG morphology and frequency content of the remaining subject might be completely different than all other subjects. Therefore, the classification model might not be able to correctly predict the SCG class labels. However in the SS scenario, the classifier is trained 80% of all subjects' data. Thus, the classifier learnt about SCG waveform of different subjects and when it was tested on the remaining 20% of the data, it could predict the labels with higher accuracy and F_1 score.

Table 5.16. Classification accuracy (%) and F_1 score (%) for the LOSO scenario.

Subject #	LV		RFR		Hybrid		
	Accuracy	F_1 score	Accuracy	F_1 score	Accuracy	F_1 score	
SVM	1	73.37	67.75	83.25	81.62	42.38%	59.53
	2	60.19	53.01	74.53	66.50	31.13	44.27
	3	75.08	74.79	55.59	65.62	34.07	45.75
	4	61.38	54.66	66.31	62.33	60.67	73.04
	5	41.74	58.81	60.96	61.19	40.84	57.36
	6	59.27	70.71	74.31	46.97	73.94	70.66
	7	59.76	38.89	58.74	43.45	56.91	6.19
	8	73.71	69.89	78.72	80.95	65.41	71.04
	9	50.51	67.12	59.91	6.73	23.88	38.55
	10	59.88	45.34	67.19	23.27	59.88	22.75
Avg.	61.49	60.10	67.95	53.86	48.91	48.91	
RF	1	58.63	58.35	72.36	65.84	69.35	65.92
	2	46.04	54.75	66.23	53.98	42.45	49.08
	3	60.17	64.87	58.47	27.30	54.41	53.38
	4	55.56	62.39	59.08	42.00	69.84	70.67
	5	48.65	56.04	39.04	39.94	68.47	48.53
	6	72.66	73.15	64.77	52.48	52.84	56.66
	7	53.05	7.23	58.13	29.93	56.50	8.55
	8	55.24	60.17	60.41	63.39	59.62	67.59
	9	49.35	64.57	53.98	51.23	33.29	49.84
	10	53.03	11.18	67.50	41.78	62.99	17.93
Avg.	55.24	51.27	60.00	46.79	56.98	48.81	
NN	1	70.69	64.93	79.90	73.91	72.03	73.62
	2	59.25	43.75	67.74	58.80	33.58	38.03
	3	73.39	70.54	47.80	58.71	57.46	65.85
	4	62.79	54.23	68.08	47.84	56.26	59.34
	5	41.89	57.24	60.06	64.53	40.69	56.74
	6	72.11	76.54	74.31	62.77	82.57	77.11
	7	53.66	8.80%	55.49	37.96	56.30	3.59
	8	62.75	56.25	67.61	74.03	62.28	67.56
	9	50.22	66.86	62.95	35.03	24.75	39.68
	10	57.85	35.01	77.14	56.89	63.61	10.00
Avg.	60.46	53.42	66.11	57.05	54.95	49.15	

5.3.2.5.3 Tri-axial vs uni-axial SCG

An SVM model was used to classify the LLV/HLV and inspiratory/expiratory SCG signals using the features that were extracted from different components of the SCG signals. These

components included the x-, y-, and z- components as well as angles alpha (angle between the projection of tri-axial SCG on xy plane and x axis), beta (angle between tri-axial SCG vector and xy plane), and SCG signal magnitude. The classification accuracy is listed in Table 5.17. For the LV criterion, SCG_y resulted in the highest accuracy followed by SCG_z, SCG_{mag} and beta. However, for the RFR criterion, the classifier performed better using the SCG_z features followed by SCG_y, SCG_x, and SCG_{mag} features. For both grouping criteria, the highest accuracy was obtained when the SCG_x, SCG_y, and SCG_z (i.e. SCG_{xyz}) features were concatenated.

Table 5.17. Classification accuracy of the SVM model for different components of the SCG signal.

	SCG _x	SCG _y	SCG _z	SCG _{xyz}	alpha	beta	SCG _{mag}	SCG _{αβmag}
LV	87.8	93.9	92.9	96.2	80.1	89.1	90.1	92.7
RFR	85.9	88.2	88.6	91.6	81.2	85.3	85.7	89.4

5.3.2.5.4 Breath-Hold Data

The main goal of this experiment was to control the effect of heart displacement and pressure around heart on the SCG morphology. SCG signals were recorded at end-inspiration and end-expiration states where the LV was at its maximum and minimum values, respectively. The hypothesis was that the end-inspiration and end-expiration SCG events should be similar to HLV and LLV SCG events, respectively. Table 5.18 shows the classification accuracy of the SVM model to classify the breath-hold data. The results are reported for LV and hybrid grouping criteria. For LV grouping, it was assumed that the actual label of end-inspiration and end-expiration SCG was HLV and LLV, respectively. Similarly, for the hybrid grouping, it was assumed that the actual label of end-inspiration and end-expiration SCG was hybrid1 (updated HLV) and hybrid2 (updated LLV), respectively. The high accuracy and F_1 score for the LV grouping at $P = 0$ cm H₂O confirmed that the SCG events at end-inspiration and end-expiration states were morphologically very similar to the HLV and LLV SCG events, respectively. The classification performance was

similar (~ 90%) at different pressure values suggesting that pressure might not be an important factor in the SCG waveform variations.

The classification accuracy was significantly higher for the hybrid compared to LV grouping. These results suggested that the updated HLV and LLV (hybrid1 and hybrid2) groups were more similar to the SCG events at end-inspiration and end-expiration states, respectively. This might be due to a time delay between the lung volume and heart displacement during the respiration cycle.

Table 5.18. Classification accuracy of the SVM model for the breath-hold data. Here, the hypothesis was that the end-inspiration and end-expiration SCG events should be similar to HLV and LLV SCG events, respectively. A high accuracy (and F_1 score) confirms the hypothesis. The classification results are reported for LV and hybrid grouping criteria.

Subject #	0 cm H ₂ O				+20 cm H ₂ O				-20 cm H ₂ O			
	LV		Hybrid		LV		Hybrid		LV		Hybrid	
	Acc.	F_1	Acc.	F_1	Acc.	F_1	Acc.	F_1	Acc.	F_1	Acc.	F_1
1	98.3	98.1	100.0	100.0	98.3	98.1	100.0	100.0	99.2	99.0	100.0	100.0
2	98.1	97.4	100.0	100.0	98.1	97.4	100.0	100.0	97.2	96.1	100.0	100.0
3	95.8	95.7	98.3	98.3	97.5	97.4	97.5	97.4	97.5	97.4	98.3	98.3
4	93.0	92.7	99.1	99.1	93.9	93.7	99.1	99.1	94.7	94.5	98.2	98.3
5	95.5	93.9	98.5	97.9	95.5	94.0	98.5	97.9	96.3	94.8	98.5	97.9
6	78.0	72.1	97.2	95.7	79.8	73.8	98.2	97.1	78.0	72.1	97.2	95.7
7	88.9	88.4	94.9	94.4	88.9	88.4	94.9	94.4	88.9	88.4	93.9	93.3
8	89.1	88.3	100.0	100.0	90.6	90.2	100.0	100.0	89.1	88.3	100.0	100.0
9	87.1	85.2	95.7	94.7	87.1	85.0	97.8	97.3	87.1	85.0	99.3	99.1
10	81.4	78.6	99.2	98.9	82.9	80.0	99.2	98.9	82.2	79.3	99.2	98.9
Avg.	90.5	89.1	98.3	97.9	91.3	89.8	98.5	98.2	91.0	89.5	98.5	98.1

5.3.2.6 Clustering

Clustering was performed using both temporal and spectral features. For both LV and RFR criteria, temporal features resulted in low purity and ARI values (~ 0.55 and 0.05, respectively). Therefore, in this study, only spectral features were used for clustering. Figure 5.20 shows the clustering results for one of the subjects. In these plots, red and blue circles are the two output clusters. Figure 5.20.a and Figure 5.20.b show the output clusters against the RFR and LV signals, respectively. The clustering algorithm proves the utility of these grouping criteria if more circles with similar color were placed in either negative or positive side of LV/RFR signal. The purity and ARI metrics were summarized in Table 5.19 for all the subjects. Results show that the clusters

generated using k -means algorithm agreed better with HLV/LLV ($\{\text{purity, ARI}\} = \{0.81, 0.45\}$) labels than inspiratory/expiratory ($\{\text{purity, ARI}\} = \{0.65, 0.31\}$) labels. These findings were consistent with the results of dissimilarity analysis (section 5.1.2) and classification (section 5.3.2.5) which indicated that the LV criterion might be superior to RFR criterion in grouping similar SCG events.

Table 5.19. Clustering performance for respiratory flow rate (RFR) and lung volume (LV) grouping criteria.

Subject #	Grouping Criteria		LV	
	RFR Purity	ARI	Purity	ARI
1	0.67	0.37	0.92	0.70
2	0.74	0.44	0.90	0.63
3	0.71	0.28	0.87	0.54
4	0.65	0.17	0.86	0.53
5	0.57	0.34	0.64	0.25
6	0.67	0.38	0.82	0.40
7	0.65	0.03	0.60	0.09
8	0.55	0.31	0.89	0.61
9	0.58	0.30	0.85	0.49
10	0.70	0.46	0.77	0.30
Avg.	0.65	0.31	0.81	0.45

5.3.3 Conclusions

Different methods were implemented to compare the effectiveness of LV and RFR signals in separating SCG events into two groups where SCG events in each group were more similar to each other. These methods included statistical analysis, supervised, and unsupervised machine learning techniques. The results showed LV signal was superior to RFR in grouping similar SCG events according to their waveform morphology. A cleaning algorithm was also proposed to improve the grouping efficiency of the LV signal. This algorithm was resulted in a new grouping criterion which was called the “hybrid” criterion. The hybrid criterion might be used towards obtaining a cleaner ensemble average of SCG events which might result in more accurate characterization and classification of these signals. Future studies may explain the physiological correlations of hybrid criterion. The results of this study also showed that the SCG demonstrated morphological

differences during respiration. Future studies may extract respiration information directly from SCG signals.

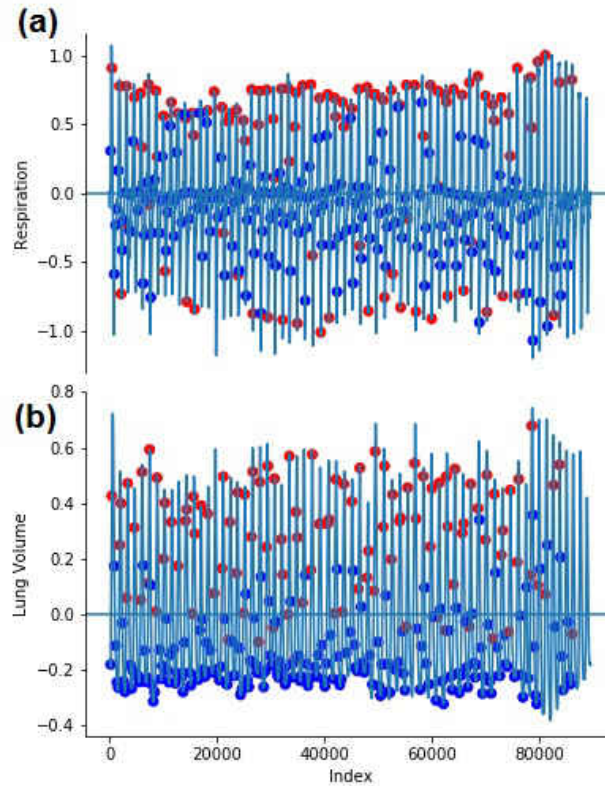


Figure 5.20. Clustering results for one of the subjects. SCG events are shown on (a) RFR and (b) LV signals with red and blue circles. Red and blue circles are the two output labels of the clustering algorithm.

5.4 Genesis of SCG Waves

SCG signals are believed to be caused by the mechanical processes associated with the heart activity (such as cardiac contraction, blood momentum changes, valve closure, etc.). The characteristics of these signals can contain useful information that correlates with cardiovascular pathologies [167]. Such information would also be complementary to other methods that detect the heart electrical activity (such as electrocardiography). Early studies [8] suggested that changes in cardiac output may be estimated using these methods. Certain signal patterns were reported in patients with myocardial infarctions [206]. These signals were also found to reflect the strength of

myocardial contractions [207,208] and have detectable waveform changes with heart disease resolution [209]. More recent studies suggested utility for monitoring left ventricle function [5,210], and heart and breathing rates [4,10,27,50,211,212]. A case study reported changes in the relative strength of the SCG waves that correspond to valve closure, rapid ventricular filling and ejection that preceded the onset of ischemic symptoms that resolved after therapy [5].

The relation between SCG waves and cardiac activity are not fully understood. However, several studies have investigated that relationship [20,166,213]. For example, SCG was found to contain a low-frequency wave during atrial systole, a high-amplitude wave during ventricular systole, a wave during early ventricular filling, and relatively high-frequency waves at the time of the first and second heart sounds [166]. A three-dimensional model of ventricular contraction indicated that the first SCG peak after electrocardiogram R-wave may be related to aortic valve opening [213]. Simultaneous recording of SCG and ECG suggested that the peaks and valleys of the dorso-ventral component of SCG correspond to different physiological events including mitral valve opening and closure, aortic valve opening and closure, isovolumetric contraction, rapid ejection, and rapid filling [20]. Electromechanical systole, PEP, and LVET were identified using simultaneous recordings of SCG and ECG signals [214]. Multi-channel SCG was used to measure the feature points in a cardiac cycle corresponding to the four valvular auscultation locations. Using this method, six new feature points (including left ventricular lateral wall contraction peak velocity, septal wall contraction peak velocity, trans-aortic valve peak flow, transpulmonary peak flow, trans-mitral ventricular relaxation peak flow, and trans-mitral atrial contraction peak flow) were extracted [40]. However, SCG signals are vulnerable to inter-subject variations such as body mass index, sex, age, and health conditions [4]. In addition, SCG vibrations have relatively low amplitudes that can be easily contaminated by building vibrations, motion artifacts (e.g. patient

movements, muscle related disease, etc.) and respiration noise, which can lead to a misinterpretation of SCG signal features [20–22,99].

In this section, two approaches have been used to elucidate the physiological background of SCG waveforms. In the first approach (section 5.4.1), simultaneous recording of some of the well-known techniques and SCG signals was used. These techniques included echocardiography, electrocardiography, and phonocardiography. These techniques have been extensively studied before, and the correlation between them and the physiological cardiac events are well established. Therefore, they might be used as gold standards to study the physiological sources of the SCG waveforms. In the second approach (section 5.4.2), finite element modeling (FEM) was used to provide some insights into this yet SCG genesis open question. The potential utility of FEM for this problem was discussed, and an FEM pipeline was proposed for future works.

5.4.1 Echocardiography

5.4.1.1 Data Acquisition

Simultaneous recording of different types of heart signals including ECG, SCG, ECHO, and PCG may help biomedical engineers and physicians to study the cardiovascular disease more effectively. This section aims at acquiring and lining up the ECG, SCG, PCG, ECHO and respiration flow rate. The SCG signal of the volunteer subjects was measured using a uniaxial accelerometer (PCB piezotronics, Depew, NY). The PCB sensor output was acquired using an iWorx TA Control Module (iWorx Systems, Inc., Dover, NH). The sensor outputs were amplified using a PCB Model 482C Signal Conditioner (PCB piezotronics, Depew, NY) with gain factor of 100. The M mode and Doppler images from echocardiography system (Model: EPIQ 5, Philips, Netherlands) were also recorded and synchronized with the SCG signals. Using the respiration flow rate, the SCG events were divided into two groups of insp. and exp. events. These events

were then aligned in time with the left ventricular strain curve supplied by the speckle tracking echocardiography (STE) technique. Figure 5.21 shows the experimental setup as well as sensor locations.

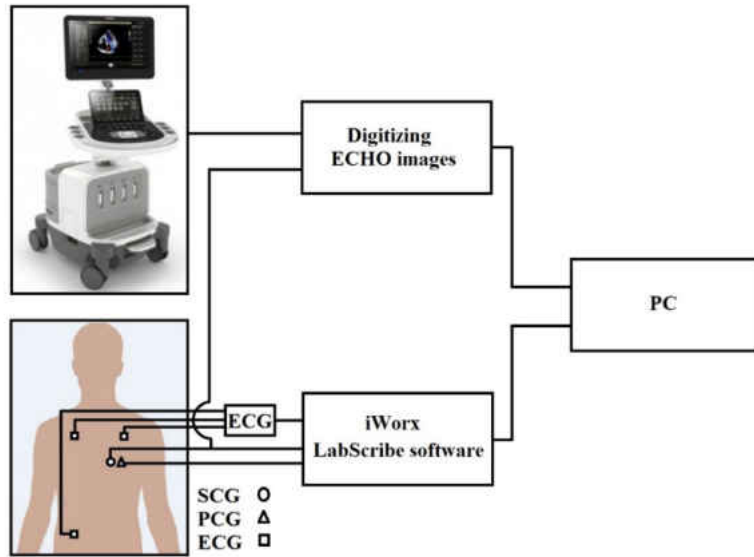


Figure 5.21. Experiment setup and ECG, PCG, and SCG sensor locations.

5.4.1.2 Data Pre-processing

5.4.1.2.1 Signals Synchronization

In the first step, the ECHO images needed to be synchronized with other recorded signals. For this purpose, the digital phonocardiogram was connected to both of iWorx unit and audio input of ECHO recordings. Therefore, it was used for an initial synchronization of the ECHO video and SCG signals. The audio of the ECHO video was first extracted using Windows Media Player software. Figure 5.22(left) shows the ECHO audio (red and blue lines) and the PCG signal (dashed black line). For an easier synchronization process, the PCG sensor was tapped 3 times during each recording to mark the signals. These marks were used to find the time shift between the ECHO audio and PCG signal. The signals were then synchronized using these time shifts. Figure 5.22(right) shows the synchronized audio files.

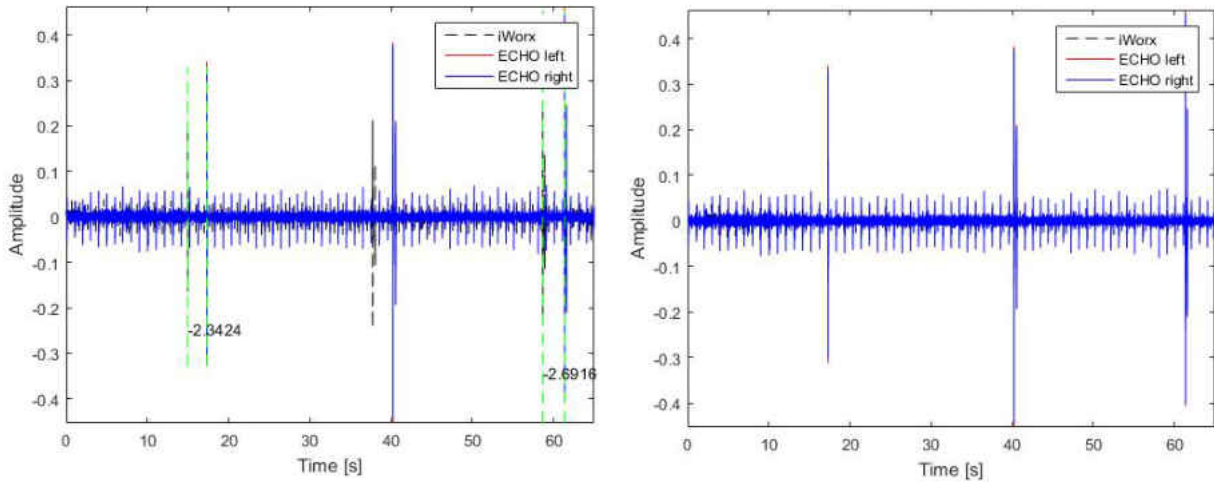


Figure 5.22. (left) ECHO audio files and PCG signal. The phonocardiograph sensor was tapped 3 times to mark the signals. These marks were then used to find the time shift between ECHO audio and PCG signal. The time shift values were shown in the figure, (right) Synchronized audio files (PCG and ECHO audio).

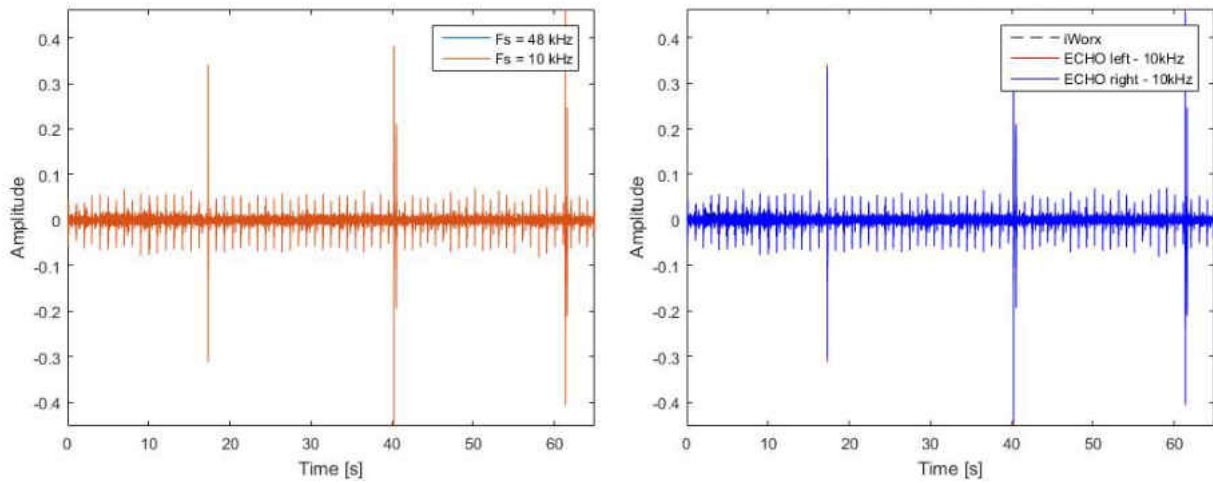


Figure 5.23. (left) ECHO audio file at two sampling frequencies of (red line) 10 kHz and (blue line) 48 kHz, (right) Synchronized audio files, (dashed line) PCG and (blue and red lines) audio files recorded by the ECHO machine at 10 kHz.

To assess the accuracy of the initial synchronization, the correlation between PCG signal and the ECHO audio was found. The PCG signal was sampled at 10 kHz using iWorx. However, the ECHO audio was sampled at 48 kHz by Windows Media Player. To find the correlation between these two signals, the ECHO audio was interpolated to a sampling frequency of 10 kHz. To make sure that the down-sampled signal was similar to the original signal, these signals were plotted in the same figure. Figure 5.23 shows the ECHO audio at two different sampling frequencies of 10

and 48 kHz. The figure confirmed that the ECHO audio at 10 kHz was similar to the one at 48 kHz. The correlation between PCG and ECHO audio was then calculated (~ 0.953).

ECG of the subjects was recorded using both the ECHO machine and iWorx module. These ECG signals were used for final synchronization of the recorded signals with the ECHO images. For this purpose, a basic image processing technique was first used to extract ECG signal from the ECHO images. Figure 5.24 shows the final synchronization of the signals step by step. These steps can be summarized as follows:

- Step 1: Raw ECHO image.
- Step 2: Identifying the green color pixels.
- Step 3: Digitizing the green color pixels identified in Step 2.
- Step 4: Comparing the ECG signals recorded by the ECHO machine and iWorx module.
- Step 5: Finding time lags between the ECG signals and synchronizing the signals.

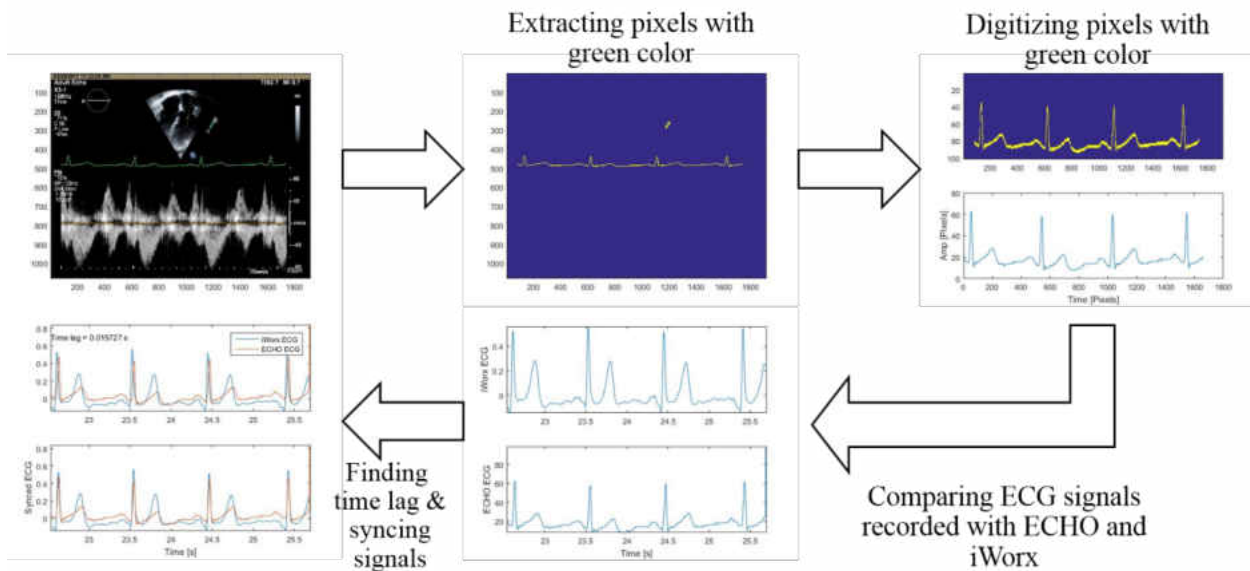


Figure 5.24. Image processing steps to extract ECG waveform from the ECHO images. These ECG waveforms were then used for a better synchronization of ECHO images and SCG signals.

5.4.1.2.2 Doppler Velocity Profile Extraction

A basic image processing algorithm, similar to the one that was used in section 5.4.1.2.1 for the extraction of ECG signals, was developed to extract Doppler velocity profiles from the ECHO images. The Doppler profile extraction was based on identification of gray color pixels in the ECHO images. Figure 5.25 shows this algorithm step by step. These steps can be summarized as follows:

- Step 1: Raw ECHO image.
- Step 2: Preprocessing of the raw ECHO images. The ECHO images were enhanced (e.g. using smoothing). Those gray pixels that were not related to the Doppler profile were removed.
- Step 3: Identifying the gray color pixels.
- Step 4: Calculating the intensity of gray pixels. There were still some gray pixels that were not related to the Doppler profile. Two different methods were used to clean these gray pixel noise from the images. These methods were based on ignoring the gray pixels that their intensity was smaller than a defined threshold. Then, the first and last vertical gray pixels at each horizontal pixel were chosen as upper and lower envelopes of the Doppler profile, respectively.
- Step 5: Digitizing upper and lower envelopes of the Doppler profile.
- Step 6: Comparing the Doppler profiles obtained from the two cleaning methods mentioned in Step 4. Results showed that these two Doppler profiles were consistent and comparable.
- Step 7: Smoothing the Doppler profiles.

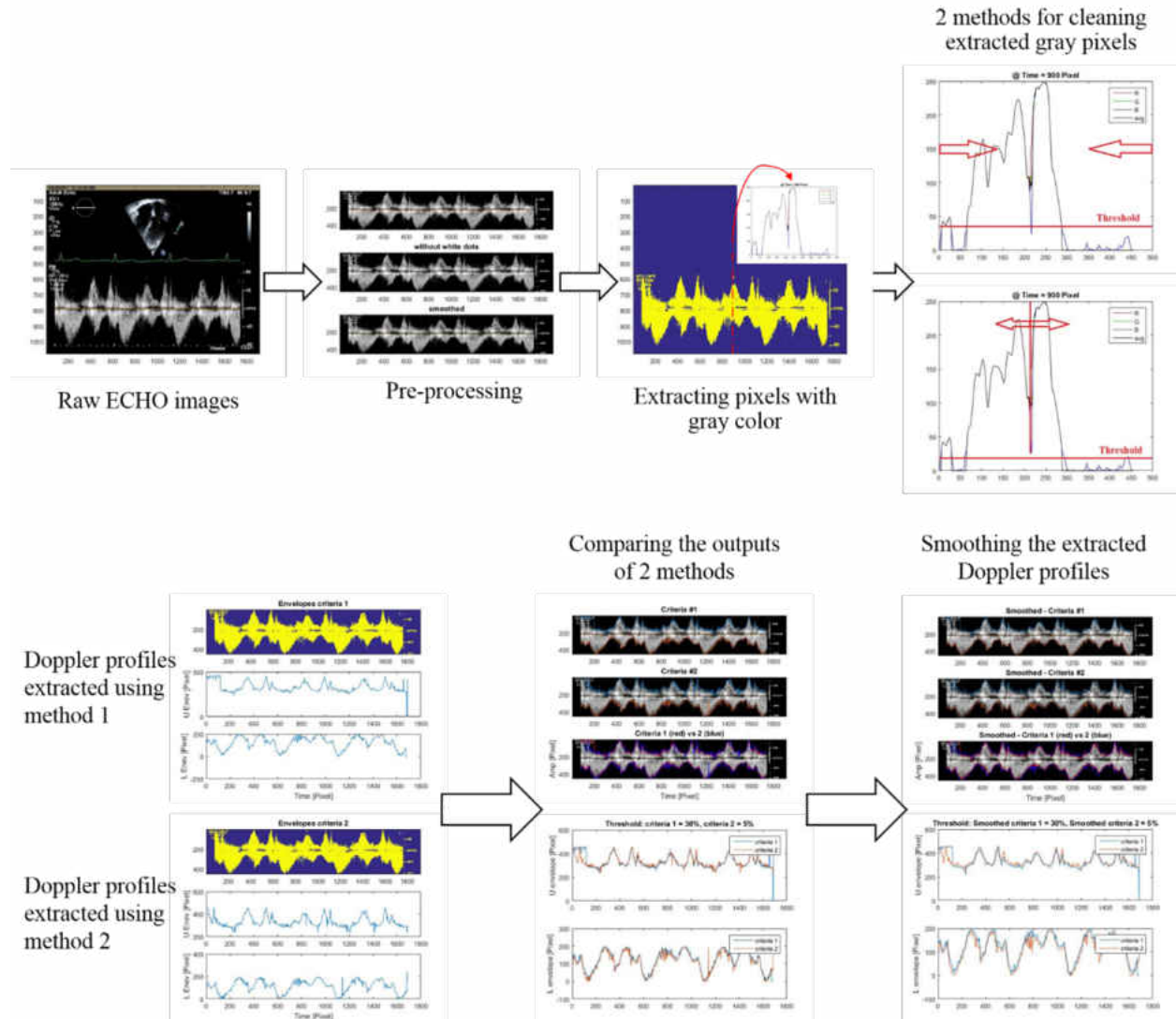


Figure 5.25. Image processing steps to extract Doppler velocity profiles from Doppler echocardiography images.

5.4.1.3 Results

The SCG, ECG, PCG and respiration flow rate were measured simultaneously using the iWorx system (Figure 5.26). The ECHO video frames were read and saved using Matlab. The “primary frames” were identified. The ECHO primary frames were then lined up with the ECG, ECHO audio, PCG, and SCG signals. One sample primary frames is shown in Figure 5.27. These simultaneously acquired signals can be useful to study CTIs. It can be seen that the ECG R wave occurred first. Then S1 and SCG1 seemed to have occurred approximately around the same time.

This is consistent with the fact that electrical stimulus precedes myocardial contractions and valve closures which may be linked to SCG1 and S1. It can also be seen that the PCG recorded by the iWorx and ECHO machine were comparable, except for the amplitude.

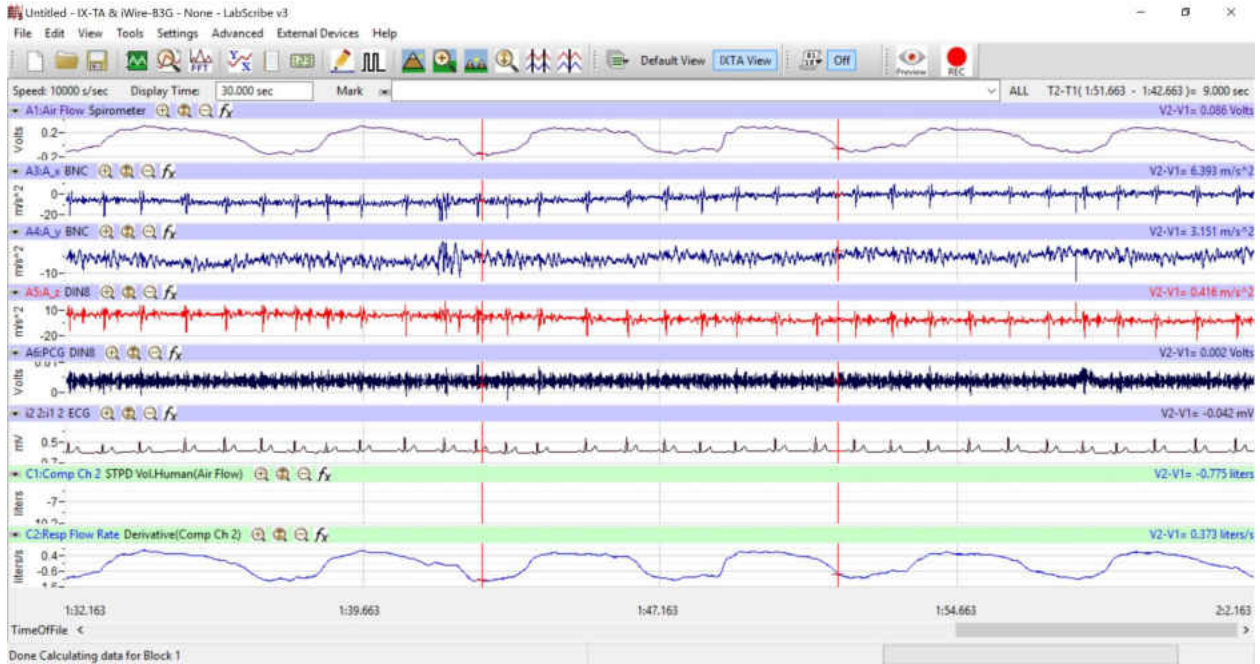


Figure 5.26. Measuring ECG, SCG, PCG and respiration flow rate simultaneously using iWorx TA Control Module and LabScribe software (iWorx Systems, Inc., Dover, NH).

5.4.1.3.1 Correlation between SCG Components and Heart Sounds

The SCG signal was bandpass filtered in certain frequency bands to extract its components. Figure 5.28 shows the synced M mode, heart sounds, and SCG signal components in different frequency bands. The SCG components in the 30 – 100 Hz band had similarities to the PCG signal. This suggests that some of the PCG information may be extracted from SCG high frequency components.

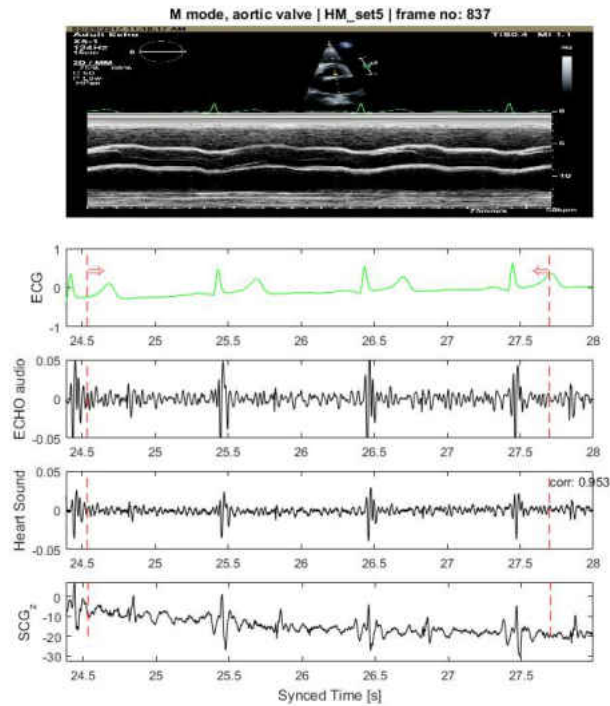


Figure 5.27. Synced ECHO image and SCG signal. The ECG, ECHO audio and PCG signals were also shown in the figure.

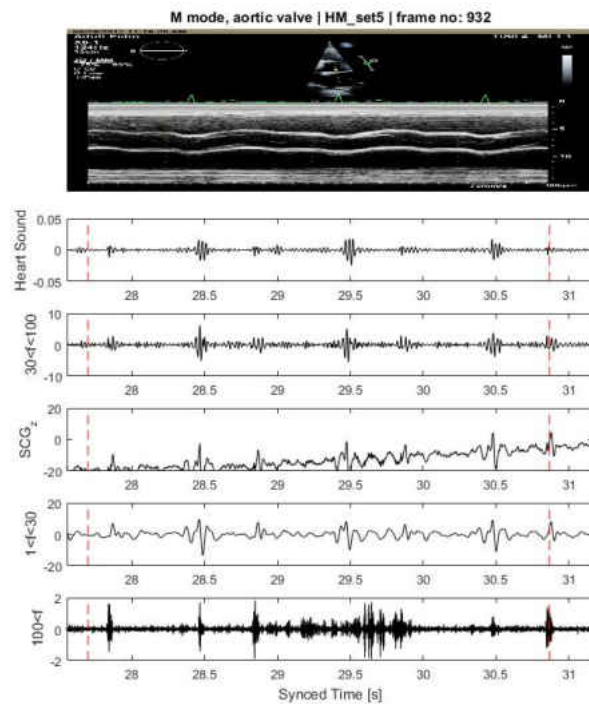


Figure 5.28. Synced ECHO image and SCG signal components. (from top to bottom) ECHO M-mode of aortic valve, heart sounds (PCG signal), band-pass filtered SCG signal between 30 and 100 Hz, SCG signal, band-pass filtered SCG signal between 1 and 30 Hz, High-pass filtered SCG signal with a cut-off of 100 Hz.

5.4.1.3.2 SCG Timing with Myocardial Strain

Figure 5.30 shows the myocardial strain curves for a representative expiratory and inspiratory SCG cycle. Small changes in the SCG waveform were seen with respiration. The strain in Figure 5.30 was negative and is defined as the fractional change in the heart tissue dimension in comparison with the original tissue dimension. The SCG waveform contained two major events, SCG1 and SCG2, which occurred close to the first and second heart sound timing, respectively. The changes in longitudinal strain was due to the well-known left ventricle twisting motion. The SCG signal peak (at SCG1 maximum) occurred shortly after the ECG R wave and during the early part of rapid ejection (RE). During ejection, the apex rotated counterclockwise while the base performed a clockwise rotation. This resulted in a decrease in the longitudinal length of the left ventricle. The myocardial strain increased (i.e. became more negative) and reached a plateau

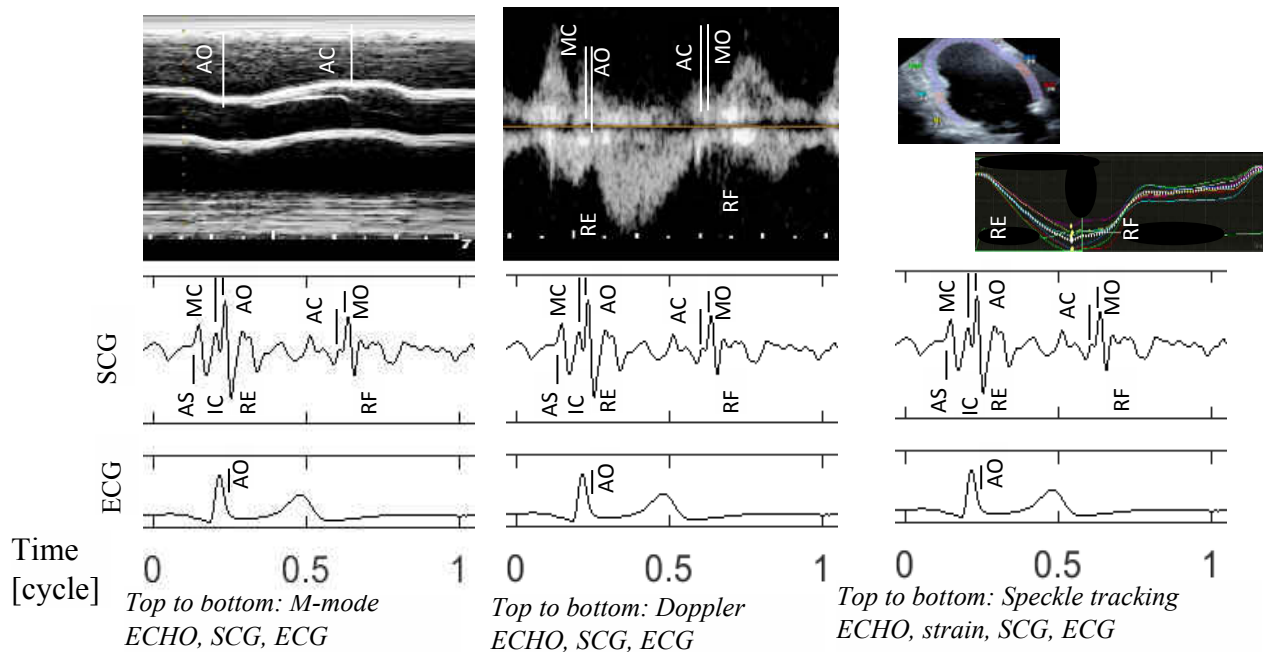


Figure 5.29. Simultaneous recording of ECHO, SCG and ECG, where several cardiac events can be identified in the SCG waveform such as: atrial systole (AS), mitral closing (MC), aortic valve opening (AO), isovolumic contraction (between MC and AO), rapid ejection (RE), aortic valve closure (AC), and rapid filling (RF).

(isovolumic relaxation) before the beginning of SCG2. Towards the end of SCG2, the strain started to be less negative and rapid filling (RF) took place.

The SCG wave timings were compared with the myocardial strain curve for the first time. The results showed that the heart muscle experienced lowest negative mechanical strain around SCG1, with the highest negative strain occurring just prior to SCG2. STE might help characterize the left ventricle (un-)twist patterns on the SCG waveforms which might lead to distinguishing normal SCG signals from abnormal ones. More studies are needed to investigate the differences in SCG morphology based on heart muscle contractile state in both healthy subjects and those with cardiovascular disease.

5.4.2 Finite Element Modeling

Finite element modeling (FEM) can be used to help understand the genesis of SCG, study the physiological sources of different SCG waves, and simulate SCG signal in different health and disease conditions. For example, the effect of sensor location, the amount of soft tissue (on the chest surface), and heart displacement on the SCG morphology might be investigated using FEM simulations. However, simulating the SCG signals using finite element analysis is a challenging engineering problem due to the complex physics (e.g. fluid-structure interaction, electromechanical model of the heart), nonlinear material properties (e.g. due to fiber orientations in heart muscles), and complex geometry involved.

In this section, a finite element model of simplified thoracic structures was developed to estimate surface response to subsurface vibratory sources. This model need to be expanded in future studies to help elucidate SCG transmission and genesis.

5.4.2.1 Methodology

The geometry was extracted from the computerized tomography (CT) scans of a male subject using image segmentations (Figure 5.30.top). The geometry was simplified to add CAD features (Figure 5.30.bottom). In this simplified geometry, the space between ribcage and spine, inside the thorax, was filled with a surrounding tissue. Heart geometry was not included in the simulation presented in this section. Instead, the heart volume was subtracted from the surrounding tissue medium to create the interface of heart and surrounding tissue. This interface is shown with red color in Figure 5.30.bottom. The spinal cord and ribcages were included and simplified to avoid high computational cost. These parts were surrounded by a layer of skin and soft tissue with a thickness of 5 mm.

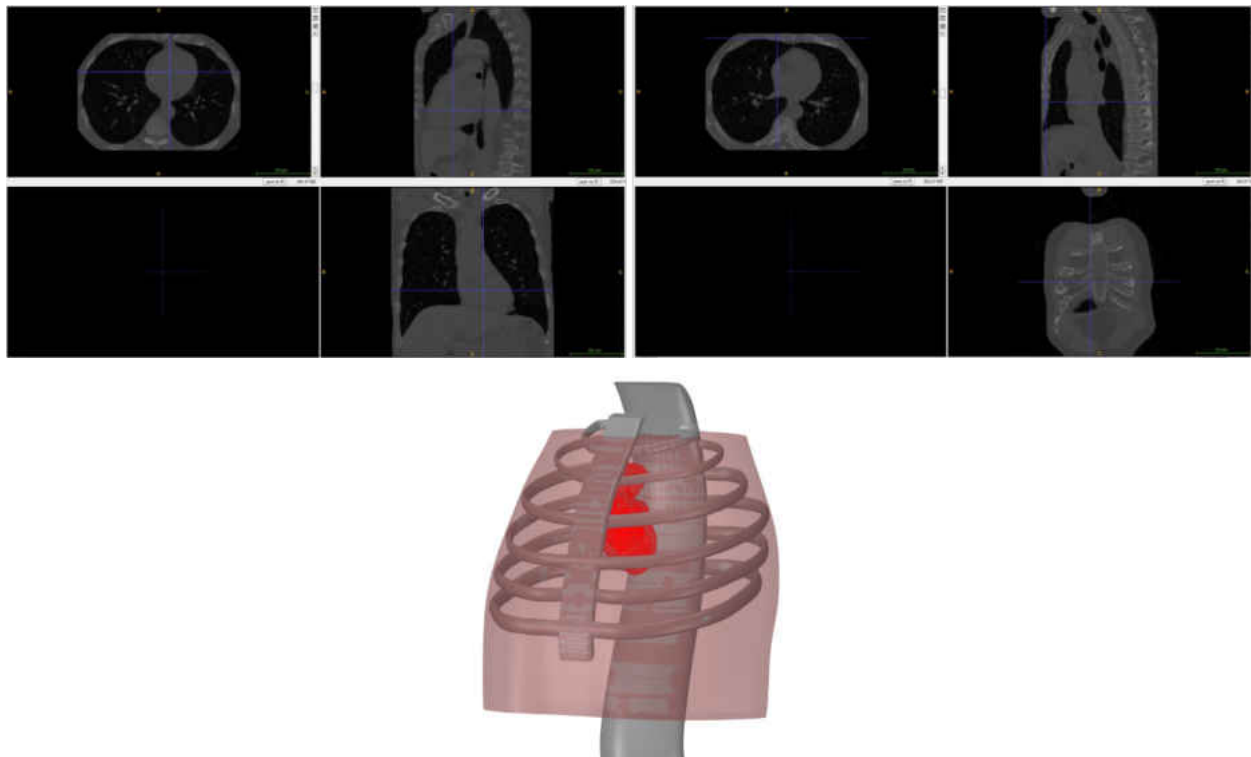


Figure 5.30. (top) CT scans of human thorax of a male subject, (bottom) computational geometry based on CT scan dimensions and simplified to add CAD features.

A smooth mesh was created using a total of 209,637 tetrahedral elements. Linear material properties were used for the tissues included in this simulation. The young modulus was 17 GPa, 21.3 kPa, and 4 MPa for ribcage, transitional tissue and soft tissue, respectively. The density was 1908, 394, and 1109 kg/m³ for ribcage, transitional tissue and soft tissue, respectively. A Poisson's ratio of 0.3, 0.49, and 0.49 was used for ribcage, transitional tissue and soft tissue, respectively. These values were obtained from literature. There are different ways to apply realistic boundary conditions to the geometry of this problem. For example:

- Using the heart wall displacement extracted by techniques such as 3D CT scan and speckle tracking echocardiography
- Using electromechanical modeling of heart muscle to simulate heart muscle movements
- Using fluid-structure interaction modeling such that after employing accurate material properties (e.g. by knowing fiber orientations in heart tissue), a realistic blood flow boundary condition lead to a realistic heart muscle movement

However, in this study, an approximate heart wall movement was applied to the interface of ventricles external walls and the transitional tissue to simulate heart movement. In addition, the top and bottom surface of spine were fixed. Simulation was done in ANSYS Mechanical.

5.4.2.2 Preliminary Findings

Figure 5.31.a shows contours of acceleration on the chest surface due to heart movement at different stages of the heart cycle (during systolic phase). The maximum acceleration was observed on the left side of chest surface in parallel to the 4th intercostal space. The acceleration and displacement on the chest surface are likely to be limited by the sternum, which can be clearly observed in the contours of displacement plotted at a cross-section of thorax as shown in Figure 5.31.b.

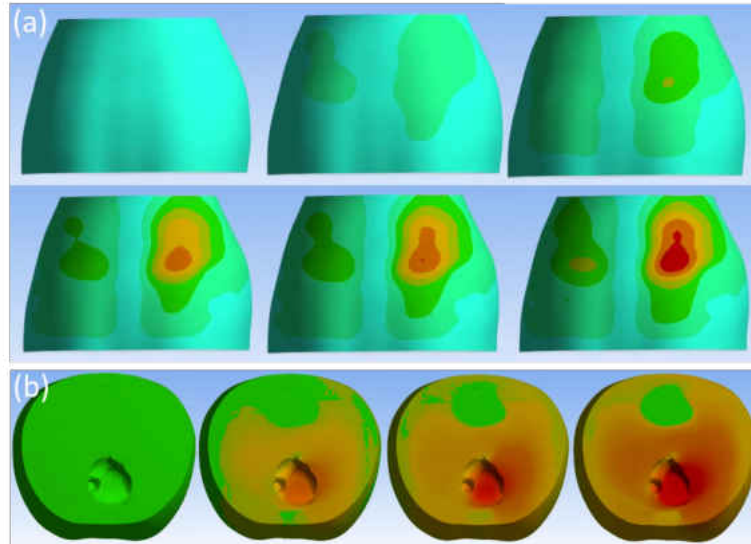


Figure 5.31. (a) Magnitude of the acceleration vector normal to the chest surface, (b) heart displacement due to the imposed boundary condition.

5.4.2.3 Future Work

The model presented in this section might be expanded in future studies to help elucidate the sources of heart induced vibrations on the chest surface. Potential improvement areas include:

- Adding more realistic geometry features (such as the geometry shown in Figure 5.32)
- Using better boundary conditions
- Adding nonlinear material properties

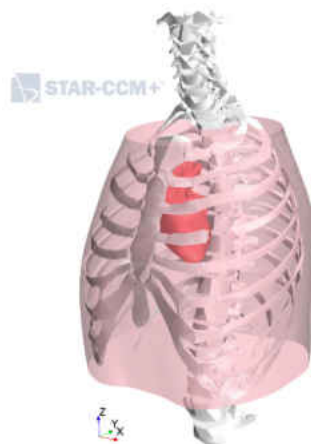


Figure 5.32. A more realistic geometry for future work. Here, the ribcage and spine are modelled with a more realistic geometry.

5.5 Summary

In this chapter, different human studies were conducted using the methods that have been described in the previous chapters. The first two studies investigated the effect of respiration on the SCG morphology and heart rate, respectively. Several criteria were used to group similar SCG events into two different clusters. These criteria included respiratory flow direction (inspiration vs expiration), lung volume (high vs low lung volume), and a hybrid criteria that combined the first two. Results showed that the respiratory flow direction was least accurate in grouping SCG events into two clusters, where SCG events in each cluster are more similar to each other. The hybrid criterion provided optimal separation of SCG events. Effective separation of SCG events into groups possessing minimal variability enables more precise estimation of SCG characteristics. In the last study, the physiological sources of the SCG waveforms were investigated using other well-known modalities such as ECHO and ECG. A finite element model of simplified thoracic structures was also developed to estimate surface response to subsurface vibratory sources. This model needs to be expanded in future studies to help elucidate SCG transmission and genesis.

The primary limitation of the human studies described in this chapter was the small number of subjects that participated. Future studies need to enroll larger number of subjects from a diverse population including different age, gender, weight, race, and clinical status.

CHAPTER 6: CONCLUSIONS

This dissertation is the result of research at the Biomedical Acoustics Research Laboratory at the University of Central Florida. The last section of CHAPTER 5 was done with the collaboration of the department of cardiovascular services at Nemours Children's Hospital. In the first section of this chapter, the contributions of this dissertation are summarized. In the second section, the current limitations in the field of SCG are described, and potential future works are discussed.

6.1 Contributions

The contributions of this dissertation includes:

- Identifying proper TFD methods for time-frequency analysis of SCG signals
- Proposing a new noise removal algorithm for SCG signals based on empirical mode decomposition
- Proposing a novel adaptive feature extraction algorithm for the classification of SCG signals
- Proposing an efficient classification pipeline for the classification of SCG signals
- Effect of lung volume on the SCG signal morphology
- Effect of lung volume on heart rate variability
- Proposing a new algorithm for efficient grouping of SCG events into two clusters where SCG events in each cluster are similar

6.2 Future Work

Despite numerous studies in the field, there are still some limitations that need to be addressed in the future work. These limitations include, but are not limited to:

- SCG variability: SCG morphology varies with different factors such as gender, heart displacements, respiration, sensor location, the amount of soft tissue between heart and sensor, and different heart diseases. Although, there are studies that have investigated the effect of some of these factors, the SCG signals morphological variations are not thoroughly investigated yet. The results of such investigations might help identify features that result in better classification of SCG signals in different conditions.
- Lack of accepted standard for the cardiomechanical fiducial points: SCG morphology changes with different factors. These factors include inter and intra subject variability, sensor locations, lung volume phases, etc. It would be useful to investigate the effect of these factors on the location of different SCG signal fiducial points such as valve opening and closure times.
- SCG genesis is still in question: Although there are several studies aiming at elucidating the physiological sources of the SCG signals, this question is still open and needs more attention. SCG signals are believed to be affected by factors such as respiration, intrathoracic pressure and heart displacement. Therefore, these parameters must be considered while the SCG genesis is investigated. The effect of other factors such as the twisting motion of heart might help understand these vibrations better.
- More realistic simulated SCG signals: Simulated signals might be used for pre-clinical studies and encourage more researchers to work in this area because of the ease of access to the signals similar to the real signals. Finite element models with realistic geometries and material properties might be used to generate synthetic signals that are

similar to the actual SCG signals. Proper mathematical and control methods might also be helpful in SCG signal modeling.

- A common comprehensive library and database of SCG signals: This database will provide raw materials for the researchers that are interested in analyzing biomedical signals. MIT-BIH arrhythmia database is a good example of biomedical signals database. This database played an important role in stimulating both basic research works and medical device developments. A similar database for SCG signals might attract a lot of researchers to study and develop the field of seismocardiography.
- Investigating correlation between SCG and other signals that are related to the mechanical aspects of the cardiac activity such as PCG and BCG: This might help develop hybrid diagnosis techniques based on “only mechanical” signals.

APPENDIX A. SCG ATTACK AND DECAY FEATURES

A.A.1 Introduction

This Appendix provides some preliminary results for the SCG attack and decay rate estimation which might be used as temporal features of SCG waveforms.

A.A.2 Methodology

Matrix pencil method (MPM) is a method to estimate poles and frequencies from exponentially damped or undamped sinusoidal sequences. One advantage of MPM is that it gives more accurate results compared to the polynomial method over all ranges of signal-to-noise ratio (SNR) and the degree of polynomial [215]. In this section, MPM is used to estimate the attack and decay rate of the SCG events. These values might then be used as temporal features of the SCG signals. Assume that x_t is a signal that is sampled at a sampling frequency of F_s . MPM can estimate x_t by a sum of L ($\sim p/2$) exponentially damped real sinusoids:

$$x_t = \sum_{i=1}^L A_i e^{-\alpha_i t} \cos(\omega_i t + \varphi_i) \quad (\text{A-A-1})$$

where $A_i, \alpha_i, \omega_i, \varphi_i$ are the initial amplitudes, damping factors, frequencies (in radian) and phases respectively.

$$x_l = [x_l, x_{l+1}, \dots, x_{N-p+l-1}]^T \quad (\text{A-A-2})$$

where L is called the pencil parameter. Then a set of vectors can be formed as follows:

$$p_l = x_l - \lambda x_{l-1} \quad l = 1, 2, \dots, p \quad (\text{A-A-3})$$

$$X_{0(N-p) \times p} = [x_{p-1}, x_{p-2}, \dots, x_0] \quad (\text{A-A-4})$$

$$X_{1(N-p) \times p} = [x_p, x_{p-1}, \dots, x_1] \quad (\text{A-A-5})$$

Then,

$$[p_p, p_{p-1}, \dots, p_1] = X_1 - \lambda X_0 \quad (\text{A-A-6})$$

The poles of x_t are the generalized eigenvalues of the matrix pencil $X_1 - \lambda X_0$. The frequencies and damping factors of the L sinusoids can then be computed as following:

$$\omega_j = \text{imag}(\lambda_j) \times F_s \quad j = 1, \dots, L \text{ (number of sinusoids)} \quad (\text{A-A-7})$$

$$\alpha_j = -\log(|\lambda_j|) \times F_s \quad (\text{A-A-8})$$

After computation of the frequencies and the damping factors, the values of initial amplitudes and phases can be calculated as following: first, we have to choose n arbitrary points from the signal, where n is the number of poles of the signal that was found by MPM.

$$n \text{ arbitrary points: } (t_1, b_1), \dots, (t_n, b_n) \quad (\text{A-A-9})$$

$$\text{Time} = [t_1, \dots, t_n], \quad B = [b_1, \dots, b_n] \quad (\text{A-A-10})$$

Now, the following set of n -equation n -unknown can be formed:

$$\begin{aligned} b_1 &= A_1 e^{-\alpha_1 t_1} \cos(\omega_1 t_1 + \varphi_1) + A_2 e^{-\alpha_2 t_1} \cos(\omega_2 t_1 + \varphi_2) + \dots \\ &\quad + A_L e^{-\alpha_L t_1} \cos(\omega_L t_1 + \varphi_L) \\ &= A_1 e^{-\alpha_1 t_1} \{ \cos(\omega_1 t_1) \cos(\varphi_1) - \sin(\omega_1 t_1) \sin(\varphi_1) \} \\ &\quad + A_2 e^{-\alpha_2 t_1} \{ \cos(\omega_2 t_1) \cos(\varphi_2) - \sin(\omega_2 t_1) \sin(\varphi_2) \} + \dots \\ &\quad + A_L e^{-\alpha_L t_1} \{ \cos(\omega_L t_1) \cos(\varphi_L) - \sin(\omega_L t_1) \sin(\varphi_L) \} \\ &\quad \vdots \\ b_n &= A_1 e^{-\alpha_1 t_n} \cos(\omega_1 t_n + \varphi_1) + A_2 e^{-\alpha_2 t_n} \cos(\omega_2 t_n + \varphi_2) + \dots \\ &\quad + A_L e^{-\alpha_L t_n} \cos(\omega_L t_n + \varphi_L) \\ &= A_1 e^{-\alpha_1 t_n} \{ \cos(\omega_1 t_n) \cos(\varphi_1) - \sin(\omega_1 t_n) \sin(\varphi_1) \} \\ &\quad + A_2 e^{-\alpha_2 t_n} \{ \cos(\omega_2 t_n) \cos(\varphi_2) - \sin(\omega_2 t_n) \sin(\varphi_2) \} + \dots \\ &\quad + A_L e^{-\alpha_L t_n} \{ \cos(\omega_L t_n) \cos(\varphi_L) - \sin(\omega_L t_n) \sin(\varphi_L) \} \end{aligned} \quad (\text{A-A-11})$$

Then, the following matrix T can be formed:

$$T = \begin{bmatrix} \eta_1^1 & \beta_1^1 & \cdots & \eta_1^L & \beta_1^L \\ \eta_2^1 & \beta_2^1 & \cdots & \eta_2^L & \beta_2^L \\ \vdots & \vdots & \ddots & \vdots & \vdots \\ \eta_n^1 & \beta_n^1 & \cdots & \eta_n^L & \beta_n^L \end{bmatrix} \quad (\text{A-A-12})$$

where

$$\eta_i^j = e^{-\alpha_j t_i} \cos(\omega_j t_i) \quad (\text{A-A-13})$$

$$\beta_i^j = e^{-\alpha_j t_i} \sin(\omega_j t_i) \quad (\text{A-A-14})$$

where $i = 1, \dots, n$ (number of poles) and $j = 1, \dots, m$ (number of sinusoids). Now,

$$A = T \setminus B = [a_1, a'_1, \dots, a_L, a'_L] \quad (\text{A-A-15})$$

From matrix A , initial amplitudes and phases of the sinusoids are derived as follows:

$$A_j = \sqrt{a_j^2 + a_j'^2} \quad (\text{A-A-16})$$

$$\tan(\varphi_j) = \frac{a_j'}{a_j} \quad (\text{A-A-17})$$

When the length N of the data record is a fixed parameter, empirical optimal values for pencil parameter range from $N/3$ for noisy signals to $N/2$ for signals with a higher SNR.

A.A.3 Results

A.A.3.1 Synthetic Damped Signal

In order to test the MPM/LMS method, a synthetic signal is generated that is the summation of three damped sinusoids with the same damping ratio and different frequencies, amplitudes and initial phases (Figure A.1.1). Different input signals with different combinations of frequencies, damping factors, amplitudes and phases were tested by the code. For all of the test signals, the code could accurately find the frequencies and damping factors. However for the sampling frequencies of multiple of 30 Hz, it has hard time to find the correct amplitudes and initial phases.

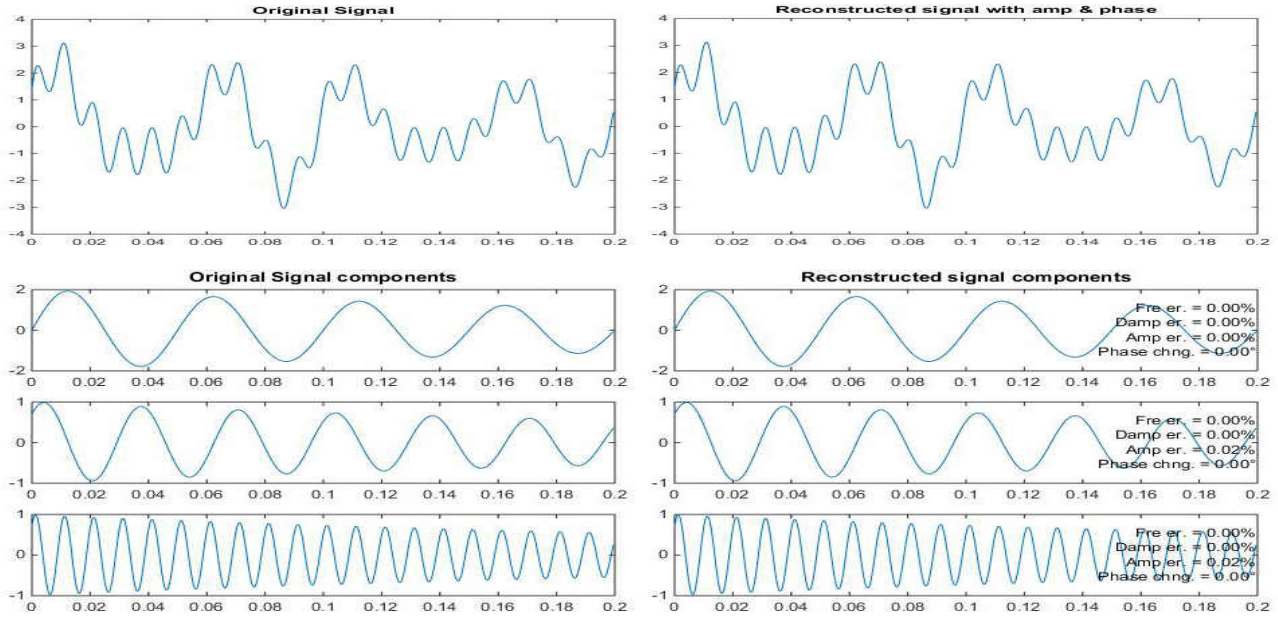


Figure A.A.1. (a) Original synthetic signal and its components (b) Reconstructed synthetic signal and its components.

A.A.3.2 Synthetic SCG

A synthetic SCG is created from the summation of 2 sinusoids. The amplitude of sinusoids is modulated once by using a cosine function and another time by using an exponential function. The synthetic signal, its components and the exponential amplitude envelope are shown in Figure A.A.2.

The synthetic SCG is composed of two parts; first a growing part and then a decaying part. In order to be able to use the MPM properly, it is required to split the SCG signal into two parts, growing (attack) and decaying (decay). Final MPM/LMS results highly depends on the location of the splitting point (separation point). Therefore, choosing a proper separation point is one of the most important factors in order to get good and reasonable results from MPM. Here, three different separation points are considered for each signal; the minimum of the signal, the maximum of the signal, and the middle point between the maximum and the minimum of the signal. The analysis

is performed in different conditions in order to find the best possible results for the synthetic SCG.

These conditions are listed below:

- Amplitude modulation by using cosine and exponential functions.
- Adding zeros to the end of the signal.
- Flipping the decaying part of the signal and finding its characteristics. Again flipping it and put it together with the growing part and reconstructing the whole synthetic SCG signal.
- Running MPM and finding the characteristics of the growing part, then flipping the signal and again running MPM and finding the characteristics of the new growing part (originally decaying part). Putting together the results and reconstructing the signal.

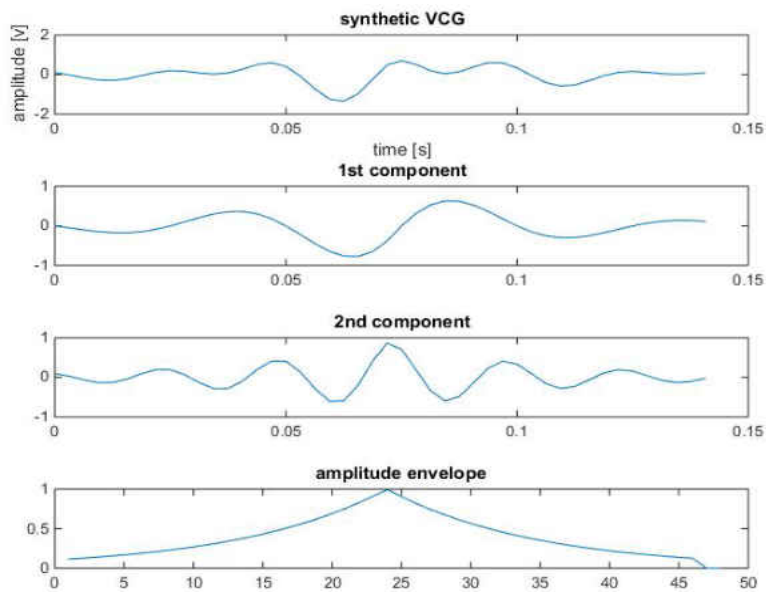


Figure A.A.2. Synthetic SCG, its components and amplitude envelope.

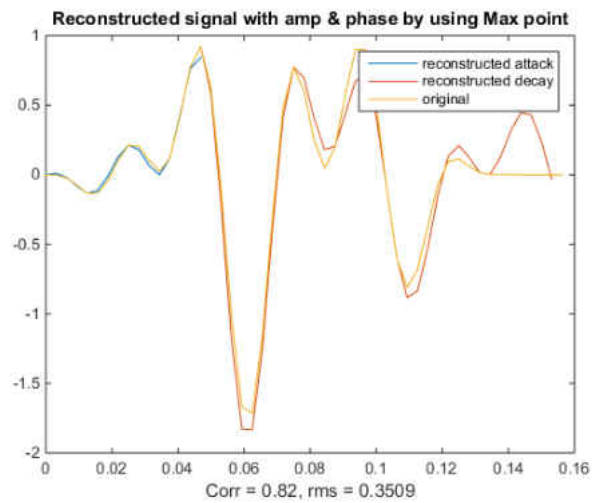
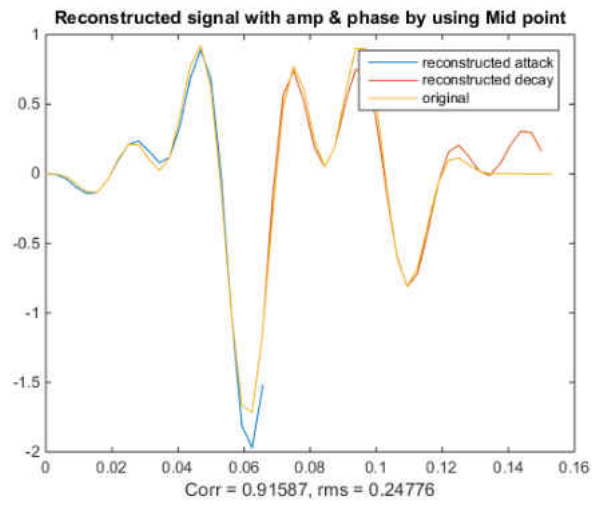
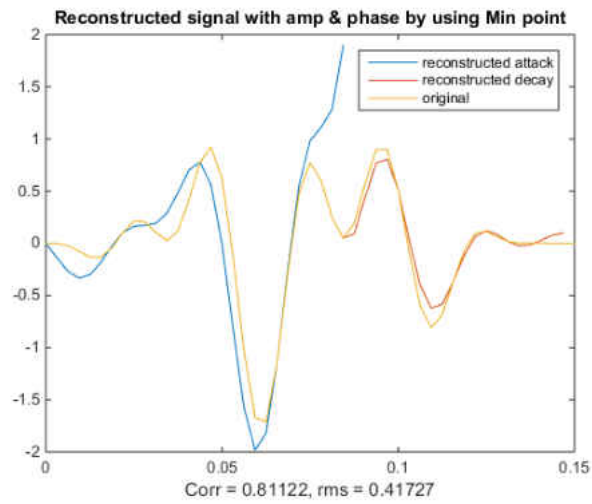
A.A.3.3 Attack and Decay Rate Results Summary

The results of MPM analysis on the 3 above mentioned signal categories were summarized in Table A.A.1.

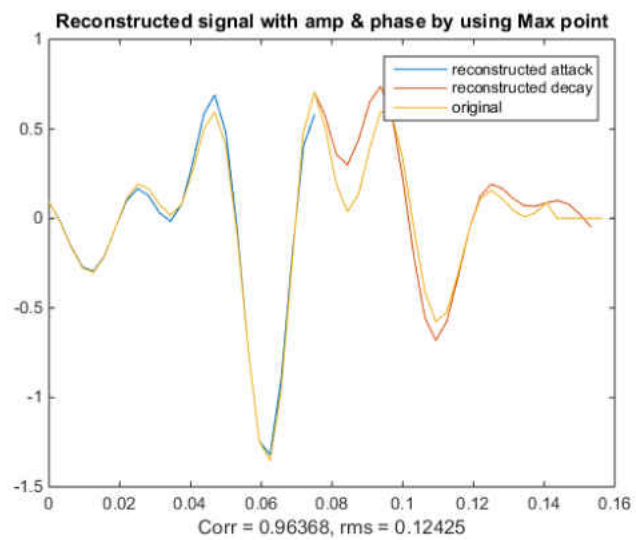
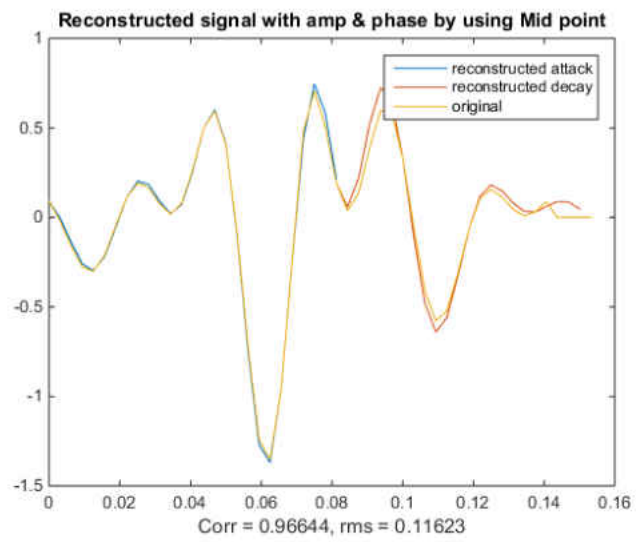
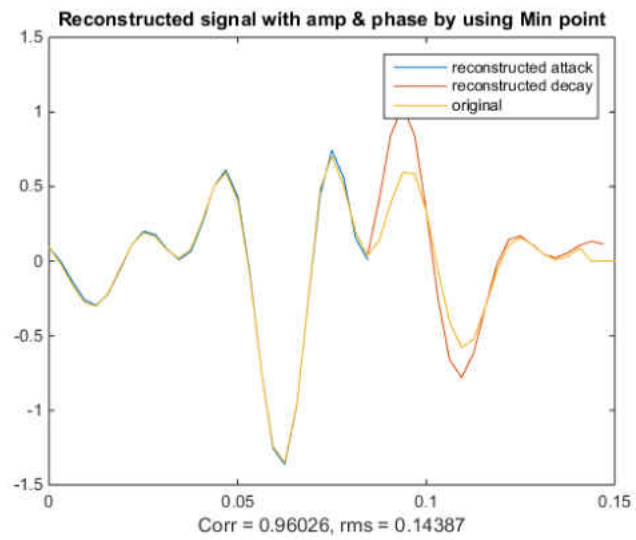
Table A.A.1. Results summary of attack and decay rate feature.

Signal	Frequency	Damping	Amplitude	Phase	Issues
Synthetic signal	✓ Error 0%	✓ Error 0%	✓ Error less than 0.1% ** See issues.	✓ Error less than 0.1% ** See issues.	** For sampling frequencies of multiple of 30, it gives the correct frequency and damping of the signal, but the amplitude and phase have high error.
Synthetic SCG (cosine envelope)	Error less than 5%	NA (because the amplitude is not exponentially damped.)	** See figures.	** See figures.	
Synthetic SCG (exponential envelope)	Error less than 2.5% (e.g. while the signal frequencies were: (20, 40), the method could estimate them as: (19.7153, 40.5603), (20.0000, 40.0000), (19.5421, 40.5603), (20.0350, 39.3186))	Error less than 2% (e.g. while the signal damping was 30, the method could estimate it as: 30.0000, 33.8837, 32.2189, 30.7499, 31.8445, 34.0729)	** See issues and figures.	** See issues and figures.	** The signal with exponential envelope has lower rms and higher correlation with respect to the one with cosine envelope
Actual SCG					The result highly depend on the general appearance of the SCG. For instance, for those SCGs that don't look like they are damped, the code even can't run. See

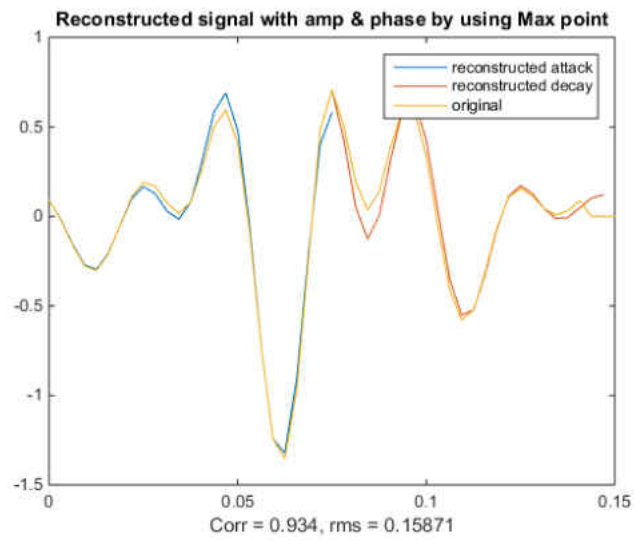
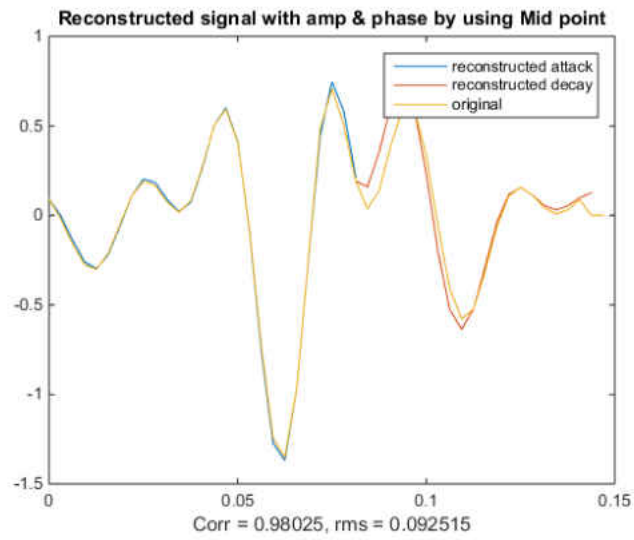
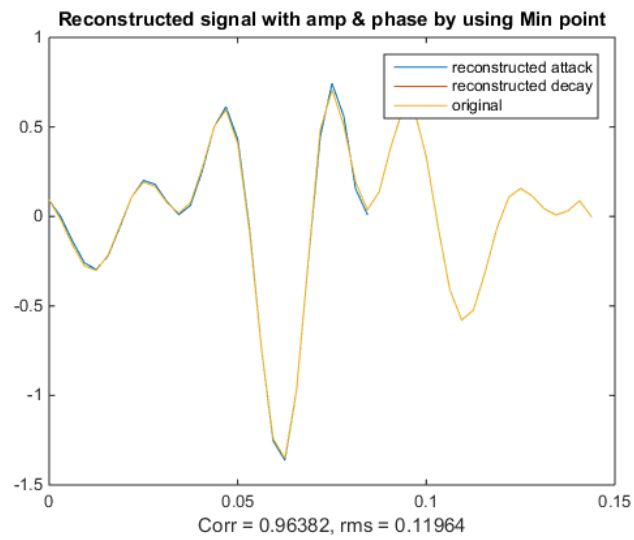
Synthetic VCG with cosine envelope (zeros at end, FlipDecay = 0):



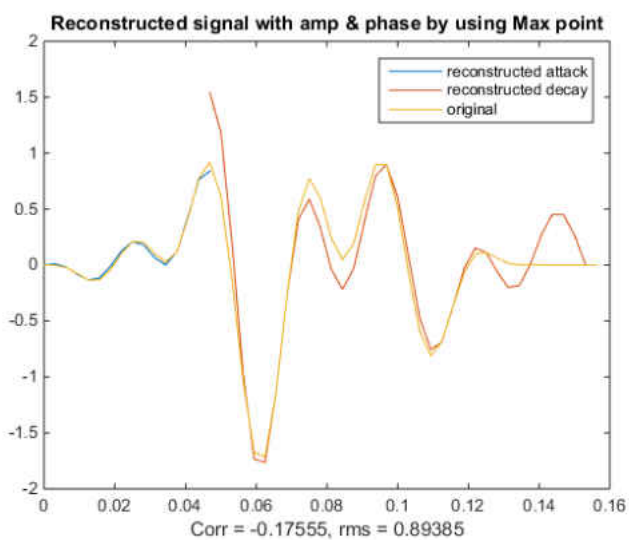
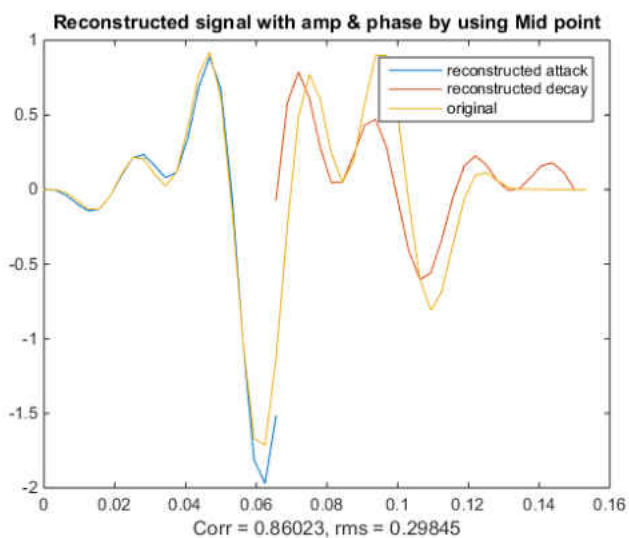
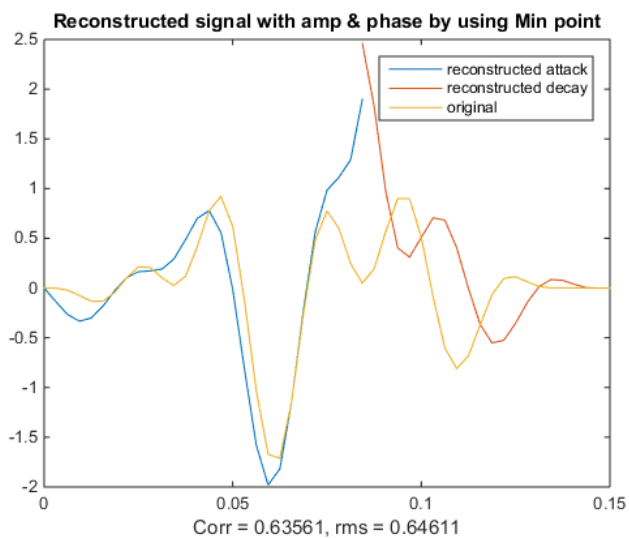
Synthetic VCG with exponential envelope (zeros at end, FlipDecay = 0)



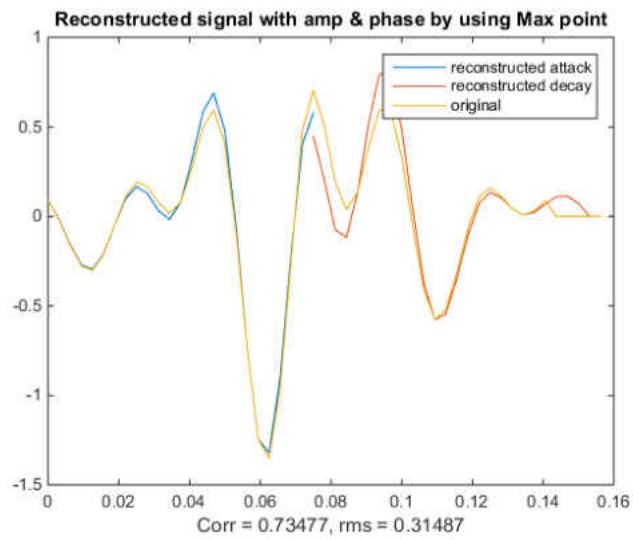
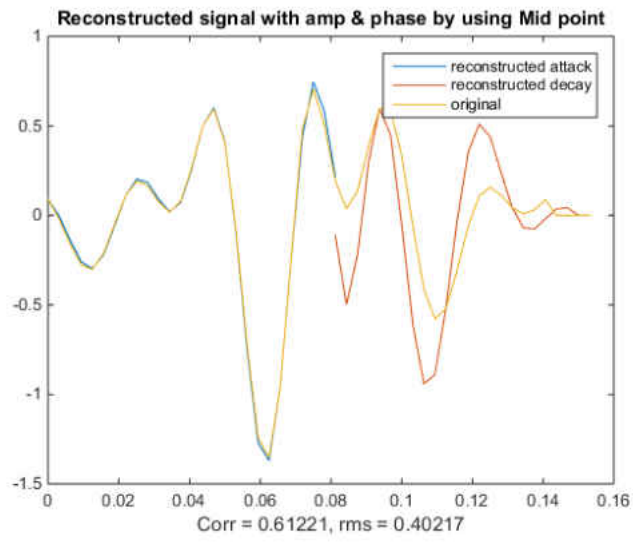
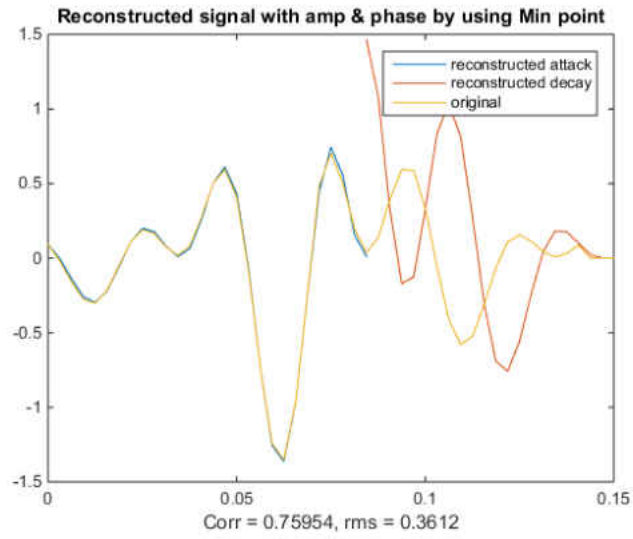
Synthetic VCG with exponential envelope (removing zeros at end, FlipDecay = 0)



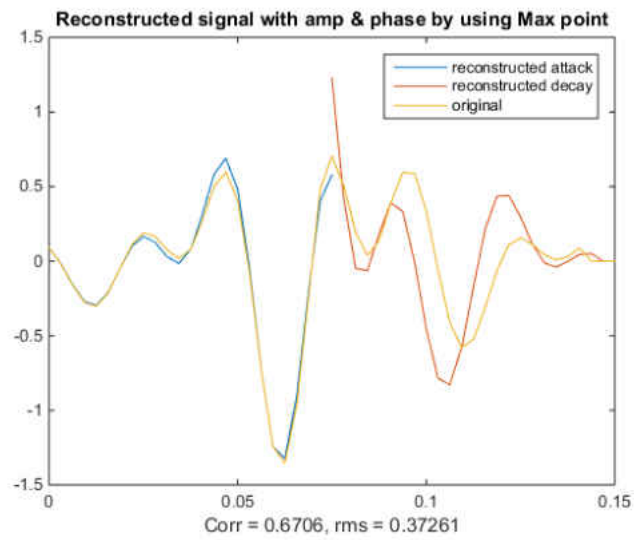
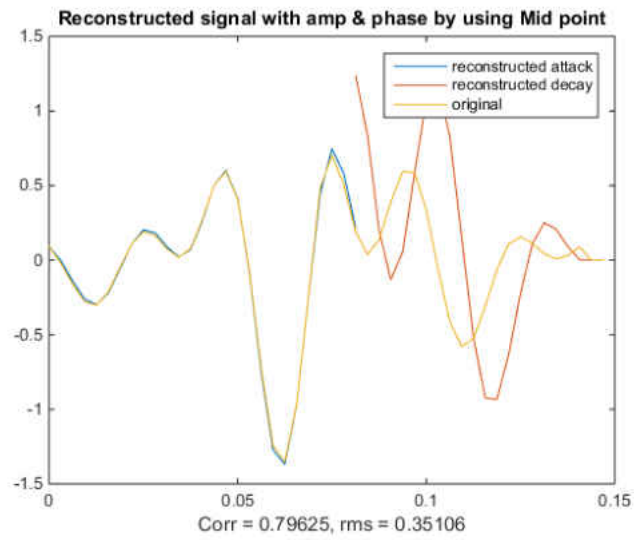
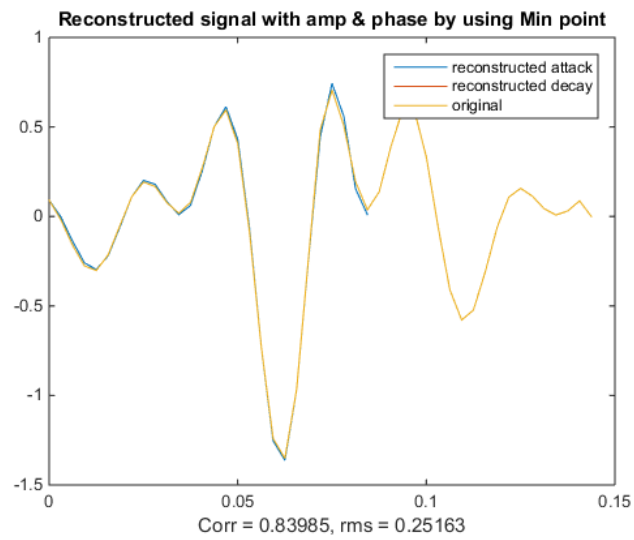
Synthetic VCG with cosine envelope (zeros at end, FlipDecay = 1)



Synthetic VCG with exponential envelope (zeros at end, FlipDecay = 1)



Synthetic VCG with exponential envelope (removing zeros at end, FlipDecay = 1)



APPENDIX B. CWT TFD SMOOTHING

A.B.1 Introduction

This Appendix provides complementary data about techniques that were used to smooth CWT TFD.

A.B.2 Methodology

The pure WT gives a TFD that consists of discrete regions. The following solutions is tried to get a smoother TFD.

- Using Hilbert transform to smoothen the WT spectrum
- Using “envelope1” function taken from Matlab central: smoothen a matrix (e.g. the spectrum of a TFD) in one direction (in direction of rows or columns)
- Using “smooth2a” function taken from Matlab central: smoothen a matrix (e.g. the spectrum of a TFD) in both direction
- Using Matlab built “envelope” function: smoothen a matrix (e.g. the spectrum of a TFD) in one direction

A.B.3 Results

Using the above solutions, the spectrums were smoothed in time direction for a decaying chirp. Also, the spectrum amplitude and the amplitude of the smoothed WTs were normalized with respect to their max value. Figure A.B.1 shows the results:

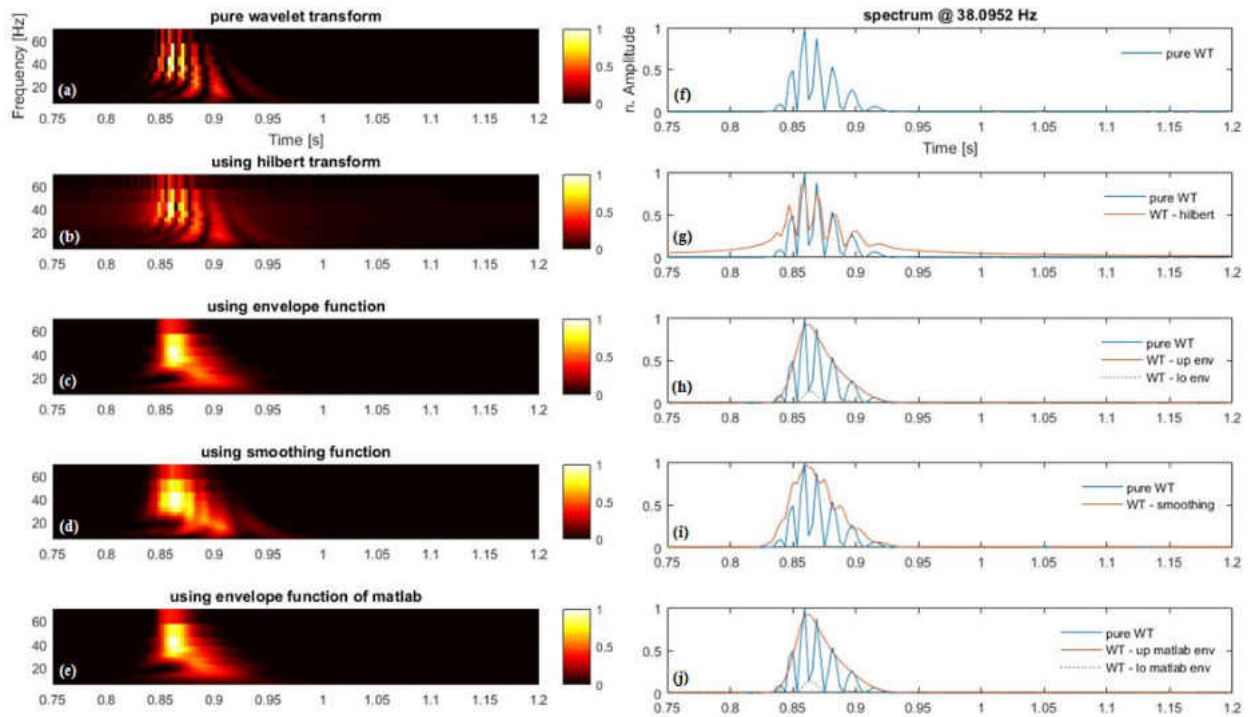


Figure A.B.1. Smoothing the spectrum of WT TFD (a) WT TFD without smoothing, (b), (c), (d) and (e) WT smoothed in time domain by HT, envelope1 (spline) function taken from Matlab central, smooth2a taken from Matlab central and Matlab built envelope (peak) function respectively. Figures (f), (g), (h), (i) and (j) represent the amplitude of the spectrum at 38.0952 Hz for WT without smoothing, WT smoothed in time domain by HT, envelope function taken from Matlab central, smooth2a taken from Matlab central and Matlab built envelope function respectively.

Then, the results were smoothed in the frequency domain for the same signal as well. When the amplitude smoothed by “envelope (peak)” and “envelope1 (spline)” in both of time and frequency domains, some regions with very high amplitude values were seen in the upper left side of the TFD plot, as seen in the following figure.

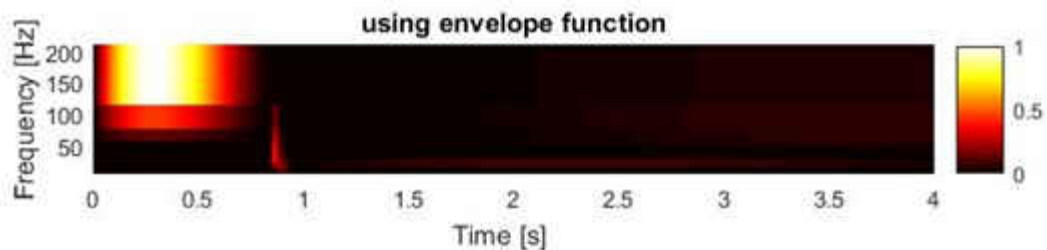


Figure A.B.2. Issue of false high amplitudes in the upper left corner of the TFD when using "envelope (peak)" or "envelope1 (spline)"

This issue was due to having two rows of zeros in the spectrum matrix and was fixed by adding a noise matrix composed of very small random numbers to the spectrum matrix. The following figure shows the results after fixing the above issue.

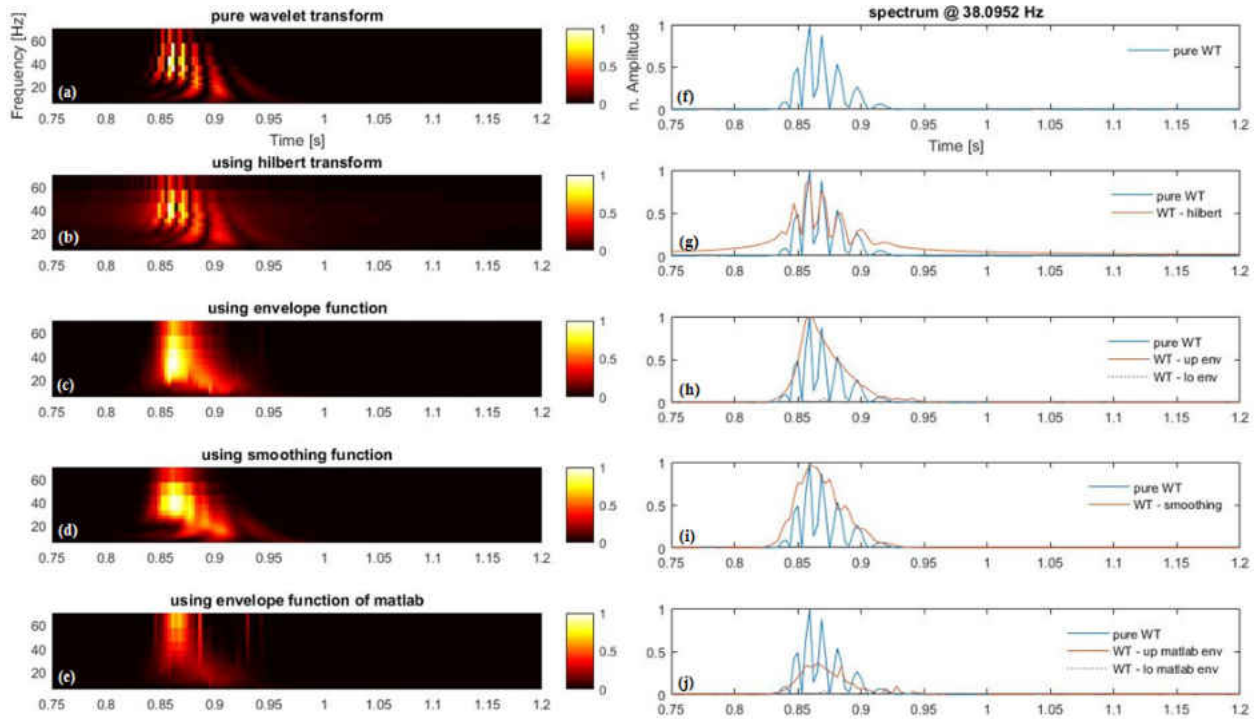


Figure A.B.3. Smoothing the spectrum of WT TFD (a) WT TFD without smoothing, (b), (c), (d) and (e) WT smoothed in both of time and frequency domains by HT, envelope function taken from Matlab central, smooth2a taken from Matlab central and Matlab built envelope function respectively. Figures (f), (g), (h), (i) and (j) represent the amplitude of the spectrum at 38.0952 Hz for WT without smoothing, WT smoothed in both of time and frequency domains by HT, envelope function taken from Matlab central, smooth2a taken from Matlab central and Matlab built envelope function respectively.

As seen in the above figure, the Matlab built “envelope” function doesn’t show good performance. To investigate this issue, the amplitude was plotted along $t = 0.86$ s for the spectrums that were smoothed by “envelope1” taken from Matlab central and Matlab built “envelope”.

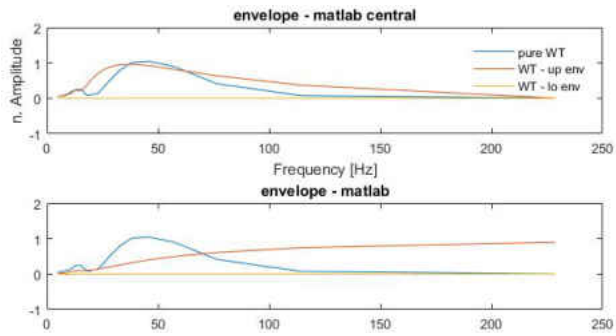


Figure A.B.4. Amplitude of the WT spectrum smoothed by envelope1 taken from Matlab central (upper) and Matlab built (lower) envelope function along $t = 0.86$ s

APPENDIX C. FURTHER TFD RESULTS

A.C.1 Introduction

This Appendix provides complementary results to section 3.3.5.7.

A.C.2 Results

Time frequency distribution for rest of the subjects are shown in Figure A.C.1. In these figures: (a) Time series. The time-frequency distribution using: (b) STFT, (c) CWT-Morl, (d) CWT-Haar, (e) CWT-db4, (f) CWT-Coif5, and (g) PCT is also shown. The PSD for each TFD is shown to the left of the distribution.

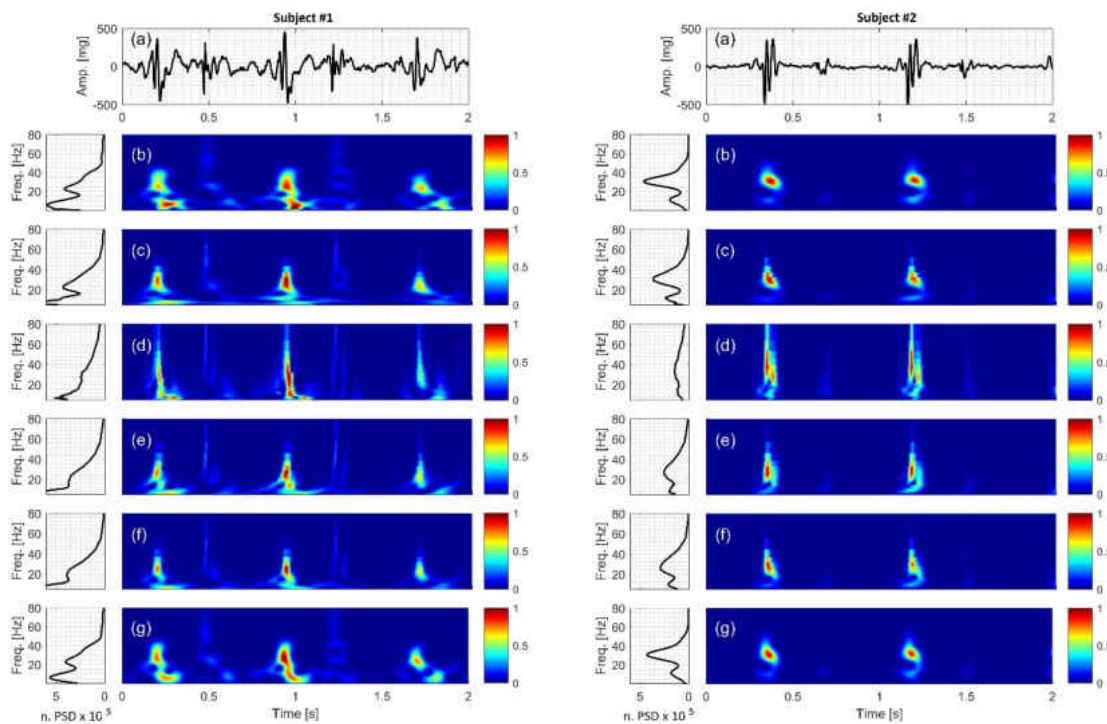


Figure A.C.1. Time-frequency distribution results for rest of the study subjects.

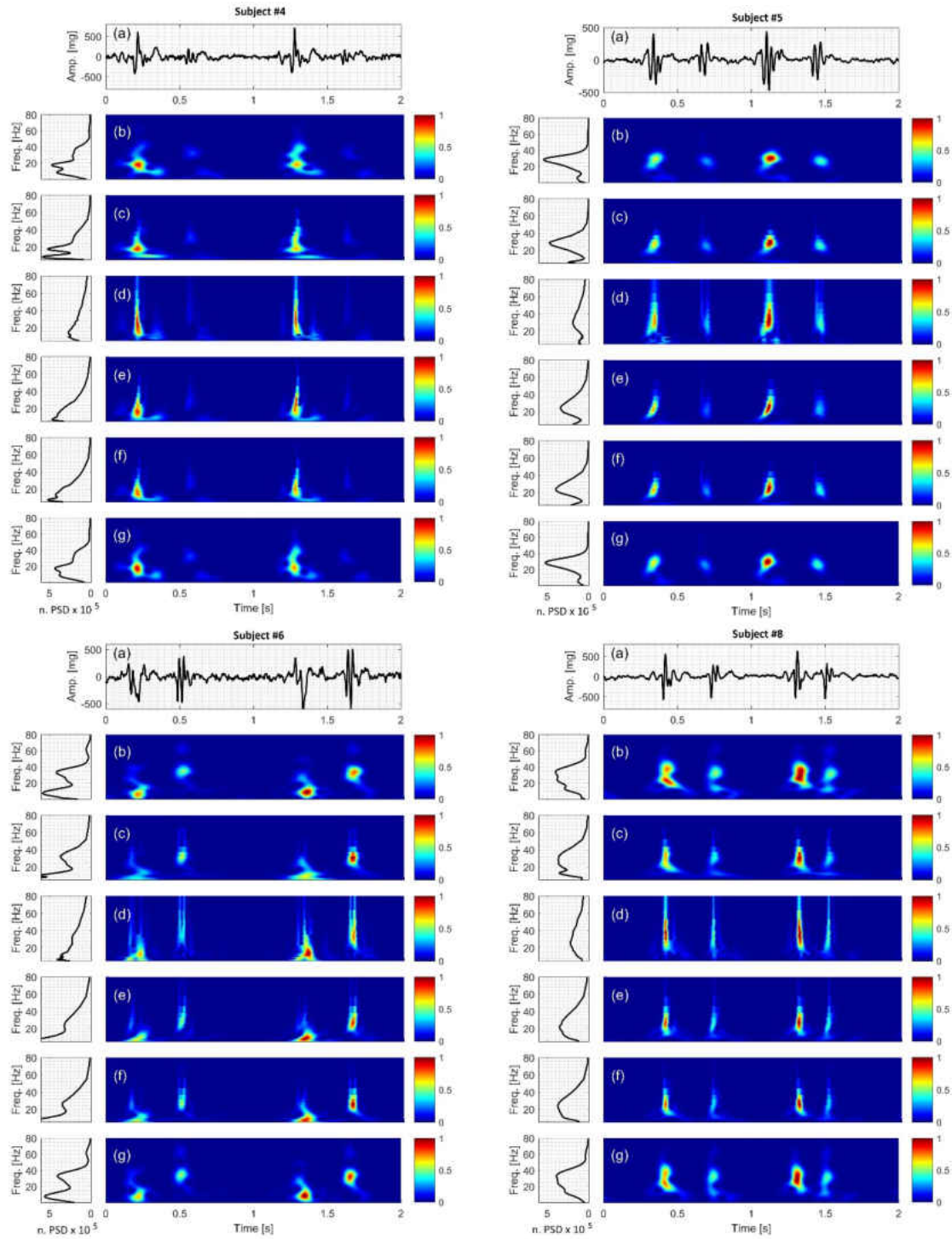


Figure A.C.1 (continued). Time-frequency distribution results for rest of the study subjects.

APPENDIX D. FURTHER EEMD RESULTS

A.D.1 Introduction

This Appendix provides complementary results to section 2.3.2.

A.D.2 Methodology

Two different signals were used in this study; a simulated SCG and an actual SCG. The simulated SCG signal consisted of a pure tone at 40 Hz and a varying frequency component ranging from 7 to 20 Hz. To measure the actual SCG, a light-weight (2 gm) accelerometer (PCB piezotronics, Depew, NY) was placed at the left sternal border along with the fourth intercostal space on the chest surface of healthy volunteers. The signal was acquired and processed using Matlab (R2015b, The MathWorks, Inc, Natick, MA) at a sampling frequency of 3200 Hz down-sampled to 320 Hz. Since respiratory noise have significant energy above 100 Hz, signals were filtered using an IIR Butterworth low-pass filter with a cut-off of 100 Hz to remove that noise. To evaluate the capability of EEMD-based filter in noise cancellation, the SCG signals were polluted by two sets of synthetic noise; white Gaussian noise and composite noise.

- 1) White Gaussian noises, n_{wgn} , were generated with the signal-to-noise ratio (SNR) ranging from 1 to 20 dB.
- 2) A synthetic respiratory noise with a reparation rate of 12 breaths per minute was modeled as

$$n_{resp} = 20 \times \sin(0.4\pi t) \quad (\text{A.D.1})$$

The composite noise was then defined as

$$n_{comp} = n_{wgn} + n_{resp} \quad (\text{A.D.2})$$

A.D.3 Results

Figure A.D.1 shows the EEMD-derived IMFs and corresponding IMFs power spectrums of the simulated SCG contaminated with the composite noise. The algorithm decomposed the signal

into 11 mode functions and a residue. The higher frequency component of the SCG events (40 Hz) was localized in the second IMF. The lower frequency component (7-20 Hz) was distributed in the IMFs #3 through #5. The first IMF predominantly consisted of Gaussian noise. In addition, the synthetic respiratory noise was concentrated in IMF #8 and #9.

The EEMD decomposed the actual SCG with composite noise into 11 IMF components and a residue (Figure A.D.2). The power spectrum of these IMFs were calculated using polynomial chirplet transform and is shown in Figure A.D.2 as well. The previous study [201] shows that this SCG signal consists of two dominant frequency components; a component at 37.50 Hz and a varying frequency component between 10 and 21 Hz (peaked at 18.75 Hz). Figure A.D.2 shows that the 37.50 Hz component was localized in IMF #2, while the varying frequency component was distributed in IMF #3 and #4. The high frequency Gaussian noise was resided in the first IMF. IMF #8 and #9 contained the synthetic respiratory noise.

A.D.4 Conclusions

Partial summation of IMF components was an effective way to reduce the high-frequency Gaussian noise and low-frequency respiratory noise from SCG signals. The physical meaning and statistical significance of the EMD- and EEMD-derived IMF components are still in question. More studies may be warranted to document the correlation between the physiological sources of SCG and intrinsic mode functions which in turn may result in more accurate and efficient EEMD-based filtering performance.

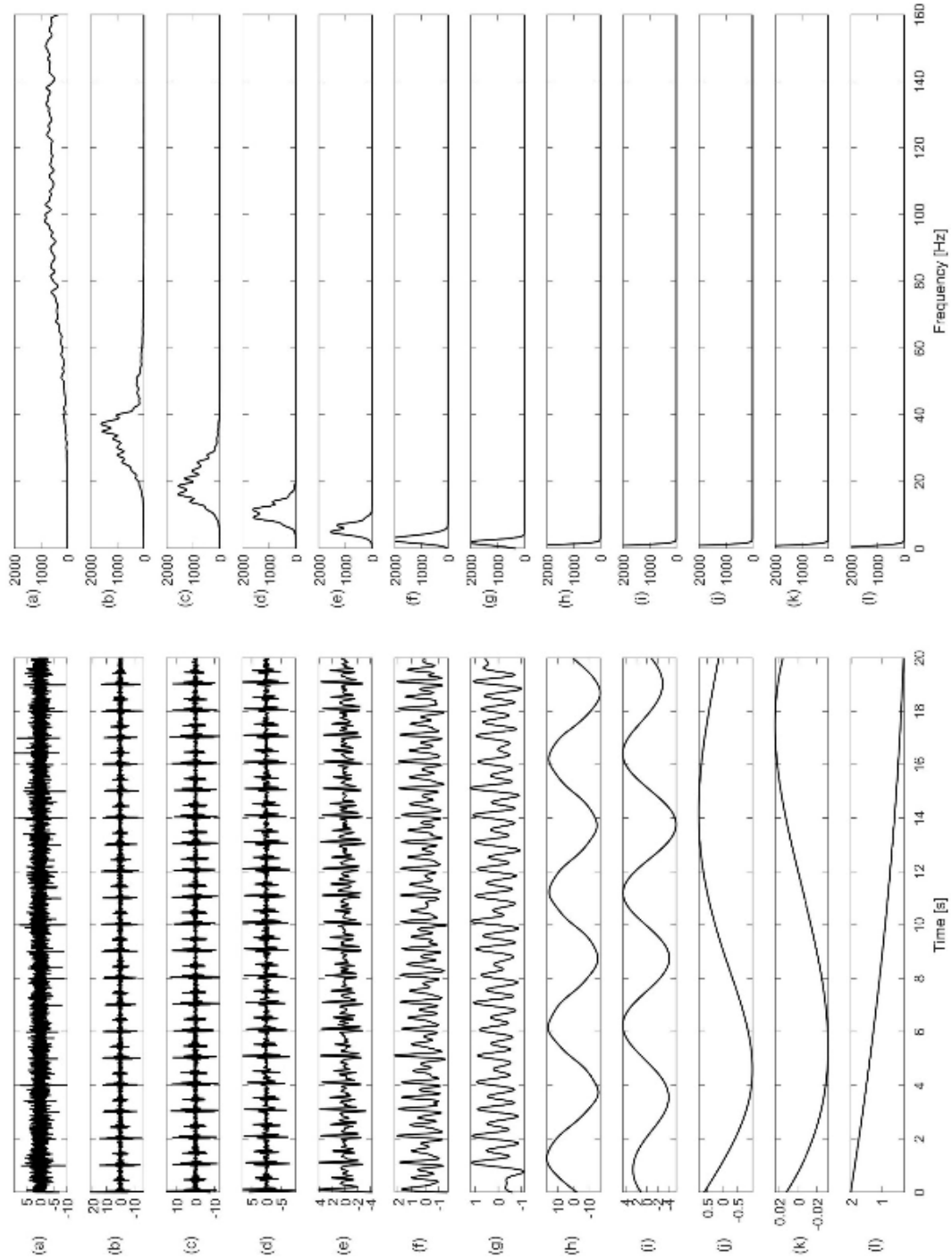


Figure A.D.1. Simulated SCG contaminated by composite noise (respiratory noise + Gaussian noise with SNR = 10 dB). (left) EEMD-derived IMF components. The signal was decomposed into 11 IMFs (subfigure a through k) and a residue (subfigure l). (right) The power spectral density of the IMFs and residue. Most part of the high-frequency Gaussian noise is concentrated and localized in the first IMF. However, some low amplitude noises can be seen above 45 Hz in the second IMF. Low-frequency respiratory noises are localized in IMF #8 and #9 (subfigures h and i)

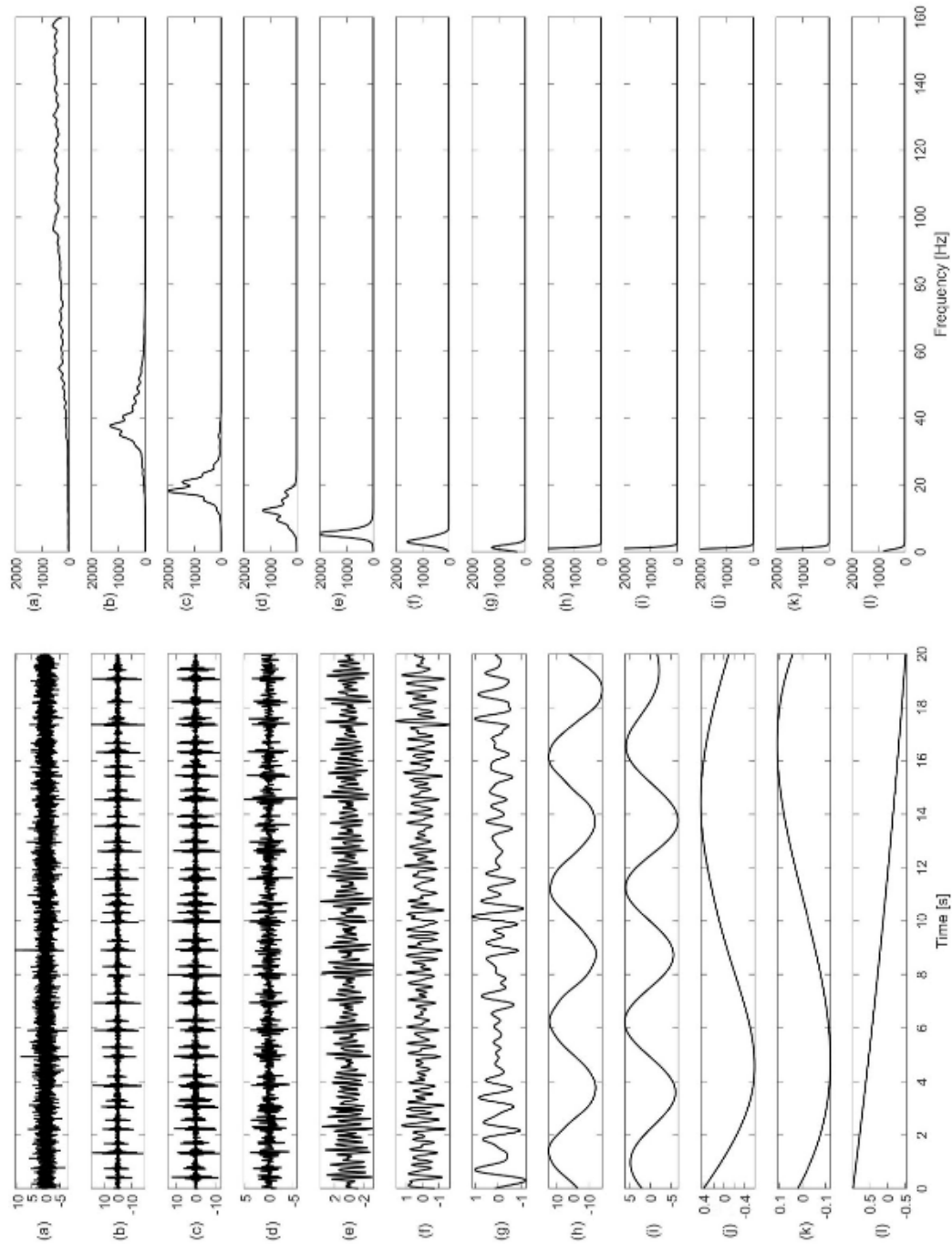


Figure A.D.2. Actual VCG contaminated by composite noise (respiratory noise + Gaussian noise with SNR = 10 dB). (left) EEMD-derived IMF components. The signal was decomposed into 11 IMFs (subfigure a through k) and a residue (subfigure l). (right) The power spectral density of the IMFs and residue shown in the previous figure. The high-frequency Gaussian noise is mostly distributed in the IMF #1. However, some low amplitude noises can be seen above 45 Hz in the second IMF. Low-frequency respiratory noises are localized in IMF #8 and #9 (subfigures h and i)

APPENDIX E. PUBLICATIONS

- [1] Taebi, A., Solar, B.E., Sandler, R.H., Mansy, H.A. Effect of Respiration and Intrathoracic Pressure on Seismocardiographic Signals Morphology and Frequency Content. In Process.
- [2] Taebi, A., Solar, B.E., Bomar, A.J., Sandler, R.H., Mansy, H.A. Recent Advances in Seismocardiography. Submitted.
- [3] Taebi, A., Solar, B.E., Mansy, H.A. (2018). An Adaptive Feature Extraction Algorithm for Classification of Seismocardiographic Signals. IEEE SoutheastCon, St Petersburg (FL).
- [4] Taebi, A., Bomar, A.J., Sandler, R.H., Mansy, H.A. (2018). Heart Rate Monitoring During Different Lung Volume Phases Using Seismocardiography. IEEE SoutheastCon, St Petersburg (FL).
- [5] Taebi, A., Mansy, H.A. (2017). Grouping Similar Seismocardiographic Signals Using Respiratory Information, IEEE Signal Processing in Medicine and Biology, Philadelphia (PA).
- [6] Taebi, A., Sandler, R.H., Kakavand, B., Mansy, H.A. (2017). Seismocardiographic Signal Timing with Myocardial Strain, IEEE Signal Processing in Medicine and Biology, Philadelphia (PA).
- [7] Taebi, A., Mansy, H.A. (2017). Analysis of Seismocardiographic Signals Using Polynomial Chirplet Transform and Smoothed Pseudo Wigner-Ville Distribution, IEEE Signal Processing in Medicine and Biology, Philadelphia (PA).
- [8] Solar, B.E., Taebi, A., Mansy, H.A. (2017). Classification of Seismocardiographic Cycles into Lung Volume Phases, IEEE Signal Processing in Medicine and Biology, Philadelphia (PA).
- [9] Taebi, A., Mansy, H. A. (2017). Time-frequency Distribution of Seismocardiographic Signals: A Comparative study. Bioengineering 4(2), 32.
- [10] Taebi, A., Mansy, H. A. (2017). Noise Cancellation from Vibrocardiographic Signals Based on the Ensemble Empirical Mode Decomposition. J Appl Biotech & Bioengineer, 2(2), 00024.
- [11] Taebi, A., Mansy, H. A. (2016). Effect of Noise on Time-frequency Analysis of Vibrocardiographic Signals. J Bioengineer & Biomedical Sci, 6(202), 2.
- [12] Taebi, A., Mansy, H. A. (2016). Time-frequency Description of Vibrocardiographic Signals. In 38th Annu Int Conf IEEE Eng Med Biol Soc Orlando FL.
- [13] Taebi, A., Mansy, H. A. (2015). Time-frequency Analysis of Vibrocardiographic Signals. In BMES Annu Meet Orlando FL.

REFERENCES

- [1] Rosamond, W., Flegal, K., Friday, G., Furie, K., Go, A., Greenlund, K., Haase, N., Ho, M., Howard, V., Kissela, B., Kissela, B., Kittner, S., Lloyd-Jones, D., McDermott, M., Meigs, J., Moy, C., Nichol, G., O'Donnell, C. J., Roger, V., Rumsfeld, J., Sorlie, P., Steinberger, J., Thom, T., Wasserthiel-Smoller, S., Hong, Y., and American Heart Association Statistics Committee and Stroke Statistics Subcommittee, 2007, "Heart Disease and Stroke Statistics--2007 Update: A Report from the American Heart Association Statistics Committee and Stroke Statistics Subcommittee.," *Circulation*, **115**(5), pp. e69–171.
- [2] Murphy, S. L., Xu, J., and Kochanek, K. D., 2013, "Deaths: Final Data for 2010.," *Natl. Vital Stat. Rep.*, **61**(4), pp. 1–117.
- [3] Salerno, D. M., Zanetti, J. M., Green, L. A., Mooney, M. R., Madison, J. D., and Van Tassel, R. A., 1991, "Seismocardiographic Changes Associated with Obstruction of Coronary Blood Flow during Balloon Angioplasty," *Am. J. Cardiol.*, **68**(2), pp. 201–207.
- [4] Jafari Tadi, M., Lehtonen, E., Humanen, T., Koskinen, J., Eriksson, J., Pänkäälä, M., Teräs, M., and Koivisto, T., 2016, "A Real-Time Approach for Heart Rate Monitoring Using a Hilbert Transform in Seismocardiograms.," *Physiol. Meas.*, **37**(11), pp. 1885–1909.
- [5] Salerno, D. M., and Zanetti, J., 1991, "Seismocardiography for Monitoring Changes in Left Ventricular Function during Ischemia," *Chest*, **100**(4), pp. 991–993.
- [6] Pandia, K., Inan, O. T., Kovacs, G. T. a, and Giovangrandi, L., 2012, "Extracting Respiratory Information from Seismocardiogram Signals Acquired on the Chest Using a Miniature Accelerometer.," *Physiol. Meas.*, **33**(10), pp. 1643–60.
- [7] Bifulco, P., Gargiulo, G. D., D'Angelo, G., Liccardo, A., Romano, M., Clemente, F., Cesarelli, M., Angelo, G., Liccardo, A., Romano, M., Clemente, F., and Cesarelli, M., 2014, "Monitoring of Respiration , Seismocardiogram and Heart Sounds by a PVDF Piezo Film Sensor," *Proc. Int. Work. ADC Model. Test.*, pp. 786–789.
- [8] Starr, I., Rawson, J., Schroeder, H., and Joseph, N., 1939, "Studies on the Estimation of Cardiac Ouptut in Man, and of Abnormalities in Cardiac Function, from the Heart's Recoil and the Blood's Impacts; the Ballistocardiogram," *Am. J. Physiol*, **127**, pp. 1–28.
- [9] Matsuzaki, T., 1972, "Calibrated Low Frequency Acceleration Vibrocardiography," *Jpn. Heart J.*, **13**(1), pp. 1–19.
- [10] Morbiducci, U., Scalise, L., De Melis, M., and Grigioni, M., 2007, "Optical Vibrocardiography: A Novel Tool for the Optical Monitoring of Cardiac Activity," *Ann. Biomed. Eng.*, **35**(1), pp. 45–58.
- [11] Scalise, L., and Morbiducci, U., 2008, "Non-Contact Cardiac Monitoring from Carotid Artery Using Optical Vibrocardiography.," *Med. Eng. Phys.*, **30**(4), pp. 490–497.
- [12] Cosoli, G., Casacanditella, L., Pietroni, F., Calvaresi, A., Revel, G. M., and Scalise, L., 2015, "A Novel Approach for Features Extraction in Physiological Signals," *Medical Measurements and Applications (MeMeA), 2015 IEEE International Symposium on*, pp.

380–385.

- [13] Benchimol, A., Dimond, E., and Carson, J., 1961, “The Value of the Apexcardiogram as a Reference Tracing in Phonocardiography,” *Am Hear. J.*, **61**, pp. 485–93.
- [14] Eddleman, E., Willis, K., Reeves, T., and Harrison, T., 1953, “The Kinetocardiogram,” *Circulation*, **8**, pp. 269–75.
- [15] Johnson, F., and Overy, D., 1951, “Vibrations of Low Frequency over the Precordium,” *Circulation*, **3**, pp. 579–88.
- [16] Mounsey, P., 1957, “Praecordial Ballistocardiography,” *Br. Heart J.*, **19**(2), p. 259.
- [17] Schneider, H., and Klunhaar, E., 1961, “Precordial Low Frequency Displacements of the Thoracic Wall. Method of Recording and Registration,” *Am Hear. J.*, **61**, pp. 670–5.
- [18] Ueda, H., Dobayashi, T., Sato, C., and Sakamoto, T., 1962, “Precordial Low Frequency Vibrocardiography. Method of Recording,” *Japan Hear. J.*, **3**, pp. 176–82.
- [19] Berson, A., and Pipberger, H., 1966, “Measurement of Chest Wall Vibrations due to the Activity of the Heart,” *J Appl Physiol*, **21**, pp. 370–4.
- [20] Inan, O. T., Migeotte, P. F., Park, K. S., Etemadi, M., Tavakolian, K., Casanella, R., Zanetti, J., Tank, J., Funtova, I., Prisk, G. K., and Di Rienzo, M., 2015, “Ballistocardiography and Seismocardiography: A Review of Recent Advances,” *IEEE J. Biomed. Heal. Informatics*, **19**(4), pp. 1414–1427.
- [21] Zanetti, J., and Tavakolian, K., 2013, “Seismocardiography: Past, Present and Future,” *Conf. Proc. IEEE Eng. Med. Biol. Soc.*, pp. 7004–7.
- [22] Taebi, A., and Mansy, H. A., 2017, “Noise Cancellation from Vibrocardiographic Signals Based on the Ensemble Empirical Mode Decomposition,” *J. Appl. Biotechnol. Bioeng.*, **2**(2), p. 00024.
- [23] Feigen, L. P., 1971, “Physical Characteristics of Sound and Hearing,” *Am. J. Cardiol.*, **28**(2), pp. 130–133.
- [24] Luisada, A. A., 1972, *The Sounds of the Normal Heart*, Warren H. Green.
- [25] Libonati, J. R., Colby, A. M., Caldwell, T. M., Kasparian, R., and Glassberg, H. L., 1999, “Systolic and Diastolic Cardiac Function Time Intervals and Exercise Capacity in Women,” *Med. Sci. Sports Exerc.*, **31**(2), pp. 258–263.
- [26] Korzeniowska-kubacka, I., Kuśmierczyk-droszcz, B., Bilińska, M., Barbara, D.-W., Mazurek, K., and Ryszard, P., 2006, “Seismocardiography - a Noninvasive Method of Assessing Systolic and Diastolic Left Ventricular Function in Ischaemic Heart Disease,” *Folia Cardiol*, **13**(4), pp. 319–325.
- [27] Tavakolian, K., Vaseghi, A., and Kaminska, B., 2008, “Improvement of Ballistocardiogram Processing by Inclusion of Respiration Information.,” *Physiol. Meas.*, **29**, pp. 771–781.
- [28] Tavakolian, K., 2010, “Charachterization and Analysis of Seismocardiogram for

Estimation of Hemodynamic Parameters,” Simon Fraser University.

- [29] Taebi, A., and Mansy, H. A., 2017, “Grouping Similar Seismocardiographic Signals Using Respiratory Information,” *Signal Processing in Medicine and Biology Symposium (SPMB), 2017 IEEE*, IEEE, Philadelphia, PA, pp. 1–6.
- [30] Zakeri, V., Akhbardeh, A., Alamdari, N., Fazel-Rezai, R., Paukkunen, M., and Tavakolian, K., 2017, “Analyzing Seismocardiogram Cycles to Identify the Respiratory Phases,” *IEEE Trans. Biomed. Eng.*, **64**(8), pp. 1786–1792.
- [31] Solar, B. E., Taebi, A., and Mansy, H. A., 2017, “Classification of Seismocardiographic Cycles into Lung Volume Phases,” *Signal Processing in Medicine and Biology Symposium (SPMB), 2017 IEEE*, IEEE, Philadelphia, PA, pp. 1–2.
- [32] Javaid, A. Q., Dowling, S., Etemadi, M., Heller, J. A., Roy, S., Klein, L., and Inan, O. T., 2016, “Quantification of Posture Induced Changes in Wearable Seismocardiogram Signals for Heart Failure Patients,” *Computing in Cardiology Conference (CinC), 2016*, pp. 777–780.
- [33] Di Rienzo, M., Vaini, E., Castiglioni, P., Merati, G., Meriggi, P., Parati, G., Faini, A., and Rizzo, F., 2013, “Wearable Seismocardiography: Towards a Beat-by-Beat Assessment of Cardiac Mechanics in Ambulant Subjects,” *Auton. Neurosci. Basic Clin.*, **178**(1-2), pp. 50–59.
- [34] Jain, P. K., and Tiwari, A. K., 2016, “A Novel Method for Suppression of Motion Artifacts from the Seismocardiogram Signal,” *Digital Signal Processing (DSP), 2016 IEEE International Conference on*, pp. 6–10.
- [35] Castiglioni, P., Faini, A., Parati, G., and Di Rienzo, M., 2007, “Wearable Seismocardiography,” *Annual International Conference of the IEEE Engineering in Medicine and Biology - Proceedings*, pp. 3954–3957.
- [36] Inan, O. T., Etemadi, M., Paloma, A., Giovangrandi, L., and Kovacs, G. T. A., 2009, “Non-Invasive Cardiac Output Trending during Exercise Recovery on a Bathroom-Scale-Based Ballistocardiograph,” *Physiol. Meas.*, **30**(3), pp. 261–274.
- [37] Di Rienzo, M., Vaini, E., Castiglioni, P., Meriggi, P., and Rizzo, F., 2013, “Beat-to-Beat Estimation of LVET and QS2 Indices of Cardiac Mechanics from Wearable Seismocardiography in Ambulant Subjects,” *Conf. Proc. ... Annu. Int. Conf. IEEE Eng. Med. Biol. Soc. IEEE Eng. Med. Biol. Soc. Annu. Conf.*, **2013**, pp. 7017–7020.
- [38] Inan, O. T., Baran Pouyan, M., Javaid, A. Q., Dowling, S., Etemadi, M., Dorier, A., Heller, J. A., Bicen, A. O., Roy, S., De Marco, T., and Klein, L., 2018, “Novel Wearable Seismocardiography and Machine Learning Algorithms Can Assess Clinical Status of Heart Failure Patients,” *Circ. Hear. Fail.*, **11**(1), p. e004313.
- [39] Hlebowicz, J., Lindstedt, S., Björgell, O., and Dencker, M., 2011, “The Effect of Endogenously Released Glucose, Insulin, Glucagon-like Peptide 1, Ghrelin on Cardiac Output, Heart Rate, Stroke Volume, and Blood Pressure,” *Cardiovasc. Ultrasound*, **9**(1).
- [40] Lin, W., Chou, W., Chang, P., Chou, C., Wen, M., Ho, M., and Lee, M., 2016, “Identification of Location Specific Feature Points in a Cardiac Cycle Using a Novel

- Seismocardiogram Spectrum System,” *IEEE J. Biomed. Heal. Informatics*.
- [41] Ashouri, H., and Inan, O. T., 2017, “Automatic Detection of Seismocardiogram Sensor Misplacement for Robust Pre-Ejection Period Estimation in Unsupervised Settings,” *IEEE Sens. J.*, **17**(12), pp. 3805–3813.
- [42] Etemadi, M., and Inan, O. T., 2017, “Wearable Ballistocardiogram and Seismocardiogram Systems for Health and Performance,” *J. Appl. Physiol.*, p. jap–00298.
- [43] Yang, C., Tang, S., and Tavassolian, N., 2017, “Utilizing Gyroscopes Towards the Automatic Annotation of Seismocardiograms,” *IEEE Sens. J.*, **17**(7), pp. 2129–2136.
- [44] Sieciński, S., and Kostka, P., 2017, “Determining Heart Rate Beat-to-Beat from Smartphone Seismocardiograms: Preliminary Studies,” *Conference on Innovations in Biomedical Engineering*, pp. 133–140.
- [45] Sahoo, P. K., Thakkar, H. K., and Lee, M. Y., 2017, “A Cardiac Early Warning System with Multi Channel SCG and ECG Monitoring for Mobile Health,” *Sensors*, **17**(4), p. 711.
- [46] Landreani, F., Martin-Yebra, A., Casellato, C., Frigo, C., Pavan, E., Migeotte, P.-F., and Caiani, E. G., 2016, “Beat-to-Beat Heart Rate Detection by Smartphone’s Accelerometers: Validation with ECG,” *Engineering in Medicine and Biology Society (EMBC), 2016 IEEE 38th Annual International Conference of the*, pp. 525–528.
- [47] Metzler, J., Kroschel, K., and Willersinn, D., 2017, “Automatic Detection of Measurement Points for Non-Contact Vibrometer-Based Diagnosis of Cardiac Arrhythmias,” *SPIE Medical Imaging. International Society for Optics and Photonics*, R.J. Webster, and B. Fei, eds., p. 101351S.
- [48] Casacanditella, L., Cosoli, G., Casaccia, S., Tomasini, E. P., and Scalise, L., 2016, “Indirect Measurement of the Carotid Arterial Pressure from Vibrocardiographic Signal: Calibration of the Waveform and Comparison with Photoplethysmographic Signal,” *Engineering in Medicine and Biology Society (EMBC), 2016 IEEE 38th Annual International Conference of the*, pp. 3568–3571.
- [49] Casacanditella, L., Cosoli, G., Casaccia, S., Rohrbaugh, J. W., Scalise, L., and Tomasini, E. P., 2016, “Characterization and Calibration of the Central Arterial Pressure Waveform Obtained from Vibrocardiographic Signal,” *AIP Conference Proceedings*, p. 050006.
- [50] Cosoli, G., Casacanditella, L., Tomasini, E., and Scalise, L., 2017, “Heart Rate Assessment by Means of a Novel Approach Applied to Signals of Different Nature,” *J. Phys. Conf. Ser.*, **778**(1), p. 012001.
- [51] Wahlstrom, J., Skog, I., Handel, P., Khosrow-khavar, F., Tavakolian, K., Stein, P. K., and Nehorai, A., 2017, “A Hidden Markov Model for Seismocardiography,” *IEEE Trans. Biomed. Eng.*, pp. 1–1.
- [52] Mafi, M., 2016, “Signal Processing Methods for Heart Rate Detection Using the Seismocardiogram,” University of Saskatchewan.
- [53] Tadi, M. J., Lehtonen, E., Lahdenoja, O., Pankaala, M., and Koivisto, T., 2016, “An Adaptive Approach for Heartbeat Detection Based on S-Transform in

- Seismocardiograms,” *Engineering in Medicine and Biology Society (EMBC), 2016 IEEE 38th Annual International Conference of the*, pp. 2370–2373.
- [54] Chuo, Y., Tavakolian, K., and Kaminska, B., 2011, “Evaluation of a Novel Integrated Sensor System for Synchronous Measurement of Cardiac Vibrations and Cardiac Potentials,” *J. Med. Syst.*, **35**(4), pp. 445–455.
- [55] Neary, J. P., MacQuarrie, D. S., Jamnik, V., Gledhill, N., Gledhill, S., and Busse, E. F. G., 2011, “Assessment of Mechanical Cardiac Function in Elite Athletes,” *Open Sport. Med J*, **5**, pp. 26–37.
- [56] Giorgis, L., Hernandez, A. I., Amblard, A., Senhadji, L., Cazeau, S., Jauvert, G., and Donal, E., 2008, “Analysis of Cardiac Micro-Acceleration Signals for the Estimation of Systolic and Diastolic Time Intervals in Cardiac Resynchronization Therapy,” *Computers in Cardiology*, pp. 393–396.
- [57] Verma, A. K., Zanetti, J., Fazel-Rezai, R., and Tavakolian, K., 2017, “Pulse Transit Time Derivation Using Xiphoidal and Carotid Seismocardiograms,” *2017 Design of Medical Devices Conference*, pp. V001T01A010–V001T01A010.
- [58] Peter, L., Noury, N., and Cerny, M., 2014, “A Review of Methods for Non-Invasive and Continuous Blood Pressure Monitoring: Pulse Transit Time Method Is Promising?,” *IRBM*, **35**(5), pp. 271–282.
- [59] Yang, C., and Tavassolian, N., 2016, “Pulse Transit Time Measurement Using Seismocardiogram and in-Ear Acoustic Sensor,” *Biomedical Circuits and Systems Conference (BioCAS), 2016 IEEE*, pp. 188–191.
- [60] Yang, C., and Tavassolian, N., 2017, “Pulse Transit Time Measurement Using Seismocardiogram, Photoplethysmogram, and Acoustic Recordings: Evaluation and Comparison,” *IEEE J. Biomed. Heal. Informatics*, pp. 1–1.
- [61] Carek, A. M., Conant, J., Joshi, A., Kang, H., and Inan, O. T., 2017, “SeismoWatch: Wearable Cuffless Blood Pressure Monitoring Using Pulse Transit Time,” *Proc. ACM Interactive, Mobile, Wearable Ubiquitous Technol.*, **1**(3), p. 40.
- [62] Di Rienzo, M., Lombardi, P., Scurati, D., and Vaini, E., 2016, “A New Technological Platform for the Multisite Assessment of 3D Seismocardiogram and Pulse Transit Time in Cardiac Patients,” *Computing in Cardiology Conference (CinC), 2016*, pp. 781–784.
- [63] Lombard, W. P., and Cope, O. M., 1926, “The Duration of the Systole of the Left Ventricle of Man,” *Am. J. Physiol. Content*, **77**(2), pp. 263–295.
- [64] Weissler, A. M., Harris, W. S., and Schoenfeld, C. D., 1968, “Systolic Time Intervals in Heart Failure in Man,” *Circulation*, **37**(2), pp. 149–159.
- [65] Khosrow-Khavar, F., Tavakolian, K., Blaber, A., and Menon, C., 2017, “Automatic and Robust Delineation of the Fiducial Points of the Seismocardiogram Signal for Noninvasive Estimation of Cardiac Time Intervals,” *IEEE Trans. Biomed. Eng.*, **64**(8), pp. 1701–1710.
- [66] Pouymiro, I. R., Cordova, E. V., and Perez, F. E. V., 2016, “Robust Detection of AO and

- IM Points in the Seismocardiogram Using CWT,” *IEEE Lat. Am. Trans.*, **14**(11), pp. 4468–4473.
- [67] Jain, P. K., Tiwari, A. K., and Bhagat, O. L., 2016, “Seismocardiography: An Alternate Method to Estimate Electro-Mechanical Window,” *Systems in Medicine and Biology (ICSMB), 2016 International Conference on*, pp. 136–139.
- [68] Di Rienzo, M., Vaini, E., and Lombardi, P., 2017, “An Algorithm for the Beat-to-Beat Assessment of Cardiac Mechanics during Sleep on Earth and in Microgravity from the Seismocardiogram,” *Sci. Rep.*, **7**(1).
- [69] WHO, 2017, “WHO _ Cardiovascular Diseases (CVDs),” *Cardiovasc. Dis.*
- [70] Jain, P. K., Tiwari, A. K., and Chourasia, V. S., 2016, “Performance Analysis of Seismocardiography for Heart Sound Signal Recording in Noisy Scenarios,” *J. Med. Eng. Technol.*, **40**(3), pp. 106–118.
- [71] Pänkäälä, M., Koivisto, T., Lahdenoja, O., Kiviniemi, T., Saraste, A., Vasankari, T., and Airaksinen, J., 2016, “Detection of Atrial Fibrillation with Seismocardiography,” *Engineering in Medicine and Biology Society (EMBC), 2016 IEEE 38th Annual International Conference of the*, pp. 4369–4374.
- [72] Paukkunen, M., Parkkila, P., Hurnanen, T., Pankaala, M., Koivisto, T., Nieminen, T., Kettunen, R., and Sepponen, R., 2016, “Beat-by-Beat Quantification of Cardiac Cycle Events Detected From Three-Dimensional Precordial Acceleration Signals,” *IEEE J. Biomed. Heal. Informatics*, **20**(2), pp. 435–439.
- [73] Taebi, A., Bomar, A. J., Sandler, R. H., and Mansy, H. A., 2018, “Heart Rate Monitoring During Different Lung Volume Phases Using Seismocardiography,” *SoutheastCon 2018, IEEE, IEEE*, pp. 1–5.
- [74] Koegelenberg, S., 2014, “Application of Laser Doppler Vibrocardiography for Human Heart Auscultation,” Stellenbosch: Stellenbosch University.
- [75] Yang, C., Tang, S., and Tavassolian, N., 2016, “Annotation of Seismocardiogram Using Gyroscopic Recordings,” *Biomedical Circuits and Systems Conference (BioCAS), 2016 IEEE*, pp. 204–207.
- [76] Lahdenoja, O., Hurnanen, T., Iftikhar, Z., Nieminen, S., Knuutila, T., Saraste, A., Kiviniemi, T., Vasankari, T., Airaksinen, J., Pankaala, M., and Koivisto, T., 2018, “Atrial Fibrillation Detection via Accelerometer and Gyroscope of a Smartphone,” *IEEE J. Biomed. Heal. Informatics*, **22**(1), pp. 108–118.
- [77] XIA, Z., SHANDHI, M. D. M. H., INAN, O. T., and ZHANG, Y., 2017, “Interference and Removal of Respiration Harmonics on Noncontact Seismo-Cardiogram Signals,” *Struct. Heal. Monit.* 2017.
- [78] SHANDHI, M. D. M. H., XIA, Z., INAN, O. T., and ZHANG, Y., 2017, “Clutter Effect on the Noncontact Seismocardiogram Signals Measured Using Microwave Radars,” *Struct. Heal. Monit.* 2017.
- [79] Alamdari, N. T., 2016, “A Morphological Approach To Identify Respiratory Phases Of

Seismocardiogram,” The University of North Dakota.

- [80] Dinh, A., Bui, F. M., and Nguyen, T., 2016, “An Accelerometer Based System to Measure Myocardial Performance Index during Stress Testing,” *Engineering in Medicine and Biology Society (EMBC), 2016 IEEE 38th Annual International Conference of the*, pp. 4877–4880.
- [81] Yang, C., and Tavassolian, N., 2017, “Combined Seismo-and Gyro-Cardiography: A More Comprehensive Evaluation of Heart-Induced Chest Vibrations,” *IEEE J. Biomed. Heal. Informatics*.
- [82] Zhang, G., Cottrell, A. C., Henry, I. C., and McCombie, D. B., 2016, “Assessment of Pre-Ejection Period in Ambulatory Subjects Using Seismocardiogram in a Wearable Blood Pressure Monitor,” *Engineering in Medicine and Biology Society (EMBC), 2016 IEEE 38th Annual International Conference of the*, pp. 3386–3389.
- [83] Khosrow-Khavar, F., 2016, “Automatic and Non-Invasive Delineation of the Seismocardiogram Signal for the Estimation of Cardiac Time Intervals with Applications in Diastolic Timed Vibration and Early Stage Hemorrhage Detection,” SIMON FRASER UNIVERSITY.
- [84] Shafiq, G., Tatinati, S., and Veluvolu, K. C., 2016, “Automatic Annotation of Peaks in Seismocardiogram for Systolic Time Intervals,” *Engineering in Medicine and Biology Society (EMBC), 2016 IEEE 38th Annual International Conference of the*, pp. 2672–2675.
- [85] Shafiq, G., Tatinati, S., Ang, W. T., and Veluvolu, K. C., 2016, “Automatic Identification of Systolic Time Intervals in Seismocardiogram,” *Sci. Rep.*, **6**(1), p. 37524.
- [86] Jain, P. K., and Tiwari, A. K., 2016, “An Algorithm for Automatic Segmentation of Heart Sound Signal Acquired Using Seismocardiography,” *Systems in Medicine and Biology (ICSMB), 2016 International Conference on*, pp. 157–161.
- [87] Taebi, A., Solar, B. E., and Mansy, H. A., 2018, “An Adaptive Feature Extraction Algorithm for Classification of Seismocardiographic Signals,” *SoutheastCon 2018, IEEE, IEEE*, pp. 1–5.
- [88] Taebi, A., and Mansy, H. A., 2017, “Time-Frequency Distribution of Seismocardiographic Signals: A Comparative Study,” *Bioengineering*, **4**(2), p. 32.
- [89] Hurnanen, T., Lehtonen, E., Tadi, M. J., Kuusela, T., Kiviniemi, T., Saraste, A., Vasankari, T., Airaksinen, J., Koivisto, T., and Pankaala, M., 2017, “Automated Detection of Atrial Fibrillation Based on Time–Frequency Analysis of Seismocardiograms,” *IEEE J. Biomed. Heal. Informatics*, **21**(5), pp. 1233–1241.
- [90] Sahoo, P. K., Thakkar, H. K., Lin, W.-Y., Chang, P.-C., and Lee, M.-Y., 2018, “On the Design of an Efficient Cardiac Health Monitoring System Through Combined Analysis of ECG and SCG Signals,” *Sensors*, **18**(2), p. 379.
- [91] Yang, C., and Tavassolian, N., 2016, “Motion Artifact Cancellation of Seismocardiographic Recording From Moving Subjects,” *IEEE Sens. J.*, **16**(14), pp. 5702–5708.

- [92] Canino, N. K., Wang, R. R., and Robinson, C. J., 2016, “Using Multiple Placements of Accelerometers to Measure Cardiovascular Pulse Transit Times,” *Engineering in Medicine and Biology Society (EMBC), 2016 IEEE 38th Annual International Conference of the*, pp. 4248–4251.
- [93] Javaid, A. Q., Ashouri, H., Dorier, A., Etemadi, M., Heller, J. A., Roy, S., and Inan, O. T., 2017, “Quantifying and Reducing Motion Artifacts in Wearable Seismocardiogram Measurements During Walking to Assess Left Ventricular Health,” *IEEE Trans. Biomed. Eng.*, **64**(6), pp. 1277–1286.
- [94] Yao, J., Tridandapani, S., Wick, C. A., and Bhatti, P. T., 2017, “Seismocardiography-Based Cardiac Computed Tomography Gating Using Patient-Specific Template Identification and Detection,” *IEEE J. Transl. Eng. Heal. Med.*, **5**, pp. 1–14.
- [95] Ashouri, H., Hersek, S., and Inan, O. T., 2018, “Universal Pre-Ejection Period Estimation Using Seismocardiography: Quantifying the Effects of Sensor Placement and Regression Algorithms,” *IEEE Sens. J.*, **18**(4).
- [96] Lee, H., Lee, H., and Whang, M., 2018, “An Enhanced Method to Estimate Heart Rate from Seismocardiography via Ensemble Averaging of Body Movements at Six Degrees of Freedom,” *Sensors*, **18**(1), p. 238.
- [97] Kon, S., Oldham, K., and Horowitz, R., 2007, “Piezoresistive and Piezoelectric MEMS Strain Sensors for Vibration Detection,” *Sensors and Smart Structures Technologies for Civil, Mechanical, and Aerospace Systems 2007*, p. 65292V.
- [98] Abbasi-Kesbi, R., Valipour, A., and others, 2017, “Cardiorespiratory System Monitoring Using a Developed Acoustic Sensor,” *Healthc. Technol. Lett.*
- [99] Sundar, A., and Pahwa, V., 2017, “Evaluating the Performance of State of the Art Algorithms for Enhancement of Seismocardiogram Signals,” *Proceedings of the First International Conference on Intelligent Computing and Communication*, Springer Singapore, pp. 37–45.
- [100] Choudhary, T., Sharma, L. N., and Bhuyan, M. K., 2018, “Heart Sound Extraction from Sternal Seismocardiographic Signal,” *IEEE Signal Process. Lett.*
- [101] Mansy, H. A., Royston, T. J., Balk, R. A., and Sandler, R. H., 2002, “Pneumothorax Detection Using Computerised Analysis of Breath Sounds,” *Med. Biol. Eng. Comput.*, **40**(5), pp. 526–532.
- [102] Huang, N. E., Shen, Z., Long, S. R., Wu, M. C., Shih, H. H., Zheng, Q., Yen, N.-C., Tung, C. C., and Liu, H. H., 1998, “The Empirical Mode Decomposition and the Hilbert Spectrum for Nonlinear and Non-Stationary Time Series Analysis,” *Proc. R. Soc. A Math. Phys. Eng. Sci.*, **454**(1971), pp. 903–995.
- [103] Ur Rehman, N., and Mandic, D. P., 2010, “Empirical Mode Decomposition for Trivariate Signals,” *IEEE Trans. Signal Process.*, **58**(3 PART 1), pp. 1059–1068.
- [104] Lee, P. L., Shang, L. Z., Wu, Y. Te, Shu, C. H., Hsieh, J. C., Lin, Y. Y., Wu, C. H., Liu, Y. L., Yang, C. Y., Sun, C. W., and Shyu, K. K., 2009, “Single-Trial Analysis of Cortical Oscillatory Activities during Voluntary Movements Using Empirical Mode

- Decomposition (Emd)-Based Spatiotemporal Approach,” *Ann. Biomed. Eng.*, **37**(8), pp. 1683–1700.
- [105] Mijović, B., De Vos, M., Gligorijević, I., Taelman, J., and Van Huffel, S., 2010, “Source Separation from Single-Channel Recordings by Combining Empirical-Mode Decomposition and Independent Component Analysis,” *IEEE Trans. Biomed. Eng.*, **57**(9), pp. 2188–2196.
- [106] Zhang, Y., Gao, Y., Wang, L., Chen, J., and Shi, X., 2007, “The Removal of Wall Components in Doppler Ultrasound Signals by Using the Empirical Mode Decomposition Algorithm,” *IEEE Trans. Biomed. Eng.*, **54**(9), pp. 1631–1642.
- [107] Salisbury, J. I., and Sun, Y., 2004, “Assessment of Chaotic Parameters in Nonstationary Electrocardiograms by Use of Empirical Mode Decomposition,” *Ann. Biomed. Eng.*, **32**(10), pp. 1348–1354.
- [108] Liang, H., Wang, Z., Maier, A., and Logothetis, N. K., 2008, “Single-Trial Classification of Bistable Perception by Integrating Empirical Mode Decomposition, Clustering, and Support Vector Machine,” *EURASIP J. Adv. Signal Process.*, **2008**.
- [109] Coughlin, K. T., and Tung, K. K., 2004, “11-Year Solar Cycle in the Stratosphere Extracted by the Empirical Mode Decomposition Method,” *Adv. Sp. Res.*, **34**(2), pp. 323–329.
- [110] Cong, F., Sipola, T., Huttunen-Scott, T., Xu, X., Ristaniemi, T., and Lyytinen, H., 2009, “Hilbert-Huang versus Morlet Wavelet Transformation on Mismatch Negativity of Children in Uninterrupted Sound Paradigm,” *Nonlinear Biomed. Phys.*, **3**(1), p. 1.
- [111] Wu, Z., and Huang, N. E., 2009, “Ensemble Empirical Mode Decomposition: A Noise-Assisted Data Analysis Method,” *Adv. Adapt. Data Anal.*, **1**(1), pp. 1–41.
- [112] Wu, Z., and Huang, N. E., 2004, “A Study of the Characteristics of White Noise Using the Empirical Mode Decomposition Method,” *Proc. R. Soc. A Math. Phys. Eng. Sci.*, **460**(2046), pp. 1597–1611.
- [113] Flandrin, P., Rilling, G., and Goncalves, P., 2004, “Empirical Mode Decomposition as a Filter Bank,” *IEEE Signal Process. Lett.*, **11**(2), pp. 112–114.
- [114] Visagie, C., 2007, “Screening for Abnormal Heart Sounds and Murmurs by Implementing Neural Networks,” Stellenbosch: University of Stellenbosch.
- [115] Taebi, A., 2013, “Mechanical Energy Exchange during Plane Walking and Stepping over Obstacle in Subjects with Down Syndrome,” Politecnico di Milano University Library.
- [116] Salami, F., Vimercati, S. L., Rigoldi, C., Taebi, A., Albertini, G., and Galli, M., 2014, “Mechanical Energy Assessment of Adult with Down Syndrome during Walking with Obstacle Avoidance,” *Res. Dev. Disabil.*, **35**(8), pp. 1856–1862.
- [117] Taebi, A., and Mansy, H. A., 2016, “Time-Frequency Description of Vibrocardiographic Signals,” *38th Annual International Conference of the IEEE Engineering in Medicine and Biology Society*, Orlando, FL.

- [118] Taebi, A., and Mansy, H. A., 2016, "Effect of Noise on Time-Frequency Analysis of Vibrocardiographic Signals," *J. Bioeng. Biomed. Sci.*, **6(202)**, p. 2.
- [119] Mansy, H. A., Royston, T. J., Balk, R. A., and Sandler, R. H., 2002, "Pneumothorax Detection Using Computerised Analysis of Breath Sounds.," *Med. Biol. Eng. Comput.*, **40(5)**, pp. 526–532.
- [120] Mansy, H. a, Royston, T. J., Balk, R. a, and Sandler, R. H., 2002, "Pneumothorax Detection Using Pulmonary Acoustic Transmission Measurements.," *Med. Biol. Eng. Comput.*, **40(5)**, pp. 520–525.
- [121] Mansy, H. A., Royston, T. J., and Sandler, R. H., 2002, "Use of Abdominal Percussion for Pneumoperitoneum Detection," *Med Biol Eng Comput*, **40(4)**, pp. 439–46.
- [122] Mansy, H. A., and Sandler, R. H., 2000, "Detection and Analysis of Gastrointestinal Sounds in Normal and Small Bowel Obstructed Rats," *Med Biol Eng Comput*, **38(1)**, pp. 42–48.
- [123] Khalili, F., and Mansy, H. A., 2016, "Blood Flow through a Dysfunctional Mechanical Heart Valve," *38th Annu Int Conf IEEE Eng Med Biol Soc*, Orlando, FL.
- [124] Khalili, F., Gamage, P. P. T., and Mansy, H. A., 2018, "Verification of Turbulence Models for Flow in a Constricted Pipe at Low Reynolds Number," *3rd Thermal and Fluids Engineering Conference (TFEC)*, Fort Lauderdale, FL, USA, pp. 1–10.
- [125] Khalili, F., Gamage, P. P. T., and Mansy, H. A., 2018, "Prediction of Turbulent Shear Stresses through Dysfunctional Bileaflet Mechanical Heart Valves Using Computational Fluid Dynamics," *3rd Thermal and Fluids Engineering Conference (TFEC)*, Fort Lauderdale, FL, USA, pp. 1–9.
- [126] Khalili, F., Gamage, P. P. T., and Mansy, H. A., 2017, "Hemodynamics of a Bileaflet Mechanical Heart Valve with Different Levels of Dysfunction," *J Appl Biotechnol Bioeng*, **2(5)**, p. 00044.
- [127] Wu, M. C., and Hu, C. K., 2006, "Empirical Mode Decomposition and Synchrogram Approach to Cardiorespiratory Synchronization," *Phys. Rev. E - Stat. Nonlinear, Soft Matter Phys.*, **73(5)**.
- [128] Ari, S., and Saha, G., 2008, "Classification of Heart Sounds Using Empirical Mode Decomposition Based Features," *Int. J. Med. Eng. Inform.*, **1(1)**, pp. 91–108.
- [129] Chappell, M. A., and Payne, S. J., 2005, "A Method for the Automated Detection of Venous Gas Bubbles in Humans Using Empirical Mode Decomposition," *Ann. Biomed. Eng.*, **33(10)**, pp. 1411–1421.
- [130] Lee, J., McManus, D. D., Merchant, S., and Chon, K. H., 2012, "Automatic Motion and Noise Artifact Detection in Holter ECG Data Using Empirical Mode Decomposition and Statistical Approaches," *IEEE Trans. Biomed. Eng.*, **59(6)**, pp. 1499–1506.
- [131] Huang, W., Shen, Z., Huang, N. E., and Fung, Y. C., 1998, "Engineering Analysis of Biological Variables: An Example of Blood Pressure over 1 Day.," *Proc. Natl. Acad. Sci. U. S. A.*, **95(April)**, pp. 4816–4821.

- [132] Huang, W., Shen, Z., Huang, N. E., and Fung, Y. C., 1998, "Use of Intrinsic Modes in Biology: Examples of Indicial Response of Pulmonary Blood Pressure to +/- Step Hypoxia," *Proc. Natl. Acad. Sci. U. S. A.*, **95**(October), pp. 12766–12771.
- [133] Blanco-Velasco, M., Weng, B., and Barner, K. E., 2008, "ECG Signal Denoising and Baseline Wander Correction Based on the Empirical Mode Decomposition," *Comput. Biol. Med.*, **38**(1), pp. 1–13.
- [134] Nimunkar, A. J., and Tompkins, W. J., 2007, "EMD-Based 60-Hz Noise Filtering of the ECG," *Annual International Conference of the IEEE Engineering in Medicine and Biology - Proceedings*, pp. 1904–1907.
- [135] Krupa, B. N., Ali, M. A. M., and Zahedi, E., 2009, "The Application of Empirical Mode Decomposition for the Enhancement of Cardiocograph Signals," *Physiol. Meas.*, **30**(8), p. 729.
- [136] Lemay, M., and Vesin, J. M., 2006, "QRST Cancellation Based on the Empirical Mode Decomposition," *2006 Computers in Cardiology*, pp. 561–564.
- [137] Chang, K.-M., and Liu, S.-H., 2011, "Gaussian Noise Filtering from ECG by Wiener Filter and Ensemble Empirical Mode Decomposition," *J. Signal Process. Syst.*, **64**(2), pp. 249–264.
- [138] Balocchi, R., Menicucci, D., Santarcangelo, E., Sebastiani, L., Gemignani, A., Ghelarducci, B., and Varanini, M., 2004, "Deriving the Respiratory Sinus Arrhythmia from the Heartbeat Time Series Using Empirical Mode Decomposition," *Chaos, Solitons & Fractals*, **20**(February 2008), pp. 171–177.
- [139] Wiener, N., 1949, *Extrapolation, Interpolation, and Smoothing of Stationary Time Series*, The MIT Press, Cambridge, MA, USA.
- [140] Scalart, P., and Filho, J. V., 1996, "Speech Enhancement Based on a Priori Signal to Noise Estimation," 1996 IEEE Int. Conf. Acoust. Speech, Signal Process. Conf. Proc., **2**, pp. 629–632.
- [141] Tolwinski, S., 2007, "The Hilbert Transform and Empirical Mode Decomposition as Tools for Data Analysis Real Signals and the Hilbert Transform," *Transform*, (1), pp. 1–18.
- [142] Zakeri, V., and Tavakolian, K., 2015, "Identification of Respiratory Phases Using Seismocardiogram: A Machine Learning Approach," *Computing in Cardiology*, pp. 305–308.
- [143] Poliac, M. O., Zanetty, J. M., Salerno, D., and Wilcox, G. L., 1991, "Seismocardiogram (SCG) Interpretation Using Neural Networks," *Computer-Based Medical Systems, 1991. Proceedings of the Fourth Annual IEEE Symposium*, pp. 288–295.
- [144] Sandler, R. H., and Mansy, H. A., 2014, "Vibro-Acoustic Detection of Cardiac Conditions."
- [145] Gramatikov, B., Brinker, J., Yi-Chun, S., and Thakor, N. V., 2000, "Wavelet Analysis and Time-Frequency Distributions of the Body Surface ECG before and after Angioplasty,"

- Comput. Methods Programs Biomed., **62**(2), pp. 87–98.
- [146] Crowe, J. A., Gibson, N. M., Woolfson, M. S., and Somekh, M. G., 1992, “Wavelet Transform as a Potential Tool for ECG Analysis and Compression,” *J. Biomed. Eng.*, **14**(3), pp. 268–272.
- [147] Blanco, S., Figliola, A., Quiroga, R. Q., Rosso, O. A., and Serrano, E., 1998, “Time-Frequency Analysis of Electroencephalogram Series. III. Wavelet Packets and Information Cost Function,” *Phys. Rev. E*, **57**(1), p. 932.
- [148] Celka, P., Boashash, B., and Colditz, P., 2001, “Preprocessing and Time-Frequency Analysis of Newborn EEG Seizures,” *IEEE Eng. Med. Biol. Mag.*, **20**(5), pp. 30–39.
- [149] Obaidat, M. S., 1993, “Phonocardiogram Signal Analysis: Techniques and Performance Comparison,” *J. Med. Eng. Technol.*, **17**(6), pp. 221–227.
- [150] White, P., Collis, W., and Salmon, A., 1996, “Analysing Heart Murmurs Using Time-Frequency Methods,” *Proc. IEEE-SP Int. Symp. Time-Frequency Time-Scale Anal.*, **2**(1), pp. 2–5.
- [151] Debbal, S. M., and Bereksi-Reguig, F., 2007, “Time-Frequency Analysis of the First and the Second Heartbeat Sounds,” *Appl. Math. Comput.*, **184**(2), pp. 1041–1052.
- [152] Cherif, L. H., Debbal, S. M., and Bereksi-Reguig, F., 2010, “Choice of the Wavelet Analyzing in the Phonocardiogram Signal Analysis Using the Discrete and the Packet Wavelet Transform,” *Expert Syst. Appl.*, **37**(2), pp. 913–918.
- [153] Karlsson, S., Yu, J., and Akay, M., 2000, “Time-Frequency Analysis of Myoelectric Signals during Dynamic Contractions: A Comparative Study,” *IEEE Trans. Biomed. Eng.*, **47**(2), pp. 228–238.
- [154] Peng, Z. K., Meng, G., Chu, F. L., Lang, Z. Q., Zhang, W. M., and Yang, Y., 2011, “Polynomial Chirplet Transform with Application to Instantaneous Frequency Estimation,” *IEEE Trans. Instrum. Meas.*, **60**(9), pp. 3222–3229.
- [155] Auger, F., Flandrin, P., Gonçalves, P., and Lemoine, O., 1996, “Time-Frequency Toolbox,” CNRS Fr. Univ.
- [156] Hadjileontiadis, L. J., and Panas, S. M., 1998, “A Wavelet-Based Reduction of Heart Sound Noise from Lung Sounds,” *International Journal of Medical Informatics*, pp. 183–190.
- [157] Pourazad, M. T., Moussavi, Z., and Thomas, G., 2006, “Heart Sound Cancellation from Lung Sound Recordings Using Time-Frequency Filtering,” *Med. Biol. Eng. Comput.*, **44**(3), pp. 216–225.
- [158] Kumar, D., Carvalho, P., Antunes, M., Henriques, J., e Melo, A. S., Schmidt, R., and Habetha, J., 2007, “Third Heart Sound Detection Using Wavelet Transform-Simplicity Filter,” *Annual International Conference of the IEEE Engineering in Medicine and Biology - Proceedings*, pp. 1277–1281.
- [159] Mazomenos, E. B., Biswas, D., Acharyya, A., Chen, T., Maharatna, K., Rosengarten, J.,

- Morgan, J., and Curzen, N., 2013, "A Low-Complexity ECG Feature Extraction Algorithm for Mobile Healthcare Applications," *IEEE J. Biomed. Heal. Informatics*, **17**(2), pp. 459–469.
- [160] Ergen, B., Tatar, Y., and Gulcur, H. O., 2012, "Time-Frequency Analysis of Phonocardiogram Signals Using Wavelet Transform: A Comparative Study.," *Comput. Methods Biomech. Biomed. Engin.*, **15**(4), pp. 371–81.
- [161] Mann, S., and Haykin, S., 1992, "Adaptive Chirplet Transform: An Adaptive Generalization of the Wavelet Transform," *Opt. Eng.*, **31**(6), pp. 1243–1256.
- [162] Mann, S., and Haykin, S., 1995, "The Chirplet Transform: Physical Considerations," *IEEE Trans. Signal Process.*, **43**(11), pp. 2745–2761.
- [163] Abry, P., 1997, *Ondelettes et Turbulences: Multirésolutions, Algorithmes de Décomposition, Invariance D'échelle et Signaux de Pression*, Diderot multimédia.
- [164] Kail, E., Khor, S., Fugedi, K., Kovacs, I., Khor, B., Kail, B., Kecskemethy, P., Balogh, N., Domijan, E., and Domijan, M., 2005, "Expert System for Phonocardiographic Monitoring of Heart Failure Patients Based Onwavelet Analysis," *Comput. Cardiol.* 2005, pp. 833–836.
- [165] Inan, O. T., Etemadi, M., Wiard, R. M., Giovangrandi, L., and Kovacs, G. T. a, 2009, "Robust Ballistocardiogram Acquisition for Home Monitoring.," *Physiol. Meas.*, **30**(2), pp. 169–85.
- [166] Zanetti, J., and Salerno, D., 1990, "Seismocardiography: A New Technique for Recording Cardiac Vibrations. Concept, Method, and Initial Observations," *J. Cardiovasc. Technol.*, **9**(2), pp. 111–120.
- [167] Taebi, A., and Mansy, H. A., 2015, "Time-Frequency Analysis of Vibrocardiographic Signals," *2015 BMES Annual Meeting*.
- [168] Obaidat, M. S., 1993, "Phonocardiogram Signal Analysis: Techniques and Performance Comparison," *J. Med. Eng. Technol.*, **17**(6), pp. 221–227.
- [169] Thakor, N. V., and Zhu, Y. S., 1991, "Applications of Adaptive Filtering to ECG Analysis: Noise Cancellation and Arrhythmia Detection," *IEEE Trans. Biomed. Eng.*, **38**(8), pp. 785–794.
- [170] Gholam-Hosseini, H., Nazeran, H., and Reynolds, K. J., 1998, "ECG Noise Cancellation Using Digital Filters," *Proc. 2nd Int. Conf. Bioelectromagn. 1998*, (February), pp. 151–152.
- [171] Kabir, M. A., and Shahnaz, C., 2012, "Denoising of ECG Signals Based on Noise Reduction Algorithms in EMD and Wavelet Domains," *Biomed. Signal Process. Control*, **7**(5), pp. 481–489.
- [172] Bhateja, V., Urooj, S., Mehrotra, R., Verma, R., Lay-Ekuakille, A., and Verma, V. D., 2013, "A Composite Wavelets and Morphology Approach for ECG Noise Filtering," *Pattern Recognition and Machine Intelligence*, Springer, pp. 361–366.

- [173] Pandey, V., and Pandey, P., 2005, “Cancellation of Respiratory Artifact in Impedance Cardiography,” *Conf. Proc. IEEE Eng. Med. Biol. Soc.*, **5**, pp. 5503–5506.
- [174] Press, H., and Tukey, J. W., 1962, “Power Spectral Methods of Analysis and Their Application to Problems in Airplane Dynamics. Vol. IV of AGARD Flight Test Manual, Pt. IVC, Enoch J. Durbin, Ed.”
- [175] Fuenzalida, H., and Rosenblüth, B., 1990, “Prewhitening of Climatological Time Series,” *J. Clim.*, **3**(3), pp. 382–393.
- [176] M.J., L., and K.M., B., 1993, “Prewhitening for Intelligibility Gain in Hearing Aid Arrays,” *J. Acoust. Soc. Am.*, **93**(4 I), pp. 2139–2145.
- [177] Zala, C. A., Ozard, J. M., and Wilmot, M. J., 1995, “Prewhitening for Improved Detection by Matched-Field Processing in Ice-Ridging Correlated Noise,” *J. Acoust. Soc. Am.*, **98**(5), pp. 2726–2734.
- [178] Cichocki, A., and Amari, S., 2002, “Adaptive Blind Signal and Image Processing: Learning Algorithms and Applications,” *Neurocomputing*, **49**(1-4), pp. 439–443.
- [179] De Lathauwer, L., De Moor, B., and Vandewalle, J., 2005, “A Prewhitening-Induced Bound on the Identification Error in Independent Component Analysis,” *Circuits Syst. I Regul. Pap. IEEE Trans.*, **52**(3), pp. 546–554.
- [180] Rodríguez, J. D., Pérez, A., and Lozano, J. A., 2010, “Sensitivity Analysis of K-Fold Cross Validation in Prediction Error Estimation,” *IEEE Trans. Pattern Anal. Mach. Intell.*, **32**(3), pp. 569–575.
- [181] Powers, D. M. W., 2011, “Evaluation: From Precision, Recall and F-Measure To Roc, Informedness, Markedness & Correlation,” *J. Mach. Learn. Technol.*, **2**(1), pp. 37–63.
- [182] Pedregosa, F., and Varoquaux, G., 2011, *Scikit-Learn: Machine Learning in Python*.
- [183] Van Der Walt, S., Colbert, S. C., and Varoquaux, G., 2011, “The NumPy Array: A Structure for Efficient Numerical Computation,” *Comput. Sci. Eng.*, **13**(2), pp. 22–30.
- [184] Gamage, P. P. T., Khalili, F., and Mansy, H. A., 2018, “Numerical Modeling of Pulse Wave Propagation in a Stenosed Artery Using Two-Way Coupled Fluid Structure Interaction (FSI),” *3rd Thermal and Fluids Engineering Conference (TFEC)*, Fort Lauderdale, FL, USA.
- [185] Khalili, F., Gamage, P. P. T., and Mansy, H. A., 2018, “The Influence of the Aortic Root Geometry on Flow Characteristics of a Bileaflet Mechanical Heart Valve,” *3rd Therm. Fluids Eng. Conf.*
- [186] Khalili, F., 2018, “Fluid Dynamics Modeling and Sound Analysis of a Bileaflet Mechanical Heart Valve,” *University of Central Florida*.
- [187] Sharifi, A., Salari, A., Taebi, A., Niazmand, H., and Niazmand, M. J., 2017, “Flow Patterns and Wall Shear Stress Distribution in Human Vertebrobasilar System: A Computational Study to Investigate Smoking Effects on Atherosclerotic Stenosis at Different Ages,” *ASME International Mechanical Engineering Congress and Exposition*,

Proceedings (IMECE).

- [188] Taebi, A., Khalili, F., and Taebi, A., 2017, “Buckling Analysis of a Functionally Graded Implant Model for Treatment of Bone Fractures: A Numerical Study,” *ASME International Mechanical Engineering Congress and Exposition, Proceedings (IMECE)*.
- [189] Khalili, F., Gamage, P. P. T., and Mansy, H. A., 2018, “A Coupled CFD-FEA Study of Sound Generated in a Stenosed Artery and Transmitted through Tissue Layers,” *IEEE SoutheastCon 2018*, IEEE, St. Petersburg.
- [190] Gamage, P. P. T., Khalili, F., Azad, M. K., and Mansy, H. A., 2018, “Computational Analysis of Inspiratory and Expiratory Flow in the Lung Airway,” *3rd Thermal and Fluids Engineering Conference (TFEC)*, Fort Lauderdale.
- [191] Salerno, D. M., and Zanetti, J., 1991, “Seismocardiography for Monitoring Changes in Left Ventricular Function during Ischemia,” *Chest*, **100**(4).
- [192] Crow, R. S., Hannan, P., Jacobs, D., Hedquist, L., and Salerno, D. M., 1994, “Relationship between Seismocardiogram and Echocardiogram for Events in the Cardiac Cycle,” *Am. J. Noninvasive Cardiol.*, **8**(1), pp. 39–46.
- [193] Rangayyan, R. M., 2015, *Biomedical Signal Analysis*, John Wiley & Sons.
- [194] Malcangi, M., Quan, H., Vaini, E., Lombardi, P., and Di Rienzo, M., 2017, “Applying the EFuNN Evolving Paradigm to the Recognition of Artefactual Beats in Continuous Seismocardiogram Recordings,” *International Conference on Engineering Applications of Neural Networks*, pp. 256–264.
- [195] Klabunde, R. E., 2012, “Cardiovascular Physiology Concepts (2nd Ed.),” Lippincott Williams & Wilkins, p. 256.
- [196] Wang, Y., Riederer, S. J., and Ehman, R. L., 1995, “Respiratory Motion of the Heart: Kinematics and the Implications for the Spatial Resolution in Coronary Imaging,” *Magn. Reson. Med.*, **33**(5), pp. 713–719.
- [197] Klabunde, R. E., 2012, “Cardiovascular Physiology Concepts (2nd Ed.),” Lippincott Williams & Wilkins, p. 256.
- [198] Mansy, H. A., and Sandler, R. H., 1997, “Bowel-Sound Signal Enhancement Using Adaptive Filtering,” *IEEE Eng. Med. Biol. Mag.*, **16**(6), pp. 105–117.
- [199] Tyberg, J. V., Grant, D. A., Kingma, I., Moore, T. D., Sun, Y. H., Smith, E. R., and Belenkie, I., 2000, “Effects of Positive Intrathoracic Pressure on Pulmonary and Systemic Hemodynamics,” *Respiration Physiology*, pp. 163–171.
- [200] Taebi, A., Sandler, R. H., Kakavand, B., and Mansy, H. A., 2017, “Seismocardiographic Signal Timing with Myocardial Strain,” *Signal Processing in Medicine and Biology Symposium (SPMB), 2017 IEEE*, IEEE, Philadelphia, PA, pp. 1–2.
- [201] Taebi, A., and Mansy, H. A., 2017, “Analysis of Seismocardiographic Signals Using Polynomial Chirplet Transform and Smoothed Pseudo Wigner-Ville Distribution,” *Signal Processing in Medicine and Biology Symposium (SPMB), 2017 IEEE*, IEEE, Philadelphia,

- PA, pp. 1–6.
- [202] Mortola, J. P., Marghescu, D., and Siegrist-Johnstone, R., 2016, “Thinking about Breathing: Effects on Respiratory Sinus Arrhythmia,” *Respir. Physiol. Neurobiol.*, **223**, pp. 28–36.
- [203] Yasuma, F., and Hayano, J. I., 2004, “Respiratory Sinus Arrhythmia: Why Does the Heartbeat Synchronize with Respiratory Rhythm?,” *Chest*, **125**(2), pp. 683–690.
- [204] Bishop, C. M., 2006, *Pattern Recognition And Machine Learning*.
- [205] Kelleher, J. D., Namee, B. Mac, and D’Arcy, A., 2015, *Fundamentals of Machine Learning for Predictive Data Analytics: Algorithms, Worked Examples, and Case Studies*.
- [206] Eddleman, E., 1965, “Kinetocardiographic Changes in Ischemic Heart Disease,” *Circulation*, **32**(4), pp. 650–55.
- [207] Starr, I., and Wood, E., 1961, “Twenty-Year Studies with the Ballistocardiograph, the Relation between the Amplitude of the First Record of ‘health’ Adults and Eventual Mortality and Morbidity Form Heart Disease,” *Circulation*, **23**, pp. 714–32.
- [208] Starr, I., and Noordegroaf, A., 1967, *Ballistocardiography in Cardiovascular Research*, Lippincott. Philadelphia.
- [209] Phibbs, B., Lowe, C., and Holmes, R., 1967, “The Ultra Lowfrequency Force Ballistocardiograph in Acute Cardiomyopathy,” *Circulation*, **36**, pp. 92–100.
- [210] Scherhag, A. W., Pflieger, S., Ceconi, C., Voelker, W., Gehring, J., Staedt, U., and Heene, D. L., 1997, “Evaluation of Signal-Averaged Cardiokymography for the Detection of Ischaemic Left Ventricular Dysfunction,” *Int. J. Cardiol.*, **59**(3), pp. 305–312.
- [211] Matsui, T., Hagsisawa, K., Ishizuka, T., Takase, B., Ishihara, M., and Kikuchi, M., 2004, “A Novel Method to Prevent Secondary Exposure of Medical and Rescue Personnel to Toxic Materials Under Biochemical Hazard Conditions Using Microwave Radar and Infrared Themography,” *IEEE Trans. Biomed. Eng.*, **51**(12), pp. 2184–88.
- [212] Mack, D. C., Patrie, J. T., Suratt, P. M., Felder, R. A., and Alwan, M., 2009, “Development and Preliminary Validation of Heart Rate and Breathing Rate Detection Using a Passive, Ballistocardiography-Based Sleep Monitoring System,” *IEEE Trans. Inf. Technol. Biomed.*, **13**(1), pp. 111–120.
- [213] Gurev, V., Tavakolian, K., Constantino, J., Kaminska, B., Blaber, A. P., and Trayanova, N. A., 2012, “Mechanisms Underlying Isovolumic Contraction and Ejection Peaks in Seismocardiogram Morphology,” *J. Med. Biol. Eng.*, **32**(2), pp. 103–110.
- [214] Tadi, M., Koivisto, T., Pankaala, M., Paasio, A., Knuutila, T., Teras, M., and Hanninen, P., 2015, “A New Algorithm for Segmentation of Cardiac Quiescent Phases and Cardiac Time Intervals Using Seismocardiography,” *Sixth International Conference on Graphic and Image Processing (ICGIP 2014)*, International Society for Optics and Photonics, p. 94432K–94432K.
- [215] Hua, Y., and Sarkar, T. K., 1990, “Matrix Pencil Method for Estimating Parameters of

Exponentially Damped/Undamped Sinusoids in Noise,” IEEE Trans. Acoust., **38**(5), pp. 814–824.